

## Modelling collisionconsequences of unmanned aircraftsystems on human

RattanaGraikanakorn, B.

**DOI**

[10.4233/uuid:dfd526c6-c606-4562-b1e5-ccb984ea1170](https://doi.org/10.4233/uuid:dfd526c6-c606-4562-b1e5-ccb984ea1170)

**Publication date**

2021

**Document Version**

Final published version

**Citation (APA)**

RattanaGraikanakorn, B. (2021). *Modelling collisionconsequences of unmanned aircraftsystems on human*. [Dissertation (TU Delft), Delft University of Technology]. <https://doi.org/10.4233/uuid:dfd526c6-c606-4562-b1e5-ccb984ea1170>

**Important note**

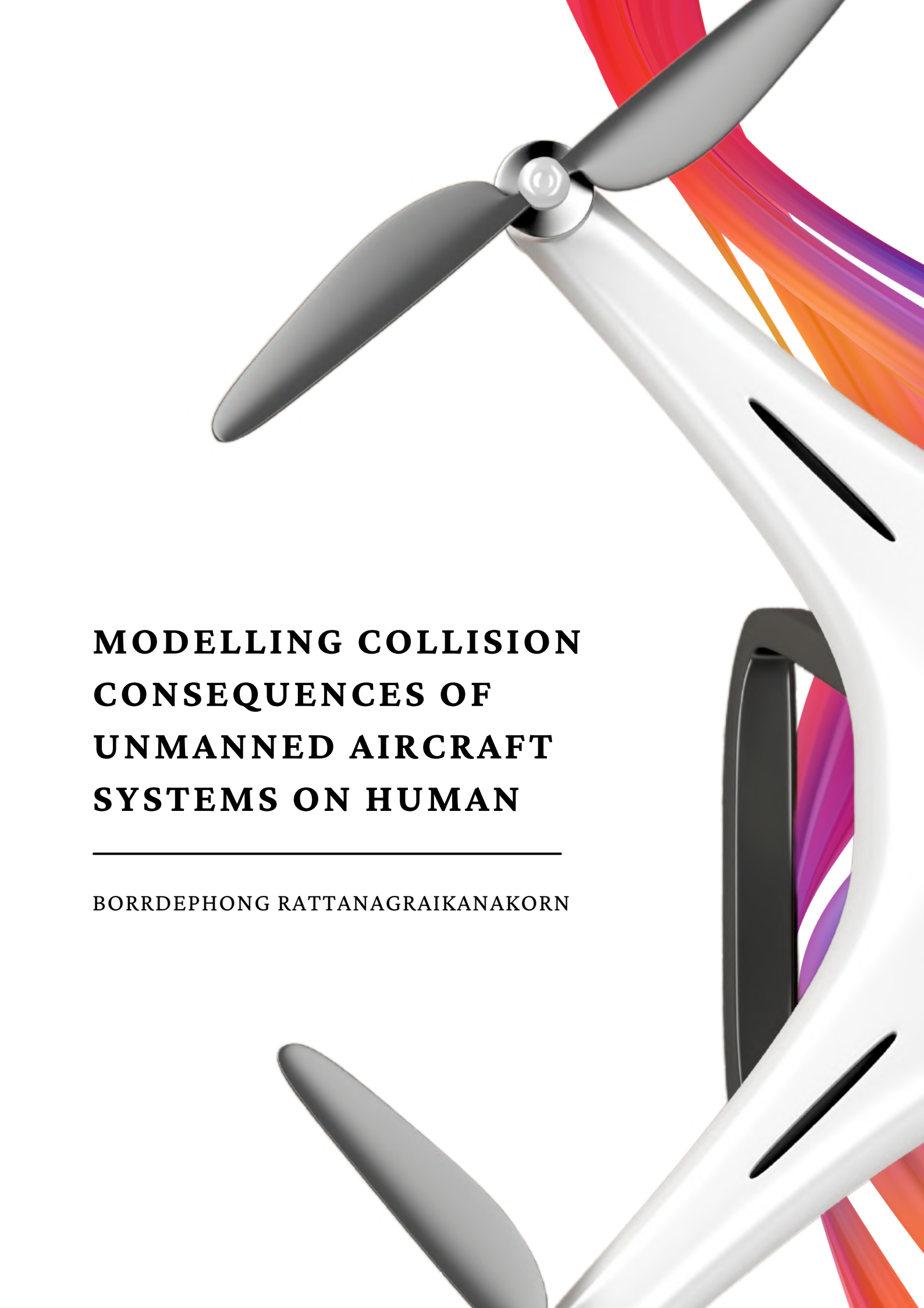
To cite this publication, please use the final published version (if applicable). Please check the document version above.

**Copyright**

Other than for strictly personal use, it is not permitted to download, forward or distribute the text or part of it, without the consent of the author(s) and/or copyright holder(s), unless the work is under an open content license such as Creative Commons.

**Takedown policy**

Please contact us and provide details if you believe this document breaches copyrights. We will remove access to the work immediately and investigate your claim.



**MODELLING COLLISION  
CONSEQUENCES OF  
UNMANNED AIRCRAFT  
SYSTEMS ON HUMAN**

---

**BORRDEPHONG RATTANAGRAIKANAKORN**

# **Modelling Collision Consequences of Unmanned Aircraft Systems on Human**

Borrdephonng Rattanagraikanakorn





# **Modelling Collision Consequences of Unmanned Aircraft Systems on Human**

Dissertation

for the purpose of obtaining the degree of doctor at Delft University of Technology  
by the authority of the Rector Magnificus prof.dr.ir. T.H.J.J. van der Hagen  
chair of the Board for Doctorates to be defended publicly on  
Wednesday 10<sup>th</sup> November 2021 at 12:30 o'clock

by

**Borrdephong RATTANAGRAIKANAKORN**  
Master of Science in Aerospace Engineering, Kingston University, United Kingdom  
born in Bangkok, Thailand

This dissertation has been approved by the promotor:

Composition of the doctoral committee:

Rector Magnificus,	chairperson
Prof.dr.ir. H.A.P. Blom	Delft University of Technology, promotor
Dr. O.A. Sharpans'kykh	Delft University of Technology, copromotor
Ir. M.J. Schuurman	Delft University of Technology, copromotor

Independent members:

Prof.dr. K.H. Low	Nanyang Technological University, Singapore
Prof.dr. J.H. Bolte	Ohio State University, United State of America
Prof.dr. C. Bisagni	Delft University of Technology
Prof.dr. G.C.H.E. de Croon	Delft University of Technology
Prof.dr.ir. R. Benedictus	Delft University of Technology

This research was funded by Delft University of Technology, Faculty of Aerospace Engineering.

Keywords: unmanned aircraft system, impact modelling, multibody system, human, injury

Printed by: Ipskamp Printing ([www.ipskampprinting.nl](http://www.ipskampprinting.nl))

Cover by: Borrdephong RATTANAGRAIKANAKORN

Copyright © 2021 by Borrdephong RATTANAGRAIKANAKORN

ISBN 978-94-6366-463-9

An electronic copy of this dissertation is available <http://repository.tudelft.nl/>.

*To my wife who always walks beside me,  
To my parents who always love me,  
and to my sisters who always stand by me*



---

# Acknowledgements

The value of any research is unmeasurable and I share the same thought for mine. However, the value of my research turns minuscule when compared to the extraordinary experience and knowledge I have received from extraordinary people who stood behind the success of this thesis. With all honesty, the experience with these people is what I will hold dear for a very long time. Getting to this point in my career and earning my PhD would not have been possible without this group of people, so here are my sincerest thanks to them.

To Dr.Alexei Sharpanskykh, whom I would like to express my greatest appreciation. Thank you very much for supporting me on the technical, and more importantly, on the emotional share throughout this PhD journey. A successful thesis will not be possible without your enormous support. Thank you for always trying to bring out the best in me, encouraging me when things got rough, and for putting sense back into me when I met my lows. The hardest part in my PhD journey, and perhaps in others, is the psychological barrier. Without your help and guidance, I probably will never be able to climb over this great barrier. You are the reason that my PhD became much more than an effort to academic excellence, but also to the discovery of one true self. I and Mai will always remember a great dinner of stampot, “The Dutch Comfort Food”, you introduced to us. We look forward to going back and have more stampot with you.

I owe my deepest gratitude to Prof.Henk Blom for shaping me into a stronger person with solid self-belief. You have taught me one of the important life’s lessons that is the integrity of oneself. You have made my PhD journey much more worthwhile than just the act of producing knowledge itself. I also thank you for helping me acquire the knowledge to produce better research and taking hours after hours iterating our papers together. Training someone to carry out proper research takes immense effort, so for that, I thank you for all your patience, mentoring and encouragement. More importantly, thank you for showing me the power of sincere and honest opinion that comes from pure intention.

Dr.Derek Gransden, you are the first person I met in Delft. I can never express enough how grateful I feel to have you as my supervisor. Since my interview week, you warmly welcome me and guided me around the city. I really enjoyed our long conversations together, and truly appreciated all the dedication and guidance you provided me along this PhD journey. Without your suggestions on lump parameter mass modelling, we will never arrive at the impact model that we have now. Even though you had to return to Canada before halfway through the project, you always made time to assist and joined-in in every meeting.

Michiel Schuurman, I am truly thankful to have you as my supervisor and have your guidance over the years. You were quick to support me on every need and always connected me to the right people. Your visions on research were remarkable and always inspiring. The first two years at SIC was very productive – thanks to your guidance and skill in experimentation and investigation. When it comes to teaching and producing high-quality works, your creativity always impresses me. Thank you for going extra mile in helping me though this journey.

Christophe De Wagter, to me, you are an engineering and research genius who always have special angles to view the problems. Your encouragement, suggestions and comments were invaluable. Your insights on UAS designs greatly contributed to taking the right direction for the project. You always challenged and encouraged me to see things differently and to do better than I already can. Thank you for showing your confidence in me and for giving me this opportunity to work with you.

I would like to express my appreciation to Prof. Rinze Benedictus, who is my second promoter, for all the support he provided during my PhD. To Prof. Rinze, you are a role model of an academic leader that I aspire to be. Your management, negotiation and charismatic communication skills are inspiring. Thank you for all the advice and mentoring on how to navigate around wisely on my PhD when collaboration with many parties can be very delicate.

One of the key persons behind the successful development of our UAS multibody system model for impact assessment is Prof. Riender Happee from 3ME. To Prof. Riender, I would like to thank you for all the valuable advice on impact modelling, and for introducing me to MADYMO and the human body model that you developed. MADYMO and its complete human body models were the game-changing ingredients of my thesis. It would not be possible to perform such elaborate and complex studies without your guidance. For this, I owe you my sincerest gratitude.

This thesis has reached its completion state by the collaborative nature of people at the university, especially at the ASML lab. One of the most important people behind the successful development of my impact model is Misja Huizinga. To Misja, thank you for your dedication, professionalism, and kind support on every experimental task. I really enjoyed our time working together in the laboratory where I got to learn so much about Dutch culture. Because of you, my model was developed based on accurate, high-quality data. I would like to express my gratitude to Dr. Jurij Sodja who supported me immensely on the ground vibration testing and structural elasticity modelling. Jurij, you were very kind and supportive. The ground vibration test that we did allow me to approximate the structural damping coefficient, which was the key ingredient to my impact model. This thesis success will never be possible without your help.

A PhD journey in itself would not be complete without good company of friends. Matthieu Vert, my neighbour in Den Haag, my colleague at ATO, my fitness partner at SportCity, my investment buddy and, more than anything, my best friend in the Netherlands. The memory of King's Day 2018 in Amsterdam will always be vivid for me and Mai when we laughed on your "Physics theorist" joke. Thank you for moving to Den Haag for which made the city much more alive than before. The memory of my PhD will never be as warm and beautiful without you in our lives.

To Chengpeng Jiang, I really enjoyed working with you on risk modelling and have someone working in a similar field. Before your arrival, it was difficult to feel inspired by working alone. Having you as a colleague and co-author really pushed my creativity and productivity. I look forward to seeing more of your excellent research and hope we can continue our work together.

To my ATO colleague, so many of you I have spent a brief time with, but it was always enjoyable and delightful at every coffee break and lunch. To Stef Janssen, the coding wizard and a very good friend and colleague. Thank you for the photography book "The Netherlands at its best" you gave me. I still look at it from time to time when I think of life in the Netherlands as a reminder of the good old days. Hao Ma, I always enjoyed

our conversation together and sharing the highs and lows of our PhD was very helpful. Wim, I was impressed to first hear of how you progress through your PhD at such a quick pace with outstanding achievement. To Juseong, Marie and Hemmo, I always enjoyed our little chat in the office and during the coffee break. Thank you for warmly welcoming me to the office and for all the support during my time there.

To my SIC colleague, thank you so much for all the enjoyable conversation we had together. Lunch during summer in front of the building will always be my favourite part at SIC. To Romina Fernandes, no one can ever ask for a more lovely officemate and colleague. I will always remember having a little walk and a fun conversation with you after lunch. To Jesse van Kuijk, I am really glad to have you as my officemate. Learning Dutch culture and politics, and every other thing in life from you were very enjoyable. Your achievement in life has been inspiring and I am certain that we will see more from you in the future. To Yuzhe, thank you for joining our little office and for bringing joy with you. It was always fun to converse with you and to bump into you in the lab. Also, to Neil, Pedro, John-Alan, Chirag, Nicolas, Xi Li, Nakash, Megan, and Bram, thank you very much for such an enjoyable time you gave me at SIC. It was always fun to listen to and join in on your conversation, whether it was on politics, life, science or even Eurovisions. Thank you so much for making my time at SIC a memorable moment.

To my two sisters, thank you very much for always standing by me and for always taking care of mom and dad while I was away doing my PhD and living my dream. No one can ever ask for better sisters who always love, care and support me. To have such a complete and happy childhood with you two is a luxury that I am lucky to have. To Aunt Yuan, thank you for all the wonderful time you gave us in London and for being our only family in Europe. To Aunt Nongkran and Aunt Gab, my sincere thanks to you for all your support and understanding, and for always being there whenever we needed you.

To my parents, thank you so much for raising me into the person I am which I know was not easy. You are the inspiration for me to get through any obstacle in life. You taught me to love people, love my work and love everything around me – that is where I always find my true strength. There is no word to describe my appreciation to you, except that this PhD thesis is for you. To mom who always dream of doing a PhD and to dad who never even got a chance to finish a Bachelor degree, you have raised a son who now holds a PhD - so this PhD degree is for you.

Last, but most important person to my PhD journey, I would like to thank my wife for walking through this PhD journey with me, for her love and constant support, for all the late nights and early mornings, and for keeping me sane over the past few years. Thank you for being my muse, editor, proofreader, and sounding board. It was a tough road for you but you never falter and never stop supporting my dream. This journey has been a true testament to our 15 years relationship. Behind the success of this work was you standing strong to support and encourage me. Thank you for turning this PhD journey into a life worth living and for making our first lovely home together in the Netherlands. No one could have asked for a better wife, and a true friend. This achievement is not mine alone, but ours.





---

# Summary

## **Modelling Collision Consequences of Unmanned Aircraft Systems on Human**

Borrdephong Rattanagraikanakorn

Unmanned aircraft system (UAS) is an emerging technology that is now gaining traction around the world. UAS operations are expected to be integrated into very-low-level rural and urban airspace via the enabling of the novel concept of unmanned traffic system (UTM). For such operations to become a reality, one of the major challenges that needs to be overcome is the assessment and, subsequently, mitigation of safety risk posed to third parties on the ground.

Third parties on the ground refer to people or pedestrians that resides within the area of operation but are not involved with the operation. To assess this risk, an approach called third-party risk (TPR) assessment has been developed in many research. Prediction of TPR of UAS operations will allow operators, authorities and stakeholders make well-informed decision on the deployment of UAS operations. If the TPR risk level of the designed operational concept exceeds the acceptable risk level, then risk mitigation can then be applied.

In a typical TPR model, one of the important sub-models is the collision consequence model used to predict probability of fatality (PoF) of human subjected to UAS collision. This sub-component requires a good understanding of human fatality due to inflicted injury by UAS collision which is, at this time of writing, still under-studied.

This thesis addresses the key component of the TPR framework that is the quantification of UAS collision consequence on human on the ground. The central aim of this thesis is to develop a quantitative, model-based collision consequence model of UAS collision on human. To achieve this main aim, a series of interrelated research studies was performed in a systematic way.

The first study investigates the novel UTM concept to characterize UAS collision consequences with other airspace users. In this study, a step-wise, systematic approach to characterize UAS collision consequences is proposed which includes UTM analysis, object

identification and classification, impact zone analysis, materials characterization and collision consequence analysis. These steps would allow an establishment of a risk picture of the possible collisions with UAS and possible consequences that follow.

The second study addresses the development of an impact model of the DJI Phantom III UAS. The reason for selecting this UAS type is that crash test data on crash dummy have been published. The aim is to develop a computationally efficient, and realistic impact model of quadcopter UAS on human body. The multibody system (MBS) modelling approach was used. The MBS UAS model was developed and validated against impact data under various scenarios on a Hybrid III crash dummy. The validation showed good convergence between the MBS model and impact data. Then, by using the validated UAS model, impact collision of UAS on the head of 50<sup>th</sup> percentile male human head was performed with variations in impact elevation angles. Using head injury criterion and neck injury criterion, injury evaluation showed that human head suffers from serious injury due to UAS impact and with minor neck injury.

From the second study, it was found that there is a discrepancy in the measured head and neck injuries between the Hybrid III crash dummy and the human body models. This leads to the third study in the series which is to evaluate such differences. Again, using the same validated UAS impact model on Hybrid III crash dummy and human body models, a range of impact scenarios was analysed. The analysis results reveal that the Hybrid III crash dummy is not well suited for horizontal-side impact or vertical load direction. Under these conditions, the crash dummy neck is substantially stiffer than the human body neck. This leads to a larger head injury and lower neck injury in the crash dummy when compared to the human body. The root cause of such discrepancy was found to come from the difference between a true human neck and the Hybrid III designed neck complex.

The fourth study is the investigation on the differences in human fatality rate between the MBS model and the commonly adopted RCC model and BC model. The RCC and BC models are the two existing collision consequence models for UAS impact on human which are widely used in UAS TPR research. An MBS UAS model of the DJI Phantom III was simulated in impact scenario on human body and the results were compared against the RCC and the BC models. Significant differences in PoF between the three models were observed, with the RCC predicting the highest PoF. The MBS model predicts lower PoF than the RCC, but higher than the BC model. Another interesting feature of the MBS model is its ability to vary impact condition such as UAS angle of attack or impact attitude. There is a large variation in PoF observed for impact on the head in the MBS model when the UAS angle of attack and impact angle was changed. Such variation is not captured by the RCC or BC models.

The final study investigates the effect of UAS types variation on human injury. In addition to the validated MBS model of DJI Phantom III, MBS models of five other small UAS types are developed. Five true UAS types were selected, namely, DJI Phantom III, DJI F450, Tarot LJI500, Parrot Bebop and TrueXS Racing UAS. These were selected due to their differences in mass, maximum speed, airframe materials and configuration design. Also, a hypothetical UAS was modelled as a single rigid body representation of the DJI Phantom III of the same mass. The study shows the effect of UAS design characteristics on injury severity. The first aspect is the maximum speed of UAS which has a major influence on impact injury. A micro racing UAS with high enough speed can yield high impact energy that results in fatal injury. The second aspect is the applicable elasticity at first contact which has not been studied before using impact simulation. Such elasticity is influenced by UAS configuration, airframe materials and airframe design, and helps to absorb and dampen impact energy. Elastic components such as flexible landing gears or camera gimbals are perfect protective materials

that can reduce impact injury significantly. Such findings show how fatal impact injury can be mitigated via the use of elastic protective components around UAS.

As can be concluded from the interrelated series of studies in this thesis, the proposed MBS modelling framework proves to be an efficient approach for UAS blunt force impact modelling and simulation. The technique allows fast model scalability and extensibility with quick model calibration using experimental inertial properties. The MBS modelling results obtained for UAS impact modelling contribute largely to the quantification of a collision consequence of UAS impact on the human body. Since the existing collision consequence model such as the RCC or the BC models are not directly derived from UAS impact data, this work offers a more realistic alternative collision consequence model for UAS impact on human. The MBS modelling approach offers a possibility to evaluate collision risk under various impact scenarios which can be implemented in UAS TPR assessment. Future TPR research can either utilize the PoF findings from this work, or develop and integrate an MBS impact model into TPR risk assessment.



# Contents

SUMMARY .....	V
<b>1. INTRODUCTION .....</b>	<b>1</b>
1.2 UAS OPERATIONS.....	2
1.3 GROUND THIRD-PARTY RISK FOR UAS OPERATIONS.....	4
1.4 UAS COLLISION CONSEQUENCE MODEL ON HUMAN BODY .....	6
1.5 IMPACT MODELLING & ANALYSIS APPROACH FOR UAS COLLISIONS.....	8
1.6 PROBLEM STATEMENT & THESIS OVERVIEW .....	9
REFERENCES .....	13
<b>2. CHARACTERIZING UAS COLLISION CONSEQUENCES IN FUTURE UTM.....</b>	<b>19</b>
2.1 INTRODUCTION .....	20
2.1.1 <i>Safety of UAS Traffic Management (UTM)</i> .....	20
2.1.2 <i>Consequence of UAS Collision</i> .....	20
2.2 MODELING AND ANALYSIS OF UAS COLLISION CONSEQUENCES .....	21
2.2.1 <i>Organization of the Research</i> .....	21
2.3 UTM DIMENSION ANALYSIS .....	22
2.3.1 <i>UTM in Europe</i> .....	22
2.3.2 <i>UTM in the USA</i> .....	25
2.3.3 <i>Dimensions of UTM</i> .....	26
2.4 IDENTIFICATION & CLASSIFICATION OF OBJECTS EXPOSED TO COLLISION RISK .....	27
2.4.1 <i>Identification of Ground Objects</i> .....	27
2.4.2 <i>Airborne Objects Identification</i> .....	29
2.4.3 <i>Non-UAS Object Classification</i> .....	30
2.4.4 <i>UAS object classification</i> .....	30
2.5 ZONE OF IMPACT ANALYSIS .....	31
2.5.1 <i>Zone of Impact Analysis for General Aviation and Rotorcraft</i> .....	31
2.5.2 <i>Zone of Impact Analysis for UAS</i> .....	35
2.6 MATERIALS IDENTIFICATION AND CLASSIFICATION .....	36
2.7 COLLISION CONSEQUENCE ANALYSIS .....	37
2.8 CONCLUSION.....	38
APPENDIX 2A: ADDITIONAL MATERIALS IDENTIFICATION RESULTS .....	40
APPENDIX 2B: PRIMARY CONSEQUENCES OF UAS COLLISION WITH NON-UAS OBJECTS FROM SECTION V.....	42
REFERENCES .....	47
<b>3. MULTIBODY SYSTEM MODELING OF UAS COLLISIONS WITH THE HUMAN HEAD.....</b>	<b>51</b>
3.1 INTRODUCTION .....	52
3.2 MULTIBODY SYSTEM MODELS .....	53
3.2.1 <i>UAS Multibody System Modeling</i> .....	53
3.2.2 <i>UAS Vehicle Parameters</i> .....	54
3.2.3 <i>Calibration of UAS Multibody System Model</i> .....	55
3.2.4 <i>Multibody System Models of Human Body and Crash Dummy</i> .....	56
3.2.5 <i>Contact Model</i> .....	56
3.3 VALIDATION OF MULTIBODY SYSTEM MODEL .....	57
3.3.1 <i>Vertical Impact Validation</i> .....	58
3.3.2 <i>Angled Impact Validation</i> .....	61
3.3.3 <i>Horizontal Impact Validation</i> .....	63
3.3.4 <i>Head Injury Criteria (HIC) Levels</i> .....	65
3.4 UAS IMPACT ON THE HUMAN BODY.....	66
3.4.1 <i>Head Injury Criteria (HIC)</i> .....	66
3.4.2 <i>Neck Injury Criteria (<math>N_{ij}</math>)</i> .....	68
3.5 DISCUSSION .....	71
3.5.1 <i>Discussion on UAS MBS Modeling and Validation Results</i> .....	71
3.5.2 <i>Discussion on Human Body Injury, Limitations and Future Work</i> .....	72
3.6 CONCLUSIONS .....	73
3.7 ACKNOWLEDGMENT.....	74
APPENDIX 3A: EFFECT OF COMPONENT STIFFNESS ON HEAD FORCE .....	75

REFERENCES .....	77
<b>4. MODELLING HEAD INJURY DUE TO UNMANNED AIRCRAFT SYSTEMS COLLISION: CRASH DUMMY VS HUMAN BODY.....</b>	<b>81</b>
4.1 INTRODUCTION .....	82
4.2 MODELLING AND SIMULATION APPROACH.....	83
4.2.1. UAS, Hybrid III and Human Body Models.....	83
4.2.2. Simulation Setup.....	83
4.3 MODELLING RESULTS FOR HYBRID III DUMMY VS. HUMAN BODY.....	85
4.3.1. UAS Impact Injuries .....	85
4.4 DISCUSSION .....	93
4.5 CONCLUSIONS .....	94
APPENDIX 4A: HEAD CG ACCELERATION-TIME HISTORY .....	96
APPENDIX 4B: UPPER NECK $F_z$ -TIME HISTORY .....	97
APPENDIX 4C: UPPER NECK $M_y$ -TIME HISTORY .....	98
REFERENCES .....	99
<b>5. MODELING AND SIMULATING HUMAN FATALITY DUE TO QUADROTOR UAS IMPACT..</b>	<b>101</b>
5.1 INTRODUCTION .....	102
5.2 REVIEW OF MAIN BACKGROUND .....	103
5.2.1. RCC Fatality Risk Curve .....	103
5.2.2. Blunt Criterion (BC) Model.....	104
5.2.3. MBS Modelling and Simulation of DJI Phantom III Impact of Human Head.....	106
5.3 MBS SIMULATION-BASED ASSESSMENT OF HEAD, THORAX AND ABDOMEN INJURY CRITERIA.....	108
5.3.1. DJI Phantom III UAS Impact Scenarios.....	108
5.3.2. Head Injury Criteria and MBS Simulation Results.....	109
5.3.3. Thorax and Abdomen Impact Criteria and MBS Simulation Results.....	110
5.4 MAPPING INJURY CRITERIA TO PROBABILITY OF FATALITY.....	112
5.4.1. Probability of Fatality Curve for Head impact.....	112
5.4.2. Probability of Fatality Curves for Thorax & Abdomen Impact.....	113
5.5 COMPARISON OF FATALITY CURVES FROM DIFFERENT MODELS .....	114
5.5.1. Comparison of PoF of Head Impact .....	114
5.5.2. Comparison of PoF of Thorax Impact.....	115
5.5.3. Comparison of PoF of Abdomen Impact .....	116
5.6 DISCUSSION OF RESULTS .....	116
5.7 CONCLUSIONS .....	117
REFERENCES .....	118
<b>6. VARIATION IN HUMAN INJURY AND FATALITY FROM IMPACTS BY DIFFERENT UAS TYPES OF SIMILAR WEIGHT.....</b>	<b>123</b>
6.1 INTRODUCTION .....	124
6.2 SELECTION OF SMALL UAS TYPES AND MBS MODELLING .....	125
6.2.1. Selection of UAS Types.....	125
6.2.2. UAS Multibody System Models.....	126
6.2.3. Joint Types and Force/Moment Characteristics.....	129
6.2.4. Contact Characteristics .....	132
6.2.5. MBS Model of Human Body and Head Injury.....	132
6.2.6. Conversion to Probability of Fatality.....	134
6.3 IMPACT SCENARIO SELECTION AND SIMULATION SETUP .....	134
6.3.1. Controlled Horizontal Flight Impact .....	134
6.3.2. Uncontrolled Vertical Drop Impact .....	135
6.4 MBS RESULTS FOR CONTROLLED HORIZONTAL FLIGHT IMPACT.....	137
6.4.1. Head Injury Criterion ( $HIC_{15}$ ).....	137
6.4.2. Probability of Fatality (PoF).....	138
6.4.3. Head CG Acceleration-Time History.....	139
6.4.4. Neck Injury ( $N_{ij}$ ) .....	140
6.4.5. Discussion of Controlled Horizontal Flight Impact Results.....	140
6.5 MBS RESULTS FOR UNCONTROLLED VERTICAL DROP IMPACT .....	143
6.5.1. Head Injury Criterion ( $HIC_{15}$ ) & Probability of Fatality (PoF) .....	143
6.5.2. Head CG Acceleration-Time History.....	144

6.5.3. <i>Discussion of Uncontrolled Vertical Drop Impact Results</i> .....	146
6.6 CONCLUSIONS .....	147
APPENDIX 6A: MBS MODEL & IMPACT TEST COMPARISON .....	149
REFERENCES .....	151
<b>7. CONCLUSION</b> .....	<b>155</b>
7.1 RESULTS OBTAINED FOR RESEARCH OBJECTIVES .....	156
7.2 CONTRIBUTIONS.....	159
7.3 FUTURE WORK.....	161
REFERENCES .....	163
<b>CURRICULUM VITAE</b> .....	<b>165</b>
<b>LIST OF PUBLICATIONS</b> .....	<b>167</b>





---

## Introduction

*This chapter provides an introduction to UAS operations, ground third party risk, UAS collision consequence and impact modelling topics addressed in this thesis. It describes the thesis goal and objectives, the problem, the UAS impact modelling approach, and the applications. Furthermore, the thesis overview will be clarified by means of short chapter descriptions which explain how each individual chapter is linked to the overall research.*

## 1.2 UAS Operations

Unmanned aircraft systems (UAS) have been gaining momentum in recent years and their extensive use has induced the quick growth of related research areas. The FAA [1] predicts that, by 2023, recreational and commercial UAS fleet size will reach 2 to 3 million in numbers. This quick growth in numbers will bring about a substantial rise in the expected volume of operations. Many commercial applications have successfully used UAS to execute missions, both in the military and in civil areas. Aerial photography has been the most popular types of UAS operations that already see real-world implementation. Major events such as a concert, or public event have used UAS for aerial shots. Parcel or food deliveries in remote and urban areas using UAS promise a new operating venue for future businesses to connect to customers excitingly and effectively. Parcel delivery using UAS also has the potential to decongest urban road traffic [2]. Research and developments of UAS delivery have already been started by main players in the logistics business. DHL Express and Ehang entered into a strategic partnership in China to develop and implement fully autonomous UAS loading and offloading that will increase efficiency and cost-effectiveness with less energy consumption [3]. In the third quarter of 2020, Amazon Prime Air which has been pushing forward UAS delivery in urban areas received flight permission to begin conducting UAS delivery operations by the Federal of Aviation Authority (FAA) [4].

To cope with this rising operational demand, rules, regulations, and concept of operations have been established and developed by aviation authorities and research institutes. The main goal is to integrate UAS into non-segregated airspace that would eventually allow novel commercial operations in congested, urban environment. In Europe, three key components addressed are rules and regulations, UTM ConOps and digitalized infrastructure.

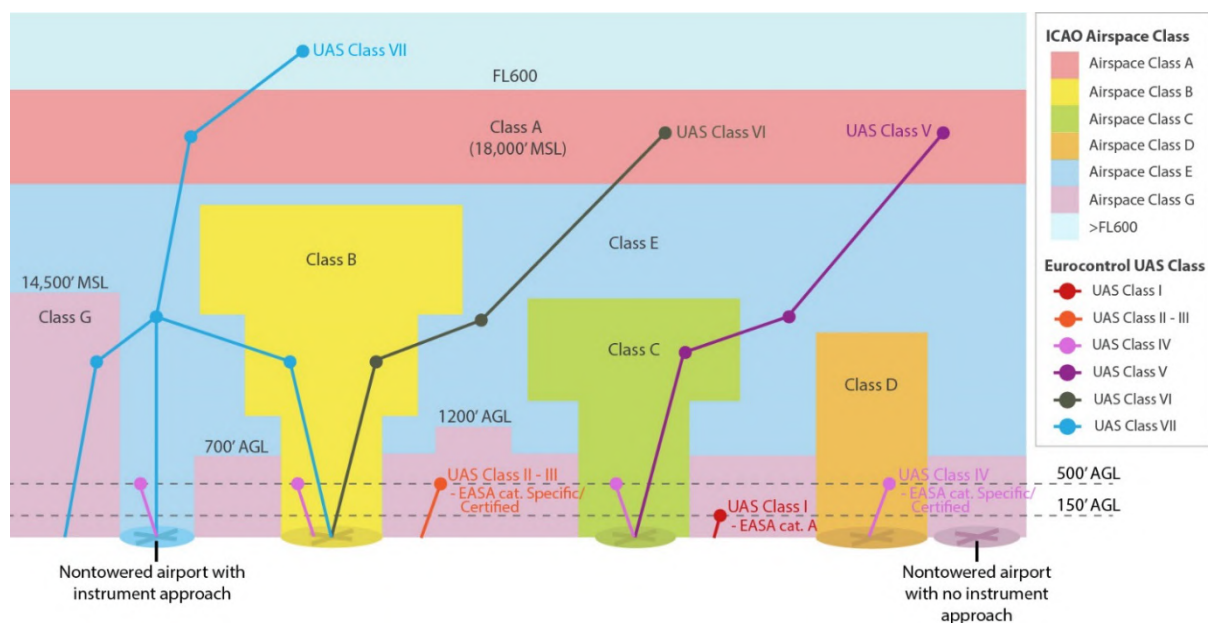
**Table 1.1. Overview of important UAS performance and operational requirements from EASA prototype rules and regulations.**

UAS Category	Weight (kg)	UAS Type	Max Alt (ft)	Horizontal Separation (m)	Operation Type	
Open	A-0	0.25	Micro UAS	150	Not specified, but less than 100 m away from operator	VLOS
	A-I	25	Micro UAS Small UAS	150	Not specified, but within VLOS range from operator	VLOS
	A-II	25	Micro UAS Small UAS	150	50 m away from uninvolved person	VLOS
	A-III	25	Micro UAS Small UAS	500	20 m away from uninvolved person for rotorcraft, or 50 m otherwise	VLOS, EVLOS
Specific	-	-	-	-	VLOS, EVLOS, BVLOS	
Certified	-	-	-	-	-	

For the first component, rules and regulations are developed by EASA [5]. As the risk of operating UAS varies according to the type of operations and the characteristics of UAS, different rules are applied to different categories based on risk-level that EASA has foreseen. EASA proposed that, for the lower risk operations, regulations should have less-stringent requirements. Open category is a lower risk category for general public use, while the Specific and Certified categories are for higher risk operations which require much stricter rules and certification. In 2016, EASA [5] published the first prototype UAS regulatory framework which define operational requirements of UAS in the Open and Specific Categories. Following the prototype regulations, additional amendments were released by EASA [6,7] with specific requirements for Certified category. EASA's regulations for UAS is summarized in Table 1.1.

The table shows that for majority of UAS operations, maximum altitude is restricted to less than 500 ft and Open category is subjected to Visual-line-of-sight (VLOS) operation only. Extended-visual-line-of-sight (EVLOS) or Beyond-visual-line-of-sight (BVLOS) is possible but mainly available for Specific and Certified category.

After the release of EASA prototype regulations, EUROCONTROL [8] proposed the second key component which is the first draft of unmanned traffic management (UTM) ConOps. This ConOps aims to enable UAS operations in manned airspace in conjunction with EASA regulations. The concept is to integrate UAS into manned operations, without disrupting or modifying the already existing manned air traffic system. Figure 1.1 illustrates how different UAS classes specified by EUROCONTROL will be integrated into different manned airspace classes. UAS operations are now categorized in Class. UAS Class I is in line with EASA Open category AI-III which is only allowed in Class G airspace under 150 ft. UAS Class II-IV are designed in conjunction with EASA Specific and Certified category to accommodate more advanced higher-risk BVLOS operations in Class B, C, D, E airspace. The planning of future use of UAS by EUROCONTROL extends to even high altitude operations in Class A and beyond through flight transition in lower airspace Classes. Such operations are categorized as UAS Class V-VII and are intended for advanced research or military operations.



**Figure 1.1.** The lines and dots show how various Eurocontrol [8] UAS classes operate through various ICAO [9] airspace classes in Europe. The idea of this presentation is based on a figure in the Instrument Flying Handbook [10]. For very low level (VLL) operation, UAS class I, II and III will only be allowed to operate in airspace class G and UAS class IV will be allowed to operate in airspace class B, C, D and E.

The third key component is the digitalized infrastructure to accommodate high UAS operational demands and UTM system complexity. This is called the U-Space concept which was proposed by SESAR Joint Undertaking [11]. The idea of U-Space is to provide digitalized services and procedures for UAS operations in order to support safe, efficient and secure access to airspace for high-density UAS traffic. It also provides an enabling framework to support routine UAS operations with a clear and effective interface to manned aviation, ATM/ANS service providers and authorities. This is a laid-out ground work for implementing UAS operations in very-low-level (VLL) operations in urban airspace that is below 150 m. With this digitalized infrastructure, it is expected that UAS operations will soon be allowed

integrated into rural and urban areas where the population density of human on the ground is high.

In the US, similar development has been taking place as well. Starting in 2012, research into small UAS management has been prompted by the Federal Aviation Administration's (FAA) under the Modernization and Reform Act [12]. This has led to several key development of rules and regulations for UAS operations by the FAA which is now known as Part 107 to Title 14 of the Code of Federal Regulations (14CFR), or Part 107 in short [13]. This current version allows visual line of sight (VLOS) operations within both segregated and unsegregated airspace. However, this regulation is not yet ready for large scale VLOS operations nor autonomous beyond visual line of sight (BVLOS) operations. To enhance UAS operations towards autonomous BVLOS and large scale multiple UASs operation, the National Aeronautics and Space Administration (NASA) [14] has initiated the unmanned traffic management (UTM) framework research and has successfully demonstrated the concept of operations through trial operations. In early 2020, NASA has been released the latest unmanned traffic management (UTM) concept of operations (ConOps) version 2 [15] that provides a digitalized infrastructure that will support UAS operations in VLL US airspace. This will enable UAS operations over an urban area.

It is clear that significant effort has been devoted to integrating UAS operations into VLL airspace via the introduction of UAS rules and regulations and UTM system. However, it also presents novel challenges. One of the major challenges is to predict and subsequently mitigate safety risk posed by UAS on other airspace users. Since majority of commercial UAS operations in rural and urban airspace will be permitted under flight altitude of 150 ft and segregated from manned aviation's based on the regulations proposed by EASA [7], this makes human on the ground exposed to UAS collision risk if an accident occurs. Therefore, for VLL UAS operations, collision risk on human third parties on the ground seems prominent. This is also called ground third-party risk. The adequate methods to predict ground third-party risk is important for how VLL UAS operations should be designed or what appropriate rules and regulations should be put in place.

### **1.3 Ground Third-Party Risk for UAS Operations**

Third-party risk (TPR) has long been an essential aspect in commercial aviation and has been well defined by Eurocontrol [16]. There also exists first and second parties risks. First-party is the aviation personnel (who provide the air transportation service); second-party are the passengers (for whom the air transportation is provided); third-party are the people exposed for reasons unrelated to the flight, for instance people living in the airport vicinity [17]. Assessment of TPR in commercial aviation is commonly performed using indicators such as Individual Risk, Collective Risk and the FN curve [18,19].

For UAS operations, risks involving first, second and third parties are defined differently from commercial aviation. Based on Clothier et al. [20], first-party risk refers to people and property directly associated with the UAS operation such as UAS pilot or the UAS vehicle. Second-party risk applies to people and property not associated with the UAS operation, but directly derive benefit from the UAS operation such as infrastructure being inspected or parcel being delivered. Third-party risk applies to people and property not associated with, nor deriving direct benefit from the UAS operation.

The ability to predict TPR of UAS operations would enable operators, authorities and stakeholders to make well informed decision on the deployment of UAS operations. If TPR assessment shows the risk level exceeds beyond the acceptable risk level, then risk mitigation

is necessary. TPR assessment for UAS operations is an essential component towards enabling UAS operations, especially in urban areas populated ground third-party.

Studies have been performed to assess the TPR of UAS flights using probabilistic or stochastic modelling approaches. Primatesta et al. [21] developed a probabilistic ground risk assessment approach for fixed-wing and quadcopter UASs by incorporating several layers, such as population density, sheltering factor or obstacles. This method also considers various descent modes of the UAS. La Cour-Harbo [22] proposed a stochastic model for quantifying the ground fatalities probability from an uncontrolled descent of BVLOS fixed-wing UAS flights. These maps are used to see if any current or future urban area is exposed to unacceptable risk levels. Ancel et al. [23] developed the UTM Risk Assessment Framework (URAF) which was developed to provide real-time safety evaluation and tracking capability within the UTM concept. This framework allows a collision risk assessment of people on the ground by calculating the potential impact area and the effects of the impact. Bertrand et al. [24] proposed a ground third-party risk assessment approach for long-range fixed-wing UAS that is based on the casualty risk analysis approach developed by Clothier et al. [25]. A Monte Carlo approach for quantifying risk on the ground of a fixed-wing UAS is proposed by Rudnick-Cohen et al. [26]. The approach incorporates kinetic energy for impact severity and the probability distribution of impact locations to construct risk metrics. Melnyk et al. [27] proposed using a Target Level of Safety approach and an event tree format, populated with data from existing studies that share characteristics of UAS crashes to enable casualty prediction for UAS operations. These works commonly measure the expected number of fatalities due to UAS colliding on the ground per flight hour as the TPR indicator. Grimme [28] proposed a Monte Carlo model using simplified quadcopter UAS dynamics model for simulating individual risk which measures probability that an average unprotected person at ground location would get killed from an accident during a given annum.

Models based on probabilistic approach for predicting ground third-party risk by UAS operations proposed in [21–28] are commonly composed of 5 sub-models.

The first sub-model is for predicting UAS ground collision frequency. Various sub-models for predicting ground collision frequency have been developed for various event types. Barr [29] developed this first sub-model using Bayesian Belief Net. Bertrand et al. [24] also proposed such sub-model using a Fault Tree model. In addition to this, probabilistic models and Monte-Carlo simulation methods have been employed to develop this first sub-model for ground collision frequency prediction. Sub-model for UAS with fixed wing configuration has been developed in [21,23,24,26,28]. Sub-models for helicopter have been developed in [22,30] and for quadcopter UAS have been developed in [21,31,32].

The second sub-model is a density map of human population on the ground. To account for population density, a uniform population density is used in [20,27,33–35].

The third sub-model is a shelter protection probability map of the operational area considered. This is commonly represented in a form of the probability that a person is sheltered against a crash of the UAS flight.

The fourth model is the probability that an unprotected person at a given location is being hit by a UAS crash. These sub-models have been developed and used in UAS TPR assessment in [22,27,33–36].

The fifth sub-model is for the collision consequence model for predicting the probability of fatality (PoF) in case of UAS impact of a human on the ground. The main model used in [21,24,37] is the Range Commanders Council (RCC) curves [38,39] and another main model used in [22,40] is the Blunt Criterion (BC) model [40].

All of these sub-models are still under-studied and present opportunity for further extension. However, because the fifth component asks for the combined discipline analysis on safety risk, impact modelling, human injury, and UAS design fundamentals, this is why it is chosen as the main focus for this thesis. This project largely benefits from a multidisciplinary supervisory teams which combines expertise in the field of safety risk, structural impact modelling, and UAS operations, therefore, the challenges presented in the fifth sub-model is appropriate for this thesis.

## 1.4 UAS Collision Consequence Model on Human Body

Most of the UAS safety risk research that requires quantification of collision consequence, or PoF, resort to existing collision consequence such as the RCC or the BC models.

One of the well-known collision consequence models that is often used for UAS impact on the human body has been proposed by Range Commanders Council (RCC) [38]. It is commonly known as the RCC curves and the curves are shown in Figure 1.2. This model originally was developed for evaluation of missile explosion on ground personal using explosive test data from the work of Feinstein et al. [41]. Feinstein assessed injury curves based on a large database of collision dynamics and effects of small, rigid, metallic fragments on human body parts. This RCC model has seen it is used in several UAS safety risk studies [21,24,37]. This RCC model was proposed as a common risk criterion where the S-shaped curves of impact energy vs probability of fatality (PoF) were developed to quantify the probability of fatality if a person is impacted in either the head, thorax or abdomen.

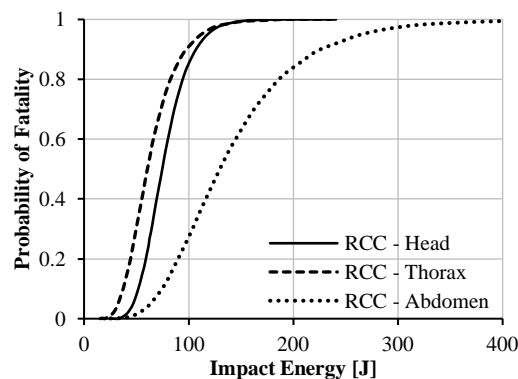
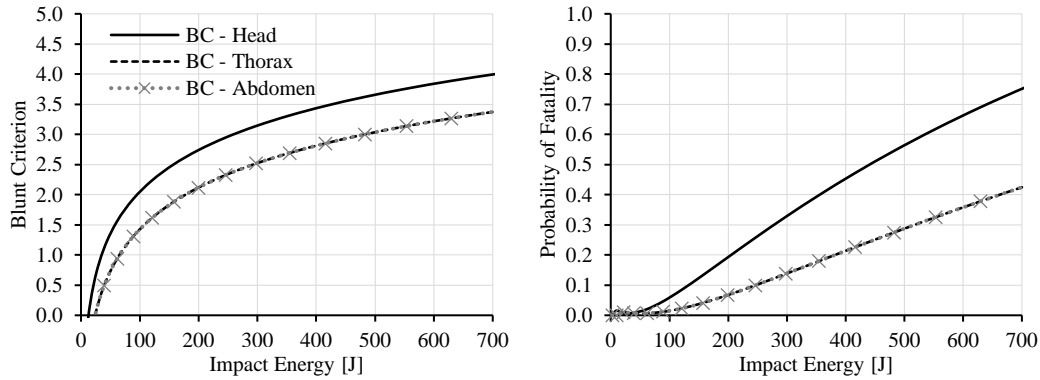


Figure 1.2. RCC log-normal fatality risk curve for head, thorax and abdomen adapted from [38].

Another impact model of thorax and abdomen injury that is widely used in UAS ground risk analysis [22,40] is the Blunt Criterion (BC) model [40] shown in Figure 1.3. Developed by Sturdivan [42,43], BC is an energy-based model that has been used by the U.S. Department of Defense to assess vulnerability to blunt weapons and projectile impacts. The main data set used for deriving the BC model is based on blunt impact injury data of human thorax [44]. By integrating BC with the Abbreviated Injury Scaling (AIS), the BC can be transformed to PoF which is a useful quantification of impact injury for safety risk assessment since PoF is an essential input for safety risk quantification model. Unlike the RCC curves, the BC model is developed purely for blunt impact force which does not inflict penetration or laceration-type of injury.



**Figure 1.3. BC curves (left) adapted from [40] and the transformed PoF curves (right) for head, thorax and abdomen impact as a function of kinetic energy.**

Even though the RCC and BC models are already widely used in UAS safety risk studies, these models show a large discrepancy of predicted PoF. Both of these models are developed to extended to be used for UAS impact, but the experimental data used to derive the model are not directly from UAS impact. The RCC is derived from small-debris explosive experimental data, while the BC is derived from large-surface area blunt force experimental data. This clearly shows the need for further investigation on such discrepancy which requires an investigation directly on UAS impact.

There is still a need to better understand and quantify the true consequence of UAS collision on human body. To do this, the ASSURE Research Group conducted testing and analysis of a DJI Phantom III UAS drop impacts on an anthropomorphic test dummy (ATD) of a human [45,46]. The experiments provide useful insights into impact dynamics between the UAS and the head and neck of the ATD. They also reveal that the RCC model predicts a much higher head injury level than what is measured in the drop tests on the ATD of a human [45]. Based on similar experimental impact test, Koh et al. [47,48] also conducted extensive drop tests and computational crash simulations of different drone weight classes on a crash dummy head. Besides, Campolettano et al. [49] performed a series of live flight test and impact drop test using three different UAS weight classes on an instrumented Hybrid III crash dummy. The test aimed to estimate the range of injury risks to humans due to UAS impact. Furthermore, a team at Ohio State University [50] performed impact tests of multiple UAS types using post mortem human surrogates (PMHS). These findings of these live tests have revealed that there is significant variation in levels of injury risks to humans due to UAS impacts. Also, the test outcomes show that impact attitude of UAS on the human body part is highly sensitive parameters for injury severity.

Experimental impact tests of UAS collision on human body parts provide valuable insights into the dynamics of UAS impact on human and injury severity sustained by human body. However, the data produced from these tests are not enough to establish a generalized collision consequence model that allows a prediction of PoF of human due to UAS collision. This is because these impact tests are both expensive and time-consuming, which limits the range of impact scenarios to be explored. Therefore, there is a need for a collision consequence model for predicting PoF that is applicable for UAS impact on human and can capture the effect of variation in impact speed, attitude and location.

## 1.5 Impact Modelling & Analysis Approach for UAS Collisions

With the deficiency in existing collision consequence models for UAS collision on human, several research focuses on experimental impact testing methods as outlined above. However, the experimental impact testing method only allows limited runs due to high experimental cost, making it difficult to cover large impact conditions (e.g. impact direction, attitude, or speed).

Such difficulty can often be overcome by using a computational model. Finite element modelling (FEM) and simulation techniques are widely used for static and dynamic structural modelling and analysis. This could be a potential option for solving the UAS collision consequence problem. Nevertheless, FEM comes with high computational cost and modelling complexity. This leads to long computational time for one impact simulation run. This long computational time is also identified in the work of Koh et al. [47] who attempted to simulate UAS collision on human head using FEM. This limited the amount of simulation runs that Koh et al. [47] could perform, and thus, limited the amount of impact data generated. FEM is most effective when the modelling problem requires a high-fidelity model that can capture materials' non-linear local deformation and breakage.

However, UAS to human collision does not require such level of detail to approximate injury level sustained from a collision. Typically, overall kinematics of the human body (e.g., head acceleration or neck force/moment) is needed to approximate, for example, head or neck injury level through various injury criteria.

A more applicable modelling technique that comes with the much lower computational cost is the multibody system (MBS) modelling. This modelling approach is a physical model-based numerical modelling technique that is widely adopted in automotive crashworthiness studies and well-suited for biomechanics injury analysis in a high-speed collision scenario.

In the work of Vadlamudi et al. [51], the MBS approach was implemented to evaluate occupant protection systems in a military helicopter under the crash scenario. This work involves the MBS model of helicopter structural deformation that interacts with a human occupant body during a collision. In high g-loading impact scenario, Guida et al. [52] used an MBS approach to simulate a 16g frontal impact a seat of a commercial aircraft to assess injury sustained by human occupant. In a similar aircraft occupant survivability analysis, Hamid et al. [53] developed an MBS model of aircraft bulkhead and coupled with human body model to measure optimal values for the bulkhead compliance and displacement requirements that minimize occupant injury. MBS approach is also widely used in automotive crashworthiness. It is often used to evaluate and optimize automotive structural compliance that minimizes collision injury on either occupant or bystander [54–56].

When compared to FEM, MBS modelling technique is more applicable for UAS blunt force analysis on two aspects which are computational cost, and model extensibility.

First, even though FEM comes with higher model fidelity, FEM technique has higher computational cost than MBS model which substantially limits the amount of impact scenario to be simulated. With cheap computational cost of the MBS model, wide range of sensitivity analysis can be performed to investigate the injury effect of, for example, UAS impact energy, impact position offset, or impact angle.

Second, MBS has a strong advantage over FEM particularly on model scalability and extensibility. Since the MBS model is a simplified lumped-mass system, extending the baseline UAS model to other UAS types can be done relatively easy compared to FEM. Inertial



characteristics of UAS can be obtained experimentally and an update can be made from the baseline MBS UAS model. On a contrary, FEM requires a completely new model development of other UAS types with precise model geometrical representation and accurate materials properties.

The MBS is a promising modelling approach for blunt-force collisions that has the potential to overcome the above-outlined limitations of the existing impact models and the expensive experimental impact test. Since the MBS approach offers fast computational time with the ability to predict accurate human injury, it can be used to simulate large variation of impact scenarios and necessary sensitivity analysis, to establish an applicable PoF curve for UAS impact on human. Therefore, this thesis aims to develop a collision consequence model of UAS collision on human body using the MBS modelling approach.

## **1.6 Problem Statement & Thesis Overview**

In the beginning of this PhD research, there was a need to develop a quantitative model-based safety risk analysis approach for very low level UAS operations. The approach would form an essential part of safety management part of UAS operations. Such modelling approach requires an in-depth and well elaborated of likelihood and consequence models. The likelihood model would involve a prediction of probability of a UAS hitting a person on the ground, while the consequence model would involve a prediction of probability of fatality when UAS hits a human on the ground. The combination of the two models would allow an evaluation of risk level of UAS operations which would allow an identification of safety requirement or bottleneck through sensitivity analysis. The identification of UAS safety criteria can be performed with such safety risk model and would serve as a very useful into further development of UAS concept of operations.

At the initial phase of this research, it was found that the consequence modelling of UAS collision on human was understudied and largely missing. There was an immediate need for such studies to be performed in order to have a better understanding of UAS collision consequences on human. Such studies would need to allow an establishment of probability of fatality threshold of UAS collisions on human body before a full safety risk analysis of UAS operations can be performed.

With the initial study done on modelling of quadcopter collision on human body, it was realized that there were further needs of a more in-depth analysis for such collisions. It was found that various UAS impact parameters and conditions play significant roles in the resulting fatality rate of the human body. This shows that there are more questions that need answers for UAS to human collisions. Therefore, the main aim of this thesis is;

**To develop a quantitative, physical model-based collision consequence model for UAS impact on human body.**

To achieve the main aim, multiple related objectives are defined in logical sequences and address in each chapter as described in the following:

**Objective 1: To characterize collision consequence types due to UAS operations within very low-level airspace under the novel UTM concept**

The unmanned traffic management system (UTM) was introduced by NASA [14] in The United States and EUROCONTROL [8] in Europe. This innovative idea brought excitement, as well as, underlying challenges because, under this concept,

UAS will be expected to operate within highly congested urban area. Understanding the complexity of the UTM concept and its operational environment is essential. UTM is an innovation concept design to accommodate UAS operations both in rural and urban area. What follows are the set of rules and regulations. All of these factors dictate the nature of UAS operations, and what possible safety issues may arise from it. Since UAS operations will happen among other airborne vehicles, ground vehicles, infrastructure, as well as, human on the ground. This widens the scope of collision consequence analysis of UAS operations. An approach is needed to help characterize collision types of UAS under such novel UTM concept.

The work addressed Objective 1 is presented in Chapter 2 where a step-wise approach for identifying the various types of collision consequence under a novel UTM concept, focusing on the VLL UAS operations, is proposed. The approach addresses the analysis of the UTM ConOps, rules, and infrastructure considered, and the identification of types of objects and UASs that will operate in the VLL UTM system. It also characterizes impact materials by applying zone of impact analysis. The overall aim is to systematically identify and characterize the types of collision consequences as well as applicable impact materials and conditions that will form the basis for follow-on research.

**Objective 2: To develop a parameterized impact model for blunt force injury assessment of UAS impact on human body.**

As this thesis started during the time in which the UTM concept was introduced, it was apparent that the knowledge on UAS collision on aircraft or human were not matured yet. It was also known that UAS operations would be designed in segregation from manned aircraft. This directs research attention towards UAS collision on human, since human on the ground would be most exposed to UAS operations. Thus, there is an immediate need to develop a realistic impact modelling approach that would allow human injury evaluation due to UAS collision. Such impact model would be a crucial element in safety risk analysis of UAS operations.

Objective 2 is addressed in Chapter 3 where impact model between a quadcopter UAS and human body is developed by employing a multibody system modelling (MBS) technique. MBS technique would allow a fast computational time and parameterization of various impact conditions. DJI Phantom III quadcopter UAS is chosen for modelling because data from experimental drop tests on a crash dummy is available. This allows the validation of the multibody system model of UAS impacting a crash dummy versus experimental data. Once the model is validated, impact of DJI Phantom III UAS on 50<sup>th</sup> percentile male human body is performed. Head and neck injury are then evaluated.

**Objective 3: To investigate differences in head and neck injury levels on a Hybrid III dummy and on a human body due to UAS collisions.**

Based on the finding in Chapter 3, it was found that there are differences in injury prediction between human body and Hybrid III crash dummy that is widely used in impact UAS collision tests. Because of the limitations in biofidelity of a crash dummy, head injury level for a crash dummy impact may differ from the human body

impact. The discrepancy may leave a large error if impact data from crash dummy is used in safety risk analysis of UAS operations.

An in-depth analysis to address Objective 3 is performed in Chapter 4 where investigation of the differences in head and neck injuries subject to UAS collision between an often-used Hybrid III crash dummy and a human body are evaluated. Multibody system (MBS) impact model is used to simulate UAS impacts on validated models of the Hybrid III crash dummy and the human body at various impact conditions. Head and neck injury are then evaluated and compared.

**Objective 4: To investigate the differences between the MBS model, the RCC curves, and the BC curves for DJI Phantom III impact of human head, thorax, and abdomen.**

In Chapter 5, human head/neck injury due to UAS impact on human head was evaluated. However, this evaluation on head impact alone is not sufficient to establish meaningful human injury threshold from UAS impact. Other body parts such as thorax and abdomen are also important and present even larger surface area than the head. In this Chapter, the multibody system (MBS) impact model for DJI Phantom III is extended to assess PoF of human from UAS impact on thorax and abdomen. Methods for transforming injury criterion to probability of fatality (PoF) for head, thorax and abdomen impact are proposed, so that injuries from three impact areas can become comparable. In addition, the PoFs obtained from MBS models for head, thorax and abdomen are compared against the RCC and Blunt Criteria models.

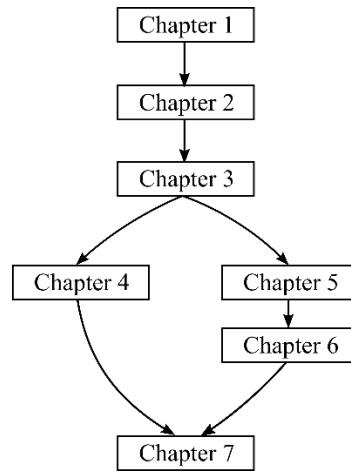
**Objective 5: To investigate the effect of variations in UAS types on human injury and fatality.**

The findings in Chapter 2 show that large variation of actors are involved in UAS operations, either directly or indirectly, especially the types of UAS configurations available to be employ. There is large variation of UAS types with different in mass, design configuration, or materials. The effect of this variations on impact injury are largely unknown. There is a need for a completed impact injury threshold of various UAS by considering variations in UAS types. By leveraging the strength in fast-computational time and easy model extension of the MBS modelling technique, the DJI Phantom III MBS model (baseline model) are extended to investigate other UAS types with different mass, design configuration or materials.

Presented in Chapter 6, the objective is to extend the MBS modelling and assessment approach of collision with human head to four other UAS types than the DJI Phantom III. UAS mass, maximum speed, airframe material and airframe design are the variables taken in to account when selecting other UAS types. In addition to four true UAS types, a hypothetically simplified UAS version of the DJI Phantom III is defined. It is included with a purpose to neutralize the effect of airframe design on head injury severity and PoF. For these selected UAS types, MBS models have been developed and integrated with the MBS model of the human. Subsequently, impact simulations with a human head are performed and the PoF results are analyzed.

Figure 1.4 shows the recommended reading paths for this thesis. Each chapter can be read on its own and each are published articles with fully written story line. However, it is recommended to read Chapters 1, 2 and 3 in consecutive order before continuing on to

Chapters 4 and 5. Chapter 3 is the introduction to impact modelling of UAS using MBS modelling technique and also contain all technical detail of model development, calibration and validation which are essential to the understanding of Chapters 4, 5 and 6. Lastly, Chapter 7 is the conclusion which ties up all major findings, novel contributions, limitations and future work.



**Figure 1.4. The recommended reading paths for this thesis.**

## References

- [1] Federal Aviation Administration, “FAA National Forecast 2019-2039,” 2019, p. 105, URL: [https://www.faa.gov/data\\_research/aviation/aerospace\\_forecasts/media/FY2019-39\\_FAA\\_Aerospace\\_Forecast.pdf](https://www.faa.gov/data_research/aviation/aerospace_forecasts/media/FY2019-39_FAA_Aerospace_Forecast.pdf).
- [2] Hader, M., and Baue, S., “Cargo drones: The future of parcel delivery — Roland Berger,” 2020 URL <https://www.rolandberger.com/en/Point-of-View/Cargo-drones-The-future-of-parcel-delivery.html>.
- [3] DHL, “DHL Express Launches Its First Regular Fully-automated and Intelligent Urban Drone Delivery Service,” 2019 URL <https://www.dhl.com/tw-en/home/press/press-archive/2019/dhl-express-launches-its-first-regular-fully-automated-and-intelligent-urban-drone-delivery-service.html>.
- [4] Business Insider US, “FAA clears Amazon’s fleet of Prime Air drones for liftoff,” 2020 URL <https://www.businessinsider.nl/amazon-prime-air-delivery-drones-faa-ruling-2020-8?international=true&r=US>.
- [5] European Aviation Safety Agency, “Prototype Commission Regulation on Unmanned Aircraft Operations,” 2016, URL: [https://www.easa.europa.eu/system/files/dfu/UAS\\_Prototype\\_Regulation\\_final.pdf](https://www.easa.europa.eu/system/files/dfu/UAS_Prototype_Regulation_final.pdf).
- [6] European Aviation Safety Agency, “Notice of Proposed Amendment 2017-05 (A) - Introduction of a Regulatory Framework for the Operation of Drones,” 2017, URL: [https://www.easa.europa.eu/sites/default/files/dfu/NPA\\_2017-05\\_\(A\)\\_0.pdf](https://www.easa.europa.eu/sites/default/files/dfu/NPA_2017-05_(A)_0.pdf).
- [7] Agency European Aviation Safety, “Notice of Proposed Amendment 2017-05 (B) - Introduction of a Regulatory Framework for the Operation of Drones,” vol. 05, 2018, pp. 1–128.
- [8] Eurocontrol, “RPAS ATM Conops,” 2017, URL: <http://www.eurocontrol.int/sites/default/files/publication/files/rpas-atm-cocept-of-operations-2017.pdf>.
- [9] ICAO, “Annex 11 - Air Traffic Services,” 2001.
- [10] FAA, “Instrument Flying Handbook,” U.S. Department of Transportation Federal Aviation Administration, 2012, doi: 10.1186/s12986.
- [11] Corus Consortium, “U-space Concept of Operations - Enhanced Overview,” 2019, doi: 10.1002/0471028959.sof055, URL: <https://www.sesarju.eu/node/3411>.
- [12] Jiang, T., Geller, J., Ni, D., and Collura, J., “Unmanned Aircraft System traffic management: Concept of operation and system architecture,” *International Journal of Transportation Science and Technology*, vol. 5, Oct. 2016, pp. 123–135, doi: 10.1016/j.ijst.2017.01.004, URL: <https://linkinghub.elsevier.com/retrieve/pii/S2046043016300260>.
- [13] FAA, “Small Unmanned Aircraft Systems, Title 14 of the Code of Federal Regulations (14 C.F.R.), Part 107,” 2017, URL: <https://www.ecfr.gov/cgibin/retrieveECFR?gp=1&SID=dcf7ddb5f58f33726d33d7bc50a36d72&ty=HTML&h=L&mc=true&r=PART&n=pt14.2.107>.
- [14] Kopardekar, P., “Unmanned Aerial System ( UAS ) Traffic Management ( UTM ) : Enabling Low-Altitude Airspace and UAS Operations,” California: 2018.

- [15] National Aeronautics and Space Administration (NASA), “Unmanned Aircraft System (UAS) Traffic Management (UTM) Concept of Operations V2,” *Enabling Civilian Low-altitude Airspace and Unmanned Aircraft System Operations*, 2019, p. <https://utm.arc.nasa.gov/index.shtml>.
- [16] EUROCONTROL, “Feasibility study on the integration of third party risk near airports into impact,” Brussels: 2015.
- [17] Jiang, C., Blom, H. A. P., and Sharpanskykh, A., “Third party risk indicators and their use in safety regulations for uas operations,” *Aiaa Aviation 2020 Forum*, vol. 1 PartF, 2020, pp. 1–15, doi: 10.2514/6.2020-2901.
- [18] Bohnenblust, H., “Risk-Based Decision Making in the Transportation Sector,” *Quantified Societal Risk and Policy Making*, R.E. Jorissen and P.J.M. Stallen, eds., Boston, MA: Springer US, 1998, pp. 132–153, doi: 10.1007/978-1-4757-2801-9\_14, URL: [https://doi.org/10.1007/978-1-4757-2801-9\\_14](https://doi.org/10.1007/978-1-4757-2801-9_14).
- [19] Jonkman, S. N., van Gelder, P. H. A. J. M., and Vrijling, J. K., “An overview of quantitative risk measures for loss of life and economic damage,” *Journal of Hazardous Materials*, vol. 99, 2003, pp. 1–30, doi: [https://doi.org/10.1016/S0304-3894\(02\)00283-2](https://doi.org/10.1016/S0304-3894(02)00283-2), URL: <https://www.sciencedirect.com/science/article/pii/S0304389402002832>.
- [20] Clothier, R. A., Williams, B. P., and Hayhurst, K. J., “Modelling the risks remotely piloted aircraft pose to people on the ground,” *Safety Science*, vol. 101, 2018, pp. 33–47, doi: 10.1016/j.ssci.2017.08.008, URL: <http://dx.doi.org/10.1016/j.ssci.2017.08.008>.
- [21] Primatesta, S., Rizzo, A., and la Cour-Harbo, A., “Ground Risk Map for Unmanned Aircraft in Urban Environments,” *Journal of Intelligent and Robotic Systems: Theory and Applications*, 2019, doi: 10.1007/s10846-019-01015-z.
- [22] la Cour-Harbo, A., “Quantifying Risk of Ground Impact Fatalities for Small Unmanned Aircraft,” *Journal of Intelligent and Robotic Systems: Theory and Applications*, vol. 93, 2019, pp. 367–384, doi: 10.1007/s10846-018-0853-1.
- [23] Ancel, E., Capristan, F. M., Foster, J. V., and Condotta, R. C., “Real-time Risk Assessment Framework for Unmanned Aircraft System (UAS) Traffic Management (UTM),” *17th AIAA Aviation Technology, Integration, and Operations Conference, Denver, Colorado*, 2017, pp. 1–17, doi: 10.2514/6.2017-3273, URL: <https://arc.aiaa.org/doi/10.2514/6.2017-3273>.
- [24] Bertrand, S., Raballand, N., Viguier, F., and Muller, F., “Ground risk assessment for long-range inspection missions of railways by UAVs,” *2017 International Conference on Unmanned Aircraft Systems, ICUAS 2017*, 2017, pp. 1343–1351, doi: 10.1109/ICUAS.2017.7991331.
- [25] Clothier, R., Walker, R., Fulton, N., and Campbell, D., “A Casualty Risk Analysis for Unmanned Aerial System (UAS) Operations over Inhabited Areas,” *2nd Australian Unmanned Air Vehicles Conference*, 2007, pp. 19–22.
- [26] Rudnick-Cohen, E., Herrmann, J. W., and Azarm, S., “Modeling Unmanned Aerial System (UAS) Risks via Monte Carlo Simulation,” *2019 International Conference on Unmanned Aircraft Systems (ICUAS)*, 2019, pp. 1296–1305, doi: 10.1109/icuas.2019.8798313.
- [27] Melnyk, R., Schrage, D., Volovoi, V., and Jimenez, H., “A third-party casualty risk model for unmanned aircraft system operations,” *Reliability Engineering and System*

- Safety*, vol. 124, 2014, pp. 105–116, doi: 10.1016/j.res.2013.11.016, URL: <http://dx.doi.org/10.1016/j.res.2013.11.016>.
- [28] Grimme, W., “Modelling and Monte Carlo Simulation of the Third-Party Risk of Drones,” Delft University of Technology, 2019.
- [29] Barr, L. C., Newman, R. L., Ancel, E., Belcastro, C. M., Foster, J. V., Evans, J. K., and Klyde, D. H., “Preliminary Risk Assessment for Small Unmanned Aircraft Systems,” *17th AIAA Aviation Technology, Integration, and Operations Conference, Denver, Colorado*, 2017, doi: 10.2514/6.2017-3272, URL: <https://arc.aiaa.org/doi/10.2514/6.2017-3272>.
- [30] Haartsen, Y., Aalmoes, R., and Cheung, Y. S., “Simulation of unmanned aerial vehicles in the determination of accident locations,” *2016 International Conference on Unmanned Aircraft Systems, ICUAS 2016*, 2016, pp. 993–1002, doi: 10.1109/ICUAS.2016.7502548.
- [31] Cunningham, K., Cox, D. E., Foster, J. V., Riddick, S. E., and Laughter, S. A., “AirSTAR beyond visual range UAS description and preliminary test results,” *2016 AIAA Guidance, Navigation, and Control Conference*, 2016, pp. 1–14, doi: 10.2514/6.2016-0882.
- [32] Foster, J. V., and Hartman, D. C., “High-fidelity multirotor unmanned aircraft system simulation development for trajectory prediction under off-nominal flight dynamics,” *17th AIAA Aviation Technology, Integration, and Operations Conference, 2017*, 2017, pp. 1–19, doi: 10.2514/6.2017-3271.
- [33] Lum, C. W., and Waggoner, B., “A Risk Based Paradigm and Model for Unmanned Aerial Systems in the National Airspace,” 2011, doi: 10.2514/6.2011-1424.
- [34] Dalamagkidis, K., Valavanis, K. P., and Pieggl, L., “Evaluating the risk of unmanned aircraft ground impacts,” *16th Mediterranean Conf. on Control and Automation*, 2008, pp. 709–716, doi: 10.1109/MED.2008.4602249.
- [35] Weibel, R., and Hansman, R. J., “Safety Considerations for Operation of Different Classes of UAVs in the NAS,” *Aiaa 3Rd “Unmanned Unlimited” Technical Conference, Workshop and Exhibit*, 2004, pp. 1–11, doi: 10.2514/6.2004-6421, URL: <http://arc.aiaa.org/doi/abs/10.2514/6.2004-6421>.
- [36] Lum, C. W., Gauksheim, K., and Kosel, T., “Assessing and Estimating Risk of Operating Unmanned Aerial Systems in Populated Areas,” *11th AIAA Aviation Technology, Integration, and Operations (ATIO) Conference*, Virginia Beach, VA: 2011, pp. 1–12, doi: 10.2514/6.2011-6918.
- [37] Dalamagkidis, K., Valavanis, K., and Pieggl, L., “On Integrating Unmanned Aircraft Systems into the National Airspace System,” Springer Netherlands, 2012, doi: 10.1007/978-94-007-2479-2.
- [38] RCC, “Common risk criteria for National test ranges; Inert debris, Supplement to Standard 321-00,” 2000.
- [39] RCC, “Range Safety criteria for Unmanned Air Vehicles, Rationale and methodology supplement; Supplement to Document 323-99,” 2001.
- [40] Magister, T., “The small unmanned aircraft blunt criterion based injury potential estimation,” *Safety Science*, vol. 48, 2010, pp. 1313–1320, doi: 10.1016/j.ssci.2010.04.012, URL: <http://dx.doi.org/10.1016/j.ssci.2010.04.012>.

- [41] Feinstein, D., Haugel, W., Kardatzke, M., and Weinstock, A., "Personnel Casualty Study. Tech. Rep. Project No. J 6067," 1968.
- [42] Sturdivan, L. M., "Modeling in Blunt Trauma Research," *Proceedings of the Second Annual Soft Body Armor Symposium*, Miami, Beach Florida: Washington DC: Law Enforcement Assistance Agency, U.S. Department of Justice, 1976.
- [43] Sturdivan, L. M., "Non-Lethal Weapons Assessment: Deterrence and Injury - Final Report. Contract M67854-99-M-1062," Quantico, VA: 2000.
- [44] Clare, V., and Sturdivan, L. M., "Blunt Trauma Data Correlation," 1975.
- [45] Arterburn, D., Ewing, M., Prabhu, R., Zhu, F., and Francis, D., "FAA UAS Center of Excellence Task A4 : UAS Ground Collision Severity Evaluation Revision 2."
- [46] Huculak, R., "NIAR UAS Drop Testing Report," Wichita: 2016, URL: [http://www.assureuas.org/projects/deliverables/a11/NIAR Test Report - FAA-UAH UAS Drop Testing.pdf](http://www.assureuas.org/projects/deliverables/a11/NIAR%20Test%20Report%20-%20FAA-UAH%20UAS%20Drop%20Testing.pdf).
- [47] Koh, C. H., Deng, C., Li, L., Zhao, Y., Tan, S. K., Chen, Y., Yeap, B. C., Li, X., and Low, K. H., "Experimental and simulation weight threshold study for safe drone operations," *AIAA Information Systems-AIAA Infotech at Aerospace, 2018*, Kissimmee, Florida: 2018, pp. 1–11, doi: 10.2514/6.2018-1725, URL: <https://doi.org/10.2514/6.2018-1725>.
- [48] Koh, C. H., Low, K. H., Li, L., Zhao, Y., Deng, C., Tan, S. K., Chen, Y., Yeap, B. C., and Li, X., "Weight threshold estimation of falling UAVs (Unmanned Aerial Vehicles) based on impact energy," *Transportation Research Part C: Emerging Technologies*, vol. 93, 2018, pp. 228–255, doi: 10.1016/j.trc.2018.04.021, URL: <https://doi.org/10.1016/j.trc.2018.04.021>.
- [49] Campolettano, E. T., Bland, M. L., Gellner, R. A., Sproule, D. W., Rowson, B., Tyson, A. M., Duma, S. M., and Rowson, S., "Ranges of Injury Risk Associated with Impact from Unmanned Aircraft Systems," *Annals of Biomedical Engineering*, 2017, doi: 10.1007/s10439-017-1921-6, URL: <http://link.springer.com/10.1007/s10439-017-1921-6>.
- [50] Stark, D. B., Willis, A. K., Eshelman, Z., Kang, Y. S., Ramachandra, R., Bolte, J. H., and McCrink, M., "Human Response and Injury Resulting from Head Impacts with Unmanned Aircraft Systems," 2019, doi: 10.4271/2019-22-0002.
- [51] Vadlamudi, S., Blundell, M., and Zhang, Y., "A multi-body systems approach to simulate helicopter occupant protection systems," vol. 8265, 2017, doi: 10.1080/13588265.2011.554203.
- [52] Guida, M., Manzoni, A., Zuppari, A., Caputo, F., Marulo, F., and De Luca, A., "Development of a multibody system for crashworthiness certification of aircraft seat," *Multibody System Dynamics*, vol. 44, 2018, pp. 191–221, doi: 10.1007/s11044-018-9612-0, URL: <http://dx.doi.org/10.1007/s11044-018-9612-0>.
- [53] Lankarani, H. M., Ma, D., and Menon, R., "Multibody dynamics of aircraft occupants seated behind interior walls," *Nonlinear Dynamics*, vol. 6, 1994, pp. 237–246, doi: 10.1007/BF00044987.
- [54] Jenefeldt, F., and Thomson, R., "A methodology to assess frontal stiffness to improve crash compatibility," *International Journal of Crashworthiness*, vol. 9, 2004, pp. 475–482, doi: 10.1533/ijcr.2004.0303.



- [55] Mukherjee, S., Chawla, A., Nayak, A., and Mohan, D., “Rollover crashworthiness of a rural transport vehicle using MADYMO,” *International Journal of Crashworthiness*, vol. 11, 2006, pp. 495–503, doi: 10.1533/ijcr.2005.0121.
- [56] Ambrósio, J., and Dias, J., “A road vehicle multibody model for crash simulation based on the plastic hinges approach to structural deformations,” *International Journal of Crashworthiness*, vol. 12, 2007, pp. 77–92, doi: 10.1533/ijcr.2006.0171.



---

## Characterizing UAS Collision Consequences in Future UTM

*UAS will be integrated into the airspace in the near future, but the risk of UAS collision is not well understood which hampers the development of adequate regulations and standards. As risk has two constituents: frequency and consequence, collision risk analysis of UAS operations in future UTM asks for a quantitative assessment of various types of frequency and consequence. However, prior to studying such quantitative assessment, it is a prerequisite to identify the various types of collisions and consequences. Doing the latter is the objective of this paper. This paper follows a step-wise approach in identifying the various types of collision consequence under a given UTM ConOps, focusing on the very-low-level UAS operations. The first steps address the analysis of the UTM ConOps, rules, and infrastructure considered, and the identification of types of objects and UASs that will operate in the very-low-level UTM system. The follow-up steps are to characterize impact materials by applying zone of impact analysis, followed by analyzing the types of collision consequence. The result is a systematic identification and characterization of types of collision consequences as well as applicable impact materials and conditions that will form the basis for safety risk analysis in follow-on research.*

This chapter has been published as “B. Rattanagraikanakorn, A. Sharpanskykh, M. Schuurman, D. Gransden, H.A.P. Blom, C. De Wagter, Characterizing UAS collision consequences in future UTM, Proc. 18th AIAA Aviation Technology, Integration, and Operations Conference (ATIO2018), 25-29th June 2018, Atlanta, Georgia.”

## **2.1 Introduction**

### **2.1.1. Safety of UAS Traffic Management (UTM)**

The idea of integrating unmanned aircraft systems (or UAS) into the airspace system and having this technology as part of daily operations is getting closer to a reality as the immense effort has been put into developing the unmanned aircraft system traffic management (UTM), rules, regulations and supporting infrastructure that are crucial to a safe operation. Several safety organizations and research institutes, such as the National Aeronautics and Space Administration (NASA) [1] and EUROCONTROL [2] are currently designing the UTM system to support a large-scale implementation of UAS technology into manned airspace. Federal Aviation Agency (FAA) [3] or European Aviation Safety and Agency (EASA) [4] are also currently devising prototype rules and regulations to ensure safety for both airborne and ground personnel. At the very same time, much effort has been made to understand the safety risk posed by UAS to other airspace users, ground vehicles, ground personnel and infrastructure within the UTM. This is a crucial process in the design of the UTM system which ensures that the high-level of safety standard in aviation can be retained, as well as to ensure the harmonization of the integration process of the system.

Many safety risk assessment methods have been proposed by many research groups in which both a qualitative and quantitative risk analysis approach, and probabilistic model-based approach have been employed. Burdett et al. [5] proposed the implementation of the functional hazard assessment (FHA) method to understand the risk of UAS operations via the derivation of hazards and an analysis of the consequence of such hazards. Belcastro et al. [6] also identified current and future hazards from UAS in the future UTM based on a collection of UAS mishaps data and UAS safety cases – such analysis formed an essential basis for further safety risk analysis. Building on the identified hazards by Belcastro et al. [6], preliminary risk assessment of UAS operations was done by Barr et al. [7] using both a standard qualitative risk analysis approach and a probabilistic model-based approach based on the Bayesian Belief Networks (BBNs) model. Clothier [8] developed a bow-tie model [9,10] for structuring a safety case for UAS operations, including mid-air collision scenarios. Clothier et al. [11] also extended this bow-tie model to ground collisions for UAS operations near populous areas to support the development of regulations and safety cases.

For a quantitative approach to determine frequency or probability of UAS collision, Tyagi and Zhang [12] proposed a system-wide UAS safety analysis model for estimating the probabilities of safety occurrences such as near-miss and mid-air collision (MAC). The model was coupled with Bayesian Belief Network based analysis tool to determine the most likely root causes and the most effective mitigation strategies of such collisions. Ground collision frequency was investigated by Lum et al. [13], who proposed a method for estimating a number of pedestrian collisions per flight hour using satellite imagery and census information. Complementary to this frequency directed studies of UAS collisions, there is an obvious need to study the large spectrum of possible collision consequences.

### **2.1.2. Consequence of UAS Collision**

In recent years, significant research has been directed to understanding the effect of UAS collisions with various types of objects, including manned aircraft and human on the ground. Through the collision task force research group, EASA [14] identified important impact consequence research directions that remain to be addressed. To improve an understanding of impact severity, the Alliance of System Safety of UAS through Research Excellence (ASSURE) [15], investigated the consequence of UAS ground and airborne

collisions. The research group employed both numerical analysis and experimental techniques to determine impact severity on the human body due to UAS collision at various impact conditions. In addition, a biomedical research team at Virginia Polytechnic institute and State University (Virginia Tech) [16] investigated injury risk to human due to UAS collision by using live flight test and drop impact test on a human dummy. Regarding UAS collision impact on aircraft, an analysis model of UAS ingestion into high-bypass engines was developed by Crash Lab at Virginia Tech [17,18]; the results showed that UAS can pose a serious threat to commercial aircraft jet engines. Also, a particular interest was paid to impact analysis of UAS collision on small aircraft and rotorcraft by the UK Department of Transport [19] in collaboration with industry which pointed out that even a small UAS can inflict a critical damage to rotorcraft tail rotors and non-impact-certified windscreen.

With the introduction of the new operational paradigm, such as the beyond-line-of-sight (BVLOS) operation with increasing use of autonomous systems, UAS operations become more complex. Moreover, UAS operations tend to be operated among other airborne vehicles, ground vehicles, infrastructure, as well as a human on the ground. This widens the scope of the collision consequence analysis of UAS operation. Therefore, the aim of this paper is to address this wider scope of collision consequence modeling and analysis.

## **2.2 Modeling and analysis of UAS collision consequences**

For a systematic modeling and analysis of consequences of UAS collisions with other objects, primary and secondary collisions are differentiated. A primary collision refers to the first contact between a UAS and another object. A secondary collision refers to a subsequent collision with another object that happens as a result of a primary collision. To limit its scope, the current paper addresses primary collisions only. In order to capture the large spectrum of potential types of primary collisions and consequences, the modeling and analysis are organized along the following sequence of systematic steps:

1. UTM Dimension Analysis
2. Object Identification and Classification
3. Zone of Impact Analysis
4. Materials Identification and Classification
5. Collision Consequence Analysis

The first step aims to conduct an analysis of the UTM ConOps, rules and regulations. The second step aims to identify and classify the various objects that are exposed to UAS collision risk. The third step analyzes the possible zones of impact for each of the object classes. The fourth step identifies the relevant materials for each type of impact zone. The last step characterizes the types of collision consequence for each impact zone. The elaboration of this systematic modeling and analysis of UAS collision consequences is expected to provide a useful framework for the collection and organization of consequence modeling, simulation, and experimentation of primary collision of UAS with another object.

### **2.2.1. Organization of the Research**

This paper is organized as follows. Section II provides an analysis of the UTM dimensions. Section III presents the identification of UAS and the objects that are exposed to UAS collision risk. Section IV presents an analysis of the Zone of Impact of a UAS collision with focus on the various types of general aviation aircraft and rotorcraft. Section V presents an identification and classification of the materials for different zones of impact of selected

objects. Section VI presents the results of the collision consequence analysis for different zones of impact of the selected objects. Section VII presents conclusions.

## **2.3 UTM Dimension Analysis**

This section analyzes the UTM concept of operations, rules, and regulations, which form the legal basis of what type of UAS will be allowed to operate in different airspace classes. Currently, both in the USA and in Europe, the future UTM concept of operations (ConOps) is in development, along with new rules and regulations. This section presents an outline and a dimension analysis of UTM currently in development in Europe and in the USA.

### **2.3.1. UTM in Europe**

In Europe, UTM is being developed by several collaborating organizations. To fully understand the whole UTM architecture, each component needs to be analyzed separately, namely; UTM ConOps, rules and regulations, and supporting infrastructure. First, the prototype rules and regulations proposed by EASA [20] are analyzed. Rules and regulations significantly dictate the operational requirements of UTM. They also specify performance requirements and operational limitations of UAS in the airspace. Next, the UTM ConOps that is under development proposed by EUROCONTROL [2] is investigated. Furthermore, the support infrastructure that is proposed by SESAR [21] called “U-Space” is examined. This digitalized infrastructure is aimed to enable complex drone operations with a high degree of automation to take place in all types of operational environments, including urban areas. Finally, the important dimension of European UTM is summarized in the table at the end of this section.

#### ***EASA UAS Prototype Rules and Regulations***

To ensure safe operations of UAS, EASA [5] has published the prototype rules and regulations for UAS operations in the Open and Specific categories. Another category is the Certified category which has not been fully proposed yet during the write up of this paper. As the risk of operating UAS varies according to the type of operations and the characteristics of UAS, different rules are applied to different categories based on risk-level that EASA has foreseen. EASA proposed that, for the lower risk operations, regulations should have less-stringent requirements. Open category is a lower risk category, while the Specific and Certified categories are for higher risk operations which require much stricter rules and certification. Detailed elaborations of each category are presented below.

##### ***Open Category:***

For the Open category, there are 4 sub-categories which are A0, AI, AII, and AIII category. Open A0 applies to micro UAS with a maximum weight of less than 0.25 kg. Open AI and AII apply to both micro and small UAS with a maximum weight of 25 kg and a maximum altitude of 150 ft. Open AIII has the same weight threshold as AI and AII but with a higher operational altitude of up to 500 ft.

##### ***Specific Category:***

Furthermore, the Specific category is designed for more advanced commercial UAS operations, such as infrastructure monitoring, aerial photography in urban areas, or operation in the vicinity of airports. However, to operate in the Specific category, the operation must comply with the ‘standard scenario’ requirements specified by EASA.

### *Certified Category:*

For the Certified category, there is no information available during the write-up of this paper, however, this category is expected to be applied to specialized high-risk operations. Different sub-categories have different UAS requirements and the important requirements are summarized in Table 2.1.

**Table 2.1. Overview of important UAS performance and operational requirements from EASA prototype rules and regulations. The UAS Open category applies to recreational, buy-and-fly UAS type which only allows operation below 500 ft. The Specific category is for commercial UAS operation in VLL airspace. The Certified category is for UAS operations that may pose higher risk to other objects.**

UAS Category	Weight (kg)	UAS Type	Max Alt (ft)	Horizontal Separation (m)	Operation Type	
Open	A-0	0.25	Micro UAS	150	Not specified, but less than 100 m away from operator	VLOS
	A-I	25	Micro UAS Small UAS	150	Not specified, but within VLOS range from operator	VLOS
	A-II	25	Micro UAS Small UAS	150	50 m away from uninvolved person	VLOS
	A-III	25	Micro UAS Small UAS	500	20 m away from uninvolved person for rotorcraft, or 50 m otherwise	VLOS, EVLOS
Specific	-	-	-	-	VLOS, EVLOS, BVLOS	
Certified	-	-	-	-	-	

### ***EUROCONTROL UTM System ConOps***

Recently EUROCONTROL [2] proposed the first draft of UTM ConOps that aims to enable UAS operations in manned airspace. The concept is to integrate UAS into manned operations, without disrupting or modifying the already existing manned air traffic system. Figure 2.1 illustrates how different UAS classes specified by EUROCONTROL will be integrated into different manned airspace classes. The main idea is to differentiate UAS operations based on traffic classes without segregating UAS categories. According to EUROCONTROL [2], a traffic class is a set of flying rules, operational procedures and system capabilities applicable to the UAS and to the operator when operating the UAS in a portion of the airspace. Each traffic class already, in its own description, specifies what type of operations are allowed. Traffic class I to IV fall within VLL airspace below 500 ft while traffic class V to VI belong to IFR/VFR airspace. Lastly, traffic class VII belongs to the very high-altitude airspace. Each UAS traffic class is elaborated below.

#### ***UAS Class I - IV***

For VLL airspace, UAS class I is designed for recreational use without any structured route for UAS to follow, and the maximum height is only 150 ft above ground level. This class is allowed to operate in airspace class G and falls into EASA Open category. UAS class II is designed for commercial operations that do not need or cannot follow a structured route, such as survey or search and rescue. UAS class III is designed to accommodate complex commercial operations such as parcel delivery by using a structured route approach where a route structure can follow a river or railway. Both UAS class II and III are allowed to operate in airspace class G but need to follow EASA Specific and Certified category rules. This already widens the scope of objects that will be involved with UAS operations, such as, trains or maritime vehicles. Moreover, UAS class IV is designed for special operations in urban areas, airports, and other restricted airspace. This UAS class is allowed to operate in airspace class B, C, D and E, and must comply with EASA Specific and Certified category rules.

### UAS Class V - VI

For IFR/VFR operations that are higher than 500 ft, the UAS operation falls under UAS class V and VI. UAS in these classes are required to comply with the airspace requirements as set for IFR/VFR manned aviation. Operations from this class can include airport operations, terminal maneuvering area (TMA) or enroute. Therefore, rules and regulations for these classes will not follow EASA rules for UAS but will follow airspace rules for manned aviation.

### UAS Class VII

Lastly, UAS class VII is designed to accommodate very high altitude UAS at flight level above 60,000 ft. Even though the operation will take place above IFR/VFR flight corridor, UAS in this class is expected to comply with IFR/VFR flight rules since the transition has to pass through this corridor. Therefore, IFR/VFR requirements need to be met by this UAS class. Operations that are envisioned to operate in this class are, for example, long-endurance UAS operation for relaying communication across the globe, or suborbital UAS operations.

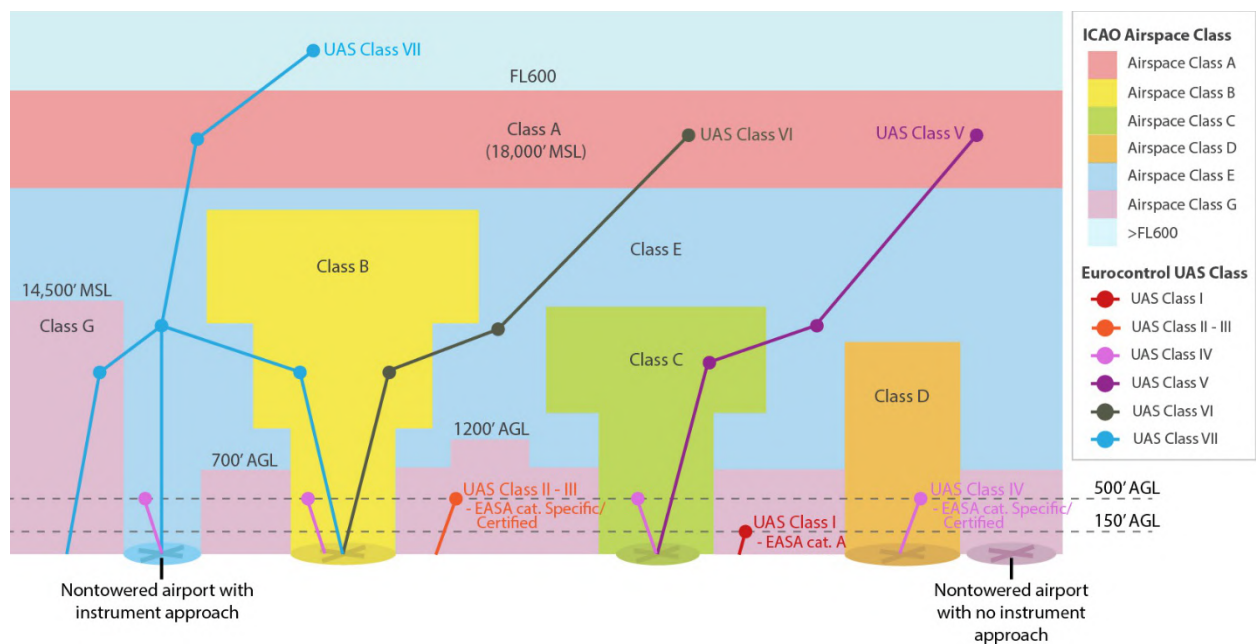


Figure 2.1. The lines and dots show how various Eurocontrol [2] UAS classes operate through various ICAO [22] airspace classes in Europe. The idea of this presentation is based on a figure in the Instrument Flying Handbook [23]. For VLL operation, UAS class I, II and III will only be allowed to operate in airspace class G and UAS class IV will be allowed to operate in airspace class B, C, D and E.

The analysis shows that the complexity and interdependencies of the ConOps, rule, and regulations lead to an intricate multi-dimension problem. Therefore, it is necessary to identify relevant dimensions that can be analyzed in a logical manner.

### SESAR U-Space Concept

In order to accommodate high UAS operational demands and UTM system complexity, SESAR Joint Undertaking proposed the concept of U-Space in 2016 [21]. U-Space provides complete services and procedures designed to support safe, efficient and secure access to airspace for high-density UAS traffic. This aims to enable complex drone operations that will take place in all types of operational environment (including urban area) with a high degree of automation. U1 is the first phase of implementing U-Space system. E-registration, E-identification, and static geofencing will be available to help control UAS from entering the segregated airspace. In the next phase, U2, flight planning management system will be



introduced. Dynamic airspace information, such as dynamic geofencing will be employed to protect a certain type of manned aircraft operations that could take place without prior notice, for example, search and rescue operations. U3 phase introduces capacity management and assistance for conflict detection. This phase relies on the availability of automated ‘detect and avoid’ system that allows UAS to operate in dense traffic area or urban area. The last phase is the U4 phase which aims to assist the full integration of UAS operations to manned airspace by providing infrastructure for information sharing and connectivity between UASs and manned aviation. In short, the U-Space system will provide the necessary support infrastructure that will allow UASs to operate fully with manned aviation, even in dense traffic areas or urban areas.

### **2.3.2. UTM in the USA**

UTM in the USA is also under development and has many similarities to UTM development in Europe. This subsection examines the UTM ConOps, rules and regulations for UAS operation in the US. To enable safe integration of UAS into airspace, NASA, working in collaboration with the FAA, is developing UTM while into account the legacy of air traffic management (ATM) for manned aviation. FAA oversees the prototyping of appropriate rules and regulations for UAS operations to ensure that such operations will not interfere or pose any harm to the current air traffic activity or human on the ground. In this subsection, first, the rules and regulations posed by the FAA are investigated and summarized. Then, the UTM ConOps proposed by NASA is examined.

#### ***FAA UAS Rules and Regulations***

Rules and regulations for UAS operating in the US airspace are specified by the FAA, under the Title 14 of Code of Federal Regulations Part 107 [24,25]. Unlike EASA rules and regulations, the FAA version does not categorize UAS into different categories. The regulations mainly enforce that UAS must weigh less than 25 kg and must be operated within visual line of sight (VLOS) not higher than 400 ft above ground level. Operation above people who are not involved with the operation is also prohibited. Airspace class G is the only airspace that UAS can operate in without the need to have any certification by the FAA or clearance by ATC. Operations in controlled airspace class B, C, D, and E are not allowed and the ATC permission is also required before an operation can be commenced. Nevertheless, the FAA offers UAS operators the option to apply for a waiver certification, which allows certain restrictions to be removed. Night time operation, beyond-visual-line of sight operation, the operation of multiple UAS, operation over people, operation in controlled airspace or operation of UAS exceeding specified operating limits; these are possible through the waiver certification system.

Rules and regulations specified by the FAA are very similar to the EASA rules and regulations in combination with EUROCONTROL ConOps. The differences are non-significant, such as the maximum height of 400 ft for the US and 500 ft for Europe. Both in Europe and in the USA, UAS operations are allowed automatically in airspace class G, while accessing controlled airspace class B, C, D or E are only possible after a special request to the authority.

#### ***NASA UTM ConOps***

Due to the heterogeneous mix of UAS types in combination with a wide range of existing manned aircraft, there is a need to develop a system that can enable safe and efficient low-altitude airspace operations. NASA UTM ConOps [26] is designed with an aim to provide a comprehensive digitalized service, such as, airspace design and dynamic configuration,

dynamic geo-fencing, congestion management, route planning and re-routing, separation management, sequencing and spacing, and contingency management. To achieve such aims, a cloud-based platform is developed to provide a wide range of services that seamlessly connect a UAS operator to other UAS operators, UAS service suppliers, and air navigation service providers. The services are, for example, registration of UAS, flight plan submission, dynamics geofencing setup or controlled-airspace access management. This NASA UTM ConOps is similar to the U-Space concept in Europe, which focuses on providing a digitalized supporting infrastructure to accommodate UAS operations.

### 2.3.3. Dimensions of UTM

From the analysis of UTM ConOps, rules, regulations and supporting infrastructure, important dimensions of UTM are identified and summarized in Table 2.2. Each row in this table presents for one specific dimension the spectrum of possible values. The full spectrum of all potential UTM possibilities is defined by combining values for each of the dimensions. For instance, a UAS of dimension Eurocontrol UAS Class I, can fly in ICAO airspace class G. To continue the dimension values for this example, the main UAS category that will operate within VLL airspace is the Open category (A0-AIII) and all UAS in this category will not weigh more than 25 kg, falling into micro and small UAS types. Furthermore, several types of micro and small UAS exist, namely; fixed-wing, multi-copter, tiltrotor, hybrid or blimp UAS. This UAS example typically flies in unstructured airspace, without authorization level, under VLOS, RLOS and may encounter static geofencing.

**Table 2.2. Overview of UTM dimensions**

Dimension	Variables within Dimension						
EuroControl UAS Class	Very Low Level (GND - 500 ft.)				IFR/VFR 500 ft. - FL600	VHL (Above FL600)	
	Class I	Class II	Class III	Class IV	Class V	Class VI	Class VII
ICAO Airspace Class	A	B	C	D	E	F	G
EASA Category of UAS	Open				Specific	Certified	
	A 0	A I	A II	A III			
Type of Operation	Recreation	Land Survey	Agriculture	Infrastructure Monitoring	Commercial Transport		
	Law Enforcement	Forest Monitoring	Border Patrol	Surveillance	Search and Rescue		
UAS Type	Fixed-wing	Mono-copter	Multi-copter	Tiltrotor	Hybrid	Blimp	
Weight Class	<= 0.25 kg	0.25 - 25kg	>= 25kg				
Flight Rules	VFR	IFR					
Airspace Structured	Unstructured	Structured					
Operation Authorisation Level	None	Declaration	Authorisation	Special Authorisation			
Range Scheme	VLOS	EVLOS	BVLOS				
UAS C2 Link	RLOS	BRLOS					
Geofencing	Static	Dynamics					

The above UAS example in using the UTM dimensions from Table 2.2 applies to most buy-and-fly UAS operations. Because commercial aircraft do not operate within class G airspace, this means that for this UAS example, an encounter with a commercial aircraft will be less likely comparing to an encounter with general aviation aircraft. The difference in vehicle types affects the collision speed and impact materials. Moreover, UAS airspace structure also defines what objects will be affected by UAS operations. Also, a certain type of UAS operations may follow ground structures, such as a river or train track; this means that train or boat needs to be incorporated in collision consequence analysis as well.

To summarize this section, the European UTM ConOps along with rules, regulations and supporting infrastructure are investigated and decomposed into main dimensions as shown in Table 2.2. UTM in the USA is shown to be in line with the European UTM and is therefore

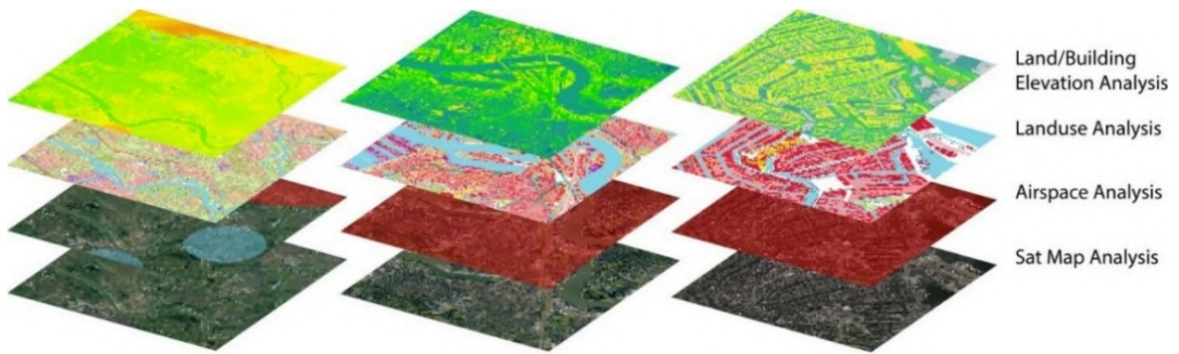
not specifically addressed further in this work. The analysis of the UTM ConOps and EASA prototype regulations clearly show what types of UAS will be allowed to operate in different airspace classes. This enables the next analysis step which is the identification of types of UAS and other objects.

## **2.4 Identification & Classification of Objects Exposed to Collision Risk**

This section describes an identification process of the objects within the VLL part of UTM that are exposed to UAS collision risk. The goal of object identification is to identify, as many as necessary, the various objects within the UAS operational airspace. Objects are divided into two main types: (i) ground objects and (ii) airborne objects. In addition, different types of UAS that will be allowed to operate within VLL airspace are identified as well. To set the analysis scope, an operational area in the Netherlands is selected as a representative site for European UTM. The following sections describe the identification of ground objects, airborne objects, and UAS types.

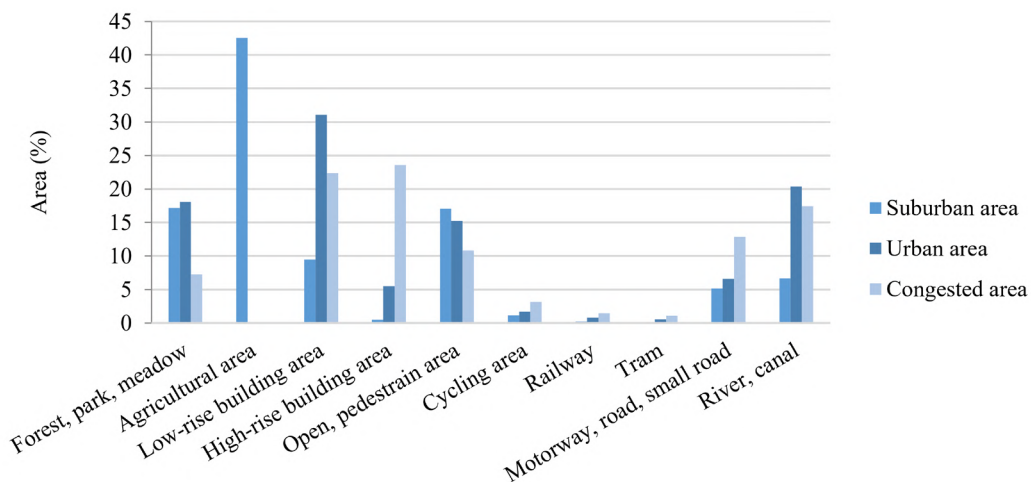
### **2.4.1. Identification of Ground Objects**

Since UAS operational airspace can cover large different areas across the country, scoping of the investigated area is necessary. Three representative areas based on NASA [7] definition of operational areas is selected for investigation. These areas are the suburban area, the urban area, and the congested area. Each area is characterized by the population density, ranging from low to high population density. For the suburban area, the area North of Nijmegen (with a population density of 600 per sq. km) [27] in the east of the Netherlands is selected as it is a potential site for several applications, such as parcel delivery, precision agriculture, infrastructure monitoring and etc. The city of Rotterdam (with a population density of 3060 per sq. km) [27] is selected for the urban operational area as it contains several landscape features suitable for operation such as urban parcel delivery, aerial photography, traffic monitoring, or law-enforcement. Lastly, for the congested operational area, the city center of Amsterdam (with a population density of 6200 per sq. km) [27] is chosen. This is a possible operating site for operations such as event photography and security, law enforcement or emergency response. Ground object identification is performed by employing map analysis based on different map types, such as satellite map, airspace class map, land-use map, and land/building elevation map. A satellite map is used to point out different objects on the ground within the operational area – this is done by visual observation. To narrow down the analysis domain, an airspace class map is superimposed to cut out any irrelevant area that UAS cannot operate in. In addition, land use map is employed to help to categorize different areas. Object identification is then done for each land use area. Lastly, a land/building elevation map is used to determine the amount of small buildings and tall buildings within the area. Figure 2 shows the layers of the different map types that are used in the analysis for the three different operational areas, namely; the suburban, urban and congested areas.



**Figure 2.2.** Map analysis of different operational area ranging from low population density to high population density; (i) rural area (the area around Nijmegen), (ii) urban area (city of Rotterdam) and (iii) congested area (city center of Amsterdam). Different map types such as satellite maps, airspace class maps, land-use maps, and land/building elevation maps are used.

From the map analysis, 10 categories of land use types (including the percentage of area) are identified and shown in Figure 2.3. The suburban area consists largely of an agricultural area of approximately 42% of the overall land area and approximately 17% of forest, park meadow and open, pedestrian areas. The composition of the low-rise buildings is 9.5% while the amount of high-rise buildings in the suburban area is considerably lower with only 0.5% of the total land area. In an urban area, around 31% of the area consists of low-rise building and almost 21% of the area is river and canal. Forest, park, meadow and open, pedestrian areas are 18% and 15% of the total area respectively. It can be observed that, for the congested area, a large amount of area is covered with high-rise buildings (23%) and low-rise buildings (22%). Open/pedestrian areas are quite significant as well in congested airspace as these open areas are often used for public events where a large crowd is expected.



**Figure 2.3.** Land-use type percentage of three operational areas (suburban, urban and congested operational areas)

For each land-use type, ground objects are identified using the land-use database and satellite map analysis. The land-use database comes with data fields which describe the type of object, while satellite map offers visual evidence of the actual objects in the area. Several objects that are deemed irrelevant or insignificant to the safety of human are excluded, for example, light poles, signs, small roadside structures, grass, trees or animals on the ground. The aim is to identify as many relevant objects as possible without classifying them yet, then the classification of these objects is done in a later stage. The results of the identification are shown in Table 2.3.

**Table 2.3. Variation of ground objects over land-use types**

Land-use Type	Objects within the land-use type
1. Forest, Park, Meadow	Human (pedestrian, hiker, camper)
2. Agricultural area	Glasshouse, Small house, Car, Truck, Tractor, Human (pedestrian, farmer, worker)
3. Low-rise building area	House, Retail store, Apartment, Condominium, Other low-level building
4. High-rise building area	High-level condominium, Other high-level building
5. Open, Pedestrian area	Human (pedestrian), Cyclist, Car (slow-speed, parking), Scooter
6. Cycling area	Cyclist, Motorcyclist (Motorbike, scooter)
7. Railway	Train, Worker
8. Tram	Tram, Worker
9. Motorway, road, small road	Car (Sedan, van, truck), Coach, Lorry, Human inside vehicle, Motorcyclist
10. River, canal	Small boat, Medium boat, Sail, Yacht, Ship

The estimated land use type area percentages in Figure 2.3 together with the types of objects per land use type in Table 2.3 provide valuable qualitative insight. These estimations illustrate what types of objects are highly expected in the operational area. However, to transform this information into quantitative estimates of frequencies of collision requires significant complementary analysis, which falls outside the scope of this paper.

### 2.4.2. Airborne Objects Identification

Within VLL, several types of UAS and non-UAS airborne objects are expected to share the airspace with UAS. Based on pilot and aviation expert opinion, and rules of air specified by EASA [28], 6 main types of airborne objects are identified. Firstly, commercial aviation such as commercial airliner or business jet is expected to share airspace with few UAS operations, such as UAS class IV that can operate in airport areas. Nevertheless, it is expected that an encounter with commercial aviation will be minimal since UAS class IV is reserved for specialized operations. Furthermore, general aviation aircraft are certainly expected to share airspace with UAS since this type of aircraft often operates at low altitude in a regulated but uncontrolled airspace. Flight training, leisure flight, commercial flight, or agricultural operation are normal operations that are performed by general aviation aircraft. Rotary wing aircraft are also largely used by the military, law enforcement, emergency services, news, and media, which often operate at very low level. It was already witnessed before when a small drone (DJI Phantom 4) collided with the US army UH-60M helicopter while operating under visual flight rules within Class G airspace about 300 ft above sea level. [29] Next, the lighter-than-air vehicle type, such as blimps, balloons or lanterns, is identified as one of the types that is susceptible to UAS collision risk. Collisions with a manned airborne vehicle can lead to direct injury or fatality to any human on-board. Furthermore, collisions between UAS are also considered. Lastly, birds are also considered as a relevant collision thread. UAS to UAS or UAS to bird collisions could potentially lead to damage on the ground due to fallen debris.

**Table 2.4. List of identified non-UAS airborne objects**

Type of Object	Object Instantiations
1. Commercial Aviation	Commercial airliner, business jet
2. General Aviation (GA)	GA (light a/c, light sports a/c, trainer a/c, cargo a/c, ultralight a/c, glider a/c)
3. Rotary Wing	Small size helicopter, Medium size helicopter, Military helicopter
4. Lighter-Than-Air	Blimp, Balloon, Lantern
5. Remotely-Piloted Aircraft System (UAS)	Micro UAS (Fixed wing, Rotary wing, Multi-copter), Small UAS (Fixed-wing, Rotary wing, Multi-copter, Blimp)
6. Other	Bird

### 2.4.3. Non-UAS Object Classification

In Figure 2.4, the relevant objects within VLL airspace are classified into appropriate categories. The first distinction is between static objects and dynamics objects. Static objects consist of permanent infrastructure and non-permanent infrastructure while the dynamics objects consist of liveware and hardware. Liveware refers to human and animal, either in the air or on the ground, while hardware refers to aircraft, automobiles, trains or marine vessels. Similar objects, such as houses, retail stores or apartments, are grouped together into the low-rise structure type for example. This classification builds an overall picture of what types of objects are expected to share an airspace with UAS. For the follow-on work in the later section, only general aviation and rotary wing will be further elaborated. This focus is selected in order to allow detail elaboration on these objects.

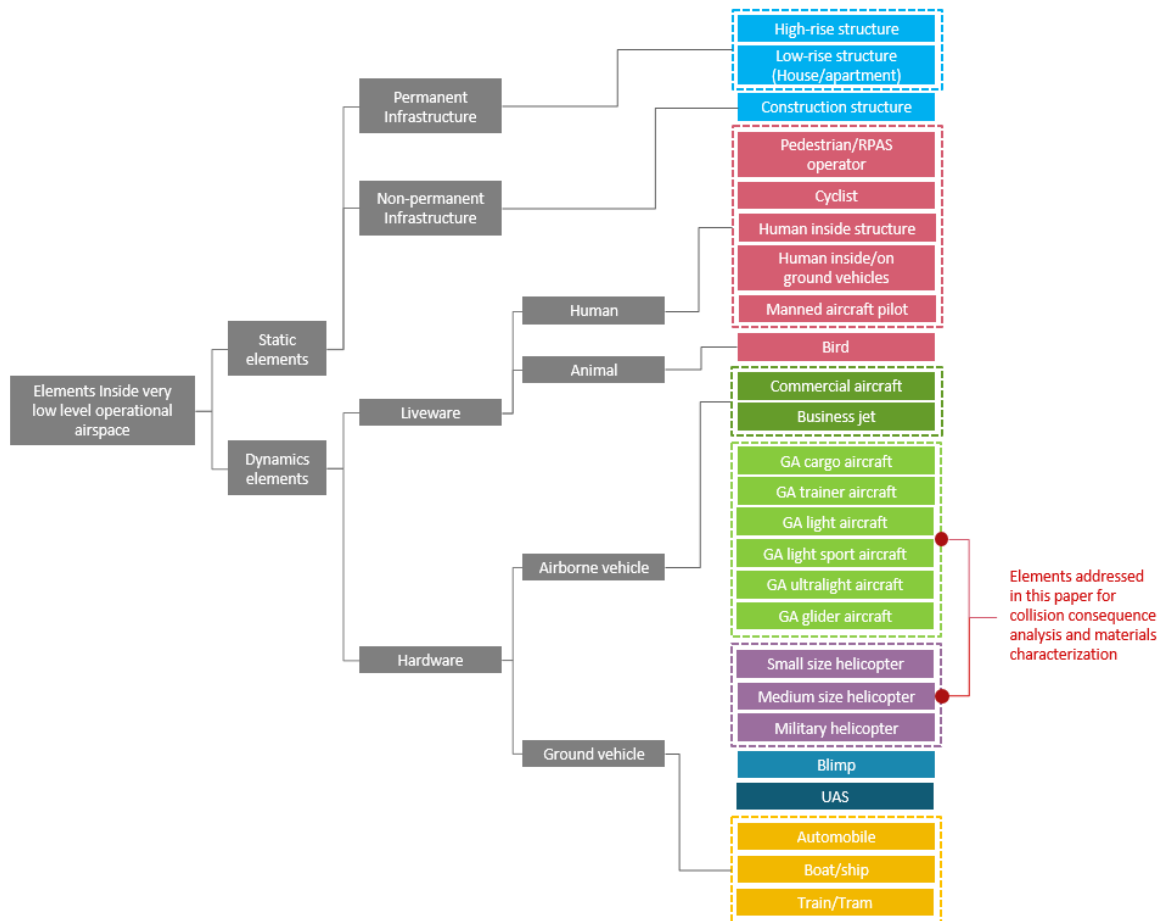


Figure 2.4. Object classification flowchart, combining both ground and airborne objects. For airborne objects (GA aircraft and rotorcraft) this paper elaborates the remaining steps in consequence analysis.

### 2.4.4. UAS object classification

A Large variety of UAS even further complicates several aspects in terms of regulatory arrangement as well as safety risk assessment. The identification process of UAS is important as different UAS weight classes consist of different design attributes, fabrication materials, and flight performance, which significantly affect collision consequence severity. Within VLL airspace, only traffic class I to IV are allowed. Traffic class I only allows UAS Open category A0 to AIII (0.25 kg for A0 and 25 kg for AI-AIII of maximum take-off gross weight). A0 category falls into a micro UAS category that is specified by the United States Department of Defense [30]. Open category A1-A3, which refer to UAS of maximum take-off gross weight of between 0.25 kg to 25 kg, falls into the small UAS category. For UAS class II, III, and IV,

similar take-off weight threshold of 25 kg is expected. In summary, it is expected that only micro UAS and small UAS can operate in VLL airspace. The identification and classification flowchart of UAS in VLL operation is illustrated in Figure 5. It is worth mentioning that for the outside of VLL airspace, UASs are required to comply with IFR/VFR requirements same as manned aircraft. Most of the tactical UASs and some of the military-grade UAS are equipped with necessary technology to operate in IFR/VFR airspace. Medium Altitude-Long Endurance (MALE) UAS also operate in IFR/VFR airspace. However, due to performance limitations of the MALE category, MALE UAS are not likely able to reach the very high-level operational airspace. This final traffic class VII only accommodates high altitude-long endurance (HALE) UAS. UAS class V to VII are not addressed in the follow-on analysis of this paper. Only small fixed-wing UAS and small multi-copter UAS are further elaborated in this paper since these are the most used types of UAS.

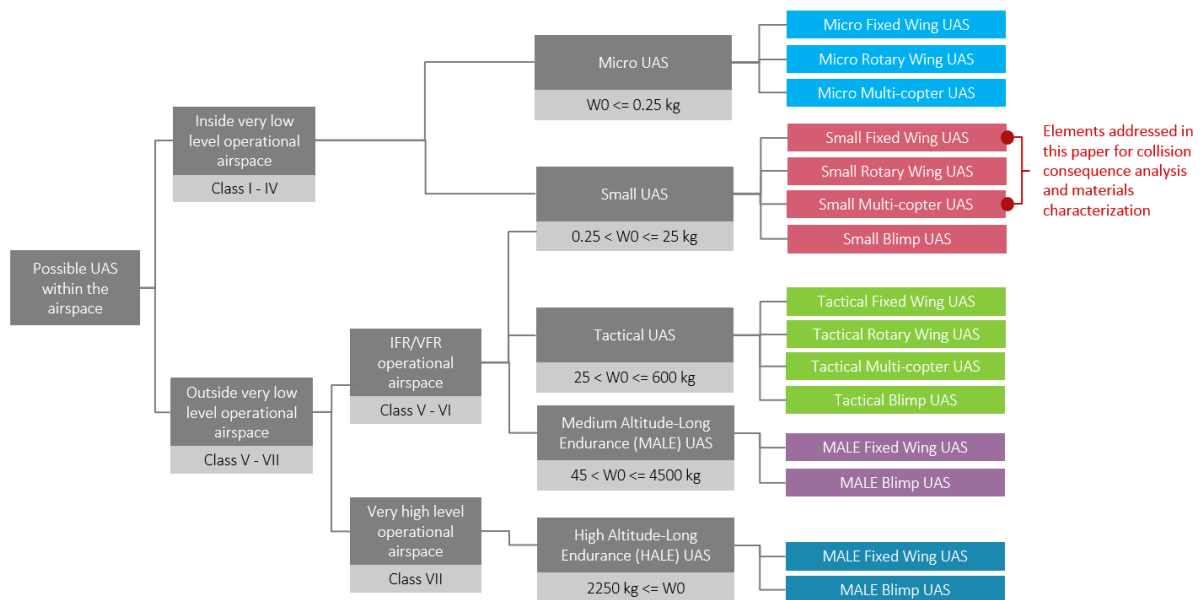


Figure 2.5. UAS identification and classification flowchart. Only small fixed-wing UAS and small multi-copter UAS are further elaborated in later sections since these two types are the most used types of UAS.

## 2.5 Zone of Impact Analysis

Having identified and classified the objects within VLL airspace, the zone of impact analysis aims to characterize impact materials. The main purpose of this analysis is to identify zones that are susceptible to primary impact so that representative materials and collision consequence of those zones can be identified and categorized. The zones of impact are presented in term of area percentage, allowing for future quantitative analysis. First, the frontal diagrams of different objects are collected, and the silhouette areas are projected onto the diagram. Then, the percentage of each area is estimated. This section describes the decomposition and analysis of zone of impact of two types of objects: Non-UAS airborne objects of types general aviation and rotorcraft and subsequently UAS objects.

### 2.5.1. Zone of Impact Analysis for General Aviation and Rotorcraft

Different types of general aviation (GA) aircraft are analyzed for the zone of impact. GA cargo aircraft, GA trainer aircraft, GA light aircraft and GA light sports aircraft share similarities in terms of configuration, size, and engine placement. Therefore, these types of GA are considered together. These GA aircraft are divided into single-engine and twin-engines. GA ultralight and GA glider are included in this analysis as well. The representative

models of these aircraft are selected based on their popularity and number of shipments in the past years [31]. The list of representative aircraft under consideration is shown in Table 2.5. Frontal impact analysis is performed, and the results are presented in this section.

Examples of the object diagrams and overlay silhouette areas are shown in Figure 2.6. The analysis is done for every representative aircraft example and then averaged over these examples. The average values of the composition of different zones of impact are shown in Figure 2.7. The results show that, for single-engine GA, the largest part is the propeller which is about 52% of the entire aircraft frontal area and second largest part is the wing which is 36%. It should be noted that the windshield of single-engine aircraft seems to be obstructed by the front propeller, however, some UAS or UAS debris can potentially slip pass the propeller. This makes windshield become one of the primary impact points. Propeller area is even larger for twin engines general aviation aircraft with takes up almost 57% of the entire area. The main wing also takes a large portion of the area with about 18% of the entire area. Ultralight, on the other hands, has 41% of wing area and 25% of the propeller. This is due to the typical rear-engine placement of the ultralight. The majority of ultralight analyzed in this paper shows the absence of a windshield, exposes human pilot which takes up to 12% of the whole area. Due to the high aspect ratio of ultralight, the wing portion is considerably large compared to other types of airborne objects and take up 76% of the area. Windshield and fuselage skin covers 7% each. For medium to large rotorcrafts, main rotor blade and fuselage skin cover 58% and 21% of the entire area. Due to large field-of-view required in rotorcraft design, almost 14% is covered with a windshield which is significantly larger compared to other types of aircraft.

**Table 2.5. Representative GA and rotorcraft examples selected for the zone of impact analysis.**

Aircraft Type		Representative examples
GA Cargo Aircraft, GA Trainer Aircraft,	Single Engine	Cirrus SR22, Cessna Skyhawk 172S, Pilatus PC-12, DA20-C1, Daher TBM930, Air Tractor AT-802A
GA Light Aircraft, GA Light Sport Aircraft	Twin Engines	Beechcraft King Air, Beechcraft Baron, Diamond DA42, Piper PA44
GA Glider		Pipistrel Taurus M, ASH 30 Mi, DG-1001 Club Neo,
GA Ultralight		Quick Silver, Pegasus Quantum 145-912, Huntair Pathfinder Mark 1
Rotorcraft		Robinson R44 Raven, Sikorsky UH-60 Black Hawk, Airbus H145, Airbus H125, Bell 407GXP



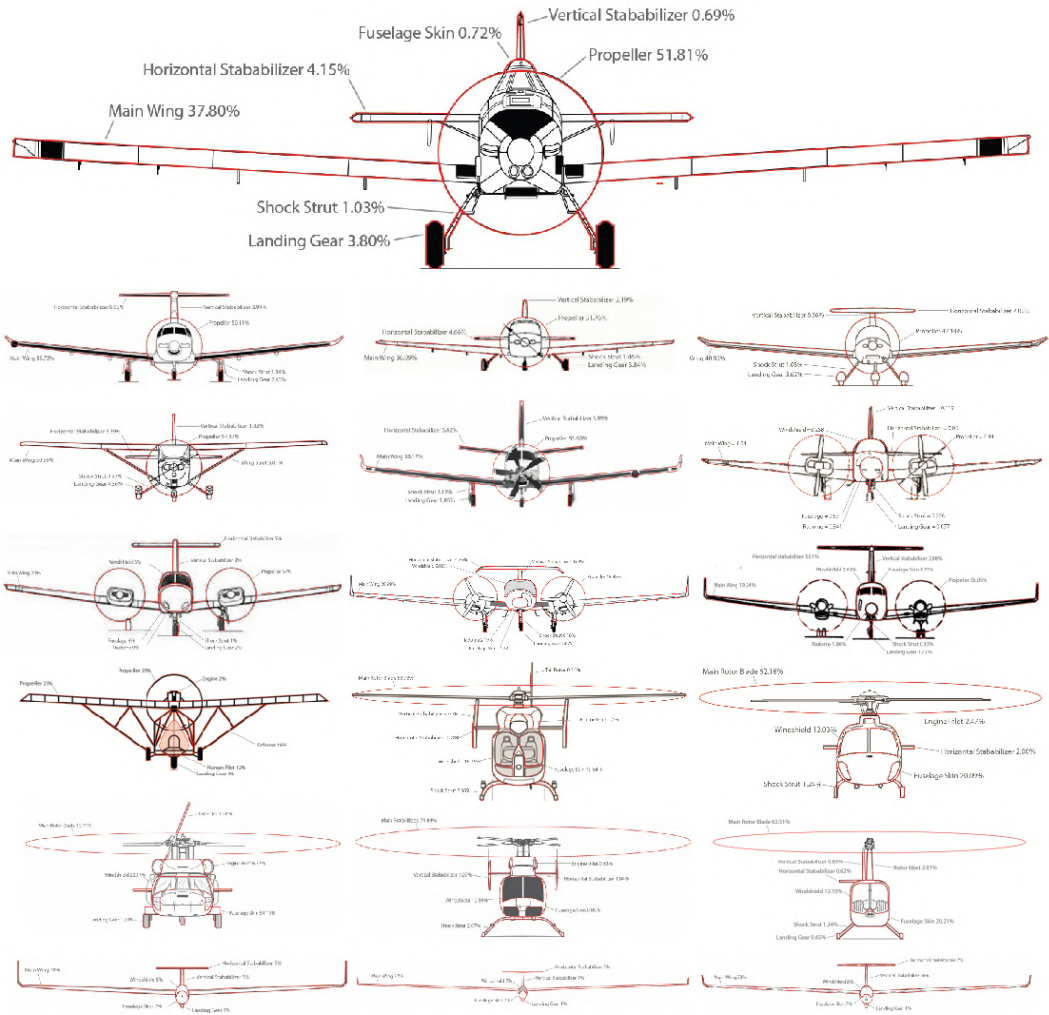
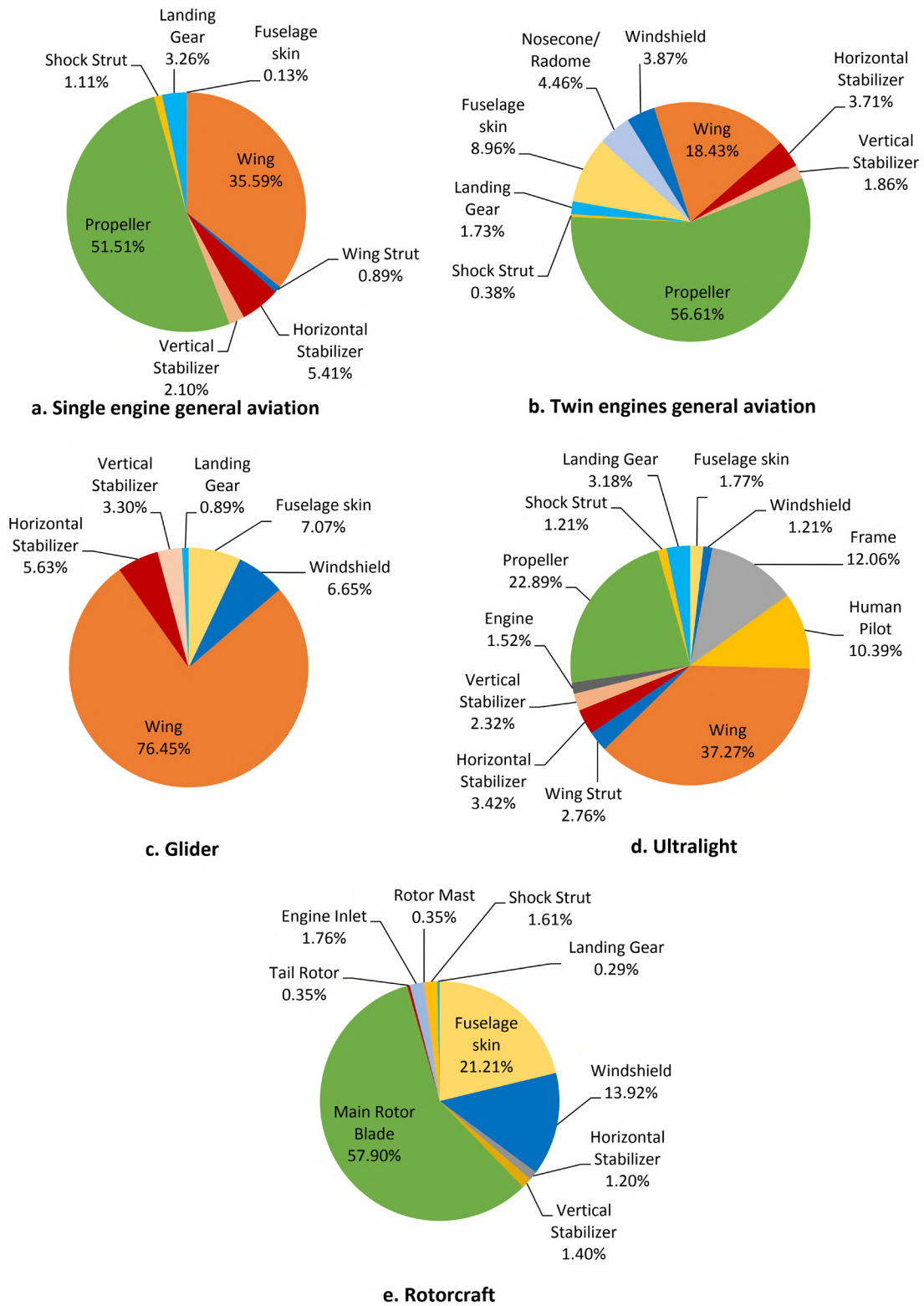


Figure 2.6. Zone of impact analysis diagrams of aircraft types in Table 2.5.



**Figure 2.7. Pie-charts showing the composition of the different zone of impact of (a.) single engine general aviation, (b.) twin engines general aviation, (c.) glider, (d.) ultralight and (e.) rotorcraft**

## 2.5.2. Zone of Impact Analysis for UAS

For small fixed-wing and multi-rotors UAS representative examples with various masses are selected for the zone of impact analysis; this is shown in Table 2.6. Similar to GA, frontal impact areas are analyzed and estimated in order to determine area composition of each model. Figure 2.8 shows the example of the zone of impact analysis of the representative UAS models where the red lines illustrate the different collision zones on the vehicle.

Table 2.6. Representative UAS examples selected for the zone of impact analysis

UAS Type	Weight Class	Representative Examples
Fixed-Wing	Small UAS	Parrot Disco (0.75 kg), Precision Hawk Lancaster (3.55 kg), AeroVironment Puma (6.3 kg), Insitu Scan Eagle (18 kg), UAV Factory Penguin B (21.5 kg)
Multi-rotors	Small UAS	Parrot Bebop 2 (0.5 kg), DJI Phantom 3 (1.39 kg), DJI Matrice 200 (3.8 kg), Yuneec Tornado H920 (4.99 kg), DJI Matrice 500 Pro (15.5 kg)

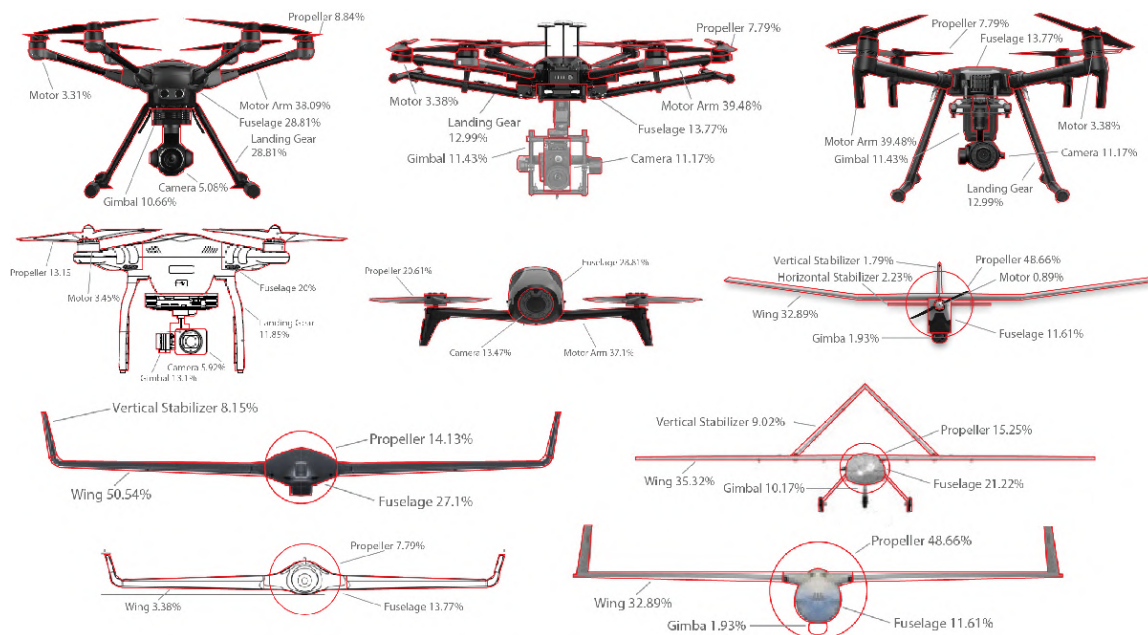


Figure 2.8. Zone of impact analysis diagrams for the types of UAS in Table 2.6.

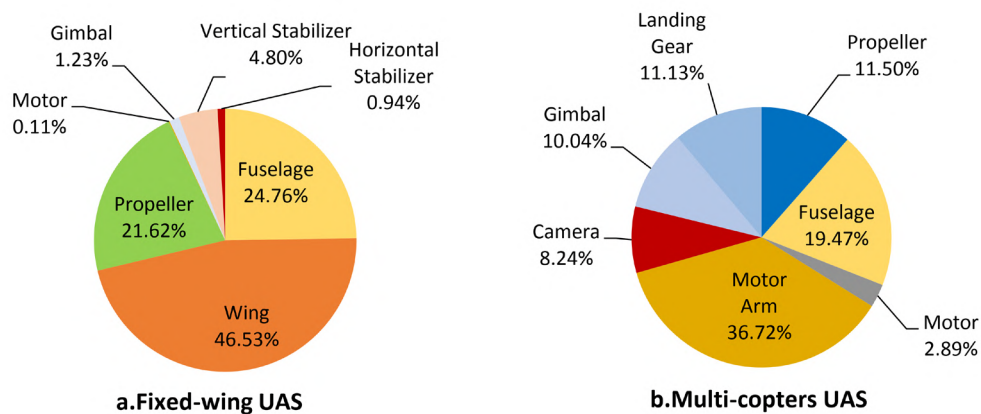


Figure 2.9. Composition of zones of impact of (a.) fixed-wing UAS and (b.) multi-copters UAS.

The area composition of fixed-wing UAS and multi-rotors UAS, which can be seen in Figure 2.9, are quite different due to distinct design. For fixed-wing UAS, about 47% of the whole frontal area is the wing area. The fuselage and propeller also cover a significant frontal area with percentages of 25% and 22% respectively. It should be noted that UAS models that are selected in this analysis only use propeller-driven propulsion systems, and not jet-engines. The vertical stabilizer is 5% of the overall area while horizontal stabilizer covers only 1% of the frontal area. Not all fixed-wing UASs are installed with gimbal which makes the averaged gimbal area for fixed-wing approximately equal to 1%.

## 2.6 Materials Identification and Classification

Next, commonly used materials for different zones of impact are identified and classified. The main aim of this characterization is twofold. Firstly, based on the identification of materials, the future analysis of collision consequence on particular materials type can then be used to speculate the possible outcomes of UAS collision on a particular zone of impact of certain objects. The prediction can also be done for each zone of impact by deducing from historical data or knowledge from other research on collision severity between materials. Secondly, the list of common materials will serve as a basis for any future investigation of UAS collision consequence severity analysis.

For general aviation and rotorcraft, the knowledge of the materials used is from literature studies [32,33]. Table 2.7 shows the list of common materials used in single-engine general aviation. As can be seen from the tables, many zones of impact use similar materials, and aluminum type is largely used for most parts. Based on this identification of materials, the future analysis of collision consequences on particular materials type can then be used to speculate on the possible outcomes of a UAS collision on a particular zone of impact of a certain object. See Appendix 2A for lists of common materials for the other four non-UAS objects (twin-engine GA, glider, ultralight, and rotorcraft).

**Table 2.7. List of common materials of single-engine GA. See Appendix 2A for other objects.**

Zone of Impact	Percentage	Common Materials
Propeller	51.5	Wood (cherry, mahogany, black walnut, oak, and birch), Aluminum, Fiber reinforced polymer (FRP) with foam core
Wing	35.5	Aluminum 2000 Series, Aluminum 7000 Series, Fiber reinforced polymer (FRP)
Horizontal Stabilizer	5.41	Aluminum 2000 Series, Fiber reinforced polymer (FRP)
Landing Gear	3.26	Steel, Titanium alloy, Rubber (for tire)
Vertical Stabilizer	2.10	Aluminum 2000 Series, Fiber reinforced polymer (FRP)
Shock Strut	1.11	Steel, Titanium alloy
Wing Strut	0.89	Aluminum 2000 Series
Fuselage	0.13	Aluminum 2000 Series, Aluminum 7000 Series, Fiber reinforced polymer (FRP)

Similarly, the common materials are identified for small fixed-wing and small multi-copter UAS as well. Table 2.8 and Table 2.9 show the list of common materials for small fixed-wing UAS and small multi-copter UAS respectively. The types of materials used in the construction of small UAS are more diverse than in larger aircraft since these small UAS can often be made from light-weight, low strength structures. Polystyrene, wood, and plastic are widely used in small fixed-wing UAS for the ease of manufacturing, while FRP can be found in a larger size of small fixed-wing and multi-copter UAS.

**Table 2.8. List of common materials for small fixed-wing UAS**

<b>Zone of Impact</b>	<b>Percentage</b>	<b>Common Materials</b>
Wing	46.5	Polystyrene, Balsa wood, Light plywood, Plastic, Fiber reinforced polymer, Aluminum
Fuselage	24.8	Polystyrene, Balsa wood, Light plywood, Plastic, Fiber reinforced polymer, Aluminum
Propeller	21.6	Wood, Plastic, Fiber reinforced polymer (FRP)
Vertical Stabilizer	4.80	Polystyrene, Balsa wood, Light plywood, Plastic, Fiber reinforced polymer, Aluminum
Gimbal	1.23	Plastic, Fiber reinforced polymer (FRP), Aluminum
Horizontal Stabilizer	0.94	Polystyrene, Balsa wood, Light plywood, Plastic, Fiber reinforced polymer, Aluminum
Motor	0.11	Aluminum

**Table 2.9. List of common materials for small multi-copter UAS**

<b>Zone of Impact</b>	<b>Percentage</b>	<b>Common Materials</b>
Motor Arm	36.7	Plastic, Fiber reinforced polymer, Aluminum
Fuselage	19.5	Plastic, Fiber reinforced polymer, Aluminum
Propeller	11.5	Wood, Plastic, Fiber reinforced polymer (FRP)
Landing Gear	11.1	Plastic, Fiber reinforced polymer, Aluminum
Gimbal	10.0	Plastic, Fiber reinforced polymer (FRP), Aluminum
Camera	8.24	Plastic, Fiber reinforced polymer (FRP), Aluminum

## 2.7 Collision Consequence Analysis

Next collision consequences due to UAS impact on each collision zone are identified. This stage aims to build a risk picture of the possible consequence and impact due to UAS collisions. In this paper, “consequence” describes the undesirable events (usually accidents or safety-related events) [34]. However, severity, on the other hands, is the description of the level of loss or damage of a particular consequence. This paper considers only three levels of consequence severity; which are “damaged”, “substantially damaged” and “destroyed”. No damage and partially damaged severity levels are not addressed since they are not expected to directly lead to injuries. For human-related accidents, three injury levels are defined, namely; “minor injury”, “serious injury” and “fatal”. These severity and injury levels are based on ICAO Annex 13 severity definition [35].

Identification of collision consequence of UAS collision is done based on literature [15,16,19,36,37] on UAS collision analysis and the important findings are presented in this section. This literature addresses the collision effect on a general aviation aircraft, commercial aircraft, and human, inflicted by different UAS types with various weights, using both crash modeling and experimentation. Mid-air collision effect of small UAS on windshields and helicopter tail rotors are examined by the MAA [19] in collaboration with BALPA and UK’s Department of Transport. It is found that non-birdstrike certified helicopter windshields proved to have a low resistance to drones collision and penetration through the windshield is very likely – the tests are done using 0.4, 1.2 and 4 kg classes of drone. These findings can also be applied to GA windshields since GA windshields do not have a requirement for

birdstrike certification. The birdstrike certified helicopter windshield, however, shows better UAS collision resistance but penetration is still possible if aircraft fly at cruising speed. If the helicopter is stationary, both multi-copters UAS and fixed-wing UAS have less tendency to penetrate through certified windshields. The helicopter tail rotor is examined as well, and it is found that tail rotors are vulnerable to all types of drones due to the very high rotor rotating speed. Damage can be easily amplified if rotors become unbalanced resulting in uncontrolled rotor vibration which could jeopardize the whole tail structural integrity. Similar deduction for GA propeller impact severity can be done based on such study. Furthermore, the ASSURE research group [37] also conducted a series of impact severity analysis tests with multi-copters and fixed-wing UAS on business jet and commercial aircraft using both computational modelling and experimentation. It is found that 1.2 kg quadcopters UAS and 1.8 kg fixed-wing UAS at 250 knots can inflict various damage levels on different parts of commercial aircraft and business jet. Horizontal and vertical stabilizers can sustain medium-high damage severity levels which includes skin fracture, penetration into airframe and failure of parts of the primary structure. UAS can also leave permanent deformation on surface and structure, skin fracture and penetration into the airframe. Commercial aircraft windshields, however, shows permanent deformation, some fracture, but no penetration. These findings can be used to deduce the possible collision consequence outcomes of UAS to GA aircraft due to the fact that many parts of GA aircraft use similar materials on commercial aircraft and business aircraft, such as, leading edge or fuselage skin. In addition, the severity of jet engine ingesting UAS is investigated through computational modelling [38]. For typical turbofan engines on commercial aircraft, fan blades can be partially destroyed due to the hard components from the UAS such as the motor or the camera. The UAS can inflict even more damage as it moves closer to nosecone (or center) of the engine. In such case, both inner and outer blades are severely damaged and there is a larger chance for UAS debris to enter core engine which leads to a system shutdown.

Using the aforementioned understandings towards the effect of UAS collisions on different types of objects, collision consequences and subsequent event types have been identified for each zone of impact (or pass) for each of the non-UAS objects addressed in Section V; these results are shown in Appendix 2B.

## **2.8 Conclusion**

In order to safely integrate UAS operations into the airspace, UAS collision risks need to be well understood. For such a complex problem, there is a need to develop a systematic approach to characterize both frequency and consequence of various UAS collisions. This paper presented and followed a step-wise method for characterizing UAS collision consequences in future UTM system, focusing on only the VLL UAS operations which are below 500 ft. The proposed method first addressed the analysis of UTM dimensions by investigating the UTM ConOps, rules and regulations, and support infrastructure under consideration. These were analyzed and decomposed into several dimensions. The second step was the identification of the relevant objects within the airspace that was susceptible to UAS collision risk. Since UAS will operate very close to the ground, the objects sharing the airspace with the UAS then consist of both ground and airborne objects. For ground objects, different kinds of maps, such as land-use map, satellite map or land elevation map, were used in the identification process. Airborne objects were identified based on rules of the air which specified what types of aircraft were allowed to operate within the airspace. Additionally, opinions from aviation experts were incorporated during the identification of airborne objects as well. Next, the third step was to analyze the zones of impact for the identified objects. This

was demonstrated for general aviation and rotorcraft. The aim of the zone of impact analysis was to decompose the overall area of an object into different impact zones that were exposed to the risk of colliding with a UAS. The areas of each zone were also estimated and represented in the form of percentages, which significantly influenced the collision probability of each impact zone. The fourth step was the materials identification and classification with the aim to characterize common materials for each zone of impact. Materials characterization is important for future research where impact analysis will be conducted for different materials. Lastly, collision consequence of the selected objects was done by identifying the possible collision outcomes for each zone of impact of each object. The collision consequence was identified based on literature which involved impact testing and simulation. Such analysis aimed to build a risk picture of the possible consequence and impact of a collision with a UAS.

The key added value of the approach developed in this paper is that the intermediate relations between the initiating events and the collision consequence outcomes are established through a systematic analysis and characterization process. Follow-up research can take advantage of this logical and well-structured decomposition that helps organizing the detailed quantitative modeling and analysis of collision consequences. Complementary follow-up research is to extend the step-wise approach proposed in this paper to a consequence analysis of primary collisions to secondary collisions, i.e., collisions that happen as a consequence of a primary collision.

## Appendix 2A: Additional Materials Identification Results

### Materials Identification Results – Twin-Engine General Aviation

Zone of Impact	Percentage	Common Materials
Propeller	56.6	Wood (cherry, mahogany, black walnut, oak, and birch), Aluminum, Fiber reinforced polymer (FRP) with foam core
Wing	18.4	Aluminum 2000 Series, Aluminum 7000 Series, Fiber reinforced polymer (FRP)
Fuselage	8.96	Aluminum 2000 Series, Aluminum 7000 Series, Fiber reinforced polymer (FRP)
Nosecone Radome	4.46	Fiber reinforced polymer (FRP)
Windshield	3.87	Acrylics, Polycarbonate
Horizontal Stabilizer	3.71	Aluminum 2000 Series, Fiber reinforced polymer (FRP)
Vertical Stabilizer	1.86	Aluminum 2000 Series, Fiber reinforced polymer (FRP)
Landing Gear	1.73	Steel, Titanium alloy, Rubber (for tire)
Shock Strut	0.38	Steel, Titanium alloy

### Materials Identification Results – Glider

Zone of Impact	Percentage	Common Materials
Wing	76.5	Aluminum 2000 Series, Aluminum 7000 Series, Fiber reinforced polymer (FRP)
Fuselage Skin	7.07	Aluminum 2000 Series, Aluminum 7000 Series, Fiber reinforced polymer (FRP)
Windshield	6.65	Acrylics, Polycarbonate
Horizontal Stabilizer	5.63	Aluminum 2000 Series, Fiber reinforced polymer (FRP)
Vertical Stabilizer	3.30	Aluminum 2000 Series, Fiber reinforced polymer (FRP)
Landing Gear	0.89	Steel, Titanium alloy, Rubber (for tire)

### Materials Identification Results – Ultralight

Zone of Impact	Percentage	Common Materials
Wing	37.2	Aluminum 2000 Series, Aluminum 7000 Series, Fiber reinforced polymer (FRP)
Propeller	22.8	Wood (cherry, mahogany, black walnut, oak, and birch), Aluminum, Fiber reinforced polymer (FRP) with foam core
Frame	12.1	Aluminum 2000 Series, Fiber reinforced polymer (FRP)
Human Pilot	10.4	Human flesh and skin
Horizontal Stabilizer	3.42	Aluminum 2000 Series, Fiber reinforced polymer (FRP)
Landing Gear	3.18	Steel, Titanium alloy, Rubber (for tire)
Wing Strut	2.76	Aluminum 2000 Series
Vertical Stabilizer	2.32	Aluminum 2000 Series, Fiber reinforced polymer (FRP)
Fuselage Skin	1.77	Aluminum 2000 Series, Aluminum 7000 Series, Fiber reinforced polymer (FRP)
Shock Strut	1.21	Steel, Titanium alloy



### Materials Identification Results – Rotorcraft

<b>Zone of Impact</b>	<b>Percentage</b>	<b>Common Materials</b>
Main Rotor Blade	57.9	Aluminum 2000 Series, Titanium, Fiber reinforced polymer (FRP)
Fuselage Skin	21.2	Aluminum 2000 Series, Aluminum 7000 Series, Fiber reinforced polymer (FRP)
Windshield	13.9	Acrylics, Polycarbonate
Engine Inlet	1.76	Aluminum, Titanium
Shock Strut	1.61	Steel, Titanium alloy
Vertical Stabilizer	1.40	Aluminum 2000 Series, Fiber reinforced polymer (FRP)
Horizontal Stabilizer	1.20	Aluminum 2000 Series, Fiber reinforced polymer (FRP)
Tail Rotor	0.35	Aluminum 2000 Series, Titanium, Fiber reinforced polymer (FRP)
Rotor Mast	0.35	Steel, Titanium

## Appendix 2B: Primary Consequences of UAS Collision with non-UAS Objects from Section V

### Consequence Characterization of UAS Collision with Single-engine General Aviation

Impact/Pass Zone	Primary Consequence(s)
Near Miss	- Pilot distracted, critical during high-workload takeoff/landing phases
Propeller	- Propeller damaged with minor permanent deformation, UAS debris damage windshield, pilot distracted - Propeller substantially damaged with partial structural failure, risk of unbalanced propeller rotation leading to uncontrolled propeller vibration, debris of UAS collide onto windshield - Propeller destroyed, instance loss of thrust and risk of unbalanced propeller rotation leading to uncontrolled propeller vibration, debris of UAS collide onto windshield- UAS pass through propeller, collide and bounce off windshield, windshield damaged with minor fracture, leading to pilot distraction - UAS pass through propeller, collide and damage windshield, leading to pilot distraction and reduced visibility - UAS pass through propeller and penetrate through windshield, leading to injury/fatality of human pilot
Wing	- Wing damaged with minor permanent deformation - Wing substantially damaged with structural penetration, reduced structural integrity of primary structure, risk of structural failure - Wing destroyed, primary structure failed, leading to uncontrolled flight and injury/fatality of human onboard
Horizontal Stabilizer	- Horizontal stabilizer damaged with minor permanent deformation - Horizontal stabilizer substantially damaged with structural penetration, reduced structural integrity of primary structure, risk of structural failure, reduced control surface movement - Horizontal stabilizer destroyed, primary structure failed, leading to uncontrolled flight and injury/fatality of human onboard
Vertical Stabilizer	- Vertical stabilizer damaged with minor permanent deformation - Vertical stabilizer substantially damaged with structural penetration, reduced structural integrity of primary structure, risk of structural failure, reduced control surface movement and pilot distracted - Vertical stabilizer destroyed, permanent structure failed, leading to uncontrolled flight and injury/fatality of human onboard
Shock Strut	- Shock strut damaged with minor permanent deformation - Shock strut substantially damaged with partial structural failure, risk of structural failure during landing - Shock strut destroyed, risk of uncontrolled touch down leading to runway skid-off, resulting in damaged to aircraft and injury/fatality of human onboard
Wing Strut	- Wing strut damaged with minor permanent deformation - Wing strut substantially damaged with partial structural failure, reduced structural integrity and risked of structural failure, leading to unsupported main wing - Wing strut destroyed leading to unsupported wing, risk of main wing structural failure, leading to uncontrolled flight and injury/fatality of human onboard
Fuselage Skin	- Fuselage skin damaged with minor permanent deformation - Fuselage skin substantially damaged, UAS penetrates fuselage, leading to injury of onboard personals and immediate termination of flight - Fuselage skin destroyed, UAS penetrates fuselage and injuring onboard personnel, risk of fuselage structural failure, leading to uncontrolled flight and injury/fatality of human onboard
Landing Gears	- Landing gears damaged with minor permanent deformation - Landing gears substantially, risk of landing gears structural failure during landing, risk of uncontrolled touch down leading to runway skid-off, resulting in damaged to aircraft and injury/fatality of human onboard - Landing gears destroyed, risk of uncontrolled touch down leading to runway skid-off, resulting in damaged to aircraft and injury/fatality of human onboard

## Consequence Characterization of UAS Collision with Twin-Engine General Aviation

Impact/Pass Zone	Collision Consequence
Near Miss	- Pilot distracted, critical during high-workload takeoff/landing phases
Propeller	- Propeller damaged with minor permanent deformation - Propeller substantially damaged with partial structural failure, risk of unbalanced propeller rotation, leading to uncontrolled propeller vibration - Propeller destroyed, instance loss of thrust and risk of unbalanced propeller rotation, leading to uncontrolled propeller vibration
Windshield	- Windshield damaged with minor fracture, pilot distracted - Windshield substantially damaged, UAS partially penetrate through, leading to pilot distraction and reduced visibility, risk of onboard injury - Windshield destroyed, UAS completely penetrate through, leading to pilot distraction and onboard injury/fatality
Wing	- Wing damaged with minor permanent deformation - Wing substantially damaged with structural penetration, reduced structural integrity of primary structure, risk of structural failure - Wing destroyed, primary structure failed, leading to uncontrolled flight and injury/fatality of human onboard
Horizontal Stabilizer	- Horizontal stabilizer damaged with minor permanent deformation - Horizontal stabilizer substantially damaged with structural penetration, reduced structural integrity of primary structure, risk of structural failure, reduced control surface movement - Horizontal stabilizer destroyed, primary structure failed, leading to uncontrolled flight and injury/fatality of human onboard
Vertical Stabilizer	- Vertical stabilizer damaged with minor permanent deformation - Vertical stabilizer substantially damaged with structural penetration, reduced structural integrity of primary structure, risk of structural failure, reduced control surface movement and pilot distracted - Vertical stabilizer destroyed, primary structure failed, leading to uncontrolled flight and injury/fatality of human onboard
Shock Strut	- Shock strut damaged with minor permanent deformation - Shock strut substantially damaged with partial structural failure, risk of structural failure during landing - Shock strut destroyed, risk of uncontrolled touch down leading to runway skid-off, resulting in damaged to aircraft and injury/fatality of human onboard
Fuselage Skin	- Fuselage skin damaged with minor permanent deformation - Fuselage skin substantially damaged, UAS penetrates fuselage, leading to injury of onboard personals and immediate termination of flight - Fuselage skin destroyed, UAS penetrates fuselage and injuring onboard personnel, risk of fuselage structural failure, leading to uncontrolled flight and injury/fatality of human onboard
Nosecone/Radome	- Nosecone/Radome damaged with minor permanent deformation - Nosecone/Radome substantially damaged, UAS penetrates skin, radar component damaged - Nosecone/Radome destroyed, UAS penetrates skin, radar component and primary structure substantially damaged, risk of structural failure
Landing Gears	- Landing gears damaged with minor permanent deformation - Landing gears substantially, risk of landing gears structural failure during landing, risk of uncontrolled touch down leading to runway skid-off, resulting in damaged to aircraft and injury/fatality of human onboard - Landing gears destroyed, risk of uncontrolled touch down leading to runway skid-off, resulting in damaged to aircraft and injury/fatality of human onboard

## Consequence Characterization of UAS Collision with Glider

Impact/Pass Zone	Collision Consequence
Near Miss	- Pilot distracted, critical during high-workload takeoff/landing phases
Wing	- Wing damaged minor permanent deformation - Wing substantially damaged with structural penetration, reduced structural integrity of primary structure, risk of structural failure - Wing destroyed, primary structure failed, leading to uncontrolled flight and injury/fatality of human onboard
Windshield	- Windshield damaged with minor fracture, pilot distracted - Windshield substantially damaged, UAS partially penetrate through, leading to pilot distraction and reduced visibility, risk of onboard injury - Windshield destroyed, UAS completely penetrate through, leading to pilot distraction and onboard injury/fatality
Horizontal Stabilizer	- Horizontal stabilizer damaged with minor permanent deformation - Horizontal stabilizer substantially damaged with structural penetration, reduced structural integrity of primary structure, risk of structural failure, reduced control surface movement - Horizontal stabilizer destroyed, primary structure failed, leading to uncontrolled flight and injury/fatality of human onboard
Vertical Stabilizer	- Vertical stabilizer damaged with minor permanent deformation - Vertical stabilizer substantially damaged with structural penetration, reduced structural integrity of primary structure, risk of structural failure, reduced control surface movement and pilot distracted - Vertical stabilizer destroyed, primary structure failed, leading to uncontrolled flight and injury/fatality of human onboard
Fuselage Skin	- Fuselage skin damaged with minor permanent deformation - Fuselage skin substantially damaged, UAS penetrates fuselage, leading to injury of onboard personals and immediate termination of flight - Fuselage skin destroyed, UAS penetrates fuselage and injuring onboard personnel, risk of fuselage structural failure, leading to uncontrolled flight and injury/fatality of human onboard
Landing Gears	- Landing gears damaged with minor permanent deformation - Landing gears substantially damaged, risk of landing gears structural failure during landing, risk of uncontrolled touch down leading to runway skid-off, resulting in damage to aircraft and injury/fatality of human onboard - Landing gears destroyed, risk of uncontrolled touchdown, leading to runway skid-off, resulting in damage to aircraft and injury/fatality of human onboard

## Consequence Characterization of UAS Collision with Ultralight

Impact/Pass Zone	Collision Consequence
Near Miss	- Pilot distracted, critical during high-workload takeoff/landing phases
Propeller	- Propeller damaged minor with permanent deformation - Propeller substantially damaged with partial structural failure, risk of unbalanced propeller rotation, leading to uncontrolled propeller vibration - Propeller destroyed, instance loss of thrust and risk of unbalanced propeller rotation, leading to uncontrolled propeller vibration
Wing	- Wing damaged with minor permanent deformation - Wing substantially damaged with structural penetration, reduced structural integrity of primary structure, risk of structural failure - Wing destroyed, primary structure failed, leading to uncontrolled flight and injury/fatality of human onboard
Human Pilot	- Human pilot minorly injured, pilot distracted and reduced physical ability - Human pilot seriously injured, reduced physical ability to control aircraft, risk of uncontrolled aircraft - Human pilot fatally injured, resulting in uncontrolled aircraft
Windshield	- Windshield damaged with minor fracture, pilot distracted - Windshield substantially damaged, UAS partially penetrate through, leading to pilot distraction and reduced visibility, risk of onboard injury - Windshield destroyed, UAS completely penetrate through, leading to pilot distraction and onboard injury/fatality
Frame	- Frame damaged with minor permanent deformation - Frame substantially damaged with partial structural failure, reduced structural integrity and risked of structural failure - Frame destroyed leading to unsupported wing, risk of structural failure, leading to uncontrolled flight and injury/fatality of human onboard
Horizontal Stabilizer	- Horizontal stabilizer damaged with minor permanent deformation - Horizontal stabilizer substantially damaged, reduced structural integrity of primary structure, risk of structural failure, reduced control surface movement - Horizontal stabilizer destroyed, primary structure failed, leading to uncontrolled flight and injury/fatality of human onboard
Vertical Stabilizer	- Vertical stabilizer damaged with minor permanent deformation - Vertical stabilizer substantially damaged with structural penetration, reduced structural integrity of primary structure, risk of structural failure, reduced control surface movement and pilot distracted - Vertical stabilizer destroyed, primary structure failed, leading to uncontrolled flight and injury/fatality of human onboard
Shock Strut	- Shock strut damaged with minor permanent deformation - Shock strut substantially damaged with partial structural failure, risk of structural failure during landing - Shock strut destroyed, risk of uncontrolled touchdown, leading to runway skid-off, resulting in damage to aircraft and injury/fatality of human onboard
Wing Strut	- Wing strut damaged with minor permanent deformation - Wing strut substantially damaged with partial structural failure, reduced structural integrity and risked of structural failure, leading to unsupported main wing - Wing strut destroyed leading to unsupported wing, risk of main wing structural failure, leading to uncontrolled flight and injury/fatality of human onboard
Fuselage Skin	- Fuselage skin damaged with minor permanent deformation - Fuselage skin substantially damaged, UAS penetrates fuselage, leading to injury of onboard personals and immediate termination of flight - Fuselage skin destroyed, UAS penetrates fuselage and injuring onboard personnel, risk of fuselage structural failure, leading to uncontrolled flight and injury/fatality of human onboard
Landing Gears	- Landing gears damaged with minor permanent deformation - Landing gears substantially damaged, risk of landing gears structural failure during touch down leading to runway skid-off, resulting in damage to aircraft and injury/fatality of human onboard - Landing gears destroyed, risk of uncontrolled touch down leading to runway skid-off, resulting in damaged to aircraft and injury/fatality of human onboard

## Consequence Characterization of UAS Collision with Rotorcraft

Impact/Pass Zone	Collision Consequence
Near Miss	- Pilot distracted, critical during high-workload takeoff/landing phases
Main Rotor Blade	- Rotor blade damaged with minor permanent deformation - Rotor blade substantially damaged with partial structural failure, risk of unbalanced propeller rotation leading to uncontrolled vibration - Rotor blade destroyed, instance loss of thrust and risk of uncontrolled vibration, leading to uncontrolled flight and onboard injury/fatality
Rotor Mast/Control Rod	- Rotor mast or control rod damaged with minor permanent deformation or surface damage - Rotor mast or control rod substantially damaged with partial structural failure, risk asymmetric rotation of rotor blades or loss of control over rotors - Rotor mast or control rod destroyed, loss of rotors and instance loss of thrust, leading to uncontrolled flight and onboard injury/fatality
Windshield	- Windshield damaged with minor fracture, pilot distracted - Windshield substantially damaged, UAS partially penetrate through, leading to pilot distraction and reduced visibility, risk of onboard injury - Windshield destroyed, UAS completely penetrate through, leading to pilot distraction and onboard injury/fatality
Tail Rotor	- Tail rotor damaged with minor permanent deformation - Tail rotor substantially damaged with partial structural failure, risk of unbalanced propeller rotation, leading to uncontrolled vibration and unstable/uncontrollable vehicle - Tail rotor destroyed, instance loss of stabilized thrust and risk of unbalanced propeller rotation, leading to uncontrollable vehicle which results in injury/fatality of human onboard
Engine Inlet	- Engine damaged, engine disrupted with significant reduction in power - Engine substantially damaged with complete loss of power, leading to vehicle uncontrolled descent, leading to uncontrolled flight and injury/fatality of human onboard - Engine destroyed with complete loss of power, engine catches on fire, risk of fire and explosion, leading to uncontrolled flight and injury/fatality of human onboard
Horizontal Stabilizer	- Horizontal stabilizer damaged minor permanent deformation - Horizontal stabilizer substantially damaged with structural penetration, reduced structural integrity of primary structure, risk of structural failure, reduced control surface movement - Horizontal stabilizer destroyed, permanent structure failed, leading to uncontrolled flight and injury/fatality of human onboard
Vertical Stabilizer	- Vertical stabilizer damaged with minor permanent deformation - Vertical stabilizer substantially damaged with structural penetration, reduced structural integrity of primary structure, risk of structural failure, reduced control surface movement and pilot distracted - Vertical stabilizer destroyed, permanent structure failed, leading to uncontrolled flight and injury/fatality of human onboard
Shock Strut	- Shock strut damaged with minor permanent deformation - Shock strut substantially damaged with partial structural failure, risk of structural failure during landing - Shock strut destroyed, risk of uncontrolled touch down leading to runway skid-off, resulting in damage to aircraft and injury/fatality of human onboard
Fuselage Skin	- Fuselage skin damaged with minor permanent deformation - Fuselage skin substantially damaged, UAS penetrates fuselage, leading to injury of onboard personals and immediate termination of flight - Fuselage skin destroyed, UAS penetrates fuselage and injuring onboard personnel, risk of fuselage structural failure, leading to uncontrolled flight and injury/fatality of human onboard
Landing Gears	- Landing gears damaged with minor permanent deformation - Landing gears substantially damaged, risk of landing gears structural failure during landing, risk of uncontrolled touch down leading to runway skid-off, resulting in damage to aircraft and injury/fatality of human onboard - Landing gears destroyed, risk of uncontrolled touch down leading to runway skid-off, resulting in damaged to aircraft and injury/fatality of human onboard

## References

- [1] Prevot, T., Rios, J., Kopardekar, P., Robinson III, J. E., Johnson, M., and Jung, J., “UAS Traffic Management (UTM) Concept of Operations to Safely Enable Low Altitude Flight Operations,” 16th AIAA Aviation Technology, Integration, and Operations Conference, 2016, pp. 1–16, doi: 10.2514/6.2016-3292, URL: <http://arc.aiaa.org/doi/10.2514/6.2016-3292>.
- [2] Eurocontrol, “RPAS ATM Conops,” 2017, URL: <http://www.eurocontrol.int/sites/default/files/publication/files/rpas-atm-cocept-of-operations-2017.pdf>.
- [3] FAA, “Small Unmanned Aircraft Systems, Title 14 of the Code of Federal Regulations (14 C.F.R.), Part 107,” 2017, URL: <https://www.ecfr.gov/cgibin/retrieveECFR?gp=1&SID=dcf7ddb5f58f33726d33d7bc50a36d72&ty=HTML&h=L&mc=true&r=PART&n=pt14.2.107>.
- [4] European Aviation Safety Agency, “Notice of Proposed Amendment 2017-05 (A) - Introduction of a Regulatory Framework for the Operation of Drones,” 2017, URL: [https://www.easa.europa.eu/sites/default/files/dfu/NPA 2017-05 \(A\)\\_0.pdf](https://www.easa.europa.eu/sites/default/files/dfu/NPA%202017-05%20(A)_0.pdf).
- [5] Burdett, H., Stoker, J., Strong, M., and Burdett, H., “Functional Hazard Assessment (FHA) Report for Unmanned Aircraft Systems,” 2009, URL: <https://www.eurocontrol.int/sites/default/files/content/documents/single-sky/uas/library/safety-uasfha-report-v2-ebeni.pdf>.
- [6] Belcastro, C. M., Newman, R. L., Evans, J., Klyde, D. H., Barr, L. C., and Ancel, E., “Hazards Identification and Analysis for Unmanned Aircraft System Operations,” 17th AIAA Aviation Technology, Integration, and Operations Conference, 2017, doi: 10.2514/6.2017-3269, URL: <https://arc.aiaa.org/doi/10.2514/6.2017-3269>.
- [7] Barr, L. C., Newman, R., Ancel, E., Belcastro, C. M., Foster, J. V., Evans, J., and Klyde, D. H., “Preliminary Risk Assessment for Small Unmanned Aircraft Systems,” 17th AIAA Aviation Technology, Integration, and Operations Conference, 2017, doi: 10.2514/6.2017-3272, URL: <https://arc.aiaa.org/doi/10.2514/6.2017-3272>.
- [8] Clothier, R. A., Williams, B. P., and Fulton, N. L., “Structuring the Safety Case for Unmanned Aircraft System Operations in Non-Segregated Airspace,” *Safety Science*, vol. 79, 2015, pp. 213–228, doi: 10.1016/j.ssci.2015.06.007, URL: <http://dx.doi.org/10.1016/j.ssci.2015.06.007>.
- [9] de Ruijter, A., and Guldenmund, F., “The Bowtie Method: A review,” *Safety Science*, vol. 88, 2015, pp. 211–218, doi: 10.1016/j.ssci.2016.03.001, URL: <http://dx.doi.org/10.1016/j.ssci.2016.03.001>.
- [10] Hong, E. S., Lee, I. M., Shin, H. S., Nam, S. W., and Kong, J. S., “Quantitative Risk Evaluation Based on Event Tree Analysis Technique: Application to the Design of Shield TBM,” *Tunnelling and Underground Space Technology*, vol. 24, 2009, pp. 269–277, doi: 10.1016/j.tust.2008.09.004, URL: <http://dx.doi.org/10.1016/j.tust.2008.09.004>.
- [11] Clothier, R. A., Williams, B. P., and Hayhurst, K. J., “Modelling the risks remotely piloted aircraft pose to people on the ground,” *Safety Science*, vol. 101, 2018, pp. 33–47, doi: 10.1016/j.ssci.2017.08.008, URL: <http://dx.doi.org/10.1016/j.ssci.2017.08.008>.

- [12] Tyagi, A., Zhang, Y., Toussaint, S., and Luxhoj, J. T., “Strategies to Model System Risk Using UAS Safety Analysis Model (USAM),” 16th AIAA Aviation Technology, Integration, and Operations Conference, 2016, pp. 1–14, doi: 10.2514/6.2016-3597, URL: <http://arc.aiaa.org/doi/10.2514/6.2016-3597>.
- [13] Lum, C. W., Gauksheim, K., and Kosel, T., “Assessing and Estimating Risk of Operating Unmanned Aerial Systems in Populated Areas,” 11th AIAA Aviation Technology, Integration, and Operations (ATIO) Conference, Virginia Beach, VA: 2011, pp. 1–12, doi: 10.2514/6.2011-6918.
- [14] European Aviation Safety Agency (EASA), “Drone Collision Task Force,” 2016, URL: [https://www.easa.europa.eu/system/files/dfu/TF\\_Drone\\_Collision\\_Report\\_for\\_Publication\\_%28005%29.pdf](https://www.easa.europa.eu/system/files/dfu/TF_Drone_Collision_Report_for_Publication_%28005%29.pdf).
- [15] Arterburn, D., Ewing, M., Prabhu, R., Zhu, F., and Francis, D., “FAA UAS Center of Excellence Task A4 : UAS Ground Collision Severity Evaluation,” 2017.
- [16] Campolettano, E. T., Bland, M. L., Gellner, R. A., Sproule, D. W., Rowson, B., Tyson, A. M., Duma, S. M., and Rowson, S., “Ranges of Injury Risk Associated with Impact from Unmanned Aircraft Systems,” *Annals of Biomedical Engineering*, 2017, doi: 10.1007/s10439-017-1921-6, URL: <http://link.springer.com/10.1007/s10439-017-1921-6>.
- [17] Schroeder, K., Song, Y., Horton, B., and Bayandor, J., “Investigation of UAS Ingestion into High-Bypass Engines, Part I: Bird vs. Drone,” 58th AIAA/ASCE/AHS/ASC Structures, Structural Dynamics, and Materials Conference, Reston, Virginia: American Institute of Aeronautics and Astronautics, 2017, pp. 1–10, doi: 10.2514/6.2017-0187, URL: <http://arc.aiaa.org/doi/10.2514/6.2017-0187>.
- [18] Schroeder, K., Song, Y., Horton, B., and Bayandor, J., “Investigation of UAS Ingestion into High-Bypass Engines, Part 2: Parametric Drone Study,” 58th AIAA/ASCE/AHS/ASC Structures, Structural Dynamics, and Materials Conference, Reston, Virginia: American Institute of Aeronautics and Astronautics, 2017, pp. 1–10, doi: 10.2514/6.2017-0187, URL: <http://arc.aiaa.org/doi/10.2514/6.2017-0187>.
- [19] Military Aviation Authority, “Small Remotely Piloted Aircraft Systems (drones) Mid-Air Collision Study,” 2017, URL: [https://www.gov.uk/government/uploads/system/uploads/attachment\\_data/file/628092/small-remotely-piloted-aircraft-systems-drones-mid-air-collision-study.pdf](https://www.gov.uk/government/uploads/system/uploads/attachment_data/file/628092/small-remotely-piloted-aircraft-systems-drones-mid-air-collision-study.pdf).
- [20] European Aviation Safety Agency, “Prototype Commission Regulation on Unmanned Aircraft Operations,” 2016, URL: [https://www.easa.europa.eu/system/files/dfu/UAS\\_Prototype\\_Regulation\\_final.pdf](https://www.easa.europa.eu/system/files/dfu/UAS_Prototype_Regulation_final.pdf).
- [21] SESAR Joint Undertaking, “U-Space Blueprint,” 2017, doi: 10.2829/614891, URL: <http://www.sesarju.eu/u-space-blueprint>.
- [22] ICAO, “Annex 11 - Air Traffic Services,” 2001.
- [23] FAA, “Instrument Flying Handbook,” U.S. Department of Transportation Federal Aviation Administration, 2012, doi: 10.1186/s12986.
- [24] Electronic Code of Federal Regulations (e-CFR), “Title 14 of Code of Federal Regulations (14 C.F.R.) - Part 107 Small Unmanned Aircraft Systems,” 2018 URL <https://www.ecfr.gov/cgi-bin/textidx?SID=8a0503d486fa747c92093b3853a20cc1&mc=true&node=pt14.2.107&rgn=div5>.



- [25] FAA, “Summary of Small Unmanned Aircraft Rule (Part 107),” 2016, URL: [http://www.faa.gov/uas/media/Part\\_107\\_Summary.pdf](http://www.faa.gov/uas/media/Part_107_Summary.pdf).
- [26] Kopardekar, P., “Unmanned Aerial System ( UAS ) Traffic Management ( UTM ): Enabling Low-Altitude Airspace and UAS Operations,” California: 2018.
- [27] City Population, “Population Statistics for Countries” URL <https://www.citypopulation.de/>.
- [28] European Aviation Safety Agency, “Standardised European Rules of the Air,” 2018 URL <https://www.easa.europa.eu/regulation-groups/sera-standardised-european-rules-air>.
- [29] National Transportation Safety Board, “Aviation Incident Final Report,” 2017 URL <https://app.nts.gov/pdfgenerator/ReportGeneratorFile.ashx?EventID=20170922X54600&AKey=1&RType=HTML&IType=IA>.
- [30] Office of the Secretary of Department of Defense, “Unmanned Systems Roadmap 2007 - 2032,” Washington: 2007.
- [31] Association General Aviation Manufacturers, “2016 General Aviation Statistical Databook & 2017 Industry Outlook,” Washington, DC: 2016, URL: [www.gama.aero](http://www.gama.aero).
- [32] Rambabu, P., Prasad, N. E., and Kutumbarao, V. V., “Aerospace Materials and Material Technologies,” 2017, doi: 10.1007/978-981-10-2143-5, URL: <http://link.springer.com/10.1007/978-981-10-2143-5>.
- [33] Pauliny, J., “The Overview of Propellers in General Aviation,” Brno University of Technology, 2012.
- [34] Civil Aviation Authority, “Bowtie Risk Assessment Models,” 2015 URL <https://www.caa.co.uk/Safety-initiatives-and-resources/Working-with-industry/Bowtie/Bowtie-elements/Consequences/>.
- [35] International Civil Aviation Organisation, “Annex 13 To the Convention on International Civil Aviation - Aircraft Accident And Incident Investigation,” 2001, URL: [http://www.emsa.europa.eu/retro/Docs/marine\\_casualties/annex\\_13.pdf](http://www.emsa.europa.eu/retro/Docs/marine_casualties/annex_13.pdf).
- [36] Civil Aviation Safety/Monash University, “Human Injury Model for Small Unmanned Aircraft Impacts,” 2013.
- [37] May, T. A., Texas, D., Gomez, L., and Cairns, D., “UAS Airborne Collision Severity Evaluation,” 2017, URL: <http://www.assureuas.org/projects/deliverables/a3/Volume I - UAS Airborne Collision Severity Evaluation - Structural Evaluation.pdf>.
- [38] D’Souza, K., Lyons, T., Lacy, T., and Kota, K., “Volume IV - UAS Airborne Collision Severity Evaluation – Engine Ingestion,” 2017, URL: <http://www.assureuas.org/projects/deliverables/a3/Volume IV - UAS Airborne Collision Severity Evaluation - Engine Ingestion.pdf>.



---

## Multibody System Modeling of UAS Collisions with the Human Head

*Understanding the impact severity of UAS collisions with the human body remains a challenge and is essential to the development of safe UAS operations. Complementary to performing experiments of UAS collisions with a crash dummy, a computational impact model is needed in order to capture the large variety of UAS types and impact scenarios. This paper presents the development of a multibody system model of a collision of one specific UAS type with the human body as well with a crash dummy. This specific UAS type has been chosen because data from experimental drop tests on a crash dummy is available. This allows the validation of the multibody system model of UAS impacting a crash dummy versus experimental data. The validation shows that the multibody system model closely matches experimental UAS drop tests on a crash dummy. Subsequently, the validated UAS multibody system model is applied to predict human body injury using a biomechanical human body model. Head and neck injury from the frontal, side and rear impact on the human head are predicted at various elevation angles and impact velocities. The results show that neck injury is not a concern for this specific UAS type, but a serious head injury is probable.*

This chapter has been published as “Rattanagraikanakorn, B., Gransden, D. I., Schuurman, M., De Wagter, C., Happee, R., Sharpanskykh, A., and Blom, H. A. P., “Multibody System Modelling Of Unmanned Aircraft System Collisions With The Human Head,” International Journal of Crashworthiness, vol. 0, 2019, pp. 1–19.”

### 3.1 Introduction

UAS (or unmanned aircraft system) operations have received much attention in the past few years and will soon become a critical part in aviation. Low-level UAS operations will likely be operated in an urban environment where population density is high. While this type of operations may pose a serious collision risk to people on the ground, the level of severity of UAS collisions on a human is not yet fully understood. This lack of understanding affects rules and regulations, as well as any necessary mitigative measures, to be established in order to prevent fatal accidents. EASA [1] has published prototype rules and regulations for UAS operations, nevertheless, additional scientific results are still required to support UAS requirements. As stated by EASA [2], there is still an urgent need to investigate UAS collision risks using experimentation and validated analytical models.

Several research groups have investigated the effect of UAS collisions on different actors on the ground. Civil Aviation Safety Authority and Monash University [3] proposed a simplified injury prediction model for the impact of small UAS on a person on the ground to determine a non-lethal UAS mass. The model predicted the severity level from blunt force trauma injuries based on the impacting projectile's kinetic energy and impact diameter. Another modeling approach was proposed by Magister [4] to assess small UAS injury biomechanics resulting from blunt ballistic impact. Nevertheless, such simplified energy-based models were not sufficient to provide physical insights into how UAS collision may inflict injury. To better understand UAS collision consequences, ASSURE conducted a series of impact drop test using DJI Phantom III on FAA Hybrid III crash dummy at various impact attitude and speed [5–7]. Koh et al. [8,9] also conducted extensive drop tests and computational crash simulations of different drone weight classes on a crash dummy head. In addition, Campolettano et al. [10] performed a series of live flight test and impact drop test using three different UAS weight classes on an instrumented Hybrid III crash dummy. The aim of the test was to estimate the range of injury risks to humans due to UAS impact.

The relatively high costs of live impact testing make it difficult to cover various impact conditions (e.g. impact direction, attitude, or speed) and to conduct sensitivity analysis. Such difficulties can be overcome by using a computational model. For modeling and analysis of crashworthiness of aircraft parts, the finite element modeling (FEM) approach is typically adopted. However, for modeling and assessment of human injury in automotive and aerospace crashworthiness, not FEM but multibody system (MBS) modeling is widely used [11–14]. An MBS model consists of masses, springs, and dampers. SOMLA [15] and MADYMO [16] are examples of a multibody system based computer codes widely used for occupant impact simulation. In spite of the physiological simplifications of MBS relative to FEM, research has shown that for human injury modeling MBS can offer similar results compared to FEM. FEM is most effective when the modeling problem requires a high-fidelity model that can capture non-linear material (tissue) local deformation and damage. However, UAS to human collision does not require such level of detail in order to approximate injury level sustained from a collision. Typically, overall kinematics of the human body (e.g. head acceleration) is needed to approximate, for example, head or neck injury level through various injury criterions.

Therefore, the aim of this paper is to develop an MBS model of a typical UAS that can be used for crash simulation against a crash dummy or the human body. This paper is organized as follows. Section II describes the modeling process of the UAS MBS model, and a description of the human body and crash dummy models used in the simulation. Section III presents the validation of the MBS model. Section IV describes a crash simulation of the MBS model on

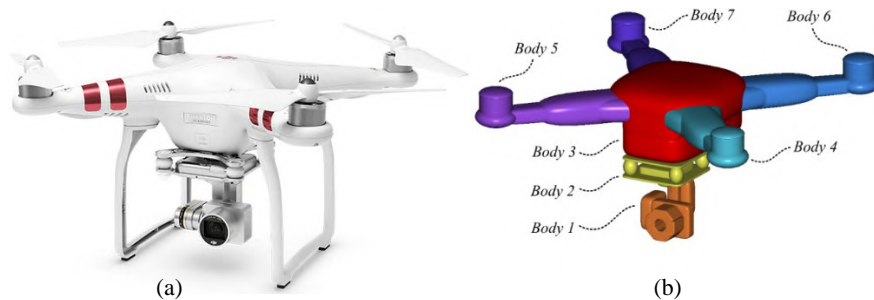
the human body and the injury severity of the human body. Section V and VI present the discussion of the results and the conclusion, respectively.

## 3.2 Multibody System Models

### 3.2.1. UAS Multibody System Modeling

The specific UAS considered is the DJI Phantom III, shown in Figure 3.1(a). For this UAS, a multibody system (MBS) model was developed, which is shown in Figure 3.1(b). In order to develop the model, impact footage from ASSURE [17] was investigated to identify a necessary number of body and joint, as well as joint type. The model is developed based on an assumption that there is no breakage of DJI Phantom III parts. The MBS model of the DJI Phantom III comprises of 7 rigid bodies, that are connected by restraint joints and dampers. The main body which includes the mainframe, avionic system and battery were lumped into Body 3. Four motors at the end of each arm were lumped into 4 bodies, which are Body 4, 5, 6 and 7. Body 2 was a lumped mass of the damp plate and avionic system for gimbal/camera control. Lastly, Body 1 was a lumped mass of the camera body and the gimbal.

The ellipsoid surface was used to model external surfaces of the DJI Phantom III drone and for contact detection and calculation. Ellipsoid surface uses force-penetration contact model to account for an interaction between the surfaces which allows the UAS model to interact with a crash dummy or the human body models in MADYMO. Kinematic joints connect bodies together while fixing the specific degrees of freedom for each body. Figure 3.2 illustrates rigid masses and dimensions of each segment as well as joint positions. Three types of joints were used in this model, namely translational-revolute for Joint 1, translational for Joint 2 and universal for joint 3 to 6. At each joint, Kelvin restraints (translational spring parallel with a damper) or Cardan restraints (torsional spring parallel with a damper) were implemented to account for force deflections from structural deformations.



**Figure 3.1. DJI Phantom III UAS considered for impact modeling: (a) real-world system and (b) multibody system (MBS) model. Notice that the two landing skids are not modeled because these are not in contact with the human head under the impact cases that are investigated.**

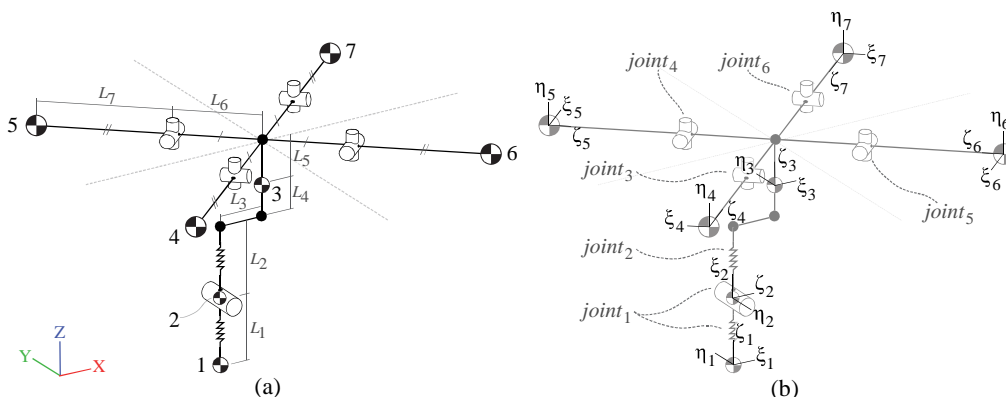


Figure 3.2. Skeletons of the MBS model of a DJI Phantom III UAS showing rigid masses, joints, and restraints. (a) illustrates rigid masses, and dimensions of each segment and (b) shows joint positions and local referential locations.

Table 3.1. Kinematic joint descriptions for UAS multibody system model

Joint	Type	Description
1	Translational-Revolute	Damp plate - Camera gimbal
2	Translational	Mainframe - Damp plate
3-6	Universal	Mainframe - Motor arm

Notice that the landing gear is not included in this DJI Phantom III MBS model. The footage analysis shows large lateral deflection of the landing gears (or skids) upon impact with the dummy head. In the collinear impact case considered, the gap between two landing gears is larger than the width of the head, resulting in no direct contact of the landing gears to the head. Also, based on preliminary stiffness tests on different components, the landing gears are made of thin ABS plastic structure which is softer than other components on the DJI Phantom III UAS. An analysis of a simplified lumped-parameter mass (LPM) model shows that the impact force on the head due to landing gear as a point of contact is non-prominent and smaller than frontal body or gimbal contacts. Therefore, the landing gears are excluded from this specific DJI Phantom III UAS model.

### 3.2.2. UAS Vehicle Parameters

Important UAS vehicle parameters, which are mass, the moment of inertia and geometrical dimensions of the UAS were obtained experimentally using the real UAS. Masses of rigid bodies were measured directly on a weight scale and bifilar tests were performed to estimate the moment of inertia of each body. Geometrical dimensions were obtained directly from physical measurements of a DJI Phantom III. Table 3.2 shows the summary of UAS masses and moment of inertias and Table 3.3 shows the summary of geometrical dimensions of the UAS.

Table 3.2. Summary of UAS vehicle parameters which were obtained experimentally.

Body	Mass [kg]	Moment of Inertia [kg m <sup>2</sup> ]
1	0.101	$I_{XX} = 1.8 \times 10^{-7}$ , $I_{YY} = 1.2 \times 10^{-7}$ , $I_{ZZ} = 1.8 \times 10^{-7}$
2	0.056	$I_{XX} = 2.3 \times 10^{-6}$ , $I_{YY} = 2.3 \times 10^{-6}$ , $I_{ZZ} = 1.9 \times 10^{-10}$
3	0.839	$I_{XX} = 4.9 \times 10^{-3}$ , $I_{YY} = 5.3 \times 10^{-3}$ , $I_{ZZ} = 9.4 \times 10^{-3}$
4, 5, 6, 7	0.055	$I_{XX} = 4.4 \times 10^{-7}$ , $I_{YY} = 4.4 \times 10^{-7}$ , $I_{ZZ} = 6.0 \times 10^{-8}$

Table 3.3. Summary geometrical dimensions of the UAS

Segment	Length [m]	Segment	Length [m]
$l_1$	0.044	$l_5$	0.030
$l_2$	0.020	$l_6$	0.014
$l_3$	0.023	$l_7$	0.165
$l_4$	0.016		

### 3.2.3. Calibration of UAS Multibody System Model

To model a UAS during an impact event, deformation of the structural components during impact is required and should be representative of the real system. Such deformation can be measured for a DJI Phantom III model in a form of joint displacement with a restraining force which is represented by a force-displacement curve (or moment-angular displacement curve for rotational joint) as shown in Figure 3.4.

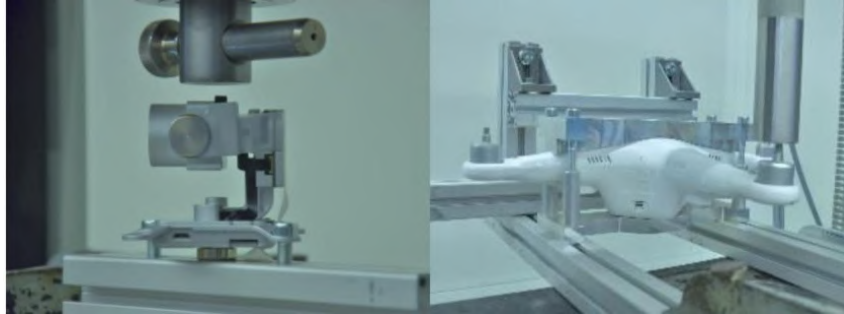


Figure 3.3. Examples of the experimental setup for compressive static test on UAS structural members to determine joint restraint characteristics curves for joint 1 (left) and joint 3 (right).

To implement these restraint characteristics in the MBS model of DJI Phantom III, the obtained curves are divided into 3 curves, namely, loading, hysteresis and unloading curves. These restraint characteristics were obtained from compressive quasi-static tests on the real system, as shown in Figure 3.3. Structural members that represent each joint were loaded (at 5 mm/s loading speed) until the structure failed or the maximum structural strength was reached. Then, the structure was unloaded at the same rate to obtain unloading characteristics.

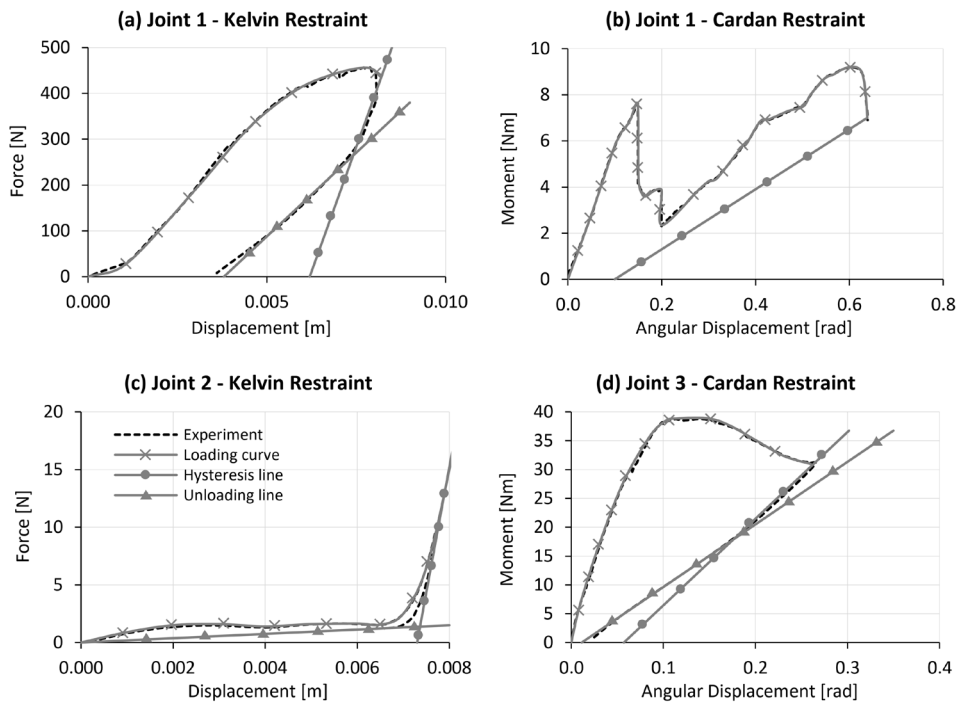


Figure 3.4. Example of restraints characteristics measured during experiments (black dotted line) and approximated curves for loading, hysteresis and unloading for joint 1-3. Simplified loading, hysteresis and unloading curves are used in the MBS model of the DJI Phantom III UAS.

Based on the sensitivity analysis, damping coefficient of Kelvin restraint of Joint 1 and Cardan restraint of joint 3-6 has a significant effect on energy transfer of the system. Structural

damping coefficient,  $c$ , of the kelvin restraint can be approximated using the equation:

$$c = 4\pi f\zeta m \quad (3.1)$$

The natural frequency of a structure was obtained from a ground vibration test (GVT) on specific joints, having the value of 631.7 Hz and 84.5 Hz for Joint 1 and joint 3-6, respectively. The structure of the camera gimbal is made from aluminum with multiple joints and has a damping ratio of 0.07 based on literature [18]. For the motor arm, ABS plastic material was used and the typical damping ratio of 0.05 was used. The calculated damping for joint 1 and joint 3-6 are 85 N·s/m and 0.23 N·m·s/rad, respectively.

### 3.2.4. Multibody System Models of Human Body and Crash Dummy

Figure 3.5(a) shows the human body model that is available in MADYMO and selected to simulate a crash test with the MBS model of the DJI Phantom III UAS. The human body model was distributed with MADYMO 7.7 (filename: h\_occ50fc, version 5.2) and was published by Happee et al. [19,20]. This facet occupant model is a representative model to the real mid-sized (50<sup>th</sup> Percentile) male human body [21]. This human body model produces a more similar response to the real human body because it has a higher bio-fidelity and better compliance with a real human body than the Hybrid III crash dummy model that is shown in Figure 3.5(b).

For validation purposes, the Hybrid III crash dummy model, shown in Figure 3.5(b), was also integrated with the MBS model of the DJI Phantom III UAS. This Hybrid III crash dummy was also distributed with MADYMO 7.7 (filename: d\_hyb350el\_Q, version 2.0) [22].

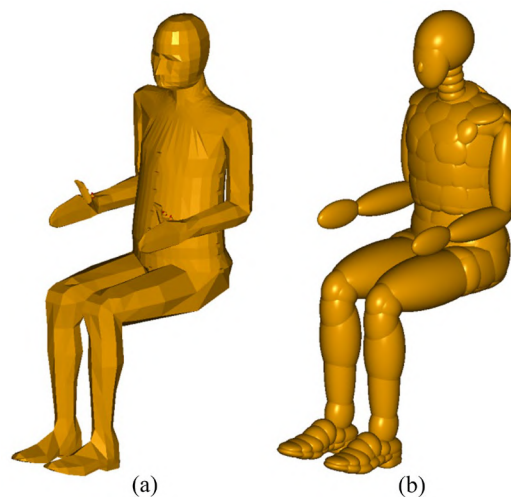


Figure 3.5. MBS models of human body and crash dummy (a) Human body model from MADYMO 7.7 and (b) Hybrid III crash dummy model from MADYMO 7.7.

### 3.2.5. Contact Model

Contact between the crash dummy and the UAS was modeled based on a non-smooth, force-penetration contact model in which the contact force is a function of the penetration and velocity of penetration [14]. Contacts compliance characteristics between a UAS model and the crash dummy was approximated using an elastic-perfectly plastic contact model based on Hertz elastic contact model proposed by Brake [23]. Materials property of UAS (e.g. ABS plastic, and Aluminium) was obtained from an online source, MATBASE [24]. For a crash dummy, the head contact surface was assumed to have characteristics of a human head scalp and the materials property was obtained from the experiment presented by Lozano-Minguez et



al. [25]. Since the materials properties come in ranges of values, the contact curves derived then consist of an upper and lower bound curve, corresponding to the lower and upper values of the materials properties. Additionally, the friction coefficient was introduced to contact models between the UAS and the dummy head. The friction coefficient of 0.3 was used for UAS front contact and camera bottom surface contact. To account for the dig-in effect of the camera frontal contact which has a small contact area, the friction coefficient of 1.2 was used.

In addition to the contact with the human head, two contacts between internal parts of the UAS are also accounted for. The first contact is between a damp plate and the main UAS body and the second contact is between the lower and upper parts of the camera gimbal. All contact points are presented in Figure 3.6. The contact compliance curves for UAS to human head contact and UAS internal parts contacts implemented in MADYMO is shown in Figure 3.7.

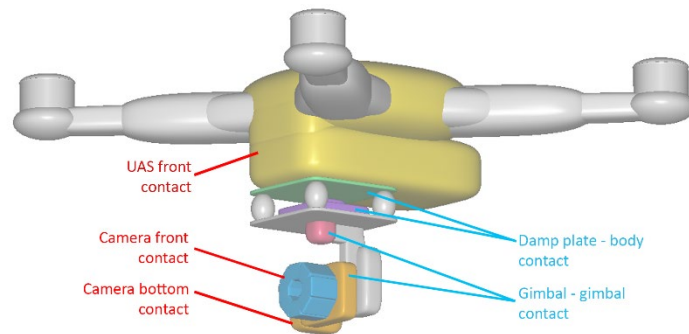


Figure 3.6. Illustration of contact areas between UAS and crash dummy head (red) and contact areas of UAS internal parts (blue).

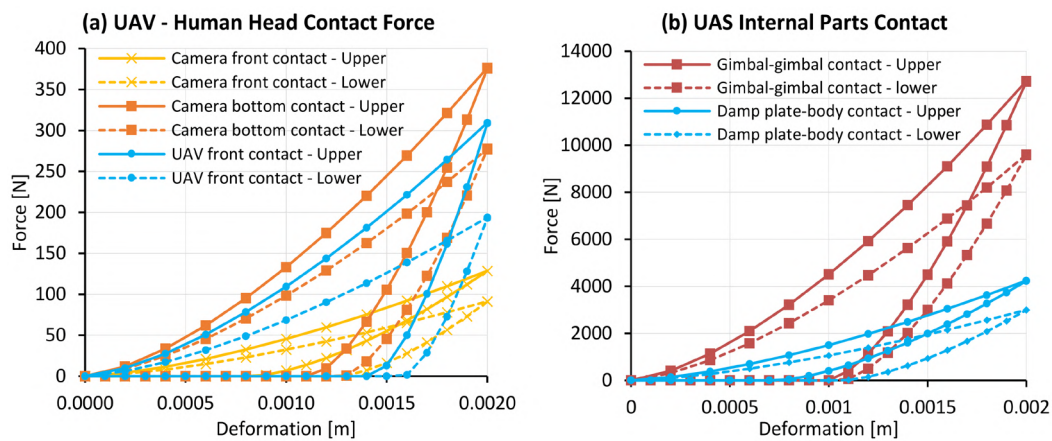


Figure 3.7. Contact compliance curves for (a) UAV – human head contacts and (b) UAS internal parts contacts derived using an elastic-perfectly plastic contact model based on Hertz contact proposed by Brake [23].

### 3.3 Validation of Multibody System Model

The MBS model of the DJI Phantom III UAS was implemented and integrated with the human body and crash dummy models in MADYMO 7.7. Subsequently, this integrated model was validated using experimental data from a full-scale crash test between a DJI Phantom III UAS and the FAA Hybrid III crash dummy performed by ASSURE [6]. The tests measured the head center of gravity (CG) accelerations, neck forces and moments of the crash dummy at various impact angles and velocities to estimate head and neck injuries.

To ensure that the UAS model has a realistic impact force transfer to the head, head CG resultant acceleration and upper neck force of the crash dummy were validated. A simulation,

which consisted of the UAS model and the Hybrid III crash dummy model, was set up in a similar manner to the ASSURE’s impact tests as shown in Figure 3.8. The crash dummy was seated on a rigid seat with full back support and the UAS impact velocity vector was aligned toward the head center of gravity to simulate CG-CG impact. UAS angle of attack was set at zero, aligning with the horizontal axis. Elevation angle,  $\theta$ , and impact velocity,  $V_{\text{impact}}$ , of the UAS model was set to simulate equivalent testing conditions to the ASSURE experiments. Three impact cases that were validated were vertical, angle and horizontal impact cases, which corresponding to  $\theta$  of  $90^\circ$ ,  $58^\circ$ ,  $65^\circ$  and  $0^\circ$ , respectively. The simulation was run on a 2.6 GHz processor, resulting in a computational time for each simulation of approximately 120 s.

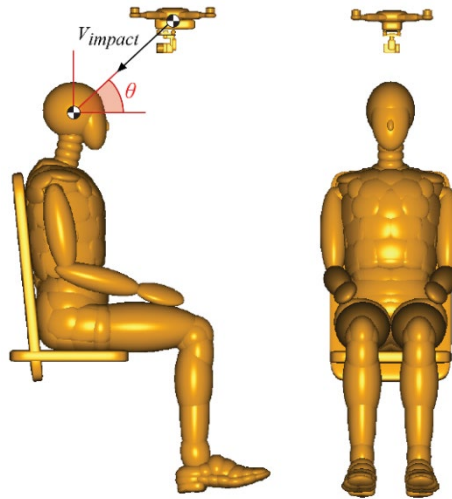


Figure 3.8. Setup for integrated model validation in MADYMO. The MBS model of the Hybrid III 50th percentile (male) crash dummy that was used in ASSURE impact drop testing [6]. For the model, the dummy is assumed to be seated on a rigid seat and the UAS impact velocity is aligned with the CG of the crash dummy.

### 3.3.1. Vertical Impact Validation

For vertical impact case ( $\theta$  of  $90^\circ$ ) in which the UAS model fell vertically on the crash dummy, validation was performed at two impact velocity: 9.9 m/s and 15.1 m/s. Figure 3.9 shows a comparison of time sequences between the model and the test of the vertical impact event at 15.1 m/s impact velocity. The kinematic of the UAS model corresponds well with the experiment, showing similar full compression phase of the UAS at approximately 7 ms, and similar rebound and rotational characteristics.

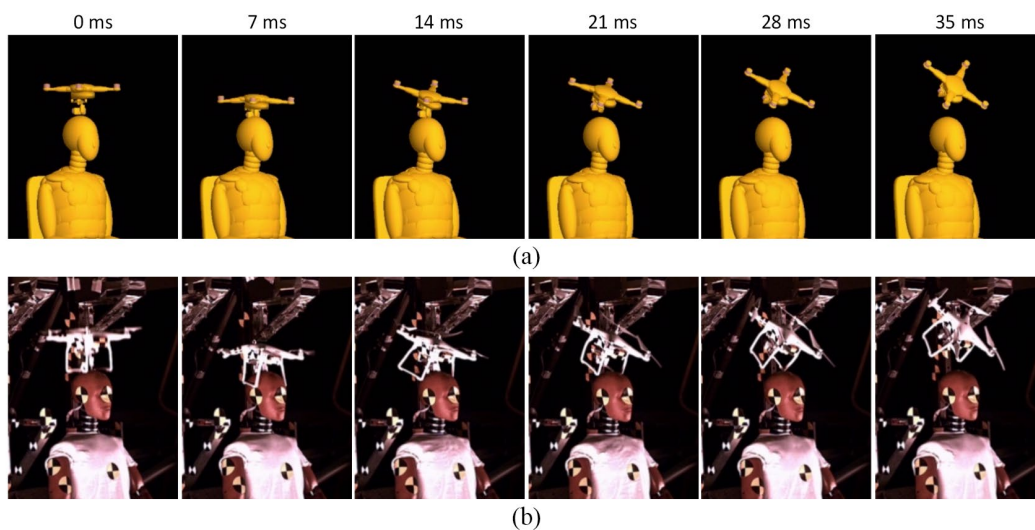


Figure 3.9. Comparison of (a) MBS model versus (b) ASSURE experiment from [17] at  $90^\circ$  elevation angle and 11.2 m/s impact velocity.

Figure 3.10 shows a comparison of head CG resultant acceleration in the time domain of the vertical impact case at 9.9 m/s and 15.1 m/s between the model and ASSURE's experiment. For impact velocity of 9.9 m/s, the simulated results show a good correlation with Experiment 2 but show slight discrepancy with Experiment 1 and 3. Despite the differences in experimental results, it is obvious that the simulated model can produce a very similar trend to the real-world system. For 15.1 m/s, the acceleration from the model agrees well with the experimental results for the first 5 ms. In the figure, the first peak represents the contact force from the contact initiation between the two bodies. The second peak occurs when the whole UAS body transfers impact energy to the dummy head, while the third peak shows the UAS bouncing off the dummy head. The primary first and second peak corresponds well with the real system, while the third peak shows a significant difference. In the third peak region, the head acceleration from the model damps out at a slower rate comparing to the experimental results. It is influenced by two main factors: rebound characteristics of the UAS model and the dummy model neck response.

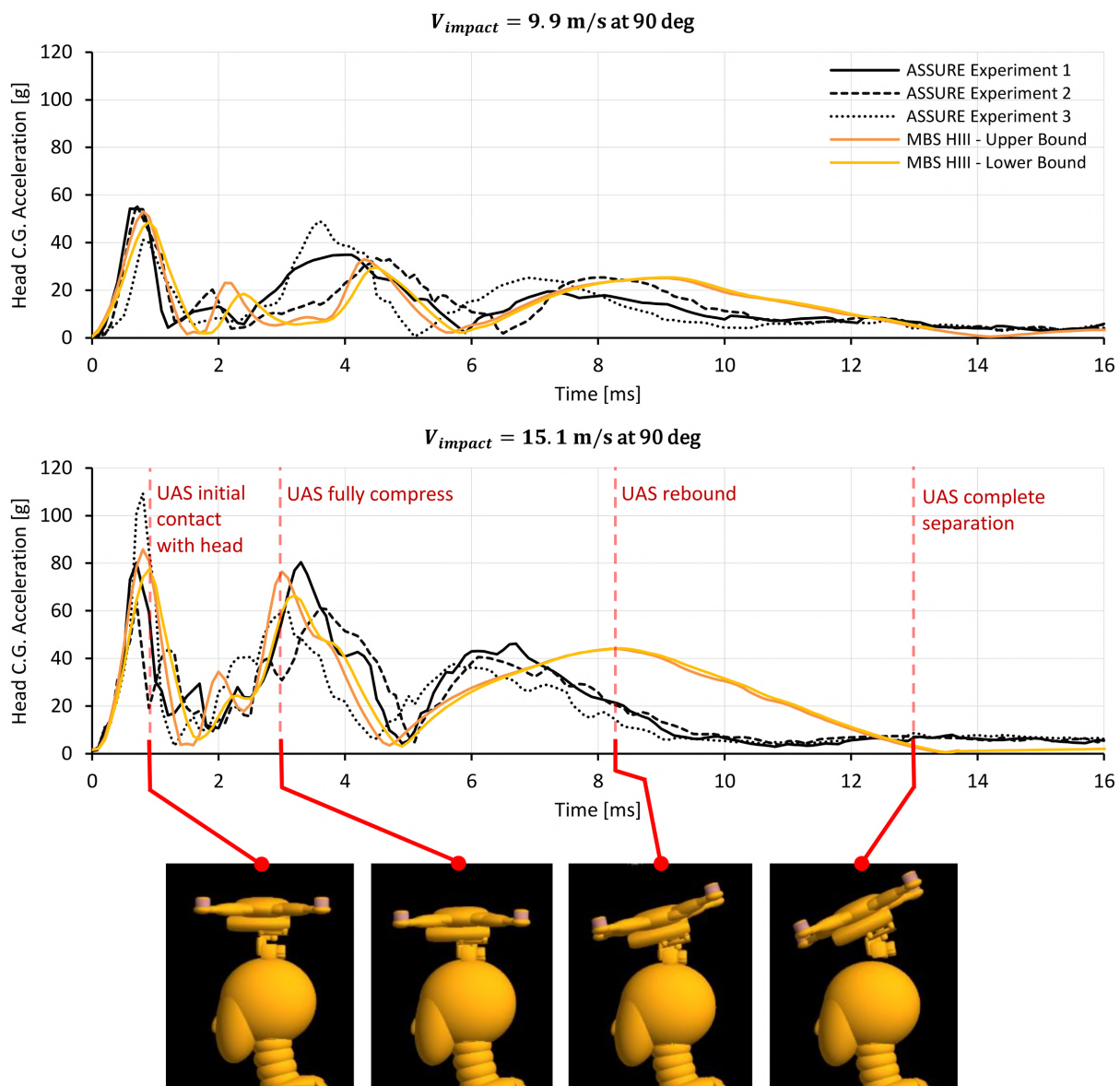
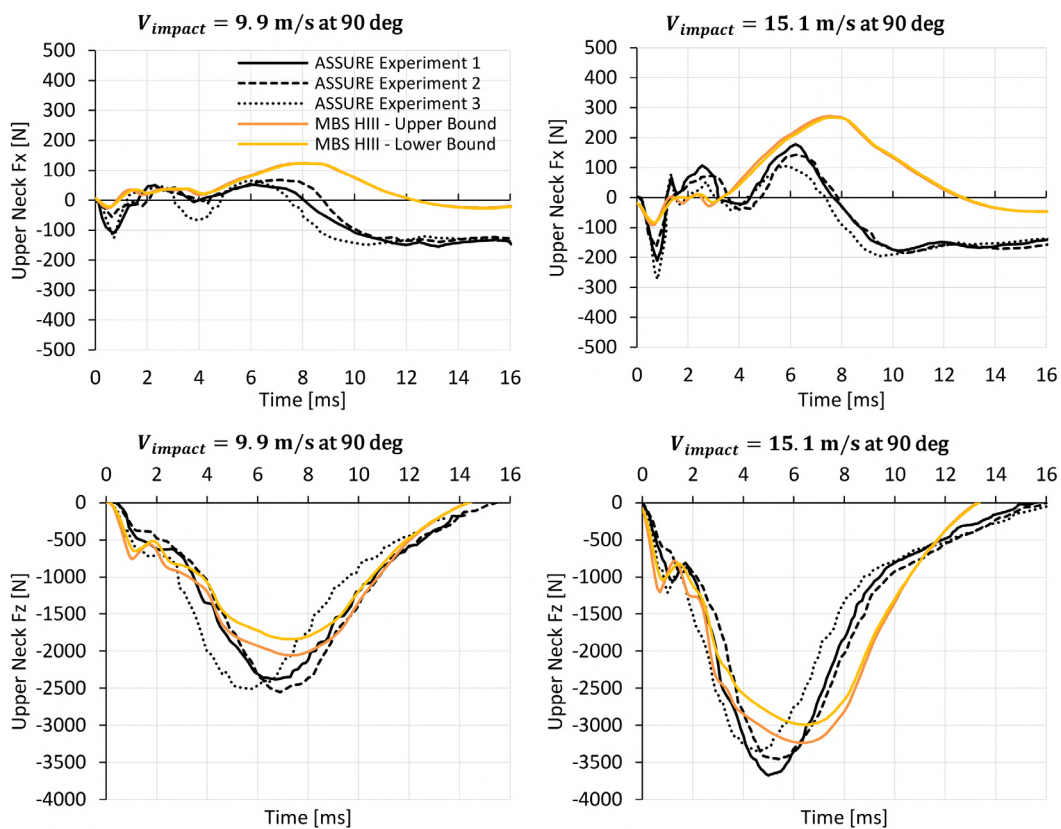


Figure 3.10. Comparison of the resultant acceleration-time history of head CG between MBS model and ASSURE experimental results at 9.9 m/s and 15.1 m/s impact velocity and 90° impact angle.

The accuracy of the model of such a complex system typically deteriorates over time, as more components are interacting and influencing one another. In addition, such discrepancy between the model and experiments may come from the lack of damping introduced in the model – these parameters are difficult to measure and model accurately. Nevertheless, for such impact case, the first two peaks are most important to the determination of the head injury criteria, such as the  $HIC_{15}$ .

Upper neck force in x and z-directions were validated for vertical impact at 9.9 m/s and 15.1 m/s impact velocity as shown in Figure 3.11. For the upper neck force in the x-direction, the model over predicts the maximum peak force by approximately 60% and 33% for 9.9 m/s and 15.1 m/s, respectively. Despite the large percentage differences, the force differences, which is less than 100 N, are not large enough to significantly affect neck injury prediction. Furthermore, upper neck force in the z-direction for both velocities from the model show good agreement with the experiments with approximately 13% and 6% differences in peak force values for 9.9 m/s and 15.1 m/s, respectively.



**Figure 3.11. Comparison of force-time history from the upper neck load cell in x- and z-directions between MBS model and ASSURE experimental results at impact velocities of 9.9 m/s and 15.1 m/s and at 90° elevation angle.**



### 3.3.2. Angled Impact Validation

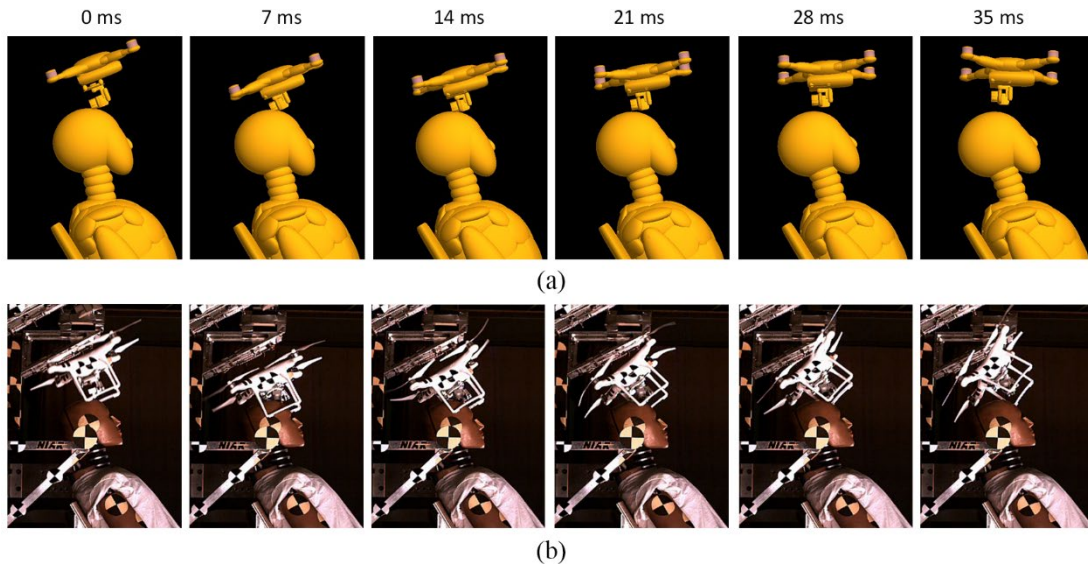


Figure 3.12. Comparison of (a) MBS model versus (b) ASSURE experiment from [17] at 65° elevation angle and 11.3 m/s impact velocity.

Head CG accelerations and upper neck forces were validated at impact angles of 59° and 65°. Figure 3.12 shows a comparison of time sequences between the model and experiment of 65° impact event at 11.3 m/s impact velocity. The overall kinematics of the UAS model is different from the experiment. Such differences can be explained by the differences in the UAS model fidelity. In this angle impact, camera-gimbal which is the contact point is modeled as a single lumped mass with only a translational and revolute joint. Such a simplified model differs from the real UAS which consists of multiple revolute joints and free-rotating parts, thus leading to the differences in the timing of parts interaction. In addition, the camera points forward in the model, while in the experiment, the camera pointed downward – resulting in different moment arm lengths.

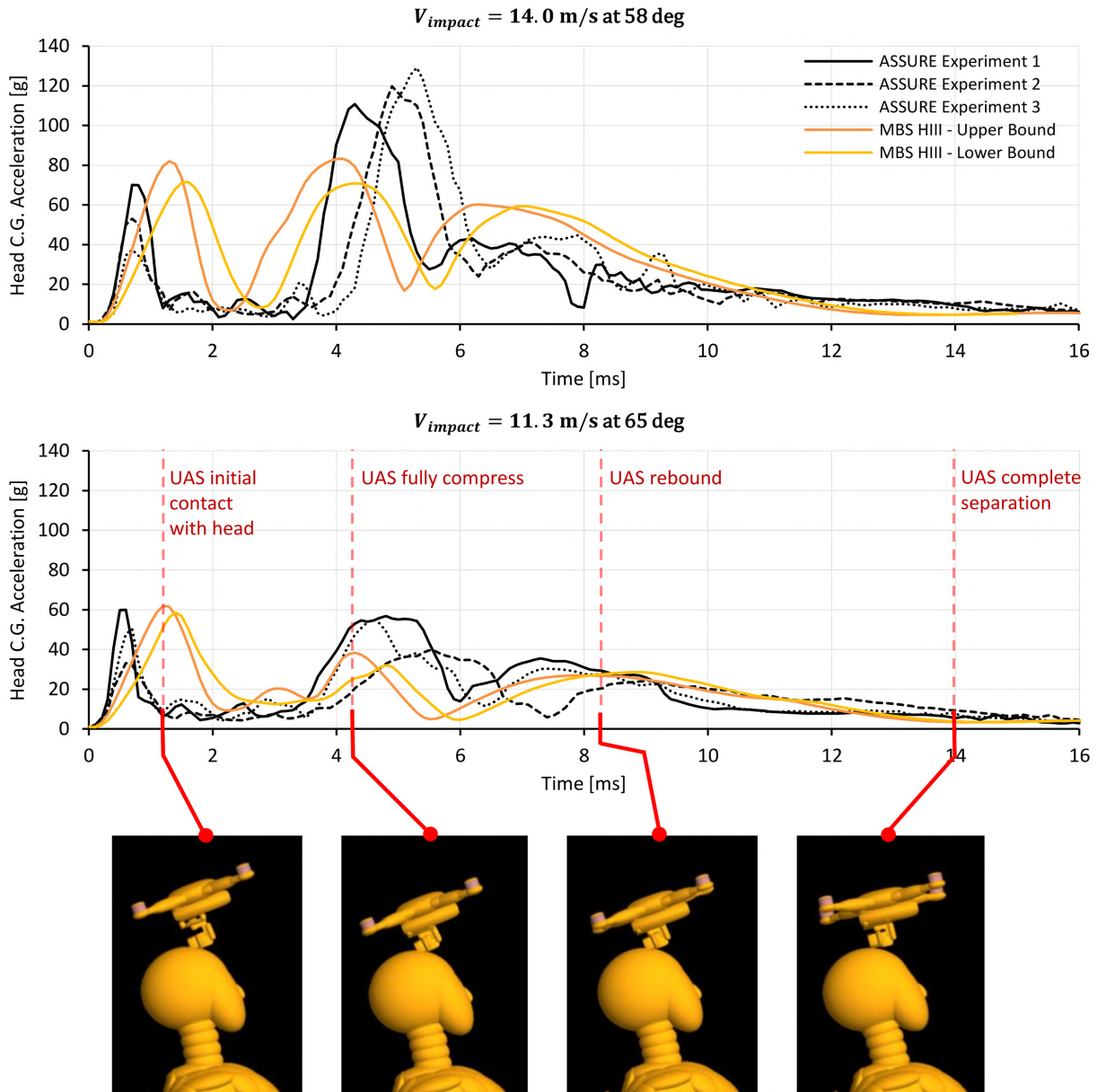


Figure 3.13. Comparison of resultant head CG acceleration-time history between the MBS model and ASSURE experimental results. Impact velocities of 11.3 m/s and 14.0 m/s at 65° and 58° impact angle respectively.

In Figure 3.13, the model produces similar trends for head CG accelerations comparing to the tests. The contact force and its damping characteristics of the model produces an over-estimated head acceleration as can be seen in the variations of the first peak. One of the influencing factors is contact damping, which is not introduced in the contact model. In the real system, skin damping is expected as the crash dummy skin is made of vinyl which is highly damped. In addition, the full compression phase of the UAS in the test (represented by the second peak of the head acceleration) occurs approximately 2 ms after the contact phase. Such lagging is different from the model because the model does not take include the effect of free rotating parts and has a lower number of joints.

For upper neck forces in x and z-directions, the model corresponds well with the tests but with a slight overestimation of the contact forces, which are shown at approximately 1.5 ms in Figure 3.14. The peak force differences for 14 m/s at 58° impact case is less than 10%. For 11.2 m/s at 65° impact case, the peak force differences are within 15%, which is within an acceptable limit of 20%.

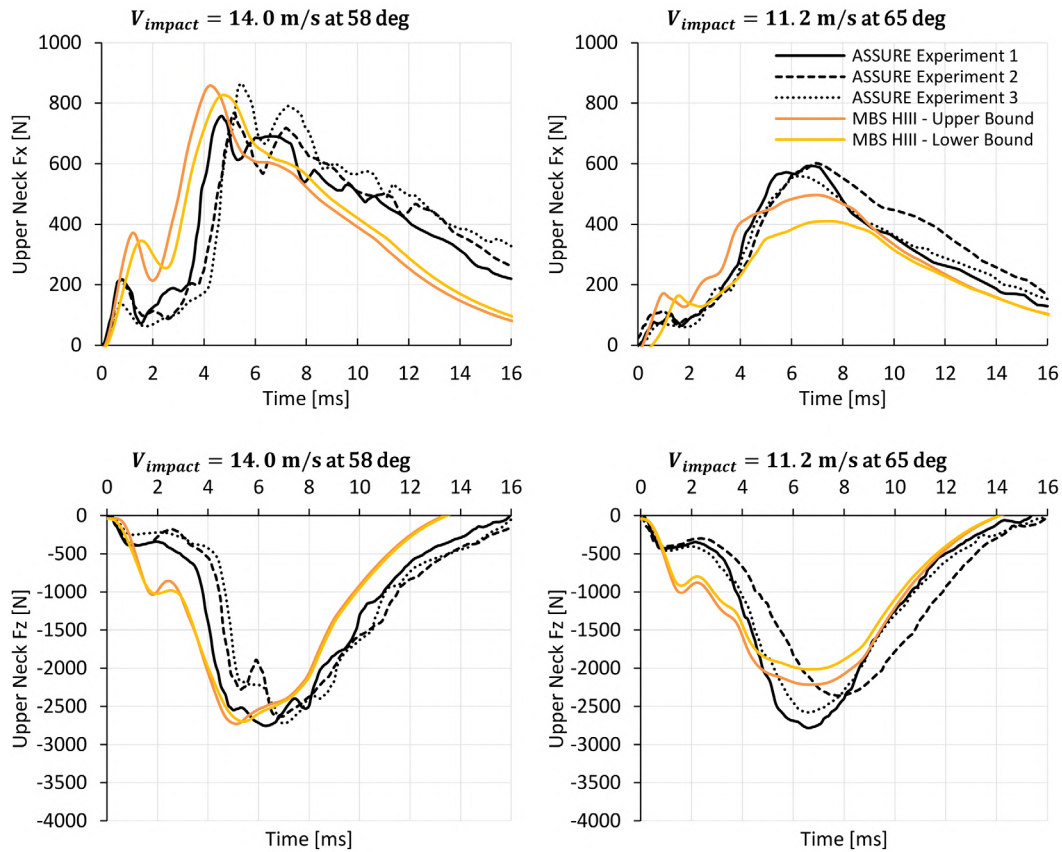


Figure 3.14. Comparison of the force-time history of angle-impact cases of the upper neck load cell in x- and z-directions between MBS model and ASSURE experimental results. Impact velocities of 11.3 m/s and 14.0 m/s at 65° and 58° impact angle respectively.

### 3.3.3. Horizontal Impact Validation

The horizontal impact was the last validation case, in which head CG accelerations and upper neck forces were validated. Figure 3.15 shows the comparison for head CG accelerations between the model and the tests. The modeling result corresponds well with Experiment 2 (with 4% difference in peak acceleration) but shows a significant difference to Experiment 1 and 3. Nevertheless, there is a large discrepancy between the experimental results. In horizontal impact case, a full-body collision occurs, meaning that only a center mass of the UAS mainframe contacted the dummy head. No other components, such as camera gimbal, in between to delay impact time. Thus, only a single peak of head C.G acceleration is observed.

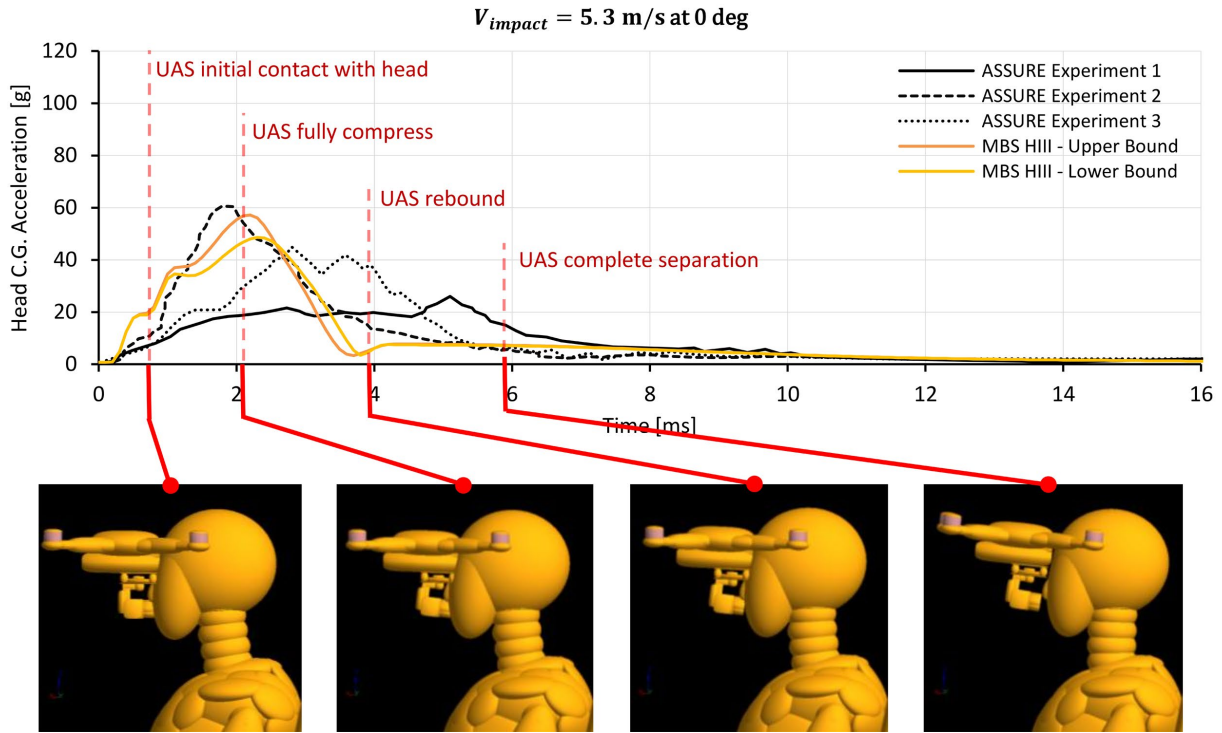


Figure 3.15. Comparison of resultant head CG acceleration-time history between the MBS model and ASSURE experimental results. Impact velocity of 5.3 m/s at 0° impact angle.

For upper neck forces shown in Figure 3.16, the model produces similar trends compare to the tests for both x and z-directions but with different peak force magnitude. For the force in the x-direction, the model peak force difference comparing to Experiment 2 was almost 58%. The model peak force difference reached almost 74% for the force in the z-direction comparing to Experiment 2. In the experimental results, upper neck force in z-direction almost doubled the force in the x-direction, which is the opposite to the modeling results where the force in x-direction doubled the force in the z-direction. The differences may stem from the contact point which may differ between the model and the tests, and MADYMO crash dummy's simplified facial details which were represented by only a smooth ellipsoid without a nose. Additionally, the gravitational effect was not included in the model, which may give a downward velocity to the UAS upon impact.

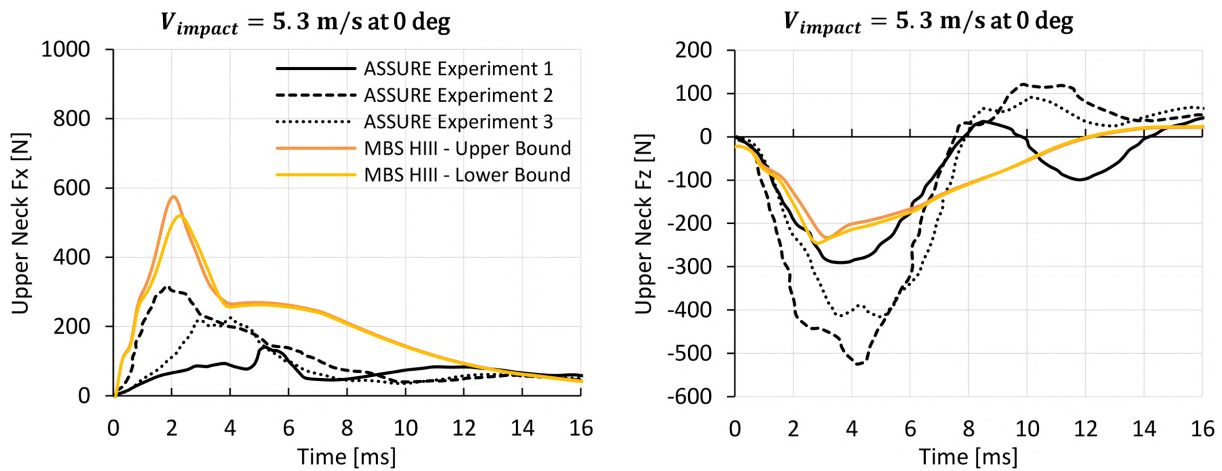


Figure 3.16. Comparison of the force-time history of angle-impact cases of the upper neck load cell in x- and z-directions between MBS model and ASSURE experimental results. Impact velocity of 5.3 m/s at 0° impact angle.



### 3.3.4. Head Injury Criteria (*HIC*) Levels

Based on the validated head CG acceleration and neck forces/moments results from the model, the head injury criteria (*HIC*) and neck injury criteria ( $N_{ij}$ ) were computed and compared against the experimental results. For the *HIC* injury criteria,  $HIC_{15}$  was implemented as it is suitable for short duration impact (The value 15 refers to the 15 ms time period starting from the moment of impact). Functionally, the *HIC* represents the peak average power delivered to the head [26]. Based on Federal Motor Vehicle Safety Standards (FMVSS), a  $HIC_{15}$  value of 700 is considered to be a minimum safety standard for non-fatal impact [27]. The equations for the *HIC* is:

$$HIC_{(t_2-t_1)} = \max_{T_0 \leq t_1 < t_2 \leq T_E} \left\{ (t_2 - t_1) \left[ \frac{1}{t_2 - t_1} \int_{t_1}^{t_2} a(t) dt \right]^{2.5} \right\} \quad (3.2)$$

Proposed by the National Highway Traffic Safety Administration (NHTSA), the  $N_{ij}$  is a neck injury criterion which considers the upper neck force and moment [28]. The “*ij*” represents indices for the 4 injury mechanisms; namely  $N_{TE}$ ,  $N_{TF}$ ,  $N_{CE}$ , and  $N_{CF}$ . The first index represents the actual load (tension or compression) while the second represent sagittal plane bending moment (neck flexion or extension). The current performance limit of the  $N_{ij}$  is 1 which represents a 22% risk of greater than the Abbreviated Injury Scale (*AIS*) level 3 [29]. The equation for the  $N_{ij}$  is:

$$N_{ij} = \left| \frac{F_{Z,i}}{F_{int,i}} \right| + \left| \frac{M_{Y,j}}{M_{int,j}} \right| \quad (3.3)$$

where  $F_Z$  is the axial load,  $F_{int}$  is the corresponding critical intercept value of load,  $M_Y$  is the flexion/extension bending moment computed at the occipital condyles (OC), and  $M_{int}$  is the corresponding critical intercept value for moment [27]. Using the equations above, the values for  $HIC_{15}$  and  $N_{ij}$  from the model were calculated and compared against the experimental results as shown in Table 3.4.

Impact Angle [°]	Impact Velocity [m/s]	MADYMO				
		$HIC_{15}$	$N_{ij} - N_{TE}$	$N_{ij} - N_{TF}$	$N_{ij} - N_{CE}$	$N_{ij} - N_{CF}$
90	9.9	14.0	0.101	0.000	0.402	0.008
	15.1	63.3	0.087	0.028	0.659	0.108
65	11.3	26.5	0.079	0.059	0.095	0.330
58	14	132.1	0.123	0.089	0.136	0.518
0	5.3	24.8	0.080	0.010	0.039	0.055
Impact Angle [°]	Impact Velocity [m/s]	Experiment				
		$HIC_{15}$	$N_{ij} - N_{TE}$	$N_{ij} - N_{TF}$	$N_{ij} - N_{CE}$	$N_{ij} - N_{CF}$
90	9.9	14.2 ± 2	0.117 ± 0.006	0.040 ± 0.000	0.447 ± 0.025	0.050 ± 0.000
	15.1	49.9 ± 8	0.097 ± 0.006	0.050 ± 0.000	0.633 ± 0.015	0.167 ± 0.202
65	11.3	28.6 ± 10	0.063 ± 0.006	0.077 ± 0.006	0.073 ± 0.006	0.520 ± 0.010
58	14	125 ± 20	0.090 ± 0.010	0.093 ± 0.006	0.090 ± 0.010	0.517 ± 0.015
0	5.3	24.36 ± 5	0.067 ± 0.006	0.010 ± 0.010	0.060 ± 0.044	0.047 ± 0.046

**Table 3.4. Comparison of  $HIC_{15}$  and  $N_{ij}$  between MADYMO simulation (average values) and experimental results. Colour scale shows percentage difference level, ranging from percentage difference interval of 0-10% (light grey), 10-20% (grey), 20-30% (dark grey), and ≥30% (black).**

Based on the comparison in Table 3.4, the  $HIC_{15}$  from the model correlates well (differences less than 10%) with the experimental results, except for 90° impact case at 15.1 m/s (difference of 20-30%). For the  $N_{ij}$  injuries prediction, the model estimated comparable values to the experimental results. Even though the upper neck force influences the  $N_{ij}$  levels, the upper neck moment is also critical. Upper neck moment is sensitive to impact positions, seating postures of the dummy, as well as dummy's neck positions and angles. Therefore, the upper neck moment is one of the contributing factors to this discrepancy. It should also be noted that the  $N_{ij}$  levels that exceeded 30% difference from the experimental data are mostly of low values that are not significant. Despite slight discrepancies, the comparison that the UAS model simulating a similar impact response and can produce a realistic head and neck injuries.

### 3.4 UAS Impact on the Human Body

Applications of UAS operations may pose ground collisions risks to human. With the validated UAS multi-body system models, impact severity on the human body due to UAS collision can be simulated and analyzed. Figure 3.17 shows an impact simulation setup between the UAS model and the human body model in MADYMO. The objective of the simulation is to determine the head ( $HIC_{15}$ ) and neck ( $N_{ij}$ ) injuries of the human body due to UAS collisions.

The simulation was performed on frontal, side and rear impact (corresponding to the impact angle,  $\alpha$ , of 0°, 90° and 180°, respectively) at various elevation angles,  $\theta$ . Impact velocities,  $V_{impact}$ , were varied from 0 to 18 m/s with an increment of 2 m/s. The human body model was seated on a non-smooth rigid seat with contact definition predefined by MADYMO. An impact velocity vector from the UAS CG was aligned towards human body head CG in order to simulate CG to CG impact conditions. The UAS angle of attack was fixed to 0° from the horizon axis for all impact case. By solving the model on a 2.6 GHz processor, the computational time for each simulation took approximately 30-40 s.

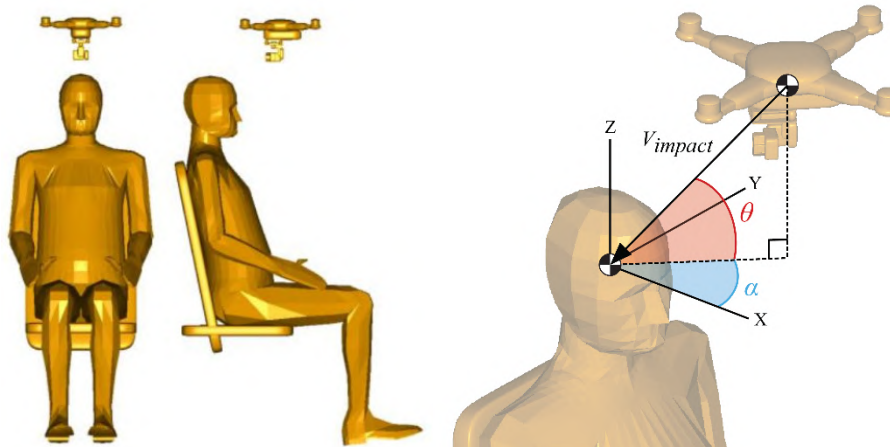


Figure 3.17. UAS to human body model impact setup in MADYMO.  $\alpha$  is the impact angle on the transverse plane in which 0°, 90°, 180° corresponds to frontal, side and rear impacts, respectively.  $\theta$  is the elevation angle in which 0°, 45° and 90° corresponds to horizontal, angle, and vertical impacts, respectively.

#### 3.4.1. Head Injury Criteria ( $HIC$ )

From the simulations, the  $HIC_{15}$  for frontal, side and rear impact were calculated and plotted in Figure 3.18. The maximum operational speed for the DJI Phantom III is 16 m/s and is overlaid in the figure to specify the limit. From the figure, the value of  $HIC_{15}$  rises non-linearly as impact velocity increases, while the slope increases as the elevation angle increases for frontal, side and rear impact.

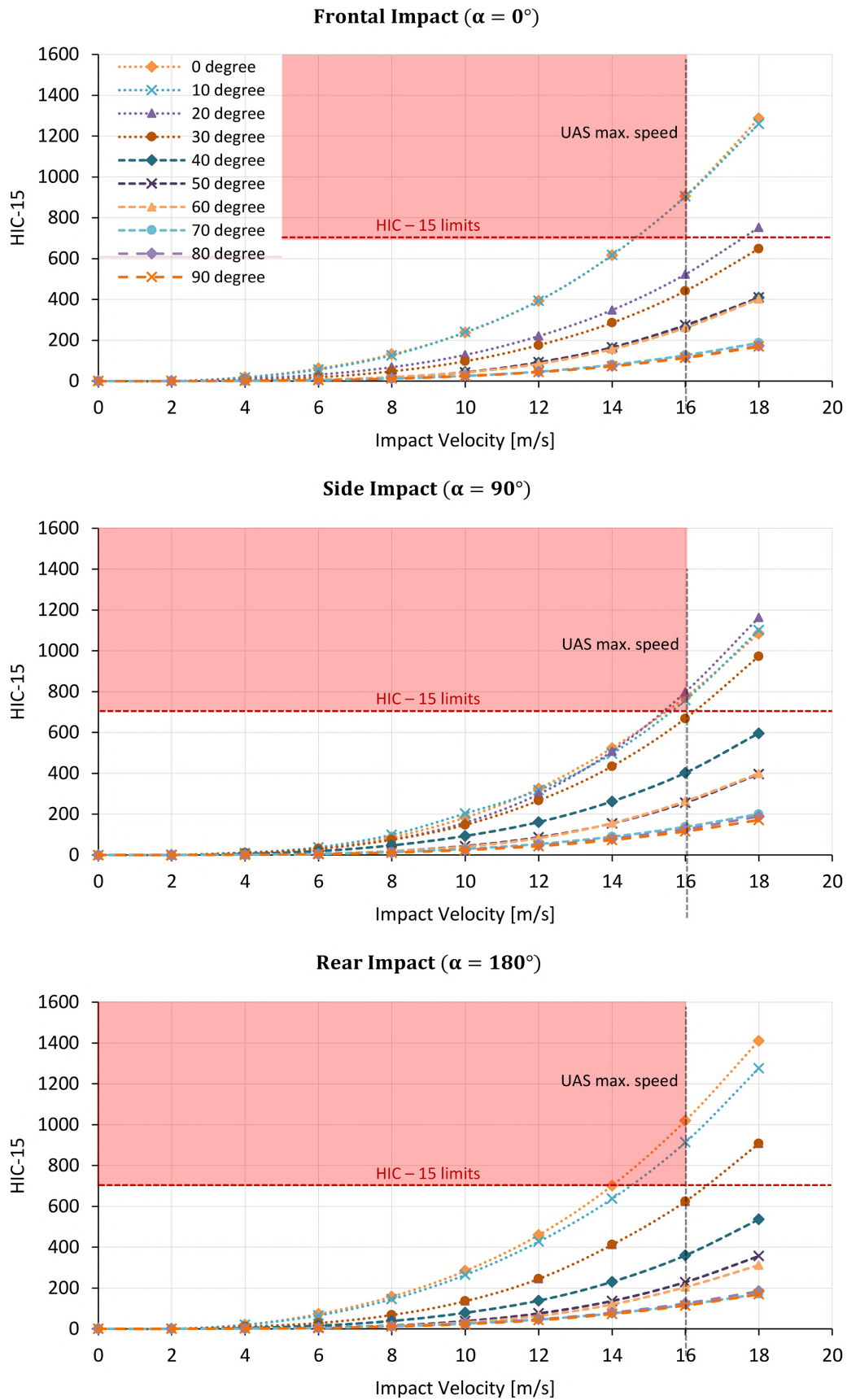


Figure 3.18. Calculated head injury criteria ( $HIC_{15}$ ) from the UAS-human body model simulation at different impact velocities and speeds for frontal, side and rear impact cases. The value of 700 is the limits for  $HIC_{15}$  in which no critical head injury occurs.

For frontal impact ( $\alpha = 0^\circ$ ), the  $HIC_{15}$  exceeds the specified limit of 700 at approximately 14.8 m/s at  $0^\circ$  elevation angle which corresponds to the horizontal impact. At the UAS maximum speed of 16 m/s, the  $HIC_{15}$  already passes the value of 903, in which a risk of serious head injury is probable. The elevation angle of more than  $20^\circ$  results in the  $HIC_{15}$  level of less than 700. For side impact, the  $HIC_{15}$  value exceeds 700 at approximately 15.5 m/s for the elevation angles of  $0^\circ$ ,  $10^\circ$  and  $20^\circ$ . At the maximum speed of 16 m/s, the maximum  $HIC_{15}$  value reaches 797 for  $20^\circ$  elevation angle. As for rear impact ( $\alpha = 0^\circ$ ), the  $HIC_{15}$  value passes 700 at 14 m/s and 14.5 m/s for the elevation angles of  $0^\circ$  and  $10^\circ$  respectively. For  $0^\circ$  elevation angle at rear impact, as the UAS reaches maximum speed, the  $HIC_{15}$  exceeds the value of 1000.

It is evident that the  $HIC_{15}$  value decreases as the elevation angle increases. For all 3 impact angles, severe head injury is less probable as the elevation angle goes beyond  $30^\circ$ . For all impact angles, the elevation angle of  $90^\circ$  (vertical impact) results in less than 200 of the  $HIC_{15}$  value at the maximum UAS velocity.

### 3.4.2. Neck Injury Criteria ( $N_{ij}$ )

The  $N_{ij}$  results from the simulations are plotted in Figure 3.19 and Figure 3.21. For all impact angles (frontal, side and rear),  $N_{TE}$  and  $N_{TF}$  values are relatively low comparing to  $N_{CE}$  and  $N_{CF}$  since the applied load often results in compression and rotation of the human neck. For all impact angles, the  $N_{CE}$  and  $N_{CF}$  values increase as the impact velocity increases and the slope of the curves rises as the elevation angle increases. Higher elevation angle means that the load direction of the UAS on the head becomes more vertical, resulting in a larger compressive force in the neck. It is evident that serious neck injury due to the DJI Phantom III UAS ( $W_0 \approx 1.2$  kg) collision is improbable to occur to the human body, as the  $N_{ij}$  values are less than 1 for all impact and elevation angles.

For frontal impact case, the neck injury is most likely to occur under vertical and angle load cases  $\theta < 60^\circ$  due to a higher compressive load in the neck. Horizontal impact case ( $\theta \approx 0^\circ$ ) is less likely to inflict any neck injury which is in contrary to the head injury. Like the side impact case in which compressive load is more prominent than the flexion/extension upper neck moment, the neck injury is also low for horizontal impact case. The  $N_{ij}$  results for side impact case is shown in Figure 3.20.

Rear impact, which is quite different from the frontal impact case, shows that neck injury is most likely to occur at elevation angle,  $\theta$ , of  $60^\circ$ . As shown in the  $N_{CE}$  plot in Figure 3.21, the  $N_{CE}$  value reaches approximately 0.52 at the maximum UAS operational speed of 16 m/s. Since there is no frontal support for the thorax, the head, neck and upper body moved forward freely, resulting in a hyperextension of the neck. The result is a lower compressive force, but a larger extension moment in the upper neck.

### Frontal Impact ( $\alpha = 0^\circ$ )

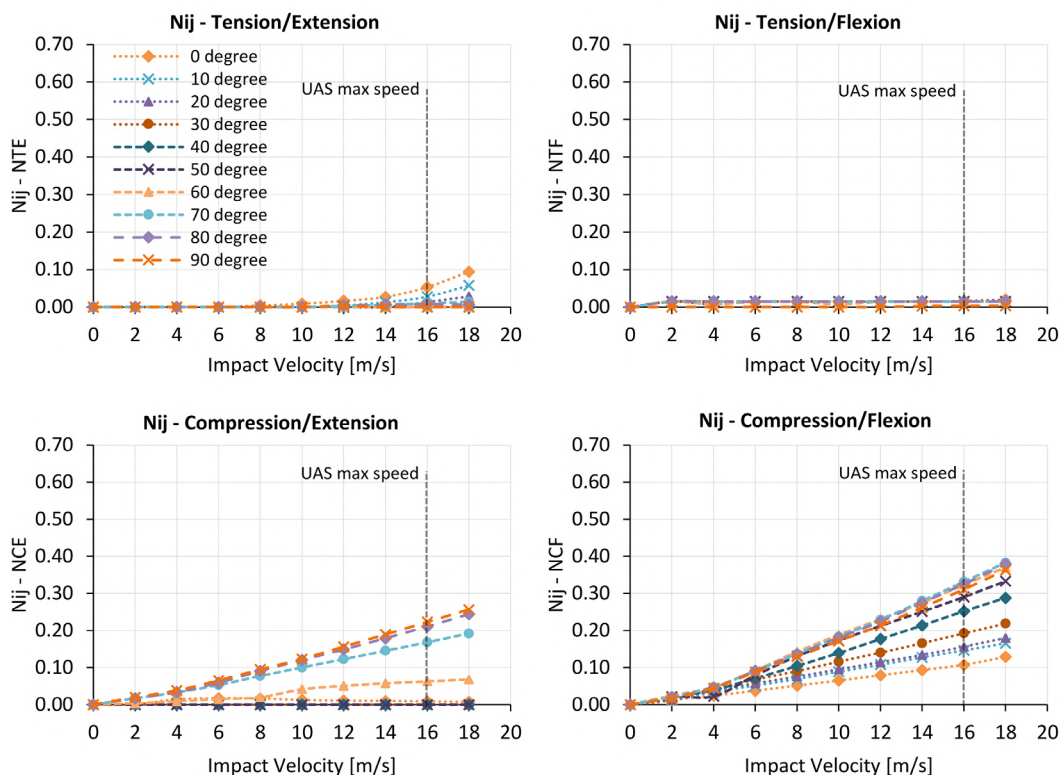


Figure 3.19. Calculated neck injury criteria ( $N_{ij}$ ) from the UAS-human body model impact simulation at different impact velocities and elevation angles for side impact case.

### Side Impact ( $\alpha = 90^\circ$ )

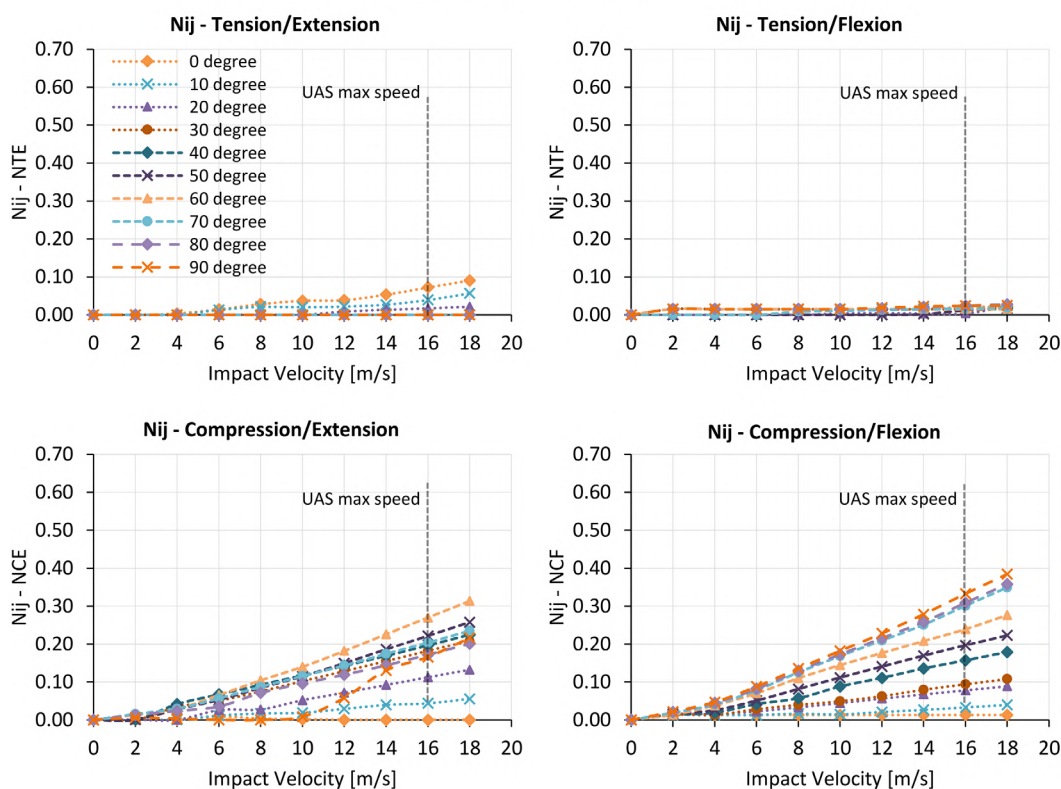


Figure 3.20. Neck injury criteria ( $N_{ij}$ ) from the UAS-human body model impact simulation at different impact velocities and elevation angles for side impact case.



Rear Impact ( $\alpha = 180^\circ$ )

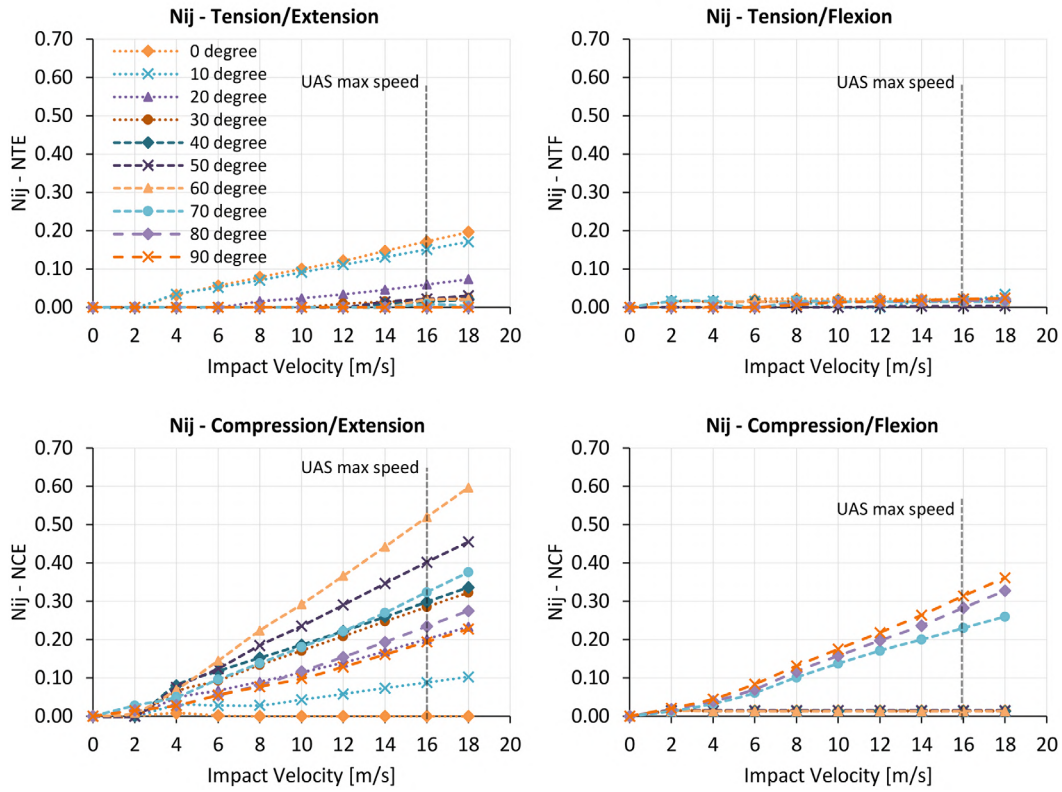


Figure 3.21. Neck injury criteria ( $N_{ij}$ ) from the UAS-human body model impact simulation at different impact velocities and elevation angles for rear impact case.

In addition, Figure 3.22 shows the comparison of the overall trends between the  $N_{ij}$  and the  $HIC_{15}$  at different elevation angles at UAS maximum velocity of 16 m/s. As the elevation angle increases, the  $N_{ij}$  values (such as  $N_{CE}$  and  $N_{CF}$ ) increases while the  $HIC_{15}$  decreases. This shows that the loading direction plays a significant role in determining the injury mechanism. Vertical load on the human head inflicts higher neck injury more than the head injury, while horizontal load inflicts head injury more. In horizontal impact where the elevation angle is at  $0^\circ$ , the neck system has minimal effect in absorbing impact energy, resulting in higher head CG acceleration. As the elevation angle increases, the impact force starts to transfer directly into the neck system, lowering and increasing the chance of head and neck injury, respectively. The neck injury is highest when the elevation angle is roughly  $60^\circ$ - $70^\circ$  due to the high compressive force in the upper neck that is coupled with neck extensive/flexion moments.

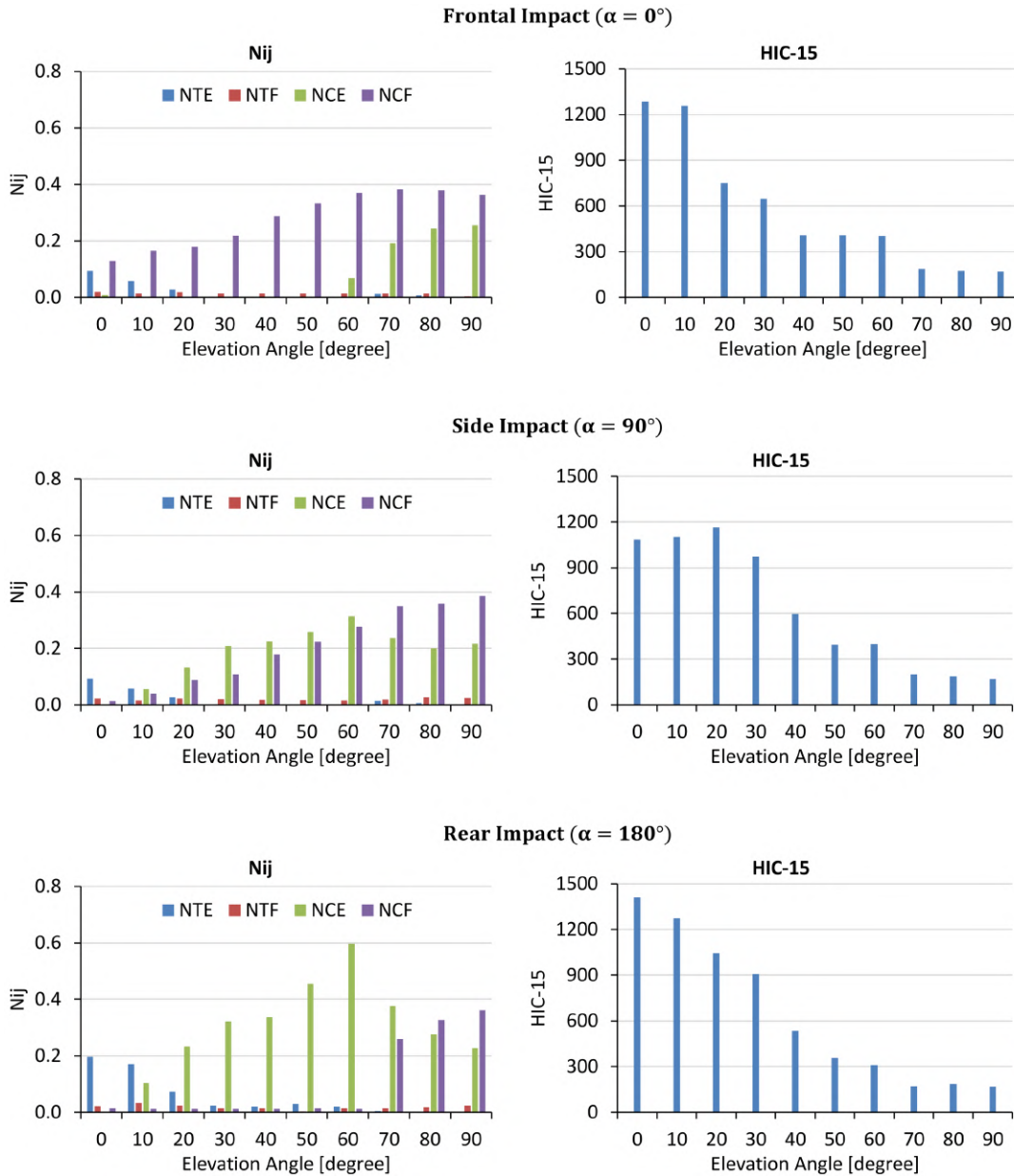


Figure 3.22. Analysis of elevation angle effect on the  $N_{ij}$  and  $HIC_{15}$  overall trends for frontal, side and rear impact at UAS maximum velocity of 16 m/s.

## 3.5 Discussion

### 3.5.1. Discussion on UAS MBS Modeling and Validation Results

The developed UAS MBS model shows a good correlation to the real impact experiments and can be used to simulate the ground impact on the Hybrid III crash dummy. This modeling technique allows a fast computational time when comparing to FEM modeling, which is preferable if various impact cases are being investigated. A single lumped mass with a single Kelvin and Cardan springs/dampers representing a gimbal system produces results in vertical impact case similar to the experiments. However, in an angle impact case, such simplified lumped mass can only produce a similar trend of impact force transfer but need further refinement in order to better match the experimental results. Improving it could result in a better impact response, but with a trade-off on model simplicity and computational time. Further investigation is still needed to see the value of such improvement.

The contact force characteristics derived using analytical equation gives a good response as shown in the validation results. However, contact damping was not included which is rather unrealistic since there are no materials without internal damping. The lack of damping resulted in an over-predicted contact force which is shown in Figure 3.13 and Figure 3.14. For joint restraint characteristics, by obtaining force-deflection curves experimentally enable the non-linear effect of the real system to be captured, which can also include internal parts breakage as shown in Figure 3.4(b). This approach produces good results in all impact cases and resulted in realistic kinematics of the UAS.

Furthermore, the estimation of the damping coefficient for joint restraints proved to be rather difficult. No simple analytical method was appropriate to use and, thus, a ground vibration test was performed for critical joint restraints to determine the natural frequencies. Using Equation 3.1, the damping coefficient was approximated and implemented in the model. This method resulted in good results. However, a better approximation can be done by performing a parameter estimation based on a set of calibration data. The optimization algorithm, such as a genetic algorithm, can be employed to automatically search and estimate damping coefficients for all joint restraints. This will be considered in future work.

### **3.5.2. Discussion on Human Body Injury, Limitations and Future Work**

According to the presented results in section 3.4 , a UAS poses serious harm to the human head when a full body collision (collision without gimbal in between the UAS and the human head) is expected. Such collision is seen in horizontal impact cases where elevation angle,  $\theta$ , is at  $0^\circ$ . A gimbal system underneath the UAS significantly lessen the head/neck impact severity by absorbing the impact energy of the UAS. In vertical impact, the UAS was assumed to fall with a constant angle of attack horizontally to the ground, resulting in the gimbal hitting the human head first. Practically, it is unlikely that such a perfect collision may occur. On the other hands, a UAS would often lose balance and spin down with uncontrolled attitude. This may result in a full body collision where the main fuselage of the UAS collides on the human head and serious head/neck injury could be expected. This impact attitude variation will be further investigated in the future work to determine the worst impact attitude.

Furthermore, both the  $HIC_{15}$  and  $N_{ij}$  plots show that rear impact, which resulted in the head moving forward, inflicted higher injury than frontal and side impacts. One possible explanation is the back seat which does not support the human body in forward motion. Without such support, the head can accelerate forward easier without a significant restraining force from the neck system. This shows that for an analysis of UAS collision on pedestrian where there is no seating support, a more elaborated simulation and analysis is needed. A future work should also include a simulation setup where the pedestrian is in a standing position and walking velocity should be incorporated.

There is also quite a significant difference in  $HIC_{15}$  and  $N_{ij}$  values between a crash dummy and the human body which is expected. Even though crash dummies are based on the human body, road vehicle crashworthiness analysis shows that limitations in biofidelity of the dummies can result in different biomechanical head and neck responses comparing to the real human [30]. Based on Sances and Kumaresan [31], an experimental work comparing between the Hybrid III crash dummy and human cadaver under an inverted drop showed that the dummy neck was two to four times stiffer than human cadavers. Additionally, a follow-on an experiment by Sances et al. [32] indicated that the crash dummy system transmits about 70-75% of the applied force from the head or upper neck to the lower neck area. On the other hands, only about 20-30% of the applied force was transmitted from the head to the lower neck in the study on a human cadaver. Future work will elaborate on such difference to understand



if an appropriate UAS weight threshold can be made based on a crash dummy.

In this paper, only a few injury criteria were used to investigate injury on the human body, namely; head injury criterion ( $HIC_{15}$ ) and neck injury criterion ( $N_{ij}$ ).  $HIC_{15}$  is quite suitable for the problem investigated but other head injury criteria should also be employed, such as, brain injury criterion ( $BrIC$ ) which considers head rotational acceleration [33].  $N_{ij}$  was implemented in this work to investigate neck injury, but this criterion is mainly designed for whiplash injury analysis which only considers injury in flexion/extension directions. Thus,  $N_{ij}$  is not appropriate for side impact analysis and other neck injury criteria will be further investigated in future works, namely;  $N_{km}$ ,  $NIC$ ,  $LNL$  or  $ND$  criteria. For example,  $N_{km}$  considers the side force in the upper neck, making it more appropriate for side impact case. Therefore, the neck injury analysis in this work needs further elaboration before a sound conclusion can be made on the human neck injury level due to UAS collision.

Lastly, one of the main advantages of employing a multibody system approach to model such collision scenarios is the scalability of the model. With a simplified model construct, this allows the UAS model to be scaled up or down in terms of size and mass. Scaling factors will need to be determined experimentally for each joint restraint characteristics, damping coefficients, and mass/inertia properties. This scalability of the model will be included in future work.

### 3.6 Conclusions

In this paper, a multibody system (MBS) model of a DJI Phantom III UAS was developed and integrated with a validated human body and crash dummy models that are available in MADYMO. The DJI Phantom III represents a small UAS weight class ( $W_0 \approx 1.2$  kg). The developed MBS consists of multiple lumped masses which are connected via restraint joints. Each joint is restrained using Kelvin spring and damper, and force-deflection characteristics of each joint were obtained experimentally. Force penetration contact model, derived analytically, was implemented to model impact interaction between the UAS and a crash dummy (or the human body), as well as interactions between the UAS internal parts.

The integrated model of DJI Phantom III UAS contacting and impacting the crash dummy has been validated by comparing model simulation results with ASSURE experimental results of DJI Phantom III UAS drop tests on a Hybrid III crash dummy. This comparison shows that the simulated impact events and impact forces are similar to those measured in the real-world impact tests of ASSURE, at various impact velocities and elevation angles.

Using the validated UAS model, impact simulation of the UAS collision on the human body was performed. The aim was to determine the impact severity of the UAS on the human body. Frontal, side and rear impacts were investigated, and the elevation angles were varied to simulate horizontal, angle and vertical impact cases. Based on the head injury criterion ( $HIC_{15}$ ), the results show that UAS horizontal impact can inflict  $HIC_{15}$  of more than 700. This means that serious head injury, such as skull fracture or brain damage, is probable. For neck injury, the prediction  $N_{ij}$  criterion shows that there is a low chance of neck injury and vertical impact tends to inflict higher neck injury, but still within the  $N_{ij}$  performance limits of 1. Therefore, based on the analysis in this paper, it can be concluded that the UAS with a mass of approximately 1.2 kg can inflict serious head injury on the human body.

Follow-up research will be to extend the MBS model development and integration with human body models in MADYMO for other UAS types and for other human body models than the 50% male one. With the extension to other UAS types, the effect of landing gears will be

included for offset impact analysis on the human head.

### **3.7 Acknowledgment**

The authors would like to thank Delft Aerospace Structures and Materials Laboratory and the technician team for providing laboratory equipment and useful technical support. Also, the authors would like to gratefully acknowledge the support from TASS International by providing us with the license for MADYMO and supporting the model implementation. In addition, sincere appreciation to Mr. David Arterburn from the ASSURE research group and its partner's university for providing us with data and video footage of the UAS impact drop test which was used for model validation.

## Appendix 3A: Effect of Component Stiffness on Head Force

This preliminary study is to determine the difference in impact force on the human head due to UAS collision at different point of contact on the DJI Phantom III UAS. Head acceleration resulted from UAS collision from three different contact points (Frontal contact, camera gimbal, and landing gear) are modelled and compared using a simplified lumped parameter mass (LPM) model. Each point of contact has different stiffness which affects the impact force between a UAS and the human head.

Figure 3.24 shows the force-deformation curves of a different point of contact. Frontal contact force-deformation curve was approximated using modified Hertz contact [23]. Camera gimbal and landing gear force-deformation curves were measured experimentally using static compressive test. Frontal contact (main fuselage body) is the stiffest point of contact with a stiffness value of approximately 83000 N/m. Camera gimbal has a stiffness of approximately 35000 N/m. The landing gear is the softest component with the stiffness of 15625 N/m.



Figure 3.23. Static compressive test to determine the force-deformation curve of each component.

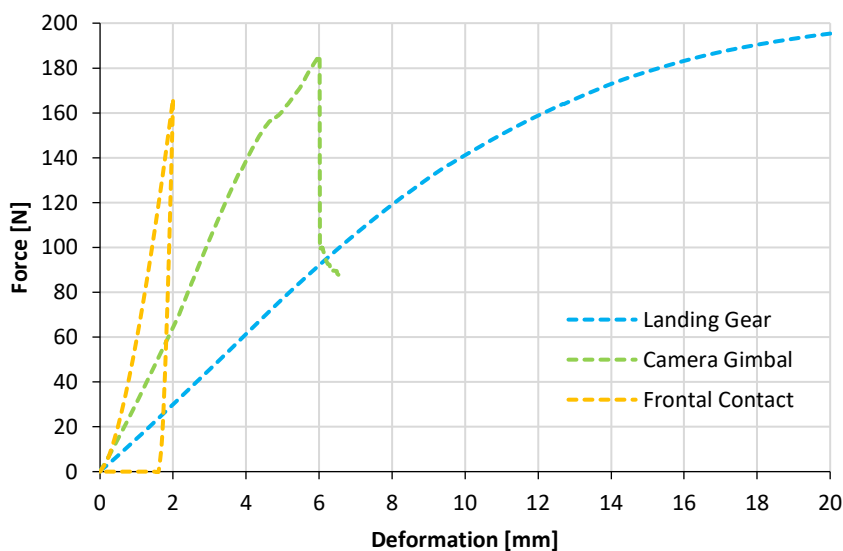
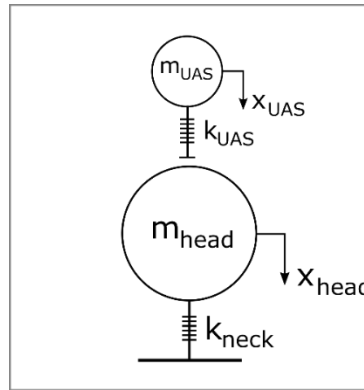


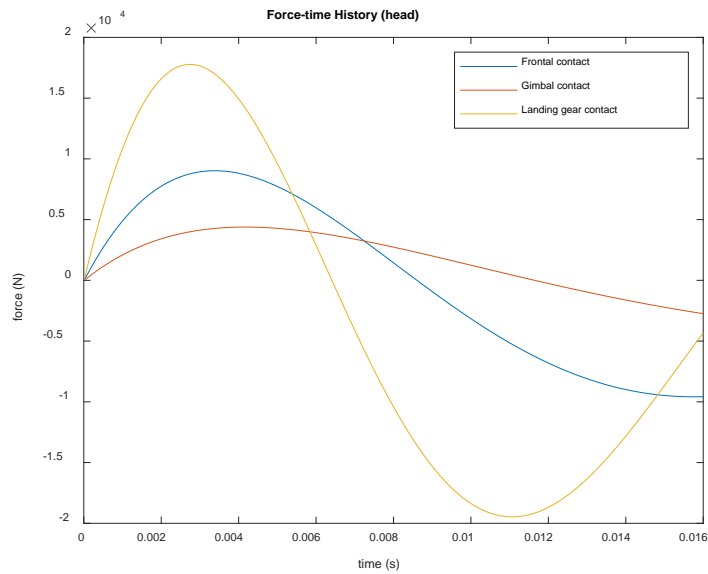
Figure 3.24. Force-deformation curve of three different points of contact.

To assess head-acceleration, the simplified LPM UAS-human head model was developed. The human head/neck LPM model is from Wei and Griffin [34]. UAS is lumped into one lumped mass with a spring representing the components (frontal contact, camera gimbal and landing gear). Stick assumption was applied, meaning that the UAS is attached to the head after the collision. The model was run for 0.016 s at UAS impact velocity of 18 m/s (maximum UAS speed). The modeling results are shown in Figure 3.26. The figure shows that frontal contact results in the highest head force with a peak force of more than 17700 N. Gimbal contact results

in the peak force of approximately 9000 N. Landing gear, which is the softest component, results in the head force of less than 4300 N.



**Figure 3.25. Simplified UAS-head lumped parameters model. Head/neck mass and stiffness is from Wei [34]**



**Figure 3.26. Force-time history of the human head at head CG due to UAS impacts with different point of contacts at impact velocity of 18 m/s.**

## References

- [1] European Aviation Safety Agency. Prototype Commission Regulation on Unmanned Aircraft Operations [Internet]. 2016. Available from: <https://www.easa.europa.eu/system/files/dfu/UAS Prototype Regulation final.pdf>.
- [2] European Aviation Safety Agency (EASA). Drone Collision Task Force [Internet]. 2016. Available from: [https://www.easa.europa.eu/system/files/dfu/TF Drone Collision\\_Report for Publication %28005%29.pdf](https://www.easa.europa.eu/system/files/dfu/TF Drone Collision_Report for Publication %28005%29.pdf).
- [3] Civil Aviation Safety/Monash University. Human Injury Model for Small Unmanned Aircraft Impacts. 2013.
- [4] Magister T. The small unmanned aircraft blunt criterion based injury potential estimation. *Saf. Sci.* [Internet]. 2010;48:1313–1320. Available from: <http://dx.doi.org/10.1016/j.ssci.2010.04.012>.
- [5] Arterburn DR, Duling CT, Goli NR. Ground Collision Severity Standards for UAS Operating in the National Airspace System (NAS). 17th AIAA Aviat. Technol. Integr. Oper. Conf. [Internet]. 2017;1–16. Available from: <https://arc.aiaa.org/doi/10.2514/6.2017-3778>.
- [6] Arterburn D, Ewing M, Prabhu R, et al. FAA UAS Center of Excellence Task A4 : UAS Ground Collision Severity Evaluation. 2017.
- [7] Huculak R. NIAR UAS Drop Testing Report [Internet]. Wichita; 2016. Available from: <http://www.assureuas.org/projects/deliverables/a11/NIAR Test Report - FAA-UAH UAS Drop Testing.pdf>.
- [8] Koh CH, Deng C, Li L, et al. Experimental and simulation weight threshold study for safe drone operations. *AIAA Inf. Syst. Infotech Aerospace*, 2018. 2018;1–11.
- [9] Koh CH, Low KH, Li L, et al. Weight threshold estimation of falling UAVs (Unmanned Aerial Vehicles) based on impact energy. *Transp. Res. Part C Emerg. Technol.* [Internet]. 2018;93:228–255. Available from: <https://doi.org/10.1016/j.trc.2018.04.021>.
- [10] Campolettano ET, Bland ML, Gellner RA, et al. Ranges of Injury Risk Associated with Impact from Unmanned Aircraft Systems. *Ann. Biomed. Eng.* [Internet]. 2017; Available from: <http://link.springer.com/10.1007/s10439-017-1921-6>.
- [11] Vadlamudi S, Blundell M, Zhang Y. A multi-body systems approach to simulate helicopter occupant protection systems. 2017;8265.
- [12] Jenefeldt F, Thomson R. A methodology to assess frontal stiffness to improve crash compatibility. *Int. J. Crashworthiness*. 2004;9:475–482.
- [13] Mukherjee S, Chawla A, Nayak A, et al. Rollover crashworthiness of a rural transport vehicle using MADYMO. *Int. J. Crashworthiness*. 2006;11:495–503.
- [14] Ambrósio J, Dias J. A road vehicle multibody model for crash simulation based on the plastic hinges approach to structural deformations. *Int. J. Crashworthiness*. 2007;12:77–92.
- [15] Laananen DH, Bolukbasi AO, Coltman JW. Computer Simulation of an Aircraft Seat and Occupant in a Crash Environment [Internet]. 1983. Available from: <http://www.dtic.mil/docs/citations/ADA127152%5Cnhttp://www.dtic.mil/dtic/tr/fulltext/u2/a127152.pdf%5Cnhttp://www.dtic.mil/get-tr-doc/pdf?AD=ADA127152>.

- [16] TASS International. MADYMO Theory Manual Version 7.7. MADYMO Util. Man. 2017.
- [17] Alliance for System Safety of UAS through Research Excellence. ASSURE UAS Ground Collision Severity Evaluation Final Report [Internet]. [cited 2018 Nov 18]. Available from: <http://www.assureuas.org/projects/deliverables/sUASGroundCollisionReport.php>.
- [18] Adams V, Askenazi A. Building Better Products with Finite Element Analysis [Internet]. OnWord Press; 1999. Available from: <https://books.google.nl/books?id=Mnv6qRz73x0C>.
- [19] Happee R, Hoofman M, Van Den Kroonenberg AJ, et al. A Mathematical Human Body Model for Frontal and Rearward Seated Automotive Impact Loading. SAE Tech. Pap. 1998;
- [20] Happee R, Ridella S. Mathematical human body models representing a mid size male and a small female for frontal, lateral and rearward impact loading. IRCOBI Conf. Proc. 2000;1–18.
- [21] TASS International. Human Body Models Manual Version 7.7. 2017.
- [22] TASS International. Model Manual Version 7.7. 2017.
- [23] Brake MR. An analytical elastic-perfectly plastic contact model. Int. J. Solids Struct. [Internet]. 2012;49:3129–3141. Available from: <http://dx.doi.org/10.1016/j.ijsolstr.2012.06.013>.
- [24] MATBASE. Matbase: the independent online material selection resource [Internet]. [cited 2017 Sep 3]. Available from: <https://www.matbase.com/material-categories/natural-and-synthetic-polymers/thermoplastics/commodity-polymers/material-properties-of-acrylonitrile-butadiene-styrene-general-purpose-gp-abs.html#properties>.
- [25] Lozano-Mínguez E, Palomar M, Infante-García D, et al. Assessment of mechanical properties of human head tissues for trauma modelling. Int. j. numer. method. biomed. eng. 2018;34:1–17.
- [26] Hutchinson J, Kaiser MJ, Lankarani M. The Head Injury Criterion ( HIC ) functional. J. Appl. Math. Comput. 1998;
- [27] Eppinger R, Sun E, Bandak F, et al. Development of Improved Injury Criteria for the Assessment of Advanced Automotive Restraint Systems - II By [Internet]. 1999. Available from: [https://www.nhtsa.gov/sites/nhtsa.dot.gov/files/rev\\_criteria.pdf](https://www.nhtsa.gov/sites/nhtsa.dot.gov/files/rev_criteria.pdf).
- [28] Klinich K, Saul R, Auguste G, et al. Techniques for Developing Child Dummy Protection Reference Values. Measurement. 1996.
- [29] Parr MJC, Miller ME, Bridges NR, et al. Evaluation of the Nij neck injury criteria with human response data for use in future research on helmet mounted display mass properties. Proc. Hum. Factors Ergon. Soc. 2012;2070–2074.
- [30] Mroz K, Bostrom O, Bengt P, et al. Comparison of Hybrid III and human body models in evaluating thoracic response for various seat belt and airbag loading conditions. IRCOBI Conf. Sept 15-16. 2010;265–280.
- [31] Sances A, Kumaresan S. Comparison of biomechanical head-neck responses of hybrid III dummy and whole body cadaver during inverted drops. Biomed. Sci. Instrum.

- [Internet]. 2001 [cited 2018 Oct 24];37:423–427. Available from: <http://www.ncbi.nlm.nih.gov/pubmed/11347428>.
- [32] Sances A, Carlin F, Kumaresan S. Biomechanical analysis of head-neck force in hybrid III dummy during inverted vertical drops. *Biomed. Sci. Instrum.* [Internet]. 2002 [cited 2018 Oct 24];38:459–464. Available from: <http://www.ncbi.nlm.nih.gov/pubmed/12085650>.
- [33] Mueller B, MacAlister A, Nolan J, et al. Comparison of HIC and BrIC Head Injury Risk in IIHS Frontal Crash Tests to Real-world Head Injuries. *Enhanc. Saf. Veh.* 2015. p. 1–18.
- [34] Wei L, Griffin J. THE PREDICITON OF SEAT TRANSMISSIBILITY FROM MEASURES OF SEAT IMPEDANCE. *J. Sound Vib.* [Internet]. 1998 [cited 2019 Apr 30];214:121–137. Available from: <https://www.sciencedirect.com/science/article/pii/S0022460X98915401>.





---

# Modelling Head Injury due to Unmanned Aircraft Systems Collision: Crash Dummy vs Human Body

*Recent developments in the concept of UAS operations in urban areas have led to risk concerns of UAS collision with human. To better understand this risk, head and neck injuries due to UAS collisions have been investigated by different research teams using crash dummies. Because of the limitations in biofidelity of a crash dummy, head injury level for a crash dummy impact may differ from the human body impact. Therefore, the aim of this paper is to investigate differences in head and neck injuries subject to UAS collision between an often-used Hybrid III crash dummy and a human body. To perform such investigation, multibody system (MBS) impact models have been used to simulate UAS impacts on validated models of the Hybrid III crash dummy and the human body at various impact conditions. The findings show that the Hybrid III predicts similar head and neck injury compared to the human body when UAS collides horizontally from front and rear. However, the Hybrid III over-predicts head injury due to horizontal side impact. Moreover, under vertical drop and 45 degree elevated impact of UAS, the Hybrid III under-predicts head injury, and over-predicts neck injury.*

This chapter has been published as “Rattanagraikanakorn, B., Schuurman, M., Gransden, D. I., Happee, R., De Wagter, C., Sharpanskykh, A., and Blom, H. A. P., “Modelling Head Injury due to Unmanned Aircraft Systems Collision: Crash Dummy vs Human Body,” International Journal of Crashworthiness, 2020, pp. 1–14.”

## 4.1 Introduction

Unmanned aircraft systems (UAS) are expected to operate in low-level airspace in an urban environment where population density is high. The risk from such implementation has given rise to the question of the safety of people on the ground. This motivates efforts to understand the impact severity of UAS collision on human through analytical or experimental approaches. In impact experiments, an anthropomorphic test device (ATD), i.e. the Hybrid III crash dummy, is widely used as a representative substitution of a real human body. Campolettano et al. [1] performed a series of live flight test and impact drop test using three different UAS weight classes on an instrumented Hybrid III. The Alliance of System Safety of UAS through Research Excellence (ASSURE) research group also conducted a series of controlled impact drop test using DJI Phantom III UAS on the Hybrid III crash dummy at various UAS impact attitudes and speeds [2-4]. These tests provide valuable insights into head and neck injury from UAS collision. The aim of the test was to estimate the range of head injury risks to humans due to UAS impact.

Even though Hybrid III is based on the human body, for road accidents it has been shown that limitations in biofidelity of a crash dummy can result in different biomechanical head and neck responses compared to the real human [5]. The human body neck complex is the spine which is a biomechanical structure composed of bony vertebrae, ligaments, and intervertebral discs [6]. It is a flexible structure with a primary function to protect the spinal cord and nerve roots while carrying loads and perform the physical motion. The Hybrid III neck is designed to represent the cervical human spine by connecting the head and torso through a rigid attachment. The neck itself is a one-piece column made of rubber separated by aluminum discs and there is no inherent curvature to the Hybrid III neck column [6].

Based on experimental work by Sances et al. [7], a comparison of inverted drops on the Hybrid III and human cadavers showed that the dummy neck was two to four times stiffer than human cadavers. Additionally, an experiment by Sances et al. [8] indicated that the Hybrid III crash dummy transmits about 70-75% of the applied force from the head or upper neck to the lower neck area. On the other hand, only about 20-30% of the applied force was transmitted from the head to the lower neck in the study on a human cadaver. Such differences can lead to a discrepancy in head injury level on a human body and a Hybrid III crash dummy used in testing.

In any investigation to determine the impact severity of a particular vehicle, it is vital that the measuring instrument is appropriate to serve the investigation objective. In this case, it is important to know whether a Hybrid III dummy is a suitable measuring instrument for an investigation on UAS collision severity and can realistically represent a human body. If the discrepancy between the Hybrid III dummy and a real human body is significant, then it is important to address the scale of such difference. Therefore, the primary aim of this paper is to investigate differences in head and neck injury levels on a Hybrid III dummy and on a human body due to UAS collisions by using validated Multi-body system (MBS) models of the Hybrid III dummy, human body, and UAS.

This paper is organized as follows. Section 4.2 describes the modelling and analysis methods including the models used in the simulation. Section 4.3 presents the comparative results from the models developed and simulated in MADYMO. Section 4.4 and 4.5 present the discussion of the results and the conclusion, respectively.

The current paper forms a significantly extended version of the paper presented at the 2019 AIAA Aviation Forum conference [9].

## 4.2 Modelling and Simulation Approach

### 4.2.1. UAS, Hybrid III and Human Body Models

For a comparison of injuries due to UAS collision with a Hybrid III crash dummy versus a human body, validated numerical simulation models are implemented in the software package called MADYMO [10] and are subsequently utilized. The UAS chosen for this study was the DJI Phantom III with a take-off weight ( $W_0$ ) of 1.28 kg. For this specific UAS, a multibody system (MBS) model shown in Figure 4.1 has been developed and validated in previous research [11]. For the validation, the simulation results obtained from this MBS model of a DJI Phantom III colliding with a Hybrid III dummy have been compared to the crash test data obtained by the ASSURE research group [4]. Impact data from the ASSURE research group was chosen for validation of this impact model because of its large range of controlled impact cases and precise measuring data.

To simulate injury levels within MADYMO, the UAS MBS model that was previously coupled with a 50<sup>th</sup> percentile MBS model of a Hybrid III dummy is now also coupled with a 50<sup>th</sup> percentile MBS model of a human body, as shown in Figure 4.2. “50<sup>th</sup> percentile” refers to the size of the human body which is equivalent to the average North American male. An MBS model of this 50<sup>th</sup> percentile Hybrid III has been validated against a real Hybrid III at various load conditions [12,13] which is distributed with MADYMO (filename: d\_hyb350el\_Q, version 2.0). A 50<sup>th</sup> percentile model of a human body is also distributed with MADYMO (filename: h\_occ50fc, version 5.2) and was originally published by Happee [14,15]. This human body model is also an MBS with a passive muscle model and the skin is modelled using a facet surface which is a mesh of shell-type massless contact elements. The skeleton of this human body model consists of chains of rigid bodies connected by kinematic joints. The biomechanical data including joint characteristics and mechanical properties are based on biomechanical data and are validated using volunteer and post mortem human subject (PMHS) [16].



Figure 4.1. DJI Phantom III UAS used in impact modelling: (a) real-world system and (b) multibody system (MBS) model developed in MADYMO [11]. The two landing skids are neglected in the MBS model since they are such flexible that their impact effect is negligible [11].

### 4.2.2. Simulation Setup

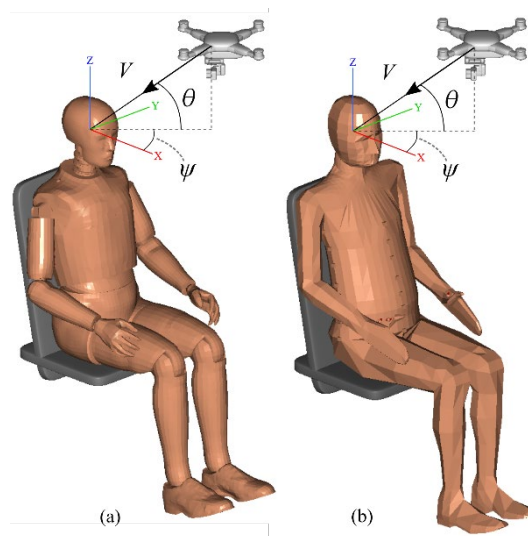
Because the head is the most vulnerable part of the human body, this paper focuses on MBS simulation of impact of DJI Phantom III collision with the head of the Hybrid III dummy versus the head of the human body. In the simulation set up, the Hybrid III dummy and the human body are seated on non-smooth rigid seats with full back support. The velocity vector of the UAS is aligned with the head centre of gravity (CG) of the Hybrid III and the human body. The UAS angle of attack was fixed at 0° from the horizontal axis for all impact case.

Impact simulations were performed by varying three main parameters; impact velocity ( $V$ ), impact elevation ( $\theta$ ), and impact direction ( $\psi$ ) (see Figure 4.2). Impact velocity ( $V$ ) is varied from 0 to 18 m/s with an increment of 2 m/s. Note that impact velocity is converted and presented in a form of impact energy, varying from 0 to 196 J which is equivalent to 0 to 18 m/s for the DJI Phantom III. Impact elevation ( $\theta$ ) is set to  $0^\circ$  (horizontal impact),  $45^\circ$  (elevated impact) and  $90^\circ$  (vertical drop). The horizontal and elevated impact cases represent a loss of control failure mode in which the UAS flies directly onto the head. The vertical drop case represents a failure mode in which a UAS falls to the ground due to the complete loss of power. Lastly, impact direction ( $\psi$ ) is set to  $0^\circ$  (frontal),  $90^\circ$  (side), and  $180^\circ$  (rear). The simulation was run on a 2.6 GHz processor, resulting in computational time of approximately 60 s and 120 s for the human body and the Hybrid III dummy, respectively.

To assess the risk of serious head injuries such as traumatic brain injury or skull fracture, the head injury criterion ( $HIC$ ) was used [17,18]. Functionally, the  $HIC$  represents the peak average power delivered to the head [19]. It measures the likelihood of head injury due to impact by integrating head CG acceleration over time, and the formula is,

$$HIC_{(t_2-t_1)} = \max_{T_0 \leq t_1 < t_2 \leq T_E} \left\{ (t_2 - t_1) \left[ \frac{1}{t_2 - t_1} \int_{t_1}^{t_2} a(t) dt \right]^{2.5} \right\} \quad (4.1)$$

Where  $a(t)$  is the head CG acceleration curve,  $t_1$  is the initial impact time and  $t_2$  is the final impact time. There are two time-range limits which are 15 ms and 36 ms. In this paper, the 15 ms time range limit is chosen as it is more appropriate for a short-duration impact study. The  $HIC$  with 15 ms time range limit is referred to as  $HIC_{15}$  which is the term used in the rest of the paper. Based on FMVSS and NCAP, the  $HIC$  value of 700 is considered to be a minimum safety standard where the probability for skull fracture ( $AIS \geq 2$ ) for the mid-sized male is 31% [20]. To measure head acceleration, both the Hybrid III and the human body models are instrumented with 3 single-axis accelerometers positioned at the CG of the heads. A low-pass filter with a channel frequency class (CFC) 1000 is applied to linear acceleration curves from the head CG accelerometers.



**Figure 4.2. Simulation setup in MADYMO of UAS collisions on (a) the Hybrid III model and (b) the human body model.**

Furthermore, the  $N_{ij}$  is a neck injury criterion that considers the upper neck force and moment proposed by the National Highway Traffic Safety Administration (NHTSA) [21]. The

“ $ij$ ” represents indices for the 4 injury mechanisms; namely  $N_{TE}$ ,  $N_{TF}$ ,  $N_{CE}$  and  $N_{CF}$ . The first index  $j$  represents the actual load (Tension or Compression) while the second index  $j$  represent sagittal plane bending moment (neck Flexion or Extension). The current performance limit of the  $N_{ij}$  is 1 which represents a 22% risk of AIS level 3 [22]. The equation for the  $N_{ij}$  is:

$$N_{ij} = \left| \frac{F_{Z,i}}{F_{int,i}} \right| + \left| \frac{M_{Y,j}}{M_{int,j}} \right| \quad (4.2)$$

where  $F_{Z,i}$  is the upper neck force in Z-axis,  $F_{int,i}$  is the threshold force,  $M_{Y,j}$  is the upper neck moment about Y-axis and  $M_{int,j}$  is the threshold moment.

## 4.3 Modelling Results for Hybrid III Dummy vs. Human Body

### 4.3.1. UAS Impact Injuries

#### *Overall Kinematic of Head/Neck System*

From the simulation, the overall kinematics of the head and neck of the Hybrid III and the human body is presented in Figure 4.3 to Figure 4.5. The impact sequences shown in the figures captured the kinematic of the head and neck of the Hybrid III and the human body at every 6 ms starting from contact initiation between the UAS and the head. The comparison is done by comparing the trajectory and displacement of the CG of the Hybrid III and human body heads.

Firstly, Figure 4.3 shows the impact sequences for  $\theta = 0^\circ$  (horizontal impact) of UAS impacting the heads for  $\psi$  equal to  $0^\circ$ ,  $90^\circ$  and  $180^\circ$  (corresponding to frontal, side, and rear impact, respectively). For  $\psi = 0^\circ$  (frontal impact), as shown in Figure 4.3(a), the Hybrid III head and neck complex can realistically mimic the movement of the human body head and neck with similar head translational and rotational displacements. The motion observed in this impact case is mostly head rotational motion head in an extension direction (backward) about the lower neck. Figure 4.3(b) shows a comparable head CG displacement between the Hybrid III and the human body. However, the head rotation about the body Z-axis is more significant in the human body in this case. For  $\psi = 180^\circ$  (rear impact) as shown in Figure 4.3(c), the Hybrid III head kinematics is comparable to the human body in which the neck section shows good bending curvature comparable to the human body neck.

Significant differences start to be observable when the impact elevation ( $\theta$ ) increases toward the vertical direction. Figure 4.4 shows the impact case of  $\theta = 45^\circ$  (elevated impact) of UAS hitting the heads from  $\psi$  of  $0^\circ$ ,  $90^\circ$ , and  $180^\circ$ . In this case, where UAS impact elevation is at  $45^\circ$ , the downward deformation of the crash dummy neck is small when compared to the human body. The human body head rotational direction when  $\psi$  equal to  $0^\circ$ ,  $90^\circ$ , and  $180^\circ$  is different from the Hybrid III. In Figure 4.4(a), for  $\psi = 0^\circ$  (frontal impact), the human body head rotates in flexion direction and vice versa in the Hybrid III. Also, in Figure 4.4(c) where the human body head rotates in extension direction but the Hybrid III rotates in flexion direction. Since the Hybrid III is designed primarily for frontal impact analysis, the head/neck construction holds anatomical difference compared to the human body head and neck construction which is more compliance in all load directions.

Lastly, the impact cases for  $\theta = 90^\circ$  (vertical drop) is shown in Figure 4.5. Even though the orientation of the UAS differs by  $90^\circ$  in each case, hitting locations are similar which results in similar head and neck kinematic in cases where  $\psi$  equals  $0^\circ$ ,  $90^\circ$ , and  $180^\circ$ . All three cases presented in Figure 4.5(a) to Figure 4.5(c) show that the human body neck deforms more than the Hybrid III neck in a vertical direction. This shows an effect of the stiff Hybrid III neck system compared to the human body neck system. Trajectory comparison shows the human head travels further down and over a longer period of time, while the Hybrid III head vertical displacement is small and with a faster rebound. In addition, the human head also rotates in extension direction when full vertical neck compression is reached, while such rotation is minimal in the Hybrid III head.

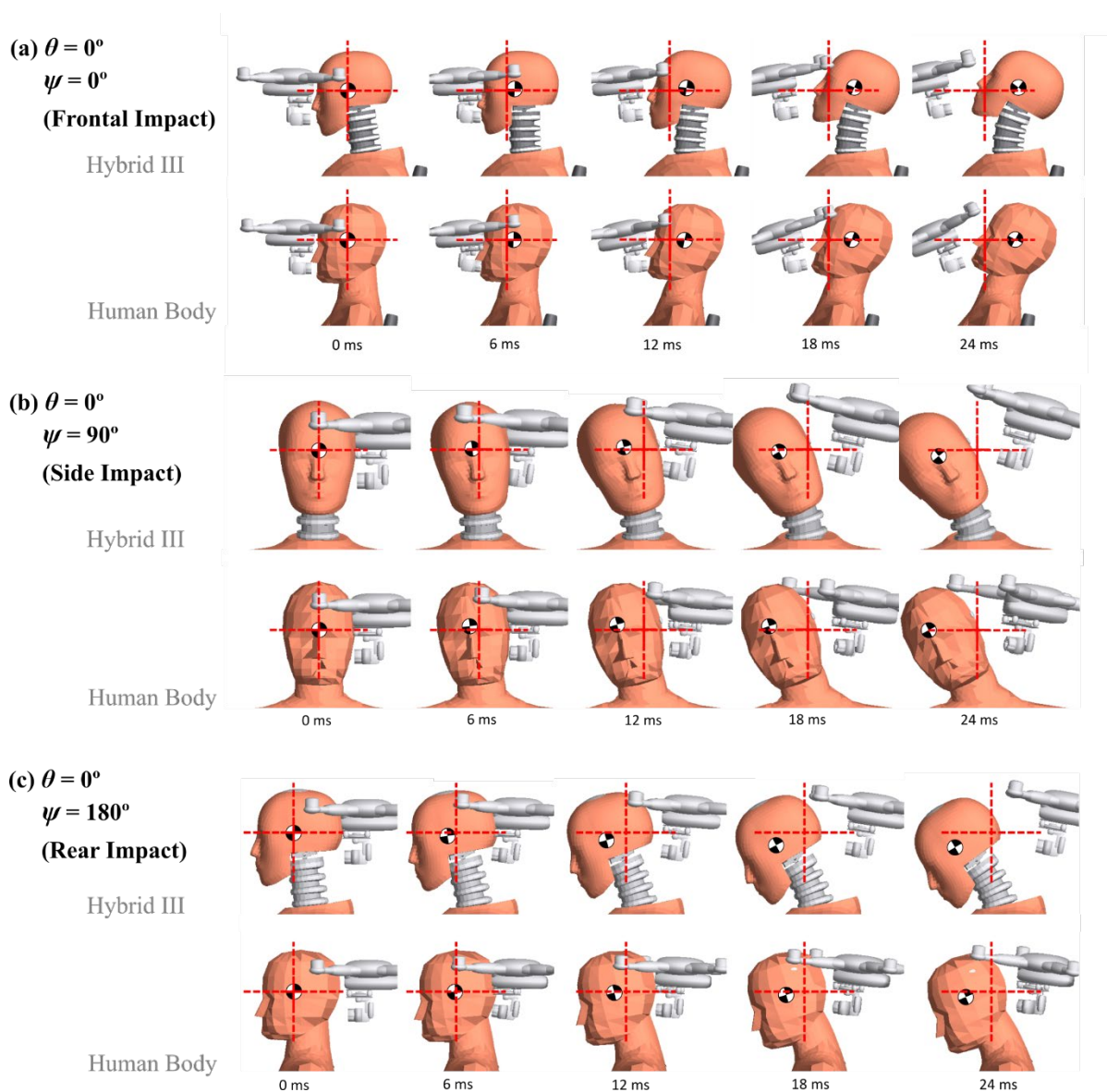


Figure 4.3. Comparison of impact sequences between the Hybrid III and the human body for  $\theta = 0^\circ$  (horizontal impact) at  $\psi = 0^\circ$ ,  $90^\circ$  and  $180^\circ$  at 196 J impact energy (equivalent to 18 m/s impact velocity).



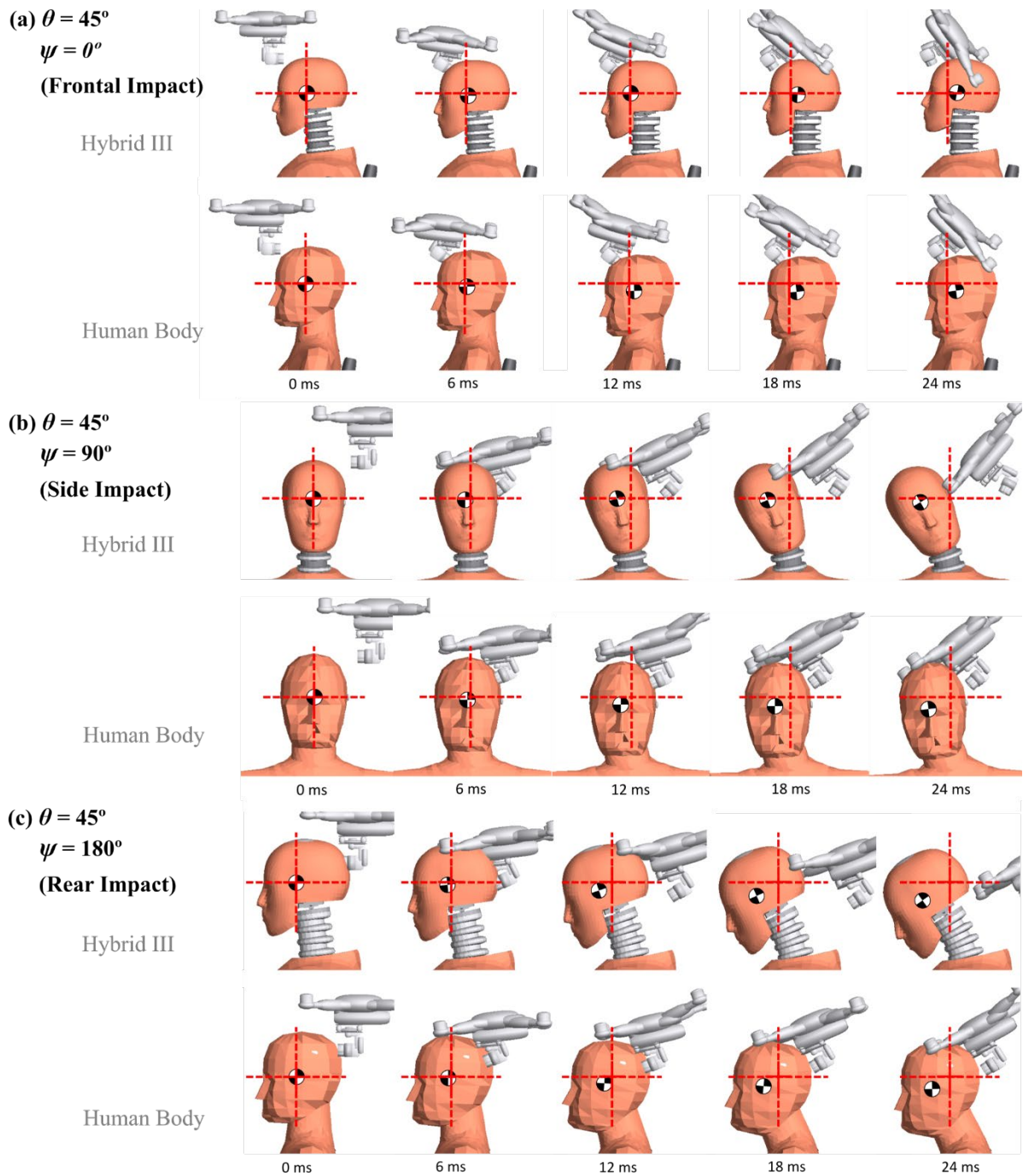


Figure 4.4. Comparison of impact sequences between the Hybrid III and the human body for  $\theta = 45^\circ$  (elevated impact) and  $\psi = 0^\circ, 90^\circ$  and  $180^\circ$  at 196 J impact energy (equivalent to 18 m/s impact velocity).

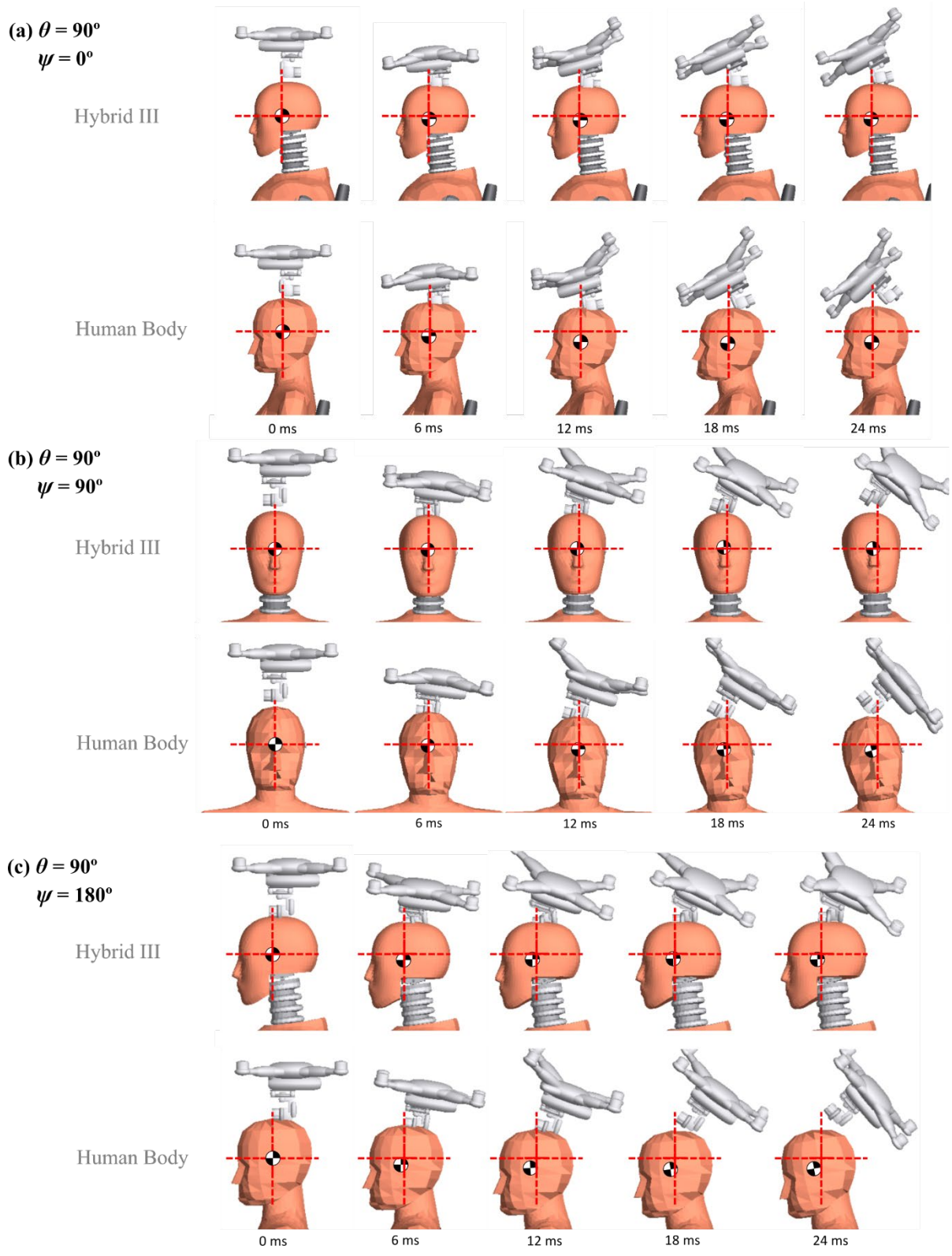


Figure 4.5. Comparison of impact sequences between the Hybrid III and the human body for  $\theta=90^\circ$  (vertical drop) and  $\psi = 0^\circ, 90^\circ$  and  $180^\circ$  at 196 J impact energy (equivalent to 18 m/s impact velocity).



## Head Injury

Head injury criteria or  $HIC_{15}$  is an integral of head CG acceleration of a crash dummy or the human body heads. Before any difference in  $HIC_{15}$  can be realized, the difference in head CG acceleration between the Hybrid III and the human body has to be addressed. Appendix 4A shows a comparison of head CG acceleration between the Hybrid III and the human body models at various  $\theta$  and  $\psi$ , and at 196 J impact energy (equivalent to an impact velocity of 18 m/s for the DJI Phantom III model).

As shown in Appendix 4A(a), for  $\theta = 0^\circ$  (horizontal impact), head CG acceleration signals produced from the Hybrid III and the human body models match well with one another, especially when  $\psi = 0^\circ$  (frontal impact). The phase of each signal also corresponds well between the model. However, the Hybrid III produces a higher acceleration peak than the human body when  $\psi = 90^\circ$  (side impact). For  $\psi = 180^\circ$  (rear impact), head CG acceleration matches well between the two models.

For impact cases where  $\theta = 45^\circ$  (elevated impact), significant differences in head CG acceleration can be observed as shown in Appendix 4A(b). For  $\psi$  of  $0^\circ$ ,  $90^\circ$ , and  $180^\circ$ , the first head CG acceleration peak which represents the contact force match well. Since both the Hybrid III and human skin share similar surface stiffness, these contact forces are similar in magnitude. The second peak, however, is higher for the human body compared to the Hybrid III for  $\psi$  of  $0^\circ$ ,  $90^\circ$ , and  $180^\circ$ . The second peak occurs when the entire UAS fully compresses and impact energy is fully transferred to the head. Overall, the area under the curves for the human body model is larger, showing the higher amount of impact energy being transferred to the head and results in higher head kinetic energy. In addition, the human body neck system damps out the impact force more than the Hybrid III since the observable third peak of the human body curve in Appendix 4A(b) dissipates out with a longer period.

Appendix 4A(c) shows impact cases when  $\theta = 90^\circ$  (vertical drop). Both models share similar trends with three observable peaks for  $\psi = 0^\circ$ ,  $90^\circ$ , and  $180^\circ$ . The phases of the first two peaks match well between the two models. Nevertheless, noted that the head CG of the human body accelerate faster as presented in the second peak. This shows that the human body neck complex is more compliant than the Hybrid III's. As for the rebound phase, the third peaks are 2.5 ms out of phase with one another. The last peak of the vertical impact case also shows a similar result to the elevated impact case where the neck of the human body rebound less and slower compared to the crash dummy. Furthermore, the differences in  $HIC_{15}$  between the two models tend to reach stable values as the energy increases beyond 100 J of impact energy.

By integrating the head CG acceleration-time history curve shows in Appendix 4A over the 15 ms time period, the  $HIC_{15}$  can be determined. Figure 4.6 shows a comparison of the  $HIC_{15}$  between the Hybrid III and the human body (upper plot) as well as the percentage difference of the  $HIC_{15}$  between the two models (lower plot). For every impact case in Figure 4.6, the  $HIC_{15}$  increases non-linearly as impact energy increases. The difference of the  $HIC_{15}$  between the two models vary differently for each impact case. The percentage plot shows a sharp drop from very low energy to approximately 20 J. This high percentage difference at very low impact energy can be neglected since the  $HIC_{15}$  values are near zero and have no practical injury significance.

For  $\theta = 0^\circ$  (horizontal impact) and  $\psi = 0^\circ$  (frontal impact), as shown in Figure 4.6(a), the Hybrid III produces similar results compared to the human body at with less than 7% difference at 196 J impact energy. For  $\psi = 90^\circ$  or  $180^\circ$  (side and rear impact), however, the human body produces higher  $HIC_{15}$  values compared to the Hybrid III by 23% and 47%,

respectively at 196 J impact energy. This agrees with the head CG acceleration-time history in Figure 4.3 which shows larger head acceleration for the human body. Furthermore, the percentage differences for  $\psi = 0^\circ$ ,  $90^\circ$ , and  $180^\circ$  reduce as the impact energy increases.

For  $\theta$  equal to  $45^\circ$  (elevated impact), large discrepancies in  $HIC_{15}$  values can be observed in Figure 4.6(b). For  $\psi = 0^\circ$  (frontal) results in the smallest  $HIC_{15}$  difference of 53% at 196 J impact energy. Side ( $\psi = 90^\circ$ ) and rear ( $\psi = 180^\circ$ ) impacts, however, results in significantly large  $HIC_{15}$  differences of 75% and 77%, respectively. These findings confirm the impact sequences shown in Figure 4.3 to Figure 4.5, which is observed that the amount of head displacement and the direction of head rotation differ between the Hybrid III and the human body. The Hybrid III head displacement is rather small and head rotation is in the opposite direction compared to the human body. This shows that more of the impact energy is transferred to the thorax through the stiff neck and results in less head acceleration for the Hybrid III. Furthermore, the percentage difference for  $\psi = 0^\circ$  and  $\psi = 90^\circ$  tend to reach stable values after the impact energy of 100 J at 50% and 80%, respectively. Impact case for  $\psi = 180^\circ$  also shows a tendency to reach a stable value of percentage difference, nevertheless, further analysis beyond 200 J is still required.

For  $\theta = 90^\circ$  (vertical impact), the  $HIC_{15}$  values for the Hybrid III and the human body are similar in all impact case ( $\psi = 0^\circ$ ,  $90^\circ$ , and  $180^\circ$ ). The  $HIC_{15}$  percentage differences between the Hybrid III and the human body are approximately 33% for all three cases at 196 J impact energy. Since only impact direction ( $\psi$ ) was varied, the UAS impact attitude and point of contact are similar in all three cases, only the facing direction of the UAS is changed by  $90^\circ$  in each case. The  $HIC_{15}$  percentage difference plot also shows the same trend for all three cases in vertical impact cases. The difference reduces as the impact energy increase, and the percentage difference reaches stable values at approximately 30% after 100 J impact energy.

Besides, it is observed in Figure 4.6 that  $HIC_{15}$  values are significantly higher at  $\theta = 0^\circ$  (horizontal impact) when compared to  $\theta = 45^\circ$  and  $90^\circ$ . The explanation lies in the different points of contact between these impact cases. For  $\theta = 0^\circ$ , UAS flies horizontally onto the head and has a front fuselage as the main point of contact. Other the other hand, for  $\theta = 45^\circ$  and  $90^\circ$ , UAS collides onto the head with camera gimbal as the first point of contact. In comparison, front fuselage is considered to be structurally more rigid than the camera gimbal which acts as a spring-damper system that damps out impact energy. This results in significantly lower impact energy transferred to the head when UAS drops vertically.

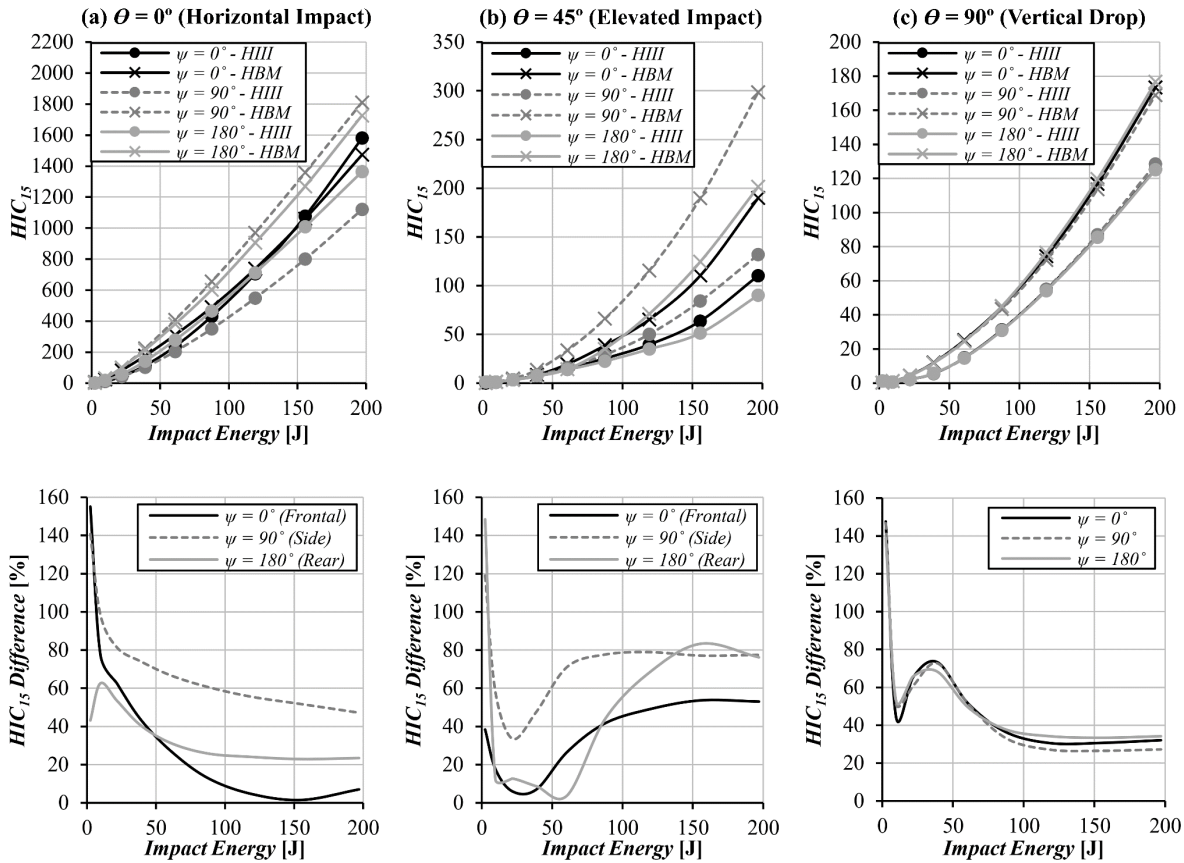


Figure 4.6. Comparison of  $HIC_{15}$  between the Hybrid III and the human body models (upper figures) and the percentage in  $HIC_{15}$  of Hybrid III dummy relative to the 100% for the human body (lower figures) at different impact energy,  $\theta$ , and  $\psi$ .

### Neck Injury

Neck responses between the Hybrid III and the human body are different due to the difference in neck biofidelic. In the Hybrid III, the neck complex is a segmented rubber and aluminum construction [23]. This results in the dummy neck to be less compliant compared to the human neck in a vertical direction. The difference can be seen in force/moment transferred to the neck system from the head. Appendix 4B and Appendix 4C show the difference in upper neck force in Z-direction ( $F_{Z,i}$ ) and upper neck moment about the Y-axis ( $M_{Y,j}$ ) between the Hybrid III and the human body.

Upper neck force  $F_{Z,i}$  produced by the Hybrid III peak upper neck force  $F_{Z,i}$  is significantly higher than that in the human body. The area under the curve is smaller for the human body compared to the Hybrid III which shows that the amount of force transfers to the neck system over the first 16 ms period is much larger in the Hybrid III. The human body upper neck  $F_{Z,i}$  curve also shows a longer energy transfer period over time. In the model, the head of both the Hybrid III and the human body models are modelled as a rigid sphere without any internal deformation such as the skull or brain deformation. This means that the force transfers from the head to the neck system in the Hybrid III are substantially higher than in the human body.

Furthermore, upper neck moment  $M_{Y,j}$  in the dummy is significantly higher than the human body especially when  $\theta = 0^\circ$  (horizontal impact). Since the human body neck is made of small vertebrae, it allows more initial translational motion between inter-vertebral disc along the horizontal line before rotation when compared to the Hybrid III. The Hybrid III neck, on the other hand, is made of rubber and aluminum discs that allow rotation. This does not

permit any translation between discs in the neck system. Therefore, the upper neck moment  $M_{Y,j}$  of a Hybrid III is larger than the human body. Moreover, the rotational direction of the head affects the measured upper neck moment  $M_{Y,j}$  in both magnitude and sign. It is shown in Appendix 4C that for  $\psi = 0^\circ$  and  $180^\circ$  impact cases, magnitude difference was observed but the measured moments all have the same sign. This is not the case when  $\psi = 90^\circ$  (side impact) and  $\theta = 0^\circ, 45^\circ$ , and  $90^\circ$  (corresponding to horizontal, elevated, or vertical impact cases respectively). As clearly shown quantitatively in Figure 4.3(b), Figure 4.4(b) and Figure 4.5(b), the impact sequences illustrate the different head translational and rotational movements between the Hybrid III and the human body models. This difference, however, is less severe for  $\theta = 0^\circ$  (horizontal impact).

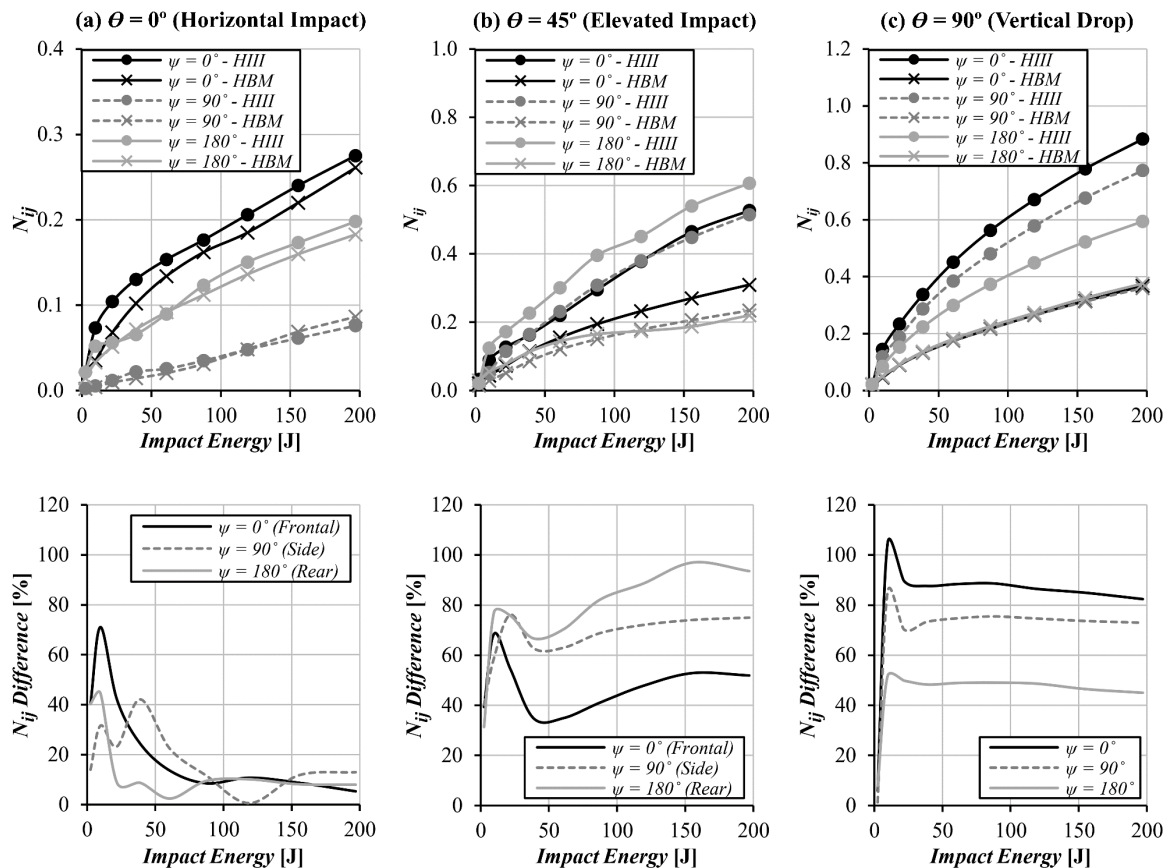


Figure 4.7. Comparison of  $N_{ij}$  between the Hybrid III and the human body models (upper figures) and the percentage in  $N_{ij}$  of Hybrid III dummy relative to the 100% for the human body (lower figures) at different impact energy,  $\theta$ , and  $\psi$ .

A neck injury in the Hybrid III dummy and the human body is assessed using the neck injury criterion,  $N_{ij}$ , and the results are shown in Figure 4.7.  $N_{ij}$  criterion consists of four values, namely  $N_{TE}$ ,  $N_{TF}$ ,  $N_{CE}$ , and  $N_{CF}$ . The  $N_{ij}$  results presented here are the maximum of all four values combined for each different impact case. The impact case for  $\theta = 0^\circ$  (horizontal impact) shown in Figure 4.7(a) shows no significant difference between the Hybrid III and the human body for frontal, side, and rear impact cases. The percentage difference plot (lower figure of Figure 4.7(a)) also shows the 7% difference at 196 J impact energy for  $\psi = 0^\circ, 90^\circ$ , and  $180^\circ$  (corresponding to frontal, side, and rear impact cases, respectively). The peak percentage difference near 10 J impact energy can be neglected since the  $N_{ij}$  at that energy level has no significant neck injury level. In addition, the percentage difference starts to converge on a stable value of 7% percentage difference after 100 J of impact energy.

However, the differences become apparent for  $\theta = 45^\circ$  and  $90^\circ$  impact cases. For  $\theta = 45^\circ$  shown in Figure 4.7(b), the results for  $\psi = 0^\circ$  and  $\psi = 90^\circ$  are approximately 51% and 75% difference in the  $N_{ij}$  value at 196 J impact energy between the two models, respectively. For the impact case with  $\theta = 45^\circ$  even a higher difference results between the  $N_{ij}$  's for the Hybrid III and the human body: 93% difference at 196 J impact energy. To illustrate the effect of such difference in injury severity, in an elevated impact case with UAS approaching from the rear, the Hybrid III has 21% chance of broken neck while the human body has 14% chance of broken neck. This is based on the AIS injury level analysis, however, detail discussion of this injury level analysis is beyond the scope of this paper.

Similarly, for the impact cases of  $\theta = 90^\circ$  (vertical impact), the differences are 45%, 72% and 82% at 196 J impact energy at  $\psi = 0^\circ$ ,  $90^\circ$ , and  $180^\circ$ , respectively. Even though the upper neck force in Z-direction is comparable for  $\psi = 0^\circ$ ,  $90^\circ$ , and  $180^\circ$ , the neck moments vary between these cases due to a slight shift in impact location of the UAS on the head. This results in a change in induced upper neck moment  $M_Y$ . This shows that neck moment has a significant impact on the neck injury.

## 4.4 Discussion

The previous Section assessed differences in injury levels of the Hybrid III dummy relative to the human body due to various DJI Phantom III UAS collisions. To accomplish this validated multibody system (MBS) models of DJI Phantom III UAS collisions with a Hybrid III dummy and with a human body have been implemented in MADYMO [11]. The MBS modelling technique allows fast simulation time with accurate results and can capture accurately the overall kinematics of the system. By varying impact elevation ( $\theta$ ) and impact direction ( $\psi$ ), a total of 9 impact cases were simulated in the previous Section both for MBS models of human body and Hybrid III dummy. Table 4.1 summarizes the results obtained for these 9 impact cases in terms of head/neck injury differences of the Hybrid III dummy relative to the human body.

Table 4.1. Summary of injury level results from Section 3 for Hybrid III dummy relative to human body

Impact Case	$\theta$ (Impact Elevation)	$\psi$ (Impact Direction)	Injury of Hybrid III relative to human body	
			Head Injury	Neck Injury
1	0° (Horizontal)	0° (Frontal)	Similar	Similar
2		90° (Side)	Higher	Similar
3		180° (Rear)	Similar	Similar
4	45° (Elevated)	0° (Frontal)	Lower	Higher
5		90° (Side)	Lower	Higher
6		180° (Rear)	Lower	Higher
7	90° (Vertical Drop)	0° (Frontal)	Lower	Higher
8		90° (Side)	Lower	Higher
9		180° (Rear)	Lower	Higher

Table 4.1 shows that, for horizontal impact with UAS approaching from the front (impact case 1) and rear (impact case 3), the dummy produces similar response and similar head/neck injuries as the human body. For horizontal UAS impact from side direction (impact case 2), the Hybrid III predicts similar neck injury, but higher head injury than the human body.

Table 4.1 also shows that for the other impact cases 4 through 9 (i.e. 45° elevated and vertical drop) the Hybrid III under-predicts head injury and over-predicts neck injury relative to the human body.

To understand these systematic differences, the MBS models of the Hybrid III and the human body were compared anatomically. These MBS models differ for the neck, though they are almost identical for the head. The heads of both MBS models are represented by a rigid body with the same contact force model and without any internal deformation. This means that the differences in head and neck injuries found in Section 3 stem from the differences in neck complexes of the two models which affect neck deformation and resistance to head acceleration.

The neck system in the Hybrid III dummy is constructed by a straight column in which a higher impact force from the head is transferred to when compared to the human head. The more compliance human body neck system is modelled realistically to represent the vertebrae structure with passive muscle force. This allows the head to travel faster in a downward direction with less resisting upward force, resulting in larger head acceleration and lower neck force. As shown in the qualitative analysis of the impact sequences in Figure 4.3 to Figure 4.5, head displacement and neck deformation in the human body is larger than the Hybrid III. A lack of biofidelity in the Hybrid III neck is attributed to high resistance to compressive force and bending of the neck and torso [6], leading to the tendency to over-estimate axial compressive force. This is confirmed by the neck injury analysis using the  $N_{ij}$  criterion which shows the Hybrid III over-predicts  $N_{ij}$  values compared to the human body.

It should be noted that the human neck stiffness and load-bearing characteristics change dramatically when spinal curvature is included [24]. Such curvature shifts the load path of the centre of the thoracic spine by more than 1 cm, resulting in less force transferred directly towards the thorax. Without neck curvature under vertical load condition, the Hybrid III neck becomes stiffer than the human spine, and load is transferred more directly to the thorax. In addition, with small vertebrae in the human body, translational motion between inter-vertebral disc is possible and allow neck compliance in all direction. The effect of this can be seen in elevated impact (impact cases 4, 5, and 6) where the human body head has a combination of both rotational and translational motions. A related effect is found when the UAS flies horizontally and approaches the head from the side (impact case 2). The head translational motions are different as well as the direction of head rotation about the Z-axis. This results in the estimation of neck moments to have an opposite sign between the two models.

## 4.5 Conclusions

When conducting impact testing research, it is important to account for the type of crash dummy used and recognize the accuracy limitation relative to a real human body. To better understand this difference, this paper investigates the differences in head and neck injury levels between a 50<sup>th</sup> percentile Hybrid III crash dummy and a 50<sup>th</sup> percentile human body subjected to UAS collisions. To simulate such collision, a validated UAS MBS model was employed in impact simulation against validated Hybrid III dummy and human body models in MADYMO. For the UAS, the DJI Phantom III was chosen as a representative model used in this study. A total of 9 impact cases were investigated which include horizontal, elevated, and vertical impacts, as well as impact directions from the front, side, and rear relative to the head.

The simulation results show that for horizontal UAS approaches from front and rear, Hybrid III head and neck injuries are similar relative to those for the human body. However, when UAS approaches horizontally from side direction, then head acceleration is higher for

Hybrid III. Furthermore, when UAS drops vertically or impacts under 45° elevation, then Hybrid III predicts lower head injury and higher neck injury for each impact direction, i.e. frontal, side and rear.

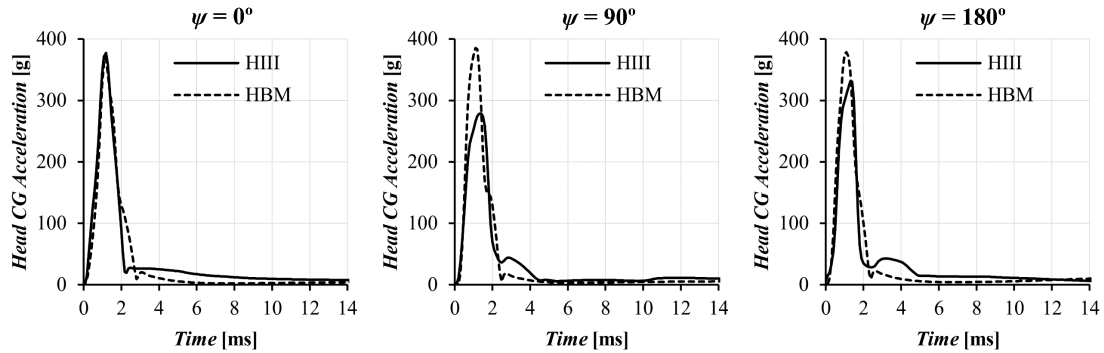
Differences in head and neck injuries are due to the difference in the neck complex between the two models. Hybrid III has a stiffer neck complex when compared to the human body, which limits Hybrid III's head movements, especially in the vertical direction. This implies smaller head acceleration for the Hybrid III head and instead a larger amount of impact energy is transferred through the Hybrid III neck to the thorax. In contrast to this, the human neck is much more compliant because it consists of a complex of small vertebrae which allows a larger neck deformation. Hence, the human neck experiences lower force and moment, while the head experiences larger head acceleration.

From a UAS impact severity analysis perspective, the Hybrid III dummy has a realistic response relative to the human body especially for horizontal impacts from frontal or rear directions. This finding reaffirms other works that show that the focus of the Hybrid III design and validation has been on a horizontal-frontal load direction [25,26]. Nevertheless, the Hybrid III dummy has serious limitations for horizontal UAS impact from side direction and vertical UAS drops as well as elevated UAS impacts. This limitation of the Hybrid III dummy does not apply to the MBS model of the human body. The latter has been validated against real human and cadavers, making it possible to realistically simulate various impact cases in all load directions. This is an important benefit of using the numerical human body model with multi-directional biofidelity [15].

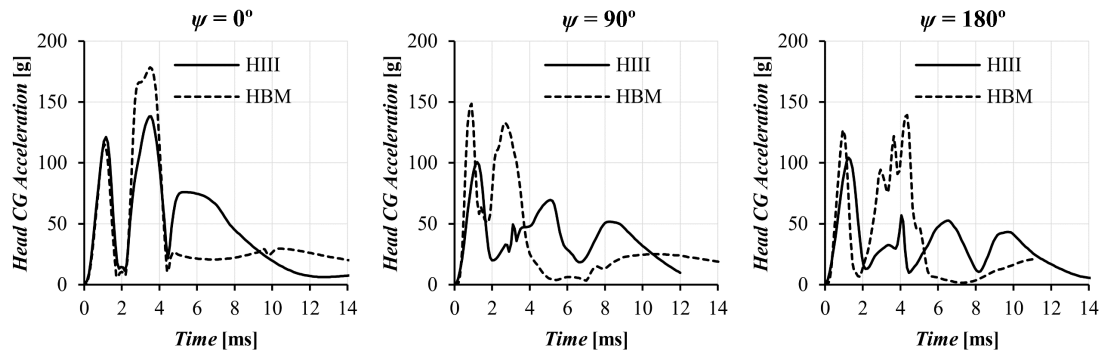
The results obtained also reveal novel insight into how different impact conditions can significantly affect injury levels. A slight change in impact elevation may change the point of contact which can result in a completely different injury level. To extend the analysis to cover larger scenarios, other parameters need to be incorporated and investigated in future works, for example, off-set between UAS CG and head CG, UAS initial rotational velocity, or yaw and roll angles. More importantly, the variation of mass, size, and shape of UAS, which are influential parameters on injury severity, will also be investigated in future works.

## Appendix 4A: Head CG Acceleration-Time History

(a)  $\theta = 0^\circ$



(b)  $\theta = 45^\circ$



(c)  $\theta = 90^\circ$

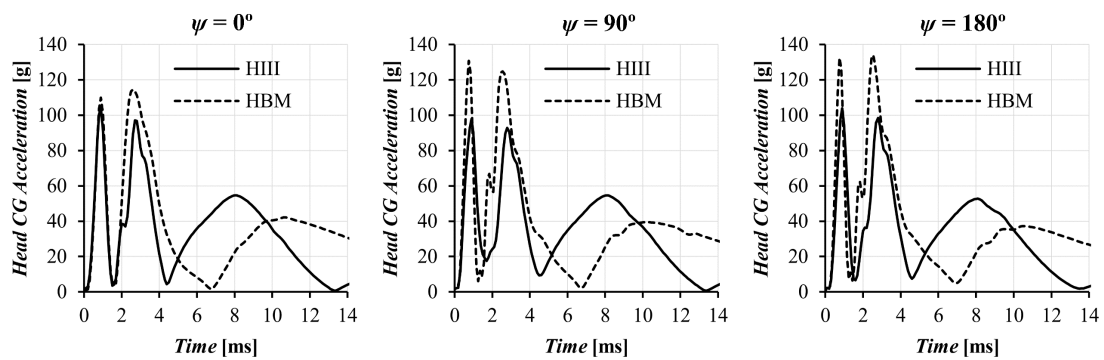


Figure 4.8. Comparison of head CG acceleration between the Hybrid III and the human body models at various impact conditions and at 196 J impact energy (equivalent to 18 m/s impact velocity)



## Appendix 4B: Upper Neck $F_z$ -Time History

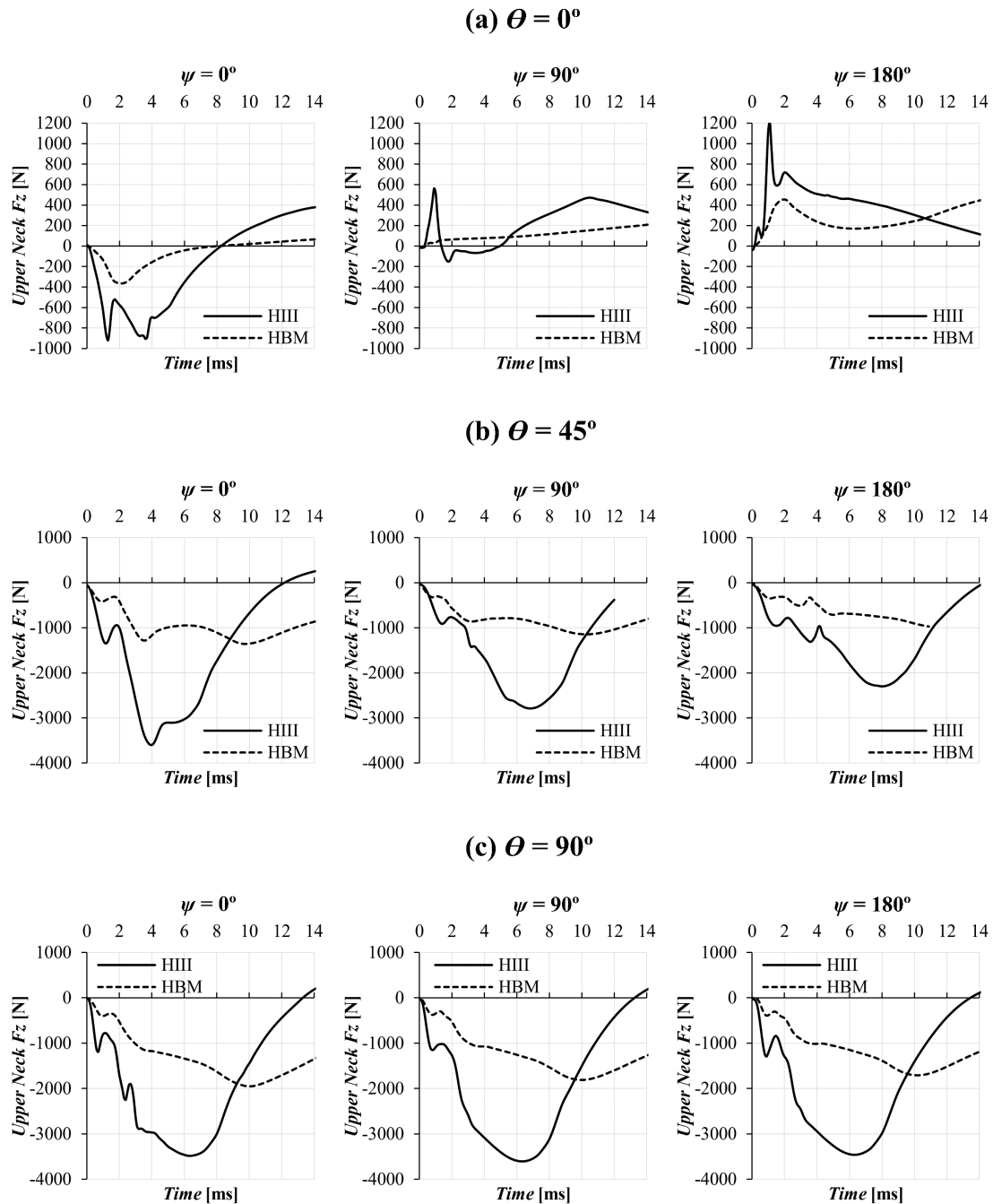


Figure 4.9. Comparison of upper neck force in Z-direction between the Hybrid III and the human body models at various impact conditions and at 196 J impact energy (equivalent to 18 m/s impact velocity)

## Appendix 4C: Upper Neck $M_Y$ -Time History

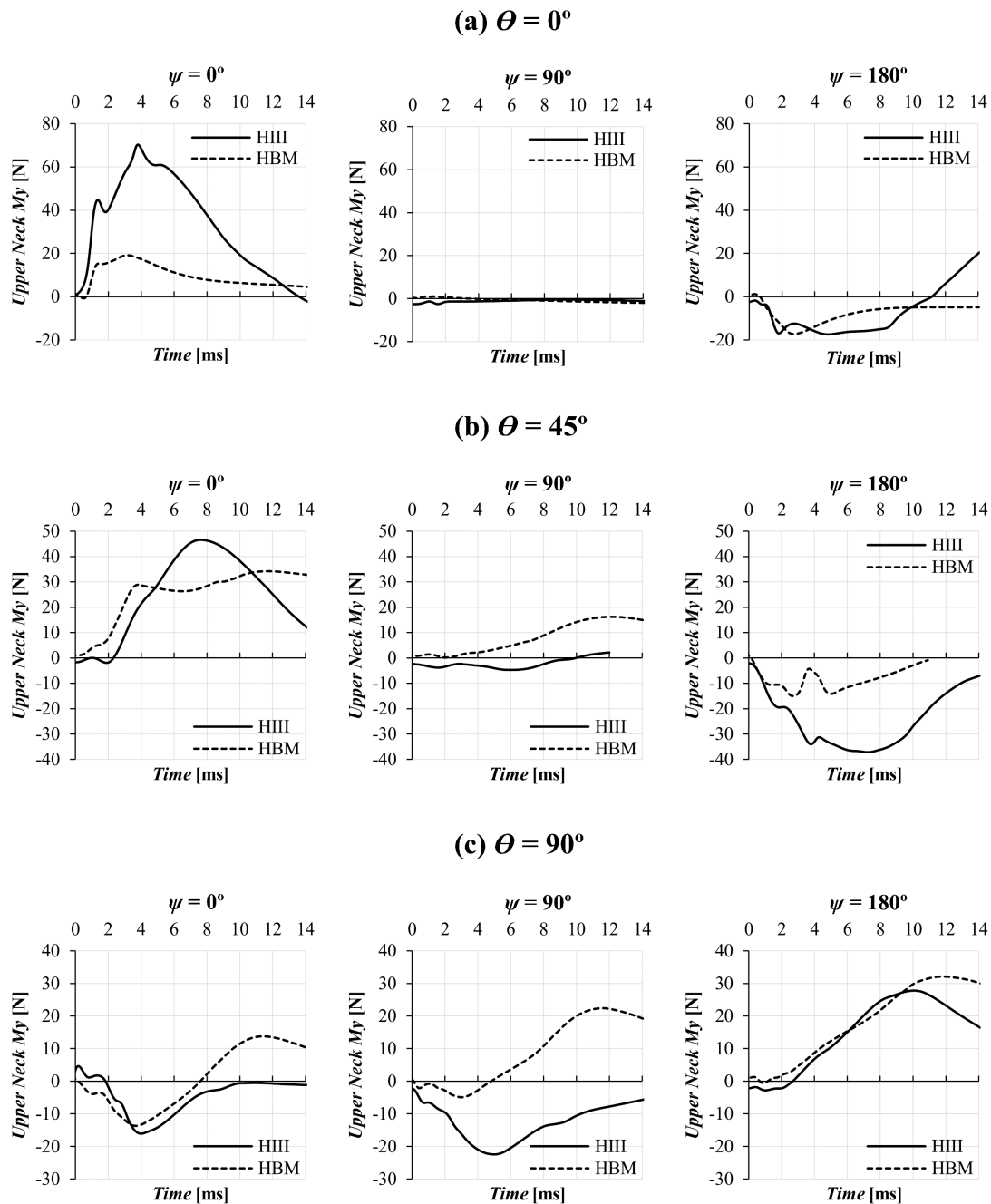


Figure 4.10. Comparison of upper neck moment about Y-axis between the Hybrid III and the human body models at various impact conditions and at 196 J impact energy (equivalent to 18 m/s impact velocity)

## References

- [1] Campolettano ET, Bland ML, Gellner RA, et al. Ranges of Injury Risk Associated with Impact from Unmanned Aircraft Systems. *Ann Biomed Eng.* 2017;45(12):2733–2741. <http://link.springer.com/10.1007/s10439-017-1921-6>.
- [2] Arterburn DR, Duling CT, Goli NR. Ground Collision Severity Standards for UAS Operating in the National Airspace System (NAS). 17th AIAA Aviation Technology, Integration, and Operations Conference; 2017. p. 1–16, <https://arc.aiaa.org/doi/10.2514/6.2017-3778>.
- [3] Arterburn D, Ewing M, Prabhu R, et al. FAA UAS Center of Excellence Task A4 : UAS Ground Collision Severity Evaluation, Huntsville; 2017. [http://www.assureuas.org/projects/deliverables/a4/ASSURE\\_A4\\_Final\\_Report\\_UAS\\_Ground\\_Collision\\_Severity\\_Evaluation.pdf](http://www.assureuas.org/projects/deliverables/a4/ASSURE_A4_Final_Report_UAS_Ground_Collision_Severity_Evaluation.pdf).
- [4] Huculak R, NIAR UAS Drop Testing Report, Wichita; 2016. [http://www.assureuas.org/projects/deliverables/a11/NIAR\\_Test\\_Report\\_-\\_FAA-UAH\\_UAS\\_Drop\\_Testing.pdf](http://www.assureuas.org/projects/deliverables/a11/NIAR_Test_Report_-_FAA-UAH_UAS_Drop_Testing.pdf).
- [5] Mroz K, Bostrom O, Bengt P, et al. Comparison of Hybrid III and human body models in evaluating thoracic response for various seat belt and airbag loading conditions. IRCOBI Conference, Sept 15-16; 2010. p. 265–280.
- [6] Herbst B, Forrest S, Chng D, et al. Fidelity of anthropometric test dummy necks in rollover accidents, <https://www-nrd.nhtsa.dot.gov/pdf/esv/esv16/98s9w20.pdf%0A>.
- [7] Sances A, Kumaresan S. Comparison of biomechanical headneck responses of hybrid III dummy and whole body cadaver during inverted drops. *Biomed Sci Instrum.* 2001;37:423–427. <http://www.ncbi.nlm.nih.gov/pubmed/11347428>.
- [8] Sances A, Carlin F, Kumaresan S. Biomechanical analysis of head-neck force in hybrid III dummy during inverted vertical drops. *Biomed Sci Instrum.* 2002;38:459–464. <http://www.ncbi.nlm.nih.gov/pubmed/12085650>.
- [9] Rattanagraikanakorn B, Schuurman MJ, Gransden DI, et al. Modelling Head Injury due to Unmanned Aircraft Systems Collision: Crash Dummy vs Human Body. AIAA Aviation 2019 Forum, Dallas, Texas; 2019. <https://arc.aiaa.org/doi/abs/10.2514/6.2019-2835>.
- [10] TASS International, MADYMO; 2019. <https://tass.plm.automation.siemens.com/madymo>.
- [11] Rattanagraikanakorn, B., Gransden, D. I., Schuurman, M., De Wagter, C., Happee, R., Sharpanskykh, A., and Blom, H. A. P., “Multibody system modelling of unmanned aircraft system collisions with the human head,” *International Journal of Crashworthiness*, vol. 25, 2020, pp. 689-707, doi: 10.1080/13588265.2019.1633818, URL: <https://doi.org/10.1080/13588265.2019.1633818>.
- [12] Manning JE, Happee R. Validation of the MADYMO Hybrid II and Hybrid in Vertical Impacts III 50th-Percentile Models. *Test.* 1998. p. 26–28.
- [13] TASS International, Model Manual Version 7.7; 2017.
- [14] Happee R, Hoofman M, Van Den Kroonenberg AJ, et al. A Mathematical Human Body Model for Frontal and Rearward Seated Automotive Impact Loading, SAE Technical paper; 1998.

- [15] Happee R, Ridella S. Mathematical human body models representing a mid size male and a small female for frontal, lateral and rearward impact loading. IRCOBI Conference Proceedings; 2000. pp. 1–18,
- [16] TASS International, Human Body Models Manual Version 7.7; 2017.
- [17] Hardy W, Khalil T, King A. Literature review of head injury biomechanics. *Int J Impact Eng.* 1994;15(4):561–586.
- [18] Henn HW. Crash tests and the head injury criterion. *Teach Math Appl.* 1998;17(4):162–170.
- [19] Hutchinson J, Kaiser MJ, Lankarani M. The Head Injury Criterion (HIC) functional. *Journal of Applied Mathematics and Computation.* 1998;96(1):1–16.
- [20] Schmitt K-U, Niederer PF, Muser MH, et al. Head Injuries. *Trauma Biomechanics.* Berlin, Heidelberg: Springer; 2010. pp. 63–93. [http://link.springer.com/10.1007/978-3-642-03713-9\\_3](http://link.springer.com/10.1007/978-3-642-03713-9_3).
- [21] Klinich K, Saul R, Auguste G, et al. Techniques for Developing Child Dummy Protection Reference Values; 1996.
- [22] Parr MJC, Miller ME, Bridges NR, et al. Evaluation of the Nij neck injury criteria with human response data for use in future research on helmet mounted display mass properties. *Proceedings of the Human Factors and Ergonomics Society*; 2012. p. 2070–2074,
- [23] Humanetics, Hybrid III 50th Male. <http://www.humaneticsatd.com/crash-test-dummies/frontal-impact/hiii-50m>.
- [24] Herbst B, Forrest S, Chng D, et al. Fidelity of Anthropometric Test Dummy Necks in Rollover Accidents; 1382. p. 14–15.
- [25] Taylor A. Comparison of the Hybrid II, FAA Hybrid III, and THOR-NT in Vertical Impacts; 2016. <https://outlook.office.com/owa/?path=/attachmentlightbox>.
- [26] Arosio B, Mongiardini M, Mattos GA, et al. Comparison of hybrid III and human body model in head injury encountered in pendulum impact and inverted drop tests. *First International Roadside Safety Conference*; 2017.

---

## Modeling and Simulating Human Fatality due to Quadrotor UAS Impact

*Evaluating safety risk posed to third parties on the ground due to UAS impact requires a model of probability of fatality (PoF) for human. For quadrotor UAS, the existing impact models predict remarkably different PoFs. The most pessimistic is the impact model adopted by Range Commanders Council (RCC) while the Blunt Criterion model is far more optimistic. The ASSURE study has assessed the third set of PoF values through conducting controlled drop tests of a DJI Phantom III on a crash dummy; these results differ again. To investigate these discrepancies, this paper employs a numerical impact analysis of UAS collisions on humans. The current paper is the third in a series of studies. The first study developed a Multi-Body System (MBS) simulation model of a DJI Phantom III impacting the head of a crash dummy; this MBS model has been validated against the experimental drop test results of ASSURE. The second study conducted simulations with the validated MBS model to systematically show the differences in head and neck injuries if the human dummy is replaced by a validated MBS model of a human body. The aim of the current paper is threefold: i) to extend the latter MBS model to assess injury levels for DJI Phantom III impact on thorax and abdomen; ii) to transform the assessed injury levels for head, thorax and abdomen to PoFs; and iii) to compare the MBS obtained PoFs to those from RCC and Blunt Criteria models. The MBS based results show that variations in the scenario of DJI Phantom III impact on the head significantly affect PoF. These variations are not captured by the RCC or BC model, and neither in the ASSURE measurements. Both for head, thorax and abdomen, in case of comparable impact scenarios, the RCC model tends to over-predicts PoF compared to the MBS model, while the BC model tends to under-predict PoF.*

This chapter has been published as “Rattanagraikanakorn, B., Blom, H. A., Sharpanskykh, A., de Wagter, C., Jiang, C., Schuurman, M. J., Gransden, D. I., and Happee, R., “Modeling and Simulating Human Fatality due to Quadrotor UAS Impact,” Proc. 20th AIAA Aviation Technology, Integration, and Operations Conference (ATIO2020), 15-19th June 2020, Virtual Event”

## 5.1 Introduction

One of the major challenges of allowing unmanned aircraft system (UAS) operations in rural and urban areas is to predict and subsequently mitigate safety risk posed to third parties on the ground. Models of safety risk posed to third parties on the ground consist of five probabilistic models [1–7]. The first model is for the frequency of a UAS ground crash. The second model is a density map of the rural or urban population. The third model is a shelter protection probability map of the rural and urban area considered. The fourth model is the probability that an unprotected person at a given location is being hit by a UAS crash. The fifth model is for the probability of fatality (PoF) in case of UAS impact of a human on the ground. The literature on the first four of these models shows healthy convergence; but this is not the case for the model of PoF in case of a quadrotor UAS impact on a human.

One of the well-known PoF models of human impact by a UAS has been proposed by Range Commanders Council (RCC) [8]. This model provides PoF curves as a function of the kinetic energy of a UAS at the moment of impact of human head, thorax, and abdomen/limbs respectively. This model is based on the work of Feinstein et al. [9] who assessed these curves on the basis of a large database of collision dynamics and effects of small, rigid, metallic fragments on human. Another impact model of thorax and abdomen injury that is widely used in UAS ground risk analysis [5,10] is the Blunt Criterion (BC) model. BC is an energy-based model developed by Sturdivan [11,12] and has been used by the U.S. Department of Defense to assess vulnerability to blunt weapons, and projectile impacts. Unlike the RCC curves, BC is developed purely for blunt impact force which does not inflict penetration or laceration-type of injury. However, the latter does not explain the large differences between the BC and the RCC models.

To develop a better and applicable approach for UAS impact on the human body based on blunt impact force analysis, the ASSURE Research Group conducted testing and analysis of a DJI Phantom III UAS drop impacts on an anthropomorphic test dummy (ATD) of a human [13,14]. The experiments provide useful insights into impact dynamics between the UAS and the head and neck of the ATD. However, the ASSURE report [13] shows that the RCC model predicts a much higher head injury level than what is measured in the drop tests on the ATD of a human.

To fill the gap between these three different PoF models, the current paper is the third one in a series of studies. In the first study [15], a numerical DJI Phantom III UAS impact model has been developed that is based on a multibody system (MBS) modeling and simulation approach and validated against the ASSURE [14] experimental data. This MBS simulation model allows large variations of UAS impact cases to be evaluated on a validated MBS model of a 50th percentile human body. The second study [16,17] performed a numerical comparison between the Hybrid III crash dummy and the 50th percentile human body model. It was found that the human ATD used (i.e. Hybrid III) has a different biofidelic level when compared to a validated MBS model of a 50th percentile human body. However, the effect of this difference in biofidelity does not explain the much larger differences between ASSURE and the RCC model.

The aim of the current, third study, is to continue the investigation of the differences between the ASSURE data, the RCC curves, and the BC curves for DJI Phantom III impact of human head, thorax, and abdomen. This is realized through three steps. The first step is to extend the MBS model to define and assess relevant injury levels for DJI Phantom III impact on thorax and abdomen of the validated MBS model of a 50th percentile human male body.

The second step is to identify valid transformations of the head, thorax and injury levels to PoFs. The third step is a comparison of the MBS obtained PoFs to those from RCC and Blunt Criteria models, and subsequent explanation of how this relates to the ASSURE results.

This paper is organized as follows. Section 5.2 reviews the main background. This consists of UAS fatality risk curves from RCC and BC models, as well as the results from our preceding two MBS studies [15–17]. Section 5.3 presents the extension of the MBS model with injury criteria for thorax and abdomen due to UAS impact, and provides simulations result of DJI Phantom III impacts of the head, thorax, and abdomen as a function of increasing impact energy. Section 5.4 addresses the transformation of the MBS measured injury criteria for head, thorax and abdomen to PoF values; this yields PoF curves for DJI Phantom III impacts of head, thorax and abdomen as a function of kinetic energy at impact. Section 5.5 compares the MBS based PoF curves for the head, thorax and abdomen to those of RCC and BC for UAS impact of head, thorax and abdomen. Section 5.6 and 5.7 present the discussion of the results and the conclusion, respectively.

## 5.2 Review of Main Background

### 5.2.1. RCC Fatality Risk Curve

Range Commanders Council proposed a common risk criterion in the Range Commanders Council report (RCC 321-00) where the S-shaped curves were developed to quantify the probability of fatality if a person is impacted in the head, thorax or abdomen by exploded inert debris [8]. These fatality risk curves were based on the work of Feinstein et al. [9] who employed log-normal distributions to relate the probability of fatality to impact which was derived from the study on the effects of the blast, debris, and other factors on human. The log-normal distribution equation for the RCC fatality risk curves is:

$$P_i(\text{Fatality} | KE < K) = \int_0^K \frac{1}{x\beta_i\sqrt{2\pi}} e^{-\frac{(\ln x - \ln \alpha_i)^2}{2\beta_i^2}} dx \quad (5.1)$$

where  $K$  is the fragment kinetic energy and  $\alpha_i, \beta_i$  are the scale and shape parameters of the log-normal. The parameters for calculating the RCC fatality risk curve accounting for different body parts are listed in Table 5.1.

Table 5.1. Log-Normal distribution parameters for different body parts

Body Part	Log-Normal Parameters	
	$\alpha$	$\beta$
Head	55	0.2302
Thorax	44	0.3737
Abdomen	96	0.4335

Using Equation 5.1 and log-normal distribution parameters in Table 5.1, the PoF curve for the head, thorax, and abdomen can be plotted as shown in Figure 5.1. The original Feinstein curve is plotted with x-axis in the natural log scale, however, the curve presented is converted into the linear scale for ease of comparison to other models in the later sections of the paper. In Figure 5.1, the RCC curve shows that fatality due to thorax has a slightly higher probability than the head, and much higher than the abdomen.

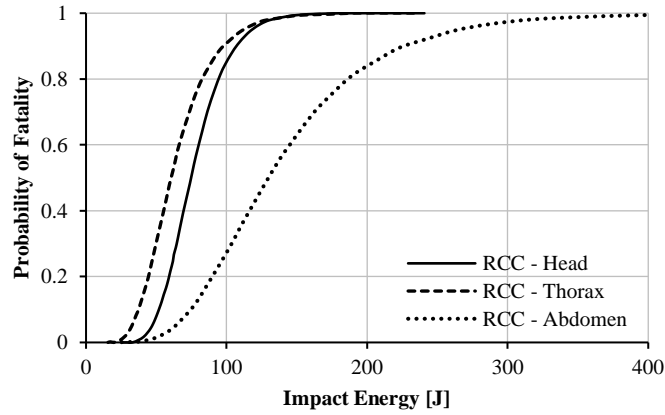


Figure 5.1. RCC log-normal fatality risk curve for head, thorax and abdomen

The RCC curve shows a steep slope for impact on all body parts. With the RCC curve, the probability of fatality for head and thorax impact reaches 1.0 at approximate 150 J impact energy. With maximum impact energy that DJI Phantom III UAS can achieve ( $E = 200$  J), the RCC curve suggests that human fatality is 100% probable if collision on head or thorax occurs. Collision on the abdomen is less severe, with 0.8 probability of fatality at 200 J impact energy. Moreover, impact on the thorax presents a higher fatality risk than the head and abdomen. Explanation of the differences is that the RCC curve is derived from hazardous debris experimentation with the original purpose of determining the fatality risk curve of ground personal due to missile explosions. Such type of small debris explosive injury does not only resolve in blunt force trauma but also penetration or laceration-type injuries.

In addition, the limitations of the RCC standard are rooted in the fundamental assumptions made to generate the curves and the basis for the probability of fatality data. For instance, the RCC curves were developed from Feinsein's work and employed weightings for hypervelocity type collisions where the debris contained a larger number of low mass fragments [13]. Besides, input data that formed Feinsein curves involved largely vertical falling inert debris since it was assumed the breakup or collisions would occur from a high altitude above the personal.

### 5.2.2. Blunt Criterion (BC) Model

Blunt criterion (BC) is proposed by the US Department of Defence and can be used to assess the risk of blunt force trauma from projectiles and blunt weapons [18]. BC was developed based on blunt impact injury data of the thorax [19] which resulted in a five parameters model defined as follow:

$$BC = \ln \frac{E}{W^{1/3}TD} \quad (5.2)$$

where  $E$  in the kinetic energy at impact,  $w$  is the mass of an impacted object,  $T$  is the thickness of the body wall (in cm), and  $D$  is the diameter of impacting object (in cm). It should be noted that  $W$  is not the mass of the entire human body, but an effective mass of the body part (head, thorax, or abdomen) which can be calculated using;

$$W = W_{total} \cdot r_{mass} \quad (5.3)$$

where  $W_{total}$  is the total mass of the human body and  $r_{mass}$  is the mass body part considered. Typical values of  $r_{mass}$  for head, thorax and abdomen are shown in Table 5.2.



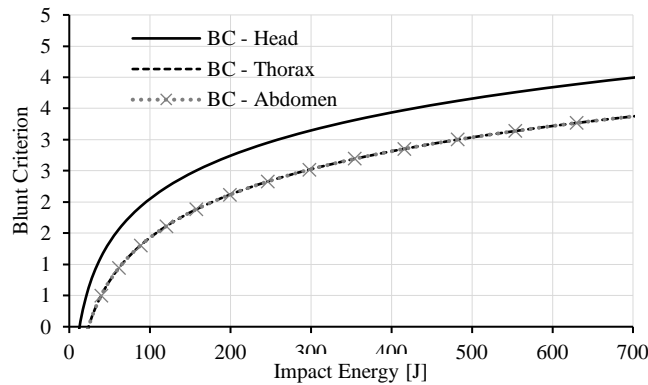
**Table 5.2. Relative body part mass ratio for injury prediction [18]**

Body Part	Body part mass ratio, $r_{\text{mass}}$
Head	0.08
Thorax	0.21
Abdomen	0.21

Furthermore, body wall thickness,  $T$ , depends mainly on the body part mass and can be calculated by,

$$T = kW^{1/3} \quad (5.4)$$

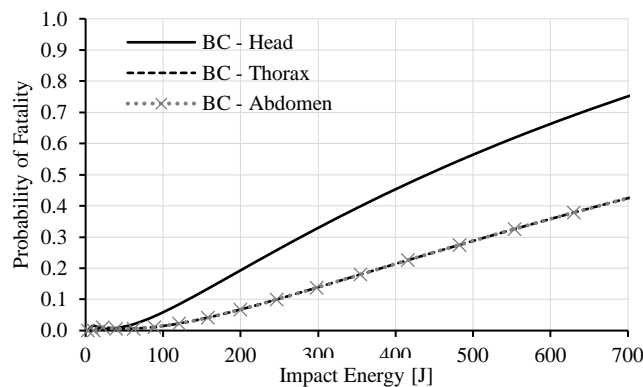
where  $k$  is equal to 0.711 for thorax and abdomen of a male human. Because BC for head impact was not developed before, the Australian Civil Aviation Safety Authority [20] has developed a BC model for UAS impact of a human head. The approximated body wall thickness  $T$  for the male human head is 1.3 cm as reported by the work performed by Raymond et al. [21]. The resulting BC values as a function of increasing Impact kinetic energy are depicted in Figure 5.2 for Head, Thorax and Abdomen.



**Figure 5.2. BC results on the head, thorax, and abdomen impact calculated as a function of impact kinetic energy. Note that thorax and abdomen curves overlap because of the identical model parameters for BC model**

In order to transform BC values in Figure 5.2, to PoF values, BC has first to be converted to AIS level using Equation 5.5. Subsequently, the AIS level has to be transformed to PoF values using the curve that is presented in Figure 5.16. The final results of this PoF transformation for BC model is shown in Figure 5.3.

$$AIS = 1.33 \cdot BC + 0.6 \quad (5.5)$$



**Figure 5.3. PoF curve from BC model for impact on head, thorax and abdomen as a function of impact kinetic energy. Note that the PoF curves for thorax and abdomen are aligned because the same BC parameters apply for both**

Figure 5.3 shows that the BC model based PoF curve for DJI Phantom III impact of head, thorax and abdomen. It should be noted that the PoF curves for thorax and abdomen are the same because the mass ratio is assumed to be the same. The PoF curve for head is two times steeper than the one for thorax or abdomen. At maximum impact energy of the DJI Phantom III at 200 J, BC predicts 0.2 and 0.08 probability of fatality for head and thorax/abdomen, respectively. Comparison of the BC curves with the RCC curves in Figure 5.1 shows that the BC curves show a much less steep slope than the RCC curves. The largest difference applies to the PoF curves for head; for the BC model this is much higher than the other two, while the RCC curve is clearly highest for thorax impact instead of head.

### 5.2.3. MBS Modelling and Simulation of DJI Phantom III Impact of Human Head

In automotive and aerospace crashworthiness analysis where an impact is highly dynamic with a range of structures interacting with the human body, multibody system (MBS) modeling is widely adopted [22-25]. These MBS models are only for blunt impact force evaluation, not for the modelling of penetration or laceration injuries. Based on this body of validated knowledge and simulation models, in Rattanagraikanakorn et al. [15] an MBS model of a DJI Phantom III impacting MBS of a human 50<sup>th</sup> percentile male body has been developed to simulate impact scenarios on the human head. The MBS model and its skeleton model structure is shown in Figure 5.4. This UAS MBS model consists of multiple lumped masses that are connected via restraint joints. Ellipsoid surface was modelled to realistically represent external surfaces of the UAS and to be used for contact detection.

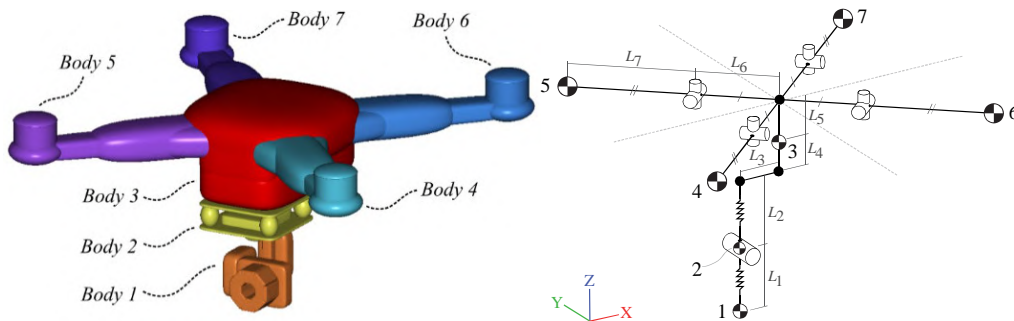


Figure 5.4. MBS model of the DJI Phantom III UAS (left), and the skeletons of the MBS model (right) [15]

To calibrate the MBS elements of the UAS model in Figure 5.4, the deformation of the structural components of the real DJI Phantom III system has systematically been measured during deformation experiments. These deformation tests yield curves of joint displacement as a function of restraining force (see Figure 3.3). Other important parameters such as restraint damping, or inertial properties were also measured experimentally.

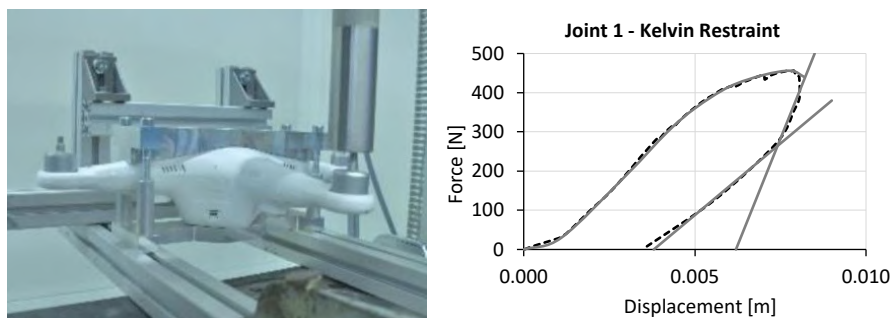


Figure 5.5. Examples of the compressive static test setup (left) for UAS structural members to determine joint restraint characteristics curves (right) used in model calibration [15]

The calibrated MBS model of DJI Phantom III has subsequently been integrated in MADYMO with a validated MBS model of the Hybrid III ATD. Subsequently, this integrated MBS model has been used to simulate the ASSURE DJI Phantom III UAS impact tests. Comparison of the MBS simulation results to the ASSURE measured data [13] showed that the response of the integrated MBS model was quite similar to the ASSURE measured data; a comparison is shown in Figure 5.6. The strong similarity in shape and strengths in dynamic responses showed that our MBS model of the DJI Phantom III and its integration within MADYMO was validated, and therefore judged to be ready for follow-on use to other impact studies than the one by ASSURE.

The first follow-on question we have addressed was: what would be the difference in the neck and head injury results when in the ASSURE drop tests the ATD of a human would have been replaced by a true human. Conducting such a test on a real human is not feasible, though such comparison can be done using MBS models of the two situations. Therefore, the validated MBS model of DJI Phantom III UAS has been integrated with a validated MBS model of a 50<sup>th</sup> percentile male human body. The latter was distributed with MADYMO 7.7 (filename: h\_occ50fc, version 5.2) and was published by Happee et al. [26,27], and has been validated for blunt impact on head, thorax, abdomen, and limbs [28]. This human body model can be seen in Figure 5.7. The comparison of these novel integrated MBS model simulations has shown that there is a discrepancy between the Hybrid III ATD and a human body model for head and neck injury [16,17]. Neck loads were found to be different fundamentally between the crash dummy and the human model. The human body sustains larger head injury, but lower neck injury compared to a crash dummy due to the different level of neck compliance between the two. This explains why neck injury assessed and presented in the ASSURE report [13] shows higher PoF from neck injury levels than to the head injury levels. Furthermore, MBS impact analysis on human body shows that the sustained neck injury from DJI Phantom III UAS vertical drop on human head is much lower than head injury.

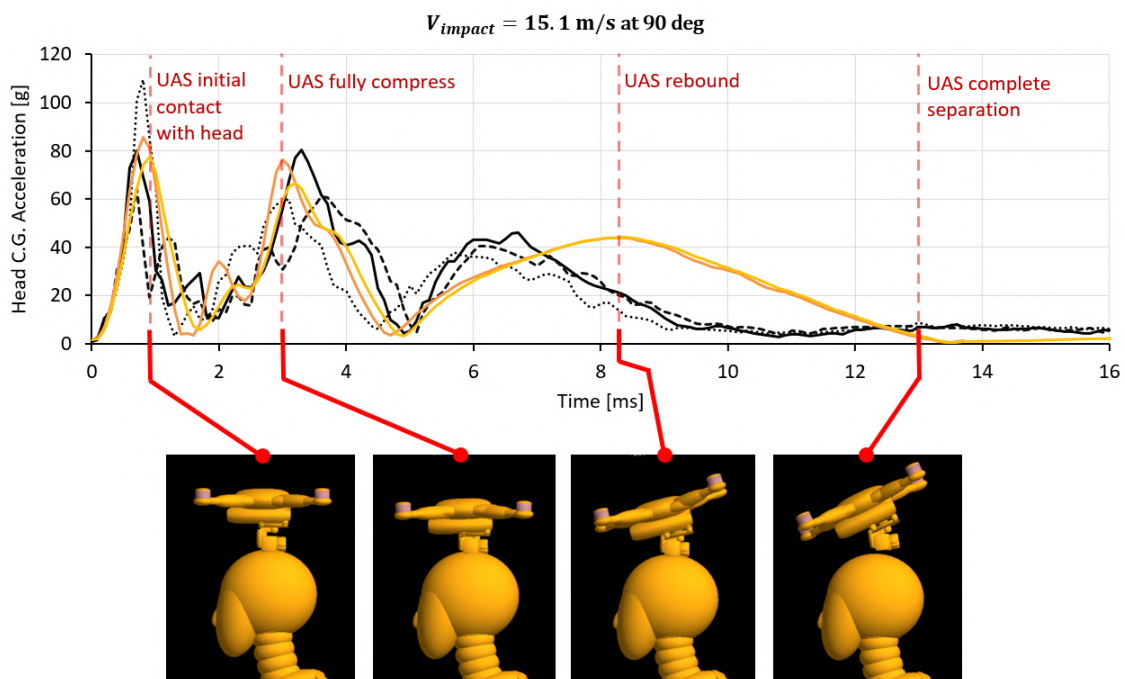


Figure 5.6. Example of validation results of the MBS model against ASSURE crash dummy impact test data at 15.1 m/s impact velocity and 90° (vertical) impact angle [15]

## 5.3 MBS Simulation-based Assessment of Head, Thorax and Abdomen Injury Criteria

In this section, the MBS model within MADYMO 7.7 of DJI Phantom III impact on 50<sup>th</sup> percentile human male body of the previous subsection is extended with injury criteria for thorax and abdomen. Subsequently, this extended MBS model is used for the simulation of UAS impact scenarios of head, thorax and abdomen.

### 5.3.1. DJI Phantom III UAS Impact Scenarios

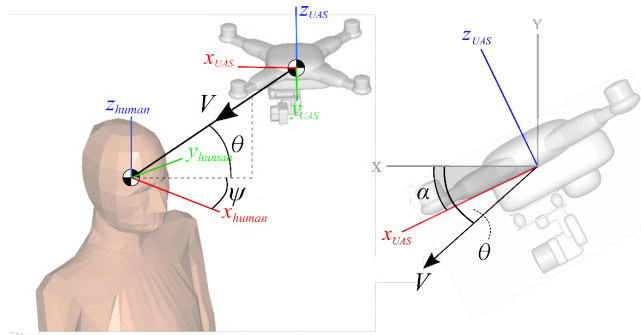
Impacts on head, thorax, and abdomen are evaluated and the simulation setup for each body part is presented in Figure 5.7. Head impact simulation is performed by varying multiple parameters to cover impact at three different impact conditions, which are frontal, side, and vertical drop impact. This is based on the knowledge that frontal and side-impact cases are the two worst impact cases that result in the highest *HIC* value based on the previous work [15]. Vertical drop is simulated to show the most optimistic impact case. Similarly, thorax and abdomen impact simulations are set up to evaluate the worst impact case. For both thorax and abdomen impact, frontal impact was setup where UAS fly directly into the body parts at various impact speed.

Head impact injury due to UAS is evaluated based on the setup in Figure 5.7(a). There are three setup parameters for impact to the head, namely: impact direction ( $\psi$ ), impact elevation ( $\theta$ ), and impact velocity ( $V$ ). In this work, three head impact cases are evaluated and the setup parameters are listed Table 5.3.

Table 5.3. Setup parameters for head impact cases

Impact Case	$\psi$ [deg]	$\theta$ [deg]	$V$ [m/s]
Frontal Impact	0	0	0 - 32
Side Impact	90	0	(equivalent to impact energy of 0
Vertical Drop	0	90	- 630 J)

(a) Head Impact Setup



(b) Thorax Impact Setup

(c) Abdomen Impact Setup

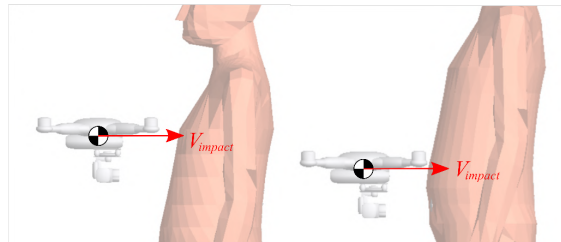
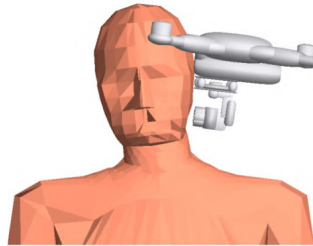


Figure 5.7. MBS impact model setup in MADYMO

The frontal impact case simulates a UAS flying horizontally into the front of the human head. Side impact also simulates horizontal flight, but onto the side of the human head. Frontal and side-impact cases both have the front fuselage as the first point of contact and are considered as two worst impact cases. A snapshot of the maximum head deflection/deformation for side impact of the head at impact energy of 196 J is pictured in Figure 5.8.



**Figure 5.8. MBS impact simulation results at maximum body part deflection/deformation for side impact on the head at 196 J impact energy**

For vertical drop, a UAS is dropped vertically with a fixed angle of attack of 0 degrees. This simulates a straight fall due to the complete power shut-down of a UAS. However, the vertical impact case has the camera gimbal underneath the UAS as the first point of contact. For all three cases, impact velocity ( $V$ ) is varied from 0 to 32 m/s with a 2 m/s increment. This velocity range is equivalent to an impact energy of 0 to 630 J.

To measure injury level from UAS impact, Head Injury Criterion ( $HIC$ ) is used for head impact, and Viscous Criterion ( $VC$ ) is used for thorax and abdomen impacts. These injury criteria have been used within the MBS simulations. In the next subsections these injury criteria are explained together with the obtained MBS simulation results for the impact scenarios for head, and thorax/abdomen respectively.

### 5.3.2. Head Injury Criteria and MBS Simulation Results

To assess head injury from the UAS impact, the head injury criterion ( $HIC$ ) is used. In particular,  $HIC_{15}$  was implemented as it is suitable for short duration impact (The value 15 refers to the 15 ms time-period starting from the moment of impact). Functionally, the  $HIC$  is an integrated value of the head acceleration curve and represents the peak average power delivered to the head [29]. Based on the Federal Motor Vehicle Safety Standards (FMVSS), a  $HIC_{15}$  value of 700 is considered to be a minimum safety standard for non-fatal impact [30]. The equations for the  $HIC$  is:

$$HIC_{(t_2-t_1)} = \max_{T_0 \leq t_1 < t_2 \leq T_E} \left\{ (t_2 - t_1) \left[ \frac{1}{t_2 - t_1} \int_{t_1}^{t_2} a(t) dt \right]^{2.5} \right\} \quad (5.6)$$

where  $a(t)$  is the head acceleration-time history curve,  $t_1$  is the initial impact time and  $t_2$  is the final impact time.

The simulation results of the head impact on the human body for three impact cases are shown in Figure 5.9. The simulation results show that  $HIC_{15}$  increases with impact energy. Side impact case on the head results in the worst impact case, while frontal impact case also results in severe injury. Vertical drop case, on the other hand, differs significantly from the other curves due to soft impact point.

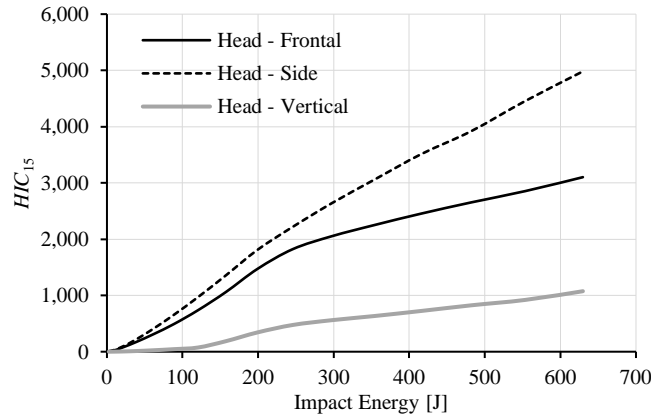


Figure 5.9.  $HIC_{15}$  results for head impact injury from MBS model

### 5.3.3. Thorax and Abdomen Impact Criteria and MBS Simulation Results

Thorax and abdomen present a large portion of the body area and can also be vulnerable to blunt impact force. UAS impact simulation setups on the thorax and abdomen are presented in Figure 5.7(b) and Figure 5.7(c), respectively. For thorax and abdomen, there is one setup parameter varied that is impact velocity ( $V$ ) which is set 0 to 36 m/s with 2 m/s increment. This velocity range is equivalent to impact energy from 0 to 800 J. Only frontal impact cases are evaluated for both thorax and abdomen. This is assumed to be the worst impact case since the velocity vector is normal to the coronal plane of the human body. For impact on the thorax, UAS is placed to collide directly on the sternum. For impact on the abdomen, UAS is placed to collide directly on the mid-abdomen location. These are the common impact locations for thorax and abdomen blunt impact evaluation.

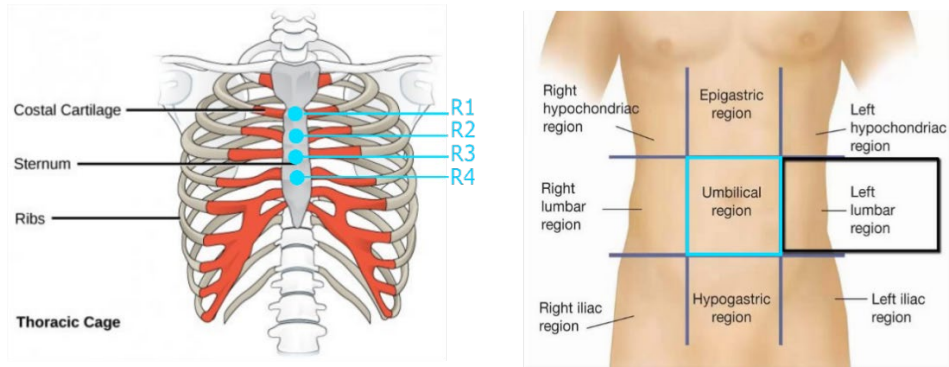
For thorax and abdomen injury evaluation, this paper employs the Viscous Criterion ( $VC$ ) which is also called the soft tissue criterion. This injury criterion takes into account that soft tissue injury is compression-dependent and rate-dependent [31]. It is a measure of the maximum momentary product of deformation speed and deformation of thorax and abdomen. Hence, for an arbitrary body part  $B$ ,  $VC_B$  satisfies:

$$VC_B(t, r) = \max_{t, r} [V_B(t, r) \times C_B(t, r)] \quad (5.7)$$

where  $V_B(t, r)$  is the deformation speed of body part  $B$  at moment  $t$  and at location  $r$  and  $C_B(t, r)$  is the compression in the percentage of the thickness of body part  $B$  at moment  $t$  and at location  $r$ . A  $VC$  value of 1.0 m/s is equivalent to 25% of  $p(AIS \geq 4)$ ; a  $VC$  of 1.3 m/s is equivalent to 50% of  $p(AIS \geq 4)$  [18].

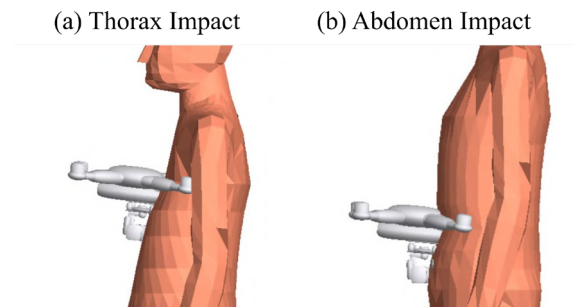
For body parts thorax and abdomen, this  $VC$  injury criterion is applicable to both frontal impact and side impact. For thorax, compression speed  $V_B(t, r)$  and compression  $C_B(t, r)$  are measured from the start of impact (i.e.  $t = 0$ ) at sternum ribs  $r = R1, \dots, R4$  as is illustrated in Figure 5.10. These are the location for the middle center of the thorax. For abdomen  $V_B(t, r)$  and  $C_B(t, r)$  are measured from the start of impact on a single point at the mid-abdomen location (or center of the umbilical region).



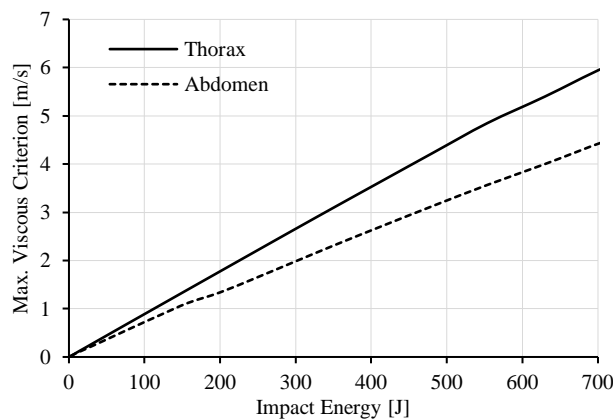


**Figure 5.10.** Measuring location for thorax VC (left) at sternum rib R1 to R4 and for abdomen VC (right) at the center of the umbilical region (or mid-abdomen) [32]

The maximum VC injury criteria given in Equation 5.7 has been implemented in the MADYMO simulation for thorax and abdomen impacts. Figure 5.11 shows the MBS simulated positions of DJI Phantom and human body at the moment of maximum compression states. The maximum VC simulation results obtained for the thorax and abdomen impact scenarios of a DJI Phantom III UAS are shown in Figure 5.12 for a range of possible UAS impact velocities.



**Figure 5.11.** MBS impact simulation results at maximum compression for (a) thorax and (b) abdomen at 196 J impact energy



**Figure 5.12.** Maximum Viscous Criterion (VC) results for thorax and abdomen impact injury from MBS model

The maximum VC curves in Figure 5.12 show that DJI Phantom III UAS impact on thorax results in a steeper VC curve when compared to the abdomen. Because the injury criteria for head differ from the VC criteria used for thorax and abdomen, a direct comparison of the curves in Figure 5.12 with those for head in Figure 5.9 is of no use. Such comparison will be made feasible by identifying appropriate transformations of the curves in Figure 5.9 and Figure 5.12 to PoF curves. This is addressed in the next section.

## 5.4 Mapping Injury Criteria to Probability of Fatality

Injury criteria for head, thorax, and abdomen presents injury severity due to blunt force impact, however, these do not present the probability of fatality. Thus, a mapping of injury criterion to the probability of fatality is needed in order to predict the fatality rate of humans on the ground due to UAS impact.

### 5.4.1. Probability of Fatality Curve for Head impact

For the head injury criterion (*HIC*), a transformational curve from the *HIC* threshold to the percentage of life-threatening injury is proposed by the U.S. ISO Delegation as shown in Figure 5.13. The curve is derived from the Prasad and Mertz injury risk curve [33]. This percentage of life-threatening injury is equivalent to the probability of fatality. Using this curve, the *HIC* values at different impact energy from Figure 5.9 for different head impact scenarios are converted to a probability of fatality as shown in Figure 5.14.

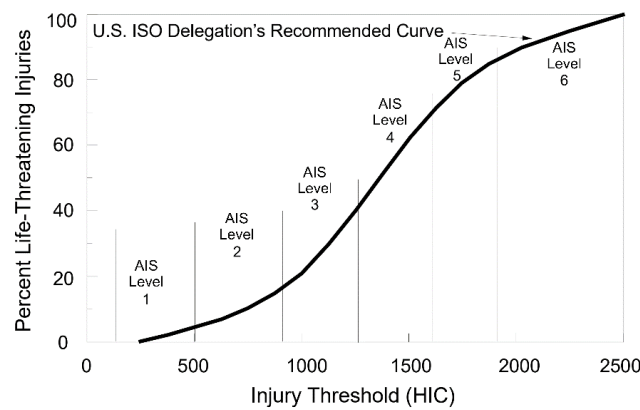


Figure 5.13. Relationship between head injury criteria and percentage of life-threatening injury recommended by U.S. ISO delegation [34] which is derived from the Prasad and Mertz injury risk curve [33]

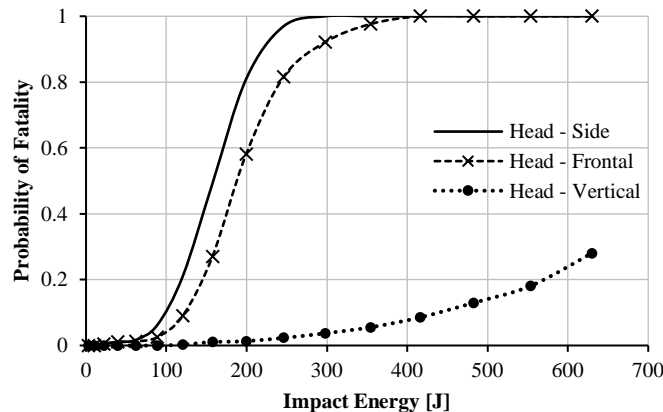


Figure 5.14. Fatality risk curves of UAS impact on the human head at different impact energy for 50<sup>th</sup> percentile male and for the side, frontal and vertical drop impact cases

The results from the MBS simulation show that frontal and side impact result in similar PoF, which is much more severe than a vertical drop. Both frontal and side impact curves form an S-curve where PoF gradually increases with impact energy. At impact energy of 200 J which is the estimated maximum impact energy of the DJI Phantom III, PoF of frontal and side are 0.6 and 0.8, respectively. Side impact leads to a more fatal impact when compared to frontal impact because of the way the neck complex plays a role in absorbing impact energy. Impact energy can be absorbed from the head more by neck complex when impact direction



falls within the sagittal plane of the human body – this leads to low head acceleration and *HIC* levels.

The vertical drop impact case from the MBS, on the other hand, results in a substantially lower PoF when compared to MBS frontal, and side impacts. The lower curve in Figure 5.13 shows that at 200 J of impact energy, PoF from the vertical drop impact case is approximately 0.013. Also, with the increasing impact energy, PoF for vertical drop impact rises with much less slope when compared to other impact cases. This low PoF is a result of having a camera gimbal as the first point of contact. A camera gimbal underneath the UAS acts like a spring-damper system which absorbs impact energy effectively.

The results of the MBS simulation in Figure 5.14 make very clear that the PoF due to a UAS impact on a human head strongly depends on the specific scenario. The lowest curve in represents the vertical drop on the head scenario that has been considered by the ASSURE drop tests; though now for a 50<sup>th</sup> percentile male human body instead of the Hybrid III ATD. The two curves with much higher PoF values represent possible case of side or frontal head impact by a flyaway DJI Phantom III UAS. In addition to this, a quadcopter falling trajectory simulation under off-nominal flight conditions performed by Foster and Hartman [35] reveals that quadcopter tends to fall with a high and unpredictable angular rate. This tumbling effect of a quadcopter before colliding into the ground leads to various possible impact attitudes that a quadcopter can impact on a human head. If a DJI Phantom III collides with the main front fuselage, instead of the camera gimbal then the PoF value is expected to be much higher than it is for the vertical drop scenario. The MBS model makes it possible to simulate all possible DJI Phantom III attitudes at moment of head impact.

#### 5.4.2. Probability of Fatality Curves for Thorax & Abdomen Impact

The Viscous Criterion (*VC*) for thorax and abdomen injury has no direct transformational curve from *VC* to the probability of fatality. Nevertheless, the transformation of *VC* to the probability of fatality is possible. This is done by, first, converting viscous criterion to *AIS* scale using a conversion curve shown in Figure 5.15. The curve is proposed by Sturdivan et al. [18] who performed an analysis of *VC* for thorax and abdomen. This curve is based on a blunt impact experiment on cadavers performed by Canavaugh et al. [36] and Viano et al. [37].

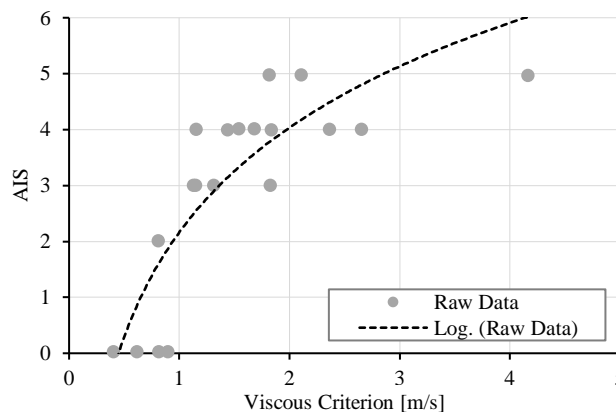


Figure 5.15. Relationship between Viscous Criterion and AIS [18] from thoracic and abdominal blunt impact, derived from cadaver impact data performed by Canavaugh et al. [36] and Viano et al. [37]

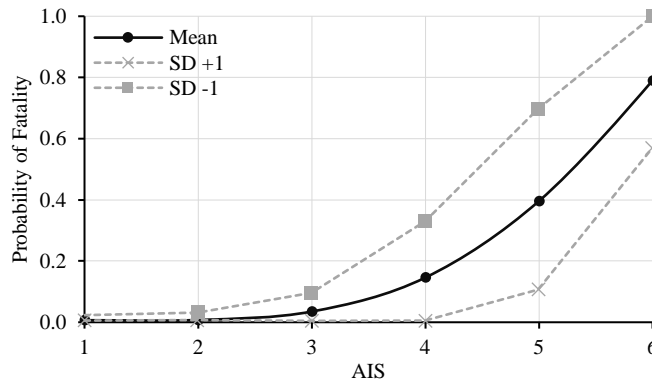


Figure 5.16. Transformation curve of single injury AIS scale to the probability of fatality presented in the AIS 2005 revision document [38]

The next step is to transform the *AIS* level that is obtained from *VC-AIS* conversion into a PoF using the *AIS* to fatality rate curve presented in Figure 5.16. This curve is a transformational curve of single injury that is derived from a collection of real-world trauma injury data presented in the AIS 2005 revision document [38]. Application of these two transformations to the MBS based BC curves in Figure 5.11 yields the MBS based PoF curves for thorax and abdomen in Figure 5.17. The MBS simulation based PoF curves in Figure 5.17 show that the impact on thorax is less fatal than the frontal or side impacts on the head as is shown in Figure 5.14. At impact energy of 200 J, the MBS model based PoF value for frontal impact on the head is approximately 8 times higher than the PoF value for impact on thorax.

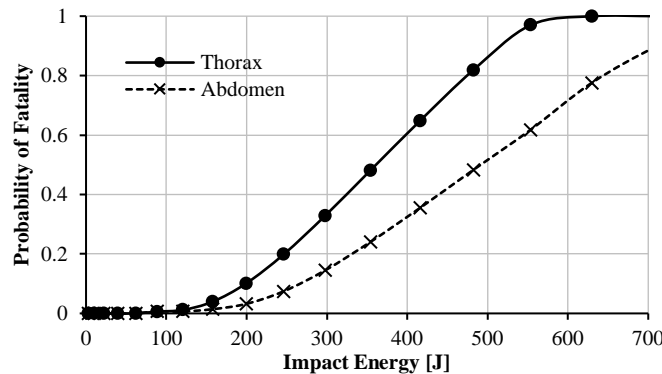


Figure 5.17. PoF curves of UAS impact on thorax and abdomen at different impact energy for 50<sup>th</sup> percentile male

## 5.5 Comparison of Fatality Curves from Different Models

This section compares the PoF curves in Figure 5.14 and Figure 5.17 with those of the RCC and BC models. This is done for head, thorax and abdomen in subsections A, B, and C respectively.

### 5.5.1. Comparison of PoF of Head Impact

In Figure 5.18, the PoF curves from MBS head impact simulation from Figure 5.14 are compared against the RCC and BC curves. Figure 5.18 shows that both the MBS based PoF curves for frontal and side impact of head and the RCC based PoF curves are S-shaped, though their 10%, 50% and 90% points differ significantly. When the RCC curve has reached the 90% point then the MBS based curves for side and frontal head impacts are around 10% only. The BC curve is not an S-shaped curve, instead it increases more linear with impact energy. As has been explained in subsection V.A the MBS based PoF curve for vertical drop shows the lowest fatality risk.

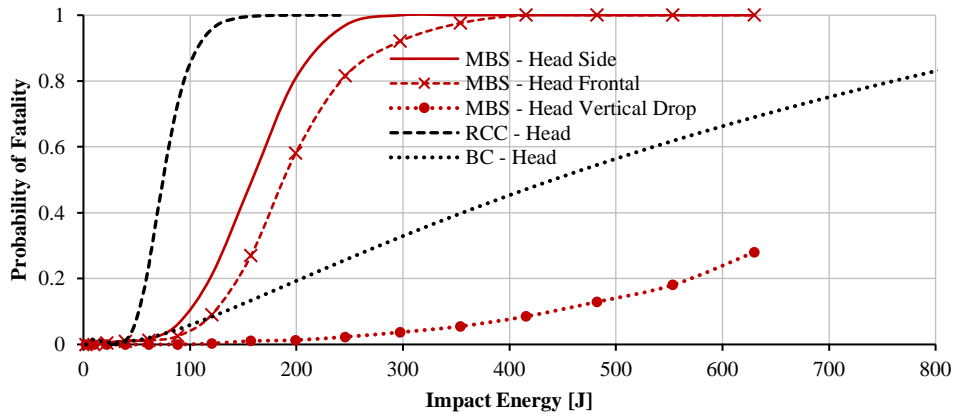


Figure 5.18. Comparison of PoF curves for head impact between MBS (frontal, side and vertical drop cases), RCC, and BC.

From the MBS model results, it becomes clear that PoF of UAS impact of head can have a large difference between upper and lower bound curves. From the three scenarios considered, in this paper, head frontal impact represents the upper bound of the possible fatality risk while head vertical drop impact represents the lower bound. This variation is not captured by the RCC model, and neither by the BC model. From the perspective of the vertical drop on a human head, Figure 5.18 shows that both the RCC curve and the BC curve overestimate the PoF. From the perspective of a side or frontal impact the RCC curve again overestimates the PoF, while the BC curve underestimates the PoF. Therefore, the main finding for UAS impact of human head is that where the RCC and BC curves for PoF do not represent differences in impact geometry, the PoF curves obtained through MBS simulation show significant differences for the three different head impact scenarios for frontal, side, and vertical drop respectively.

### 5.5.2. Comparison of PoF of Thorax Impact

The PoF curves obtained for impact on thorax from MBS, RCC, and BC models, from Figure 5.17, Figure 5.1 and Figure 5.3 respectively, are collected in Figure 5.19. Similar to side or frontal head impact, the PoF values of the RCC curve are much higher than the PoF values for the MBS model; though now the difference is even much larger. Both MBS and RCC curves for impact on thorax are S-shaped; though the 10%, 50% and 90% points of the MBS curve are at much higher kinetic energy levels than the 10%, 50% and 90% of the RCC curve. Again, the BC curve increases more linear with impact energy and has beyond the 10% point a less steep slope than the MBS curve has.

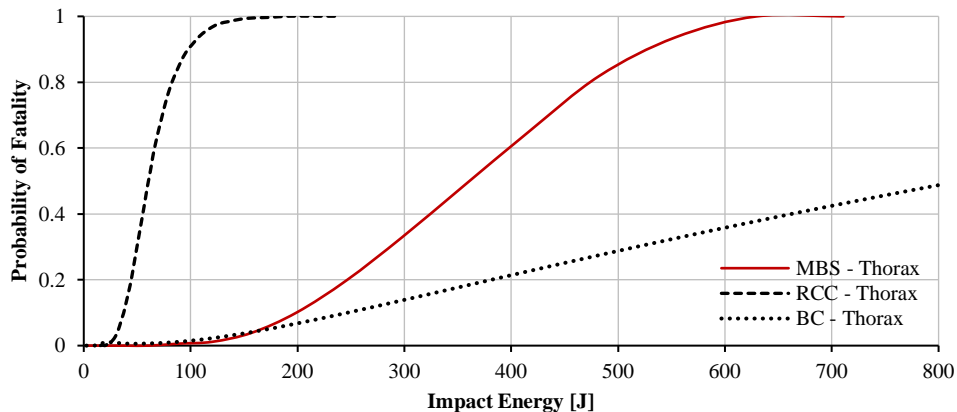


Figure 5.19. Comparison of PoF curves for thorax impact between MBS, RCC, and BC models

MBS PoF curve increases steadily between impact energy from approximately 250 J to 450 J. Due to its steep slope, this range of steady increase is much smaller for the RCC curve and have energy values between 40 J – 70 J. At maximum impact energy for the DJI Phantom III at 200 J, PoF predicted by the RCC model is 1.0, meaning that fatality from impact on thorax is certain. This is different for the MBS and BC models where PoF at 200 J impact energy is 0.1 and 0.07, respectively. Based on this difference at 200 J impact energy, RCC predicts PoF 10 times higher compared to MBS models.

### 5.5.3. Comparison of PoF of Abdomen Impact

The results of PoF curves of impact on the abdomen from MBS, RCC, and BC models, from Figure 5.17, Figure 5.1 and Figure 5.3 respectively, are collected in Figure 5.20. For impact on the abdomen, the RCC and MBS models, again, form an S-curve pattern; again the 10%, 50% and 90% points are much lower for RCC curve than for the MBS based curve. Similar as for thorax, the BC curve increase more linear with impact energy, and is much lower than the MS curve for probabilities above 10%.

PoF at 100 J impact energy by DJI Phantom III is 0.27 for the RCC model, but close to 0 for the MBS and BC models. This means that the MBS and BC models predict that UAS impact on the abdomen will not likely result in fatality at 100 J impact energy. At 200 J impact energy which is the maximum energy for DJI Phantom III, PoF predict by the MBS model is 0.05. This is lower than the BC model which predicts 0.07 PoF at the same impact energy. The MBS PoF curve is below the BC curve from 0 J to approximately 295 J. Then, the MBS PoF curve rises and crosses above the BC model after 295 J with substantially higher slope.

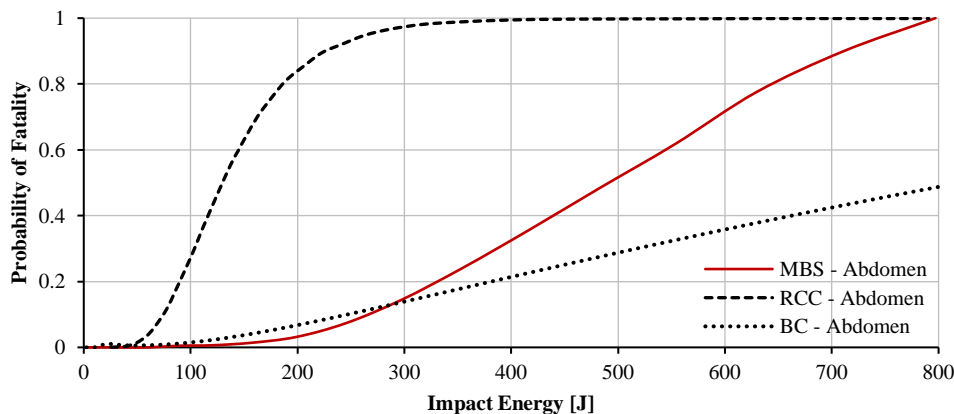


Figure 5.20. Comparison of PoF curves for abdomen impact between MBS, RCC, and BC models

## 5.6 Discussion of Results

Modelling PoF due to UAS impact is crucial in the analysis of UAS ground risk. Simulation of a validated MBS model of DJI Phantom III UAS impact on a validated MBS model of 50<sup>th</sup> percentile male human body offers the capability to simulate the impact on different parts of the human body. MBS simulations of DJI Phantom III impact on head, thorax and abdomen shows that the riskiest impact case on the head presents much higher fatality risks when compared to the riskiest impact case on thorax or abdomen. This trend is the same for the BC model but differs for the RCC model. In the RCC model, impact injury on thorax presents a higher PoF than impact on abdomen, though also higher than side or frontal impact on the head. Explanation of the differences is that the RCC curve is derived from hazardous debris experimentation with the original purpose of determining the fatality risk curve of ground personal due to missile explosions. Such type of small debris explosive injury does not

only result in blunt force trauma but also penetration or laceration-type injuries. On the other hand, the MBS impact model and BC model are created or derived specifically for blunt impact injury where soft tissue penetration is not involved. For instance, the BC model was developed based on impact tests on cadavers and animals where the diameter of the impactor is much larger than small debris explosion as mentioned in Feinsein's work. Similarly, the MBS impact model of a DJI Phantom III UAS developed and validated against real-world impact tests on the Hybrid III crash dummy where only blunt force injury is evaluated.

RCC model tends to predict a high probability of fatality at low impact energy. For example, the probability of the fatality of head impact is at 0.8 at 100 Joules impact energy. Given that the DJI Phantom III maximum kinetic energy is approximately 200 Joules, this means that fatality is very likely even if the UAS impact at half of its kinetic energy. RCC model predicts too high PoF values. On the other end of the spectrum, BC predicts the probability of fatality of head impact 0.2 at 200 Joules of impact energy. When compared to the MBS model, above 10% values, BC predicts too low PoF values. The limitations of the RCC standard are rooted in the fundamental assumptions made to generate the curves and the basis for the probability of fatality data. For instance, the RCC curves were developed from Feinsein's work and employed weightings for hypervelocity type collisions where the debris contained a larger number of low mass fragments [13]. Also, input data that formed Feinsein curves involved largely vertical falling inert debris since it was assumed the breakup or collisions would occur from a high altitude above the personal. Therefore, the analysis shows that the RCC is not a suitable curve to be used for UAS blunt impact on human body.

Furthermore, what the MBS model show is that the probability of fatality depends significantly on impact attitude and point of contact of the UAS as shown in Figure 5.18. Side impact results in the steepest fatality curve when compared to frontal impact or vertical drop because the human neck complex can absorb less impact energy in a lateral direction. In the vertical drop case, the fatality curve drops significantly even lower than thorax and abdomen impact cases. This is due to the point of contact for the vertical drop is the camera gimbal system which acts like a spring-damper that absorbs a significant amount of impact energy. This illustrates that single PoF curve models such as the RCC or BC models, do not capture this effect due to the variation of impact attitude of a DJI Phantom III UAS.

## 5.7 Conclusions

Risk analysis of UAS ground impact on humans is important to the future developments of UAS operations. An important step to take is to understand fatality of UAS impact on human on the ground. In this paper, a multi-body system impact model of the DJI Phantom III UAS is presented and compared against RCC impact model and Blunt Criterion model. The comparison is done for impacts on the head, thorax, and abdomen of a 50<sup>th</sup> percentile male human. The results show significant differences between the three models in terms of the probability of fatality. RCC model predicts a very high probability of fatality at very low impact energy when compared against MBS or BC model. On the optimistic end of the spectrum, the BC model predicts the lowest probability of fatality when compared to other models. The MBS model shows large variations in PoF for impact on the head. This large variation comes from different impact attitudes. The by far worst impact case from the MBS simulations yields a PoF curve that means more safety than the corresponding RCC curve. The by far the best impact case from the MBS was the DJI Phantom III vertical drop scenario that was also measured by ASSURE.

Furthermore, the MBS and BC model predicts higher fatality for head impact compared to thorax and abdomen. RCC curves, however, predict higher fatality for thorax than the head and abdomen. The differences stem from the fact that the RCC model was derived based on injury or fatality due to small debris explosion, which also involves penetration or laceration type injuries. MBS and BC model, in contrast, were developed purely on blunt force impact.

Taking all results together, it is concluded that thanks to the MBS modelling and simulation of DJI Phantom III UAS impact on human head, thorax and abdomen, it is now possible to understand why there are such differences between the RCC model, the BC model and the ASSURE measurements.

As follow-on research, the aim is to use the validated MBS model simulation as a replacement of the RCC and BC models that have so far been used in other works [1–7] on assessing third party risk that is posed by UAS operations to persons on the ground. As has been explained in the introduction, this asks for integration of MBS model simulation with four other models, i.e.: Frequency of a UAS ground crash; Density map of rural or urban population; Shelter protection map; and Model for the probability that an unprotected person on the ground is impacted by the crashing UAS. This MBS approach also allows to consider other variations, such as effect of human body sizes that are available within MADYMO, namely, 5<sup>th</sup> percentile female, 50<sup>th</sup> percentile male, and 95<sup>th</sup> percentile male.

## References

- [1] Dalamagkidis, K., Valavanis, K., and Piegler, L., “On Integrating Unmanned Aircraft Systems into the National Airspace System,” Springer Netherlands, 2012, doi: 10.1007/978-94-007-2479-2.
- [2] Melnyk, R., Schrage, D., Volovoi, V., and Jimenez, H., “A third-party casualty risk model for unmanned aircraft system operations,” *Reliability Engineering and System Safety*, vol. 124, 2014, pp. 105–116, doi: 10.1016/j.res.2013.11.016, URL: <http://dx.doi.org/10.1016/j.res.2013.11.016>.
- [3] Ancel, E., Capristan, F. M., Foster, J. V., and Condotta, R. C., “Real-time Risk Assessment Framework for Unmanned Aircraft System (UAS) Traffic Management (UTM),” 17th AIAA Aviation Technology, Integration, and Operations Conference, Denver, Colorado, 2017, pp. 1–17, doi: 10.2514/6.2017-3273, URL: <https://arc.aiaa.org/doi/10.2514/6.2017-3273>.
- [4] Bertrand, S., Raballand, N., Viguiere, F., and Muller, F., “Ground risk assessment for long-range inspection missions of railways by UAVs,” 2017 International Conference on Unmanned Aircraft Systems, ICUAS 2017, 2017, pp. 1343–1351, doi: 10.1109/ICUAS.2017.7991331.
- [5] la Cour-Harbo, A., “Quantifying Risk of Ground Impact Fatalities for Small Unmanned Aircraft,” *Journal of Intelligent and Robotic Systems: Theory and Applications*, vol. 93, 2019, pp. 367–384, doi: 10.1007/s10846-018-0853-1.
- [6] Rudnick-Cohen, E., Herrmann, J. W., and Azarm, S., “Modeling Unmanned Aerial System (UAS) Risks via Monte Carlo Simulation,” 2019 International Conference on Unmanned Aircraft Systems (ICUAS), 2019, pp. 1296–1305, doi: 10.1109/icuas.2019.8798313.

- [7] Primatesta, S., Rizzo, A., and la Cour-Harbo, A., “Ground Risk Map for Unmanned Aircraft in Urban Environments,” *Journal of Intelligent and Robotic Systems: Theory and Applications*, 2019, doi: 10.1007/s10846-019-01015-z.
- [8] RCC, “Common risk criteria for National test ranges; Inert debris, Supplement to Standard 321-00,” 2000.
- [9] Feinstein, D., Haugel, W., Kardatzke, M., and Weinstock, A., “Personnel Casualty Study. Tech. Rep. Project No. J 6067,” 1968.
- [10] Magister, T., “The small unmanned aircraft blunt criterion based injury potential estimation,” *Safety Science*, vol. 48, 2010, pp. 1313–1320, doi: 10.1016/j.ssci.2010.04.012, URL: <http://dx.doi.org/10.1016/j.ssci.2010.04.012>.
- [11] Sturdivan, L. M., “Modeling in Blunt Trauma Research,” *Proceedings of the Second Annual Soft Body Armor Symposium*, Miami, Beach Florida: Washington DC: Law Enforcement Assistance Agency, U.S. Department of Justice, 1976.
- [12] Sturdivan, L. M., “Non-Lethal Weapons Assessment: Deterrence and Injury - Final Report. Contract M67854-99-M-1062,” Quantico, VA: 2000.
- [13] Arterburn, D., Ewing, M., Prabhu, R., Zhu, F., and Francis, D., “FAA UAS Center of Excellence Task A4 : UAS Ground Collision Severity Evaluation,” Huntsville: 2017, URL: [http://www.assureuas.org/projects/deliverables/a4/ASSURE\\_A4\\_Final\\_Report\\_UAS\\_Ground\\_Collision\\_Severity\\_Evaluation.pdf](http://www.assureuas.org/projects/deliverables/a4/ASSURE_A4_Final_Report_UAS_Ground_Collision_Severity_Evaluation.pdf).
- [14] Alliance for System Safety of UAS through Research Excellence, “ASSURE UAS Ground Collision Severity Evaluation Final Report” URL <http://www.assureuas.org/projects/deliverables/sUASGroundCollisionReport.php>.
- [15] Rattanagraikanakorn, B., Gransden, D. I., Schuurman, M., De Wagter, C., Happee, R., Sharpanskykh, A., and Blom, H. A. P., “Multibody system modelling of unmanned aircraft system collisions with the human head,” *International Journal of Crashworthiness*, vol. 25, 2020, pp. 689-707, doi: 10.1080/13588265.2019.1633818, URL: <https://doi.org/10.1080/13588265.2019.1633818>.
- [16] Rattanagraikanakorn, B., Schuurman, M. J., Gransden, D. I., Happee, R., Wagter, C. De, Sharpanskykh, A., and Blom, H. A., “Modelling Head Injury due to Unmanned Aircraft Systems Collision: Crash Dummy vs Human Body,” *AIAA Aviation 2019 Forum*, Dallas, Texas: 2019, doi: 10.2514/6.2019-2835, URL: <https://arc.aiaa.org/doi/abs/10.2514/6.2019-2835>.
- [17] Rattanagraikanakorn, B., Schuurman, M., Gransden, D. I., Happee, R., Wagter, C. De, Sharpanskykh, A., and Blom, H. A. P., “Modelling Head Injury due to Unmanned Aircraft Systems Collision: Crash Dummy vs Human Body,” *International Journal of Crashworthiness* (Submitted for publication), 2020.
- [18] Sturdivan, L. M., Viano, D. C., and Champion, H. R., “Analysis of Injury Criteria to Assess Chest and Abdominal Injury Risks in Blunt and Ballistic Impacts,” *Journal of Trauma - Injury, Infection and Critical Care*, vol. 56, 2004, pp. 651–663, doi: 10.1097/01.TA.0000074108.36517.D4.
- [19] Clare, V., and Sturdivan, L. M., “Blunt Trauma Data Correlation,” 1975.
- [20] Civil Aviation Safety/Monash University, “Human Injury Model for Small Unmanned Aircraft Impacts,” 2013.

- [21] Raymond, D., Van Ee, C., and Bir, C., “Tolerance of the skull to blunt ballistic temporo-parietal impact,” *Journal of Biomechanics*, vol. 42, 2009, pp. 2479–2485.
- [22] Vadlamudi, S., Blundell, M., and Zhang, Y., “A multi-body systems approach to simulate helicopter occupant protection systems,” *International Journal of Crashworthiness*, vol. 16, 2011, pp. 207–218, doi: 10.1080/13588265.2011.554203.
- [23] Jenefeldt, F., and Thomson, R., “A methodology to assess frontal stiffness to improve crash compatibility,” *International Journal of Crashworthiness*, vol. 9, 2004, pp. 475–482, doi: 10.1533/ijcr.2004.0303.
- [24] Mukherjee, S., Chawla, A., Nayak, A., and Mohan, D., “Rollover crashworthiness of a rural transport vehicle using MADYMO,” *International Journal of Crashworthiness*, vol. 11, 2006, pp. 495–503, doi: 10.1533/ijcr.2005.0121.
- [25] Ambrósio, J., and Dias, J., “A road vehicle multibody model for crash simulation based on the plastic hinges approach to structural deformations,” *International Journal of Crashworthiness*, vol. 12, 2007, pp. 77–92, doi: 10.1533/ijcr.2006.0171.
- [26] Happee, R., Hoofman, M., Van Den Kroonenberg, A. J., Morsink, P., and Wismans, J., “A Mathematical Human Body Model for Frontal and Rearward Seated Automotive Impact Loading,” SAE Technical paper, 1998, doi: 10.4271/983150.
- [27] Happee, R., and Ridella, S., “Mathematical human body models representing a mid size male and a small female for frontal, lateral and rearward impact loading,” IRCOBI Conference Proceedings, 2000, pp. 1–18, doi: 10.1378/chest.120.6\_suppl.464S.
- [28] TASS International, “Human Body Models Manual Version 7.7,” 2017.
- [29] Hutchinson, J., Kaiser, M. J., and Lankarani, M., “The Head Injury Criterion ( HIC ) functional,” *Journal of Applied Mathematics and Computation*, 1998.
- [30] Eppinger, R., Sun, E., Bandak, F., Haffner, M., Khaewpong, N., Maltese, M., Kuppa, S., Nguyen, T., Takhounts, E., Tannous, R., Zhang, A., and Saul, R., “Development of Improved Injury Criteria for the Assessment of Advanced Automotive Restraint Systems - II By,” 1999, URL: [https://www.nhtsa.gov/sites/nhtsa.dot.gov/files/rev\\_criteria.pdf](https://www.nhtsa.gov/sites/nhtsa.dot.gov/files/rev_criteria.pdf).
- [31] Lau, I. V., and Viano, D. C., “The viscous criterion - Bases and applications of an injury severity index for soft tissues,” SAE Technical Papers, vol. 95, 1986, pp. 672–691, doi: 10.4271/861882.
- [32] Schmitt, K.-U., Niederer, P. F., Cronin, D. S., Morrison III, B., Muser, M. H., and Walz, F., “Trauma Biomechanics,” 2019, doi: 10.1007/978-3-030-11659-0.
- [33] Prasad, P., and Mertz, H. J., “The Position of the United States Delegation to the ISO Working Group 6 on the Use of HIC in the Automotive Environment,” SAE Technical Papers, 1985, doi: 10.4271/851246.
- [34] Tyrell, D. C., Severson, K. J., and Marquis, B. P., “Analysis of occupant protection strategies in train collisions,” American Society of Mechanical Engineers, Applied Mechanics Division, AMD, vol. 210, 1995, pp. 539–557.
- [35] Foster, J. V., and Hartman, D., “High-Fidelity Multi-Rotor Unmanned Aircraft System (UAS) Simulation Development for Trajectory Prediction Under Off-Nominal Flight Dynamics,” 17th AIAA Aviation Technology, Integration, and Operations Conference, 2017, pp. 1–19, doi: 10.2514/6.2017-3271, URL: <https://arc.aiaa.org/doi/10.2514/6.2017-3271>.



- [36] Cavanaugh, J. M., Walilko, T. J., Malhotra, A., Zhu, Y., and King, A. I., “Biomechanical response and injury tolerance of the pelvis in twelve sled side impacts,” SAE Technical Papers, vol. 99, 1990, pp. 1678–1693, doi: 10.4271/902305.
- [37] Viano, D. C., Lau, I. V., Asbury, C., King, A. I., and Begeman, P., “Biomechanics of the human chest, abdomen, and pelvis in lateral impact,” Accident Analysis and Prevention, vol. 21, 1989, pp. 553–574, doi: 10.1016/0001-4575(89)90070-5.
- [38] Gennarelli, T. A., and Wodzin, E., “AIS 2005: A contemporary injury scale,” Injury, vol. 37, 2006, pp. 1083–1091, doi: 10.1016/j.injury.2006.07.009.



---

## Variation in Human Injury and Fatality from Impacts by Different UAS Types of Similar Weight

*As new UAS operational concepts are established and more UAS populate the airspace, there is a need to understand and quantify consequences of UAS impact on human on the ground. Common practice is regulation is to make use of weight criteria for the classification of different UAS types. Through a Finite Element (FE) model study of small UAS impact on human head, thresholds for these weight categories have also been assessed. The aim of this paper is to evaluate the effect of other UAS characteristics on fatality risk. In earlier work by the authors, it has been shown that multibody system (MBS) modelling and simulation allows to assess the injury and fatality levels of the impact of a DJI Phantom III UAS on human. The current paper uses this MBS modelling and simulation approach for the evaluation of impact consequences under different UAS characteristics. This is done for five UAS types carrying a camera, one of which is DJI Phantom III. Two new UAS types are of similar weight as DJI Phantom III and two have half this weight. These five cover a wide spectrum of maximum speed, airframe material and UAS design. Through MBS modelling and simulation for each of these five UAS types consequences of impact on the human head are assessed; this is done for two scenarios: controlled horizontal flight impact and uncontrolled vertical drop impact. The results show that UAS weight alone is not a valid predictor of fatality of impact with human head, and that UAS design, airframe material and cruising speed must be taken into account.*

This chapter has been submitted on September 2021 as “Rattanagraikanakorn, B., Blom, H. A., Gransden, D. I., Schuurman, M. J., de Wagter, C., Sharpanskykh, A., and Happee, R., Variation in Human Injury and Fatality from Impacts by Different UAS Types of Similar Weight”

## 6.1 Introduction

Application of unmanned aircraft system (UAS) technology will have a significant impact on our society by enabling various commercial operations, such as aerial delivery, precision agriculture, or search and rescue. Conducting such an operation in an urban area may expose people on the ground to the risk of UAS collisions. To manage this safety risk, injury and fatality severity of UAS impact on human needs to be understood. A widely adopted management approach is to work with UAS weight thresholds. In support of this basic approach, a research team at Nanyang Technological University (NTU) performed a parametric study of UAS impact on human head using experimental impact test and finite element model in order to identify UAS weight threshold for safe operation (Koh et al., 2018a, 2018b). In addition to this basic approach, experimental tests have been conducted by several research groups have used human crash dummies to assess head and neck injury severities due to small UAS impacts. The Alliance for System Safety of UAS through Research Excellence (ASSURE) conducted a series of controlled impact drop tests using the DJI Phantom III UAS on the FAA Hybrid III crash dummy at various impact attitudes and speeds (Huculak, 2016; Arterburn et al., 2017). Live flight test impact analysis of other small UAS types on the Hybrid III crash dummy have been conducted by a team at Virginia Tech (Campolettano et al., 2017). In one of the subsequent ASSURE studies (Arterburn et al., 2019), impact tests of small UAS types on post mortem human surrogates (PMHS) have been conducted and analyzed by a team at the Ohio State University (Stark et al., 2019). The findings of these live tests reveal that the injury levels inflicted by the impact of one type of UAS on human head significantly varies stronger with impact conditions than due to weight and impact speed alone.

The aim of the current study is to gain a proper understanding of the role played by other UAS characteristics. Such understanding has a dual role: 1) to guide future design of small UAS that are inherently safer; and 2) to guide regulation in adopting thresholds beyond UAS weight alone. Because it is difficult to cover a wide range of impact conditions through conducting experimental tests, for the current study we make use of computational models of UAS collision with a human. In automotive and aerospace crashworthiness analysis where impacts are highly dynamic with a range of structures interacting with the human body, there are two approaches in doing so: multibody system (MBS) modelling and Finite Element (FE) modelling (Ambrósio and Dias, 2007; Jenefeldt and Thomson, 2004; Mukherjee et al., 2006; Vadlamudi et al., 2011). For application to UAS impact on human (Arterburn et al., 2019) has developed FE models of three small UAS types, and have integrated this with THUMS (Total Human Model for Safety) from the automotive domain (Toyota, 2015). In another series of studies (RattanaGraikanakorn et al., 2019, 2020a, 2020b, 2020c) an MBS modelling and simulation approach has been developed for evaluating injury and fatality levels of small UAS impact on a human. Now the MBS model of a UAS is integrated with the MBS model MADYMO (Happee et al., 1998) of a human or a human dummy.

The first study of this MBS series (RattanaGraikanakorn et al., 2020a) involved modelling and validation of an MBS model of a DJI Phantom III UAS impact on an MBS model of the crash dummy that was used by (Arterburn et al., 2017; Campolettano et al., 2017; Huculak, 2016; Koh et al., 2018a, 2018b). In the second study (RattanaGraikanakorn et al., 2019, 2020c) the MBS model of DJI Phantom III was coupled with an MBS model of a 50<sup>th</sup> percentile human body to evaluate head and neck injuries due to UAS collision. This second study revealed significant differences in injury levels of DJI Phantom III hitting a human head versus hitting a human dummy that was used in the experimental drop tests. The less flexible neck of the human dummy yields larger neck loading and smaller head acceleration than for a

human body (RattanaGraikanakorn et al., 2019, 2020c). In a third study (RattanaGraikanakorn et al., 2020b) the MBS model was extended to evaluate impact injury on thorax and abdomen of the 50<sup>th</sup> percentile male human body model, and a comparison was made against the commonly adopted fatality models from the Rangers Command Council (RCC, 2001) as well as the blunt criterion model (Magister, 2010). This third study showed that for DJI Phantom III the MBS approach revealed a large effect of impact geometry on fatality risk; and that these effects are ignored by the commonly adopted fatality models of (RCC, 2001) and (Magister, 2010).

The objective of the current paper is to use the MBS modelling and simulation approach to evaluate and compare injury and fatality consequences of human head impact for five small UAS types, one of which is the DJI Phantom III. In selecting the four new UAS types, in addition to UAS weight, the following variables are taken into account: maximum speed, airframe material and airframe design. These UAS characteristics have not been systematically studied before in literature. In addition to four true UAS types, a hypothetically simplified UAS version of the DJI Phantom III is defined. It is included with a purpose to neutralize the effect of airframe design on head injury severity. For these selected UAS types, the first step is to develop MBS models and to integrate them with the human MBS model in MADYMO. Subsequently, impact simulations with a human head are performed and the results are analyzed.

This paper is organized as follows. Section 6.2 presents the UAS selection, the MBS modelling, the calibration and the injury criteria used. Section 6.3 develops two prominent UAS collision scenarios to be simulated with the MBS models; i.e., UAS controlled horizontal collision with human head and UAS uncontrolled vertical drop on a human head. Section 6.4 and 6.5 present the results and discussion for these two encounter scenarios respectively. Section 6.6 presents the conclusion of this paper.

In Appendix 6A, a comparison is made between live UAS impact test results and MBS model results. The motivation for conducting this analysis stems from the recently PHMS impact test results (Stark et al., 2019). Based on the analysis in Appendix 6A it is assessed that the MBS model-based assessment tends to systematically underestimate head injury criterion by 11%. Although this is a relatively small difference, this systematic difference is compensated in Section 6.4 and 6.5 of this paper.

## **6.2 Selection of small UAS types and MBS modelling**

### **6.2.1. Selection of UAS Types**

Using the DJI Phantom III UAS studied in (RattanaGraikanakorn et al., 2019, 2020a, 2020b, 2020c) as a reference, four true other UAS types are selected based on the parameters: UAS weight, maximum speed, airframe material and design. In addition to these four true UAS types, a hypothetical UAS is defined: a rigid body representation of the DJI Phantom III without having any flexible components, such as, motor arm, camera gimbal or landing gear attached to it, though with the same total weight ( $W_0 \approx 1.2$  kg). Two of the four true UAS are selected from the same weight classes and maximum speed class as DJI Phantom III ( $W_0 \approx 1.2$  kg) but having different airframe materials or design. The other two true UAS are selected from a lower weight class ( $W_0 \approx 0.4$  kg). Because it has become clear from the previous studies (RattanaGraikanakorn et al., 2019, 2020a, 2020b, 2020c) that DJI Phantom III can inflict serious head injury on the mid-size male human body, therefore, heavier UAS types are not considered in the current study.

Table 6.1 shows true UAS types with their characteristics that have been selected in addition to DJI Phantom III. Within the weight class  $W_0 \approx 1.2$  kg, DJI F450 and Tarot LJI500 are newly selected. DJI F450 has an ABS plastic frame with sandwich plate fuselage structure and with molded plastic motor arms. Tarot LJI500 is fully made out of stiff carbon fibre materials with sandwich plate fuselage structure and with carbon fibre motor arm. Within the weight class  $W_0 \approx 0.4$  kg, TrueXS Racing UAS and Parrot Bebop are selected. TrueXS Racing UAS has a thick, light-weight carbon fibre frame, and a much higher maximum speed than the DJI Phantom III. As a kind of opposite UAS type in this lower weight class, Parrot Bebop is selected for its lower maximum speed than DJI Phantom III. Parrot Bebop has a molded ABS plastic frame, and the front of the fuselage is made out of polystyrene foam.

**Table 6.1. Summary of mass, maximum speed, and design characteristics of selected UAS types.**

UAS Type	Total Mass [kg]	Maximum Speed [m/s]	Configuration	Airframe Materials	Airframe Design
DJI Phantom III (Baseline)	1.21	18		ABS Plastic	Sandwich shell structure
DJI F450	1.16	18	Quadcopter with camera gimbal system	ABS Plastic	Sandwich plate structure with molded plastic motor arm
Tarot LJI500	1.18	18		Carbon fibre	Sandwich plate structure with carbon fibre rod as motor arm
Parrot Bebop	0.40	16	Quadcopter with front camera cover with polystyrene foam	ABS Plastic	Molded ABS plastic structure
TrueXS Racing UAS	0.40	48	Racing quadcopter with onboard camera	Carbon Fiber	Sandwich plate structure of thick laminates, including motor arm

### 6.2.2. UAS Multibody System Models


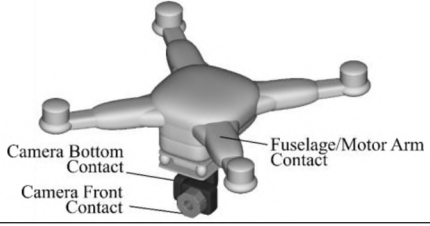
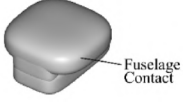

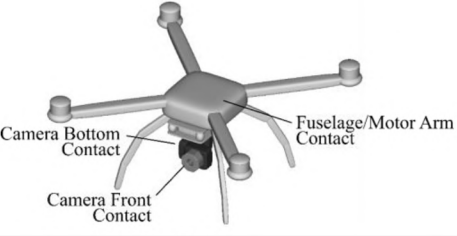

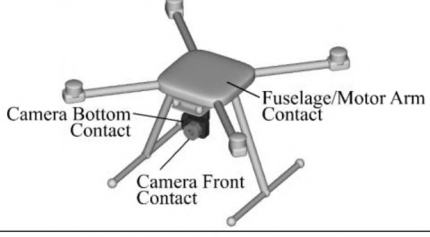

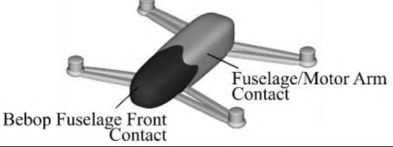

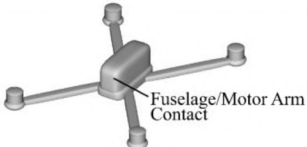
For each UAS type, an MBS is developed. Table 6.2 shows images of the selected UAS types and their MBS views. For the DJI Phantom III, the MBS model of (Rattanagraikanakorn et al., 2020a) is used; there it is explained that the DJI Phantom III landing gears are so flexible that their impact effect is negligible, and therefore are not included in the DJI Phantom III MBS model.

For the Hypothetical UAS, the base model of DJI Phantom III is used but modified into a single lump mass with a rigid body mass concentrated in the center of the fuselage and cutting out all other flexible components. In essence, this Hypothetical UAS represents the stiffest structure UAS type. The Tarot LJI500 and DJI F450 MBS models share a similar model structure to the DJI Phantom III and with landing gears modelled. Since they are customizable UASs camera gimbal is not already installed as seen in real-world system in Table 6.2. However, they both have camera gimbal options similar to the DJI Phantom III. Therefore, both DJI F450 and Tarot LJI500 use the same camera gimbal MBS model as in the DJI Phantom III. For Parrot Bebop and TrueXS Racing, UAS MBS models consist simply of main fuselage and motor arms similar to their real-world system.

Similar as was done for the DJI Phantom III, the MBS views of the five additional UAS types are translated into a network of rigid bodies, kinematic joints, and force restraints. Ellipsoid surfaces are attached to these bodies to realistically represent the model's external geometry and are used for contact modelling. For the Hypothetical UAS there are no joints

and only one rigid body. Figure 6.1 and Figure 6.6 shows the construction of the MBS model for each of the five UAS types respectively. Bodies, joints and restraints highlighted in red colour shown in Figure 6.1 to Figure 6.6 show new parts that are extended relative to the MBS model of the DJI Phantom III in Figure 6.1.

**Table 6.2. Selected UAS types for model extension study and comparisons between real-world systems and multibody system views. Note that real-world systems of Tarot LJI500 and DJI F450 are without camera gimbal. So, in the MBS model, the camera gimbal of the DJI Phantom III is used.**

Weight Class	UAS Type	Real-world System	Multibody System View
	DJI Phantom III (Baseline)		
	Hypothetical UAS	N/A	
Mid-size UAS ( $W_0 \approx 1.2 \text{ kg}$ )	Tarot LJI500		
	DJI F450		
Micro UAS ( $W_0 \approx 0.4 \text{ kg}$ )	Parrot Bebop		
	TrueXS Racing UAS		

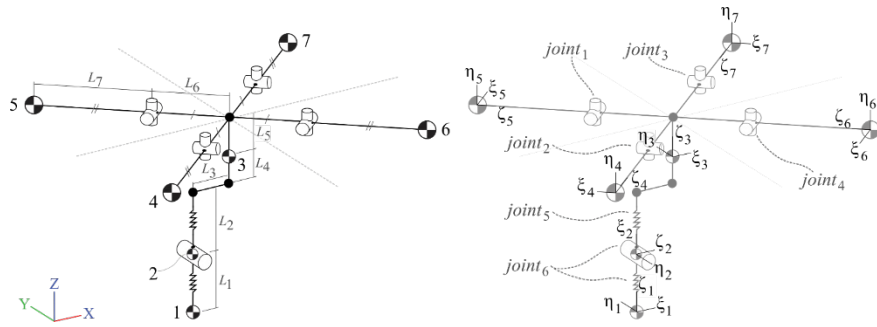


Figure 6.1. Skeletons of DJI Phantom III UAS multibody system model. This MBS model construct is a baseline model that is used for the model extension.

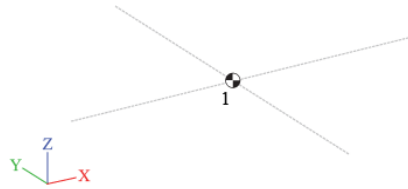


Figure 6.2. Skeletons of Hypothetical UAS multibody system model; it has no joints and only one single rigid body.

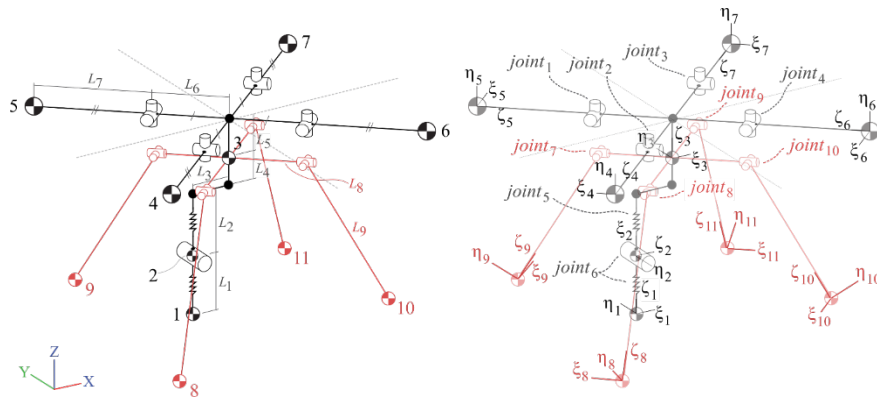


Figure 6.3. Skeletons of DJI F450 UAS multibody system model. Body, joint and restraint highlighted in red show part extension from the baseline model.

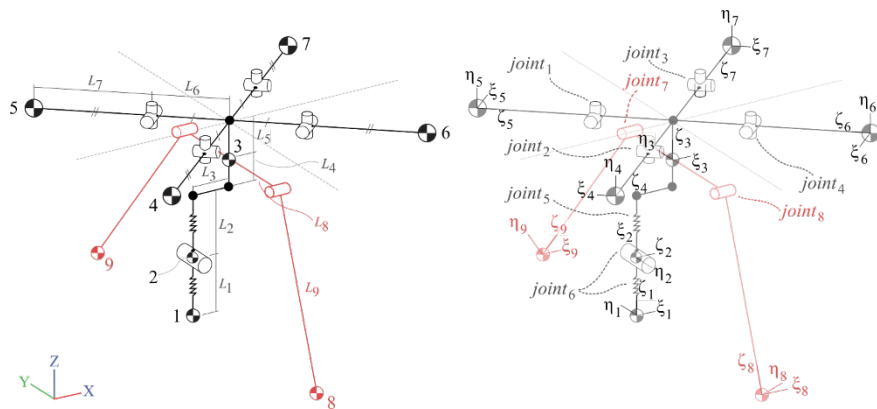


Figure 6.4. Skeletons of Tarot LJI500 UAS multibody system model. Body, joint and restraint highlighted in red show part extension from the baseline model.



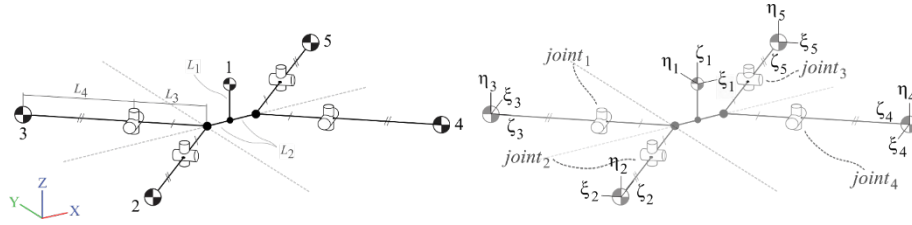


Figure 6.5. Skeletons of Parrot Bebop UAS multibody system model.

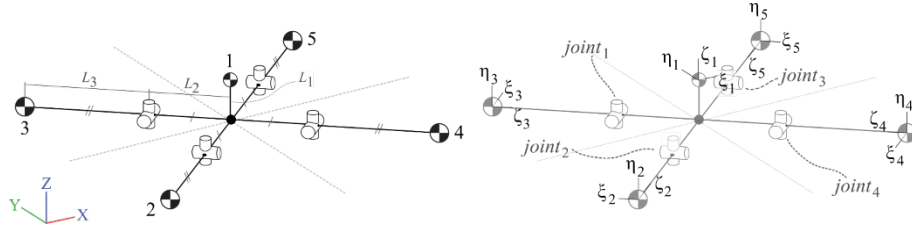


Figure 6.6. Skeletons of TrueXS Racing UAS multibody system model.

To realistically model the dynamics and impact characteristics of the UAS MBS model, mass and geometrical properties of the segments are obtained experimentally using real UAS systems (see Table 6.3). Mass of each segment body is measured using digital weight scale and geometrical dimensions are obtained directly from physical measurements on the real systems.

Table 6.3. Summary of geometrical parameters for the five UAS models.

UAS Model	Segment Body Masses [kg]	Segment Lengths [m]
DJI Phantom III (Baseline)	$W_1 = 0.101, W_2 = 0.056,$ $W_3 = 0.839, W_{4-7} = 0.055$	$l_1 = 0.040, l_2 = 0.020, l_3 = 0.023, l_4 = 0.016, l_5 = 0.030, l_6 = 0.014, l_7 = 0.165$
Hypothetical UAS	$W_1 = 1.21$	-
DJI F450	$W_1 = 0.101, W_2 = 0.056,$ $W_3 = 0.640, W_{4-7} = 0.087,$ $W_{8-11} = 0.017$	$l_1 = 0.040, l_2 = 0.020, l_3 = 0.023,$ $l_4 = 0.020, l_5 = 0.008, l_6 = 0.030,$ $l_7 = 0.170, l_8 = 0.049, l_9 = 0.100$
TarotLJI500	$W_1 = 0.101, W_2 = 0.056,$ $W_3 = 0.621, W_{4-7} = 0.090,$ $W_{8-9} = 0.040$	$l_1 = 0.040, l_2 = 0.020, l_3 = 0.023,$ $l_4 = 0.020, l_5 = 0.008, l_6 = 0.030,$ $l_7 = 0.170, l_8 = 0.060, l_9 = 0.200$
Parrot Bebop	$W_1 = 0.360, W_{2-5} = 0.010$	$l_1 = 0.015, l_2 = 0.025, l_3 = 0.055, l_4 = 0.080$
TrueXS Racing UAS	$W_1 = 0.360, W_{2-5} = 0.010$	$l_1 = 0.012, l_2 = 0.032, l_3 = 0.080$

### 6.2.3. Joint Types and Force/Moment Characteristics

Structural deformation is modelled using various joint types that give each body segments degree of freedom (DoF). For each joint applicable restraint force and moment characteristics shall be measured. Table 6.4 shows for each UAS joint which force and moment characteristics have been measured using quasi-static compressive tests on each part of the UAS; details of these test are in (Rattanagraikanakorn et al., 2020a). The measured moment-angular displacement and force-displacement curves are shown in Figure 6.7 and Figure 6.8, respectively. These measured curves form input to the MBS models in MADYMO.

**Table 6.4. Joint types used in each UAS MBS model, and moment/force characteristics allocated to each joint.**

UAS Type	Joint Type	Moment Characteristics	Force Characteristics
DJI Phantom III	Joint 1-4 (Universal)	R1, R2	-
	Joint 5 (Translational)	-	F1
	Joint 6 (Translational-Revolute)	R3	F2
Hypothetical UAS	-	-	-
DJI F450	Joint 1-4 (Universal)	R1, R2	-
	Joint 5 (Translational)	-	F1
	Joint 6 (Translational-Revolute)	R3	F2
	Joint 7-10 (Universal)	R4, R5	-
Tarot LJI500	Joint 1-4 (Universal)	R1, R2	-
	Joint 5 (Translational)	-	F1
	Joint 6 (Translational-Revolute)	R3	F2
	Joint 7-8 (Revolute)	R4	-
Parrot Bebop	Joint 1-4 (Universal)	R1, R2	-
TrueXS Racing UAS	Joint 1-4 (Universal)	R1, R2	-

For DJI Phantom III, Joint 1-4 represents motor arms. Universal joint type is used for Joint 1-4, providing 2 rotational DoF (upward and sideward deflections). Moment characteristics R1 and R2 are measured for these joints. Joint 5 uses Translational joint to model damp plate motion with 1 translational DoF. Attached to Joint 5 is force characteristics F1. Next, camera gimbal Joint 6 is modelled using Translational-Revolute joint types. This joint type provides 1 translational DoF and 1 rotational DoF. For this joint type moment characteristics R3 and force characteristics F2 have been measured. Because the Hypothetical UAS is a rigid body version of the DJI Phantom III, no additional measurements are needed.

DJI F450 motor arms are also modelled using universal joint type with moment characteristics R1 and R2 attached to each joint. DJI F450 uses the same camera gimbal as the DJI Phantom III. This makes Joint 5 and Joint 6, along with moment/force characteristics, identical to that of DJI Phantom III. An additional four landing gears in DJI F450 are modelled using universal Joint 7 to 10 with moment characteristics R4 and R5 are measured on each DoF.

For Tarot LJI500, motor arms are modelled using universal Joint 1-4 with moment characteristics R1 and R2 measured for each joint. Camera gimbal is identical to that of DJI Phantom III. An additional extension of two landing gears attached to the fuselage is modelled with revolute Joint 7 and 8. Both joints are restraint using moment characteristic R4 and R5 on each DoF.

Bebop and TrueXS Racing UAS MBS models are simply made up of fuselage and 4 motor arms. There 4 motor arms are modelled using universal Joint 1-4. Moment characteristics R1 and R2 are measured for all 4 joints.

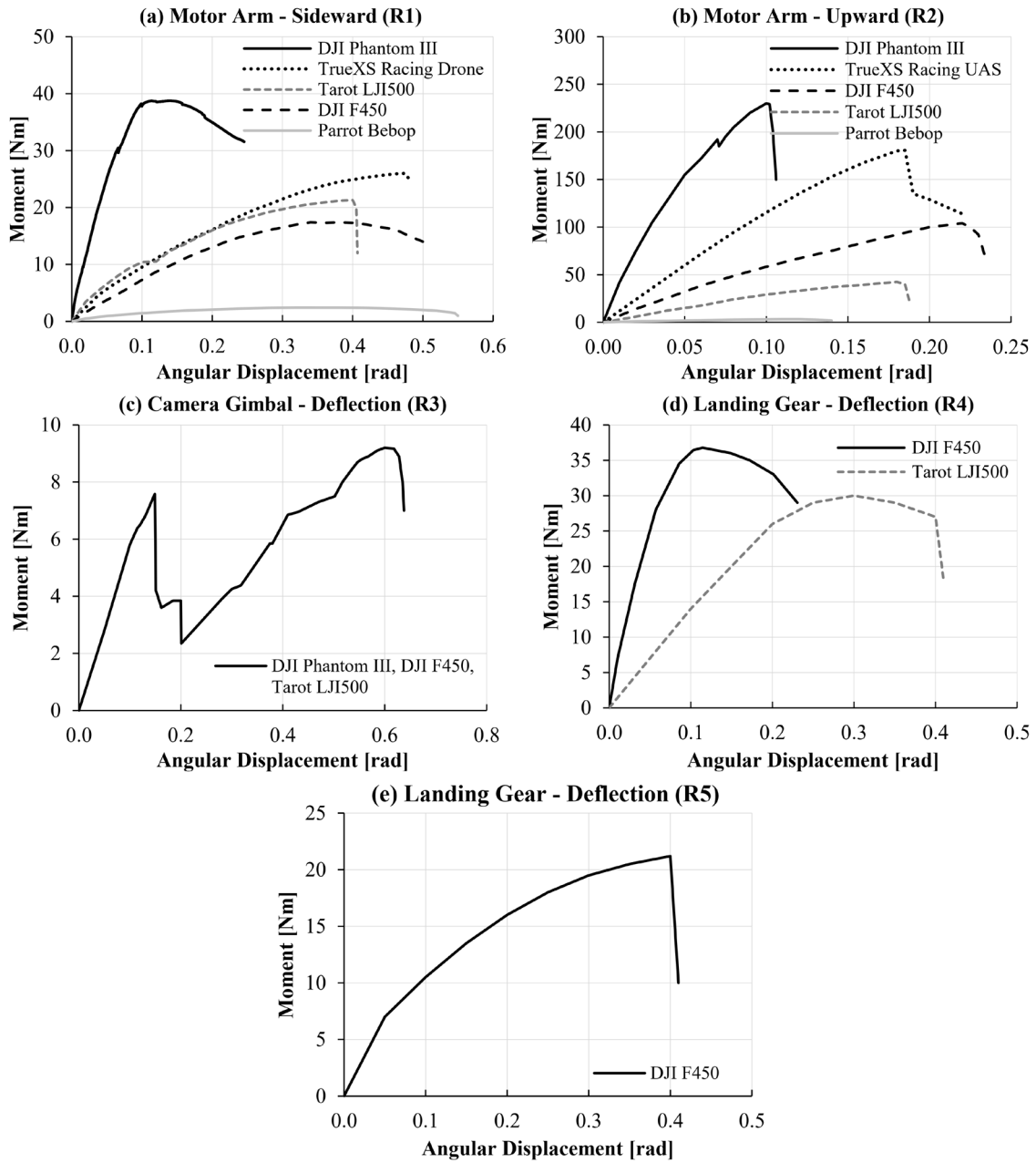


Figure 6.7. Measured moment characteristics R1 to R5.

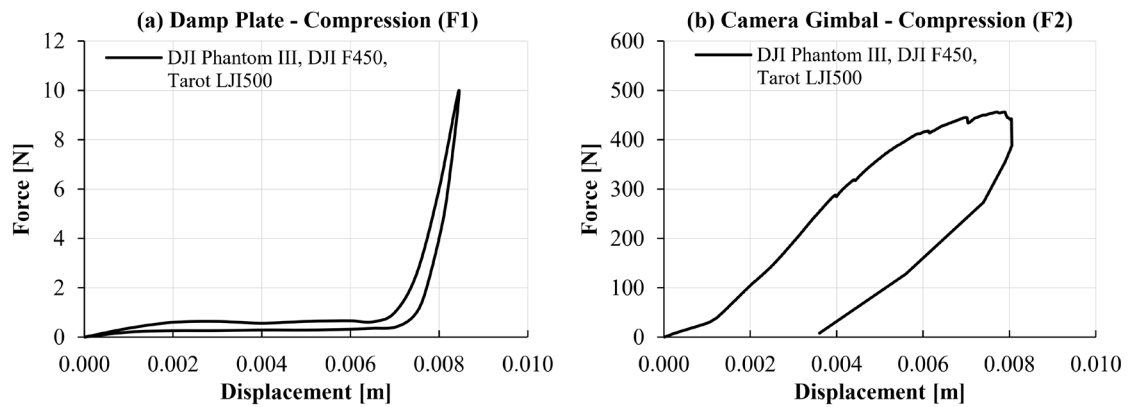


Figure 6.8. Measured hysteresis loop of Force Characteristics F1 and F2 that apply for DJI Phantom III, DJI F450 and Tarot LJ1500.

## 6.2.4. Contact Characteristics

Contact characteristics between UAS and human head are modelled for different parts of the UAS using an analytical elastic-perfectly inelastic contact model (Brake, 2012). There are four types of contact characteristics used in the model. Locations of these four contact types are illustrated in the MBS views in the right column of Table 6.2. These contact types differ due to the difference in materials and geometrical properties of the two contact bodies. ‘Camera Bottom Contact’ and ‘Camera Front Contact’ are for the camera gimbal and human head scalp where the gimbal materials are aluminium. The difference between ‘Camera Bottom Contact’ and ‘Camera Front Contact’ is the contact radius. ‘Camera Bottom Contact’ is for the bottom of the gimbal where surface area is large and Camera Front Contact is for the circular front part of the camera with a small contact radius. ‘Fuselage/Motor Arm Contact’ is the contact characteristics between plastic and human head scalp – this applies to the fuselage, motor arms and landing gears. Lastly, ‘Bebop Front Fuselage Contact’ is the contact between a polystyrene part of the Parrot Bebop and the human scalp.

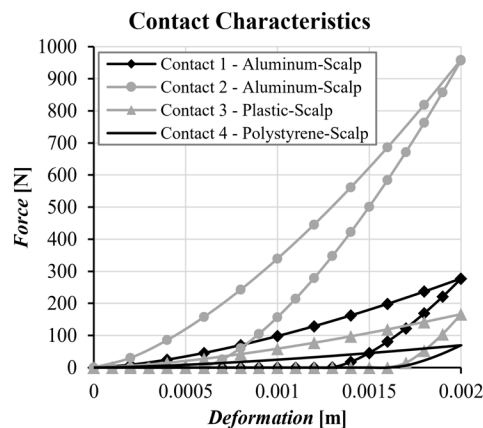
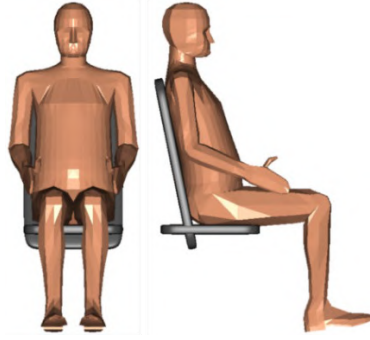


Figure 6.9. UAS contact type characteristics derived from an analytic contact model (Brake, 2012). Note that each curve consists of loading and unloading parts which form a hysteresis loop. Contact types 1 and 2 differ in contact radius.

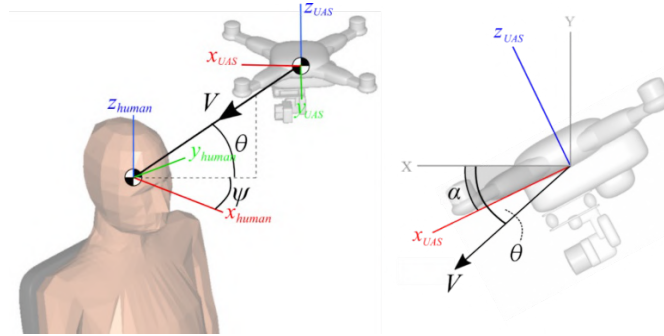
## 6.2.5. MBS Model of Human Body and Head Injury

The assessment of the effect of different UAS types on human head injury is performed using the UAS MBS models shown in Table 6.2 and the 50% percentile male body model distributed with MADYMO 7.7 shown in Figure 6.10. The human body model is a validated biofidelic model that is representative of the mid-size North American male human body and was originally published by Happee (Happee et al., 1998; Happee and Ridella, 2000). The model is a multibody system model with passive muscle, consisting of chains of rigid bodies connected by kinematic joints. The skin is made up of a mesh of shell-type massless contact elements. The biomechanical data including joint characteristics and mechanical properties are based on biomechanical data and are validated using volunteer and post mortem human subjects (PMHS) (TASS International, 2017a).



**Figure 6.10. 50<sup>th</sup> Percentile male human body model in a seated position in MADYMO.**

MBS simulation of UAS impact on human head involve impact parameters that are shown in Figure 6.11; i.e. impact velocity ( $V$ ), head direction ( $\psi$ ), UAS elevation ( $\theta$ ), and UAS pitch ( $\alpha$ ). The UAS is positioned relative to the human head, having a velocity vector pointing toward the head CG (Center of Gravity). An impact condition for central impact is applied, meaning that the line of action of the impact velocities are collinear and passing through the centre of masses of the two bodies.



**Figure 6.11. UAS - Human head impact simulation setup parameters.**

MADYMO supports measurement of Head Injury Criterion ( $HIC_{15}$ ), where the subscript value of 15 refers to the duration in ms of the worst time interval after the first moment of impact. The equation for calculating the  $HIC$  value (TASS International, 2017b) is given as an integral over the head CG (Centre of Gravity) acceleration:

$$HIC_{(t_2-t_1)} = \max_{T_0 \leq t_1 < t_2 \leq T_E} \left\{ (t_2 - t_1) \left[ \frac{1}{t_2 - t_1} \int_{t_1}^{t_2} a(t) dt \right]^{2.5} \right\} \quad (6.1)$$

where  $T_0$  is the first moment of impact, and  $T_E$  is the end time of the period considered after the first impact, and  $a(t)$  is the acceleration-time curve of the head CG. Based on the Federal Motor Vehicle Safety Standards (FMVSS), a  $HIC_{15}$  value of 700 is the minimum safety threshold for non-fatal impact (Eppinger et al., 1999). It should be noted that the  $HIC_{15}$  injury criterion is mainly developed for blunt force injury type. One of the limitations of this injury criterion is when dealing with impact from an object with a small surface area where local penetration is more prominent than an impact force transfer over a large surface area.

MADYMO also supports measurement of the neck injury level in terms of a neck injury criterion  $N_{ij}$  that considers the upper neck force and moment proposed by the National Highway Traffic Safety Administration (NHTSA) (Klinich et al., 1996). This criterion is designed for a frontal-collision injury evaluation in automotive accidents. The “ $ij$ ” represents indices for the 4 injury mechanisms; namely  $N_{TE}$ ,  $N_{TF}$ ,  $N_{CE}$ ,  $N_{CF}$ . The first index  $j$  represents

the actual load (Tension or Compression) while the second index  $j$  represents the sagittal plane bending moment (neck Flexion or Extension). The equation for  $N_{ij}$  is,

$$N_{ij} = \left| \frac{F_{Z,i}}{F_{int,i}} \right| + \left| \frac{M_{Y,j}}{M_{int,j}} \right| \quad (6.2)$$

Where  $F_{Z,i}$  is the upper neck force in Z-axis,  $F_{int,i}$  is the threshold force,  $M_{Y,j}$  is the upper neck moment about Y-axis and  $M_{int,j}$  is the threshold moment. The current performance limit of the  $N_{ij}$  is 1 which represents 22% of  $p(AIS \geq 3)$  (Parr et al., 2012) which can be described as multiple nerve root laceration in the cervical thoracic spine (Schmitt et al., 2019). The equation for converting  $N_{ij}$  to  $p(AIS \geq 3)$  is as follows,

$$p(AIS \geq 3) = \frac{1}{1 + e^{3.227 - 1.969N_{ij}}} \quad (6.3)$$

### 6.2.6. Conversion to Probability of Fatality

To assess the probability of life-threatening injuries due to UAS impact on a human head, a conversion curve from HIC15 to Probability of Fatality (PoF) is adopted. Figure 6.12 illustrates the adopted curve from the U.S. ISO delegation (Tyrell et al., 1995) which is based on Prasad and Mertz injury risk curve (Prasad and Mertz, 1985). This curve allows the conversion of the  $HIC_{15}$  level measured in the MBS simulations to the PoF value.

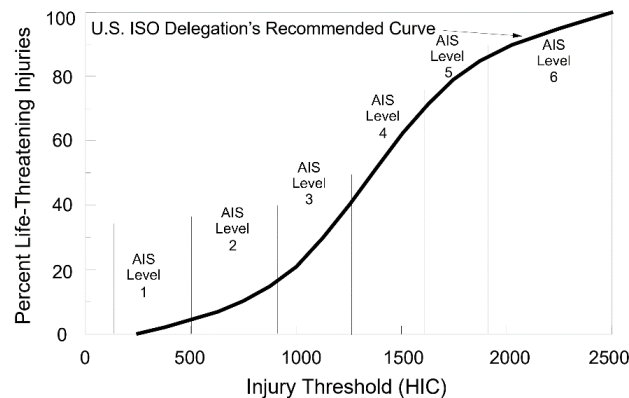


Figure 6.12. Conversion of HIC15 level to the percentage of life-threatening injury recommended by U.S. ISO delegation (Tyrell et al., 1995) which is derived from Prasad and Mertz injury risk curve (Prasad and Mertz, 1985).

## 6.3 Impact Scenario Selection and Simulation Setup

Two UAS impact scenarios will be simulated with the MBS model in MADYMO: Controlled horizontal flight impact and Uncontrolled vertical drop impact. The relevance and details of these two scenarios are described in subsections 6.2.1. and 6.2.2. respectively.

### 6.3.1. Controlled Horizontal Flight Impact

Under a controlled horizontal flight, a UAS is capable of reaching maximum designed operational speed. It is particularly interesting since it yields the highest possible impact energy for each of the UAS types. This impact scenario can occur when, for example, loss-of-link between UAS and operator takes place which makes UAS continue flying in a controlled manner by an autopilot system. Without manual control override from an operator or automatic safety cutoff, UAS will continue its original course and may accidentally hit a person nearby.

This scenario may also arise from pilot accidentally flying UAS too close to nearby bystanders and fail to react to avoid a collision, leading to an impact on a human at full operational speed. This is particularly relevant to racing UAS where flight altitude is close to ground level and close to bystanders.

For controlled horizontal flight, the simulation parameter values are given in Table 6.5, and the encounter setup is illustrated in Figure 6.13. For this scenario, it is of interest to look at the parameters setup that results in the worst impact. DJI Phantom III impact on the side ( $\psi = 90^\circ$ ) of human head results in the worst impact case (Rattanagraikanakorn et al., 2020b). Therefore, head direction ( $\psi$ ) is set to  $90^\circ$ . Impact elevation is set to  $0^\circ$  since only horizontal impact is considered. In reality, at full maximum operational velocity, UAS has to pitch downward with a small angle in order to produce forward thrust force. Nevertheless, this angle is rather small and is neglected in the simulation. Hence, UAS pitch is set to  $0^\circ$ .

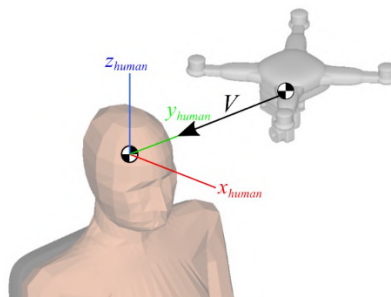


Figure 6.13. Encounter scenario for controlled horizontal flight impact.

Furthermore, for the DJI Phantom III, the maximum attainable speed is up to 18 m/s. DJI F450 and Tarot do not have specific maximum operational speed due to its customizability. However, since they are similar in size and weight compared to DJI Phantom III, it is assumed that the maximum operational speed is equal to the DJI Phantom III. Hypothetical UAS, maximum attainable speed is 18 m/s similar to the DJI Phantom III. The Bebop maximum operational speed is 16 m/s based on manufacturing data (Parrot Drones SAS, 2019).

Lastly, the TrueXS Racing UAS also does not have a specific maximum operational speed due to its customizability. So, an average maximum operational speed of 48 m/s compiled from 14 racing UASs is used (FPV Drone Reviews, 2018). Hence, the simulated impact speed of each UAS is set from 0 m/s to the maximum operational speed with 2 m/s increments.

Table 6.5. Simulation parameters for controlled horizontal flight impact scenario.

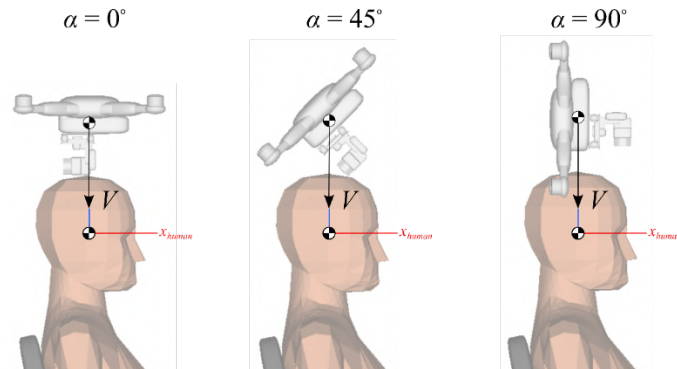
UAS Type	Impact Direction	Impact Elevation	UAS Pitch	$V$ [m/s]	$E$ [J]
	$\psi$	$\theta$	$\alpha$		
DJI Phantom III	$90^\circ$	$0^\circ$	$0^\circ$	0 – 18	0 - 196
Hypothetical UAS	$90^\circ$	$0^\circ$	$0^\circ$	0 – 18	0 - 196
DJI F450	$90^\circ$	$0^\circ$	$0^\circ$	0 – 18	0 - 196
Tarot LJI500	$90^\circ$	$0^\circ$	$0^\circ$	0 – 18	0 - 196
Parrot Bebop	$90^\circ$	$0^\circ$	$0^\circ$	0 – 16	0 - 51
TrueXS Racing UAS	$90^\circ$	$0^\circ$	$0^\circ$	0 – 48	0 - 460

### 6.3.2. Uncontrolled Vertical Drop Impact

The second impact scenarios chosen is the uncontrolled vertical drop. This case may occur due to loss-of-control (Belcastro et al., 2017) which may be caused by partial or complete propulsion failure, control system failure, UAS entering unstable wake region

outside of its operational envelope and etc. This scenario applies to many urban UAS operation, such as aerial photography over crowd or parcel delivery in a populated area. UAS falling vertically downward on a pedestrian is deemed to be a critical case since UAS can reach terminal speed and the pedestrian may not be aware of the falling UAS, making self-protection not possible.

For uncontrolled vertical drop simulation setup, simulation parameters are summarized in Table 6.5. This scenario is depicted in Figure 6.14. Because UAS under such flight conditions typically tumbles down towards the ground (Foster and Hartman, 2017), the impact geometry may vary. To capture this, three sub-scenarios are evaluated for different UAS pitch values of  $0^\circ$ ,  $45^\circ$  and  $90^\circ$  respectively, as is shown in Figure 6.14.



**Figure 6.14. Encounter scenario for vertical drop impact cases. Three cases simulated are with pitch of  $0^\circ$ ,  $45^\circ$  and  $90^\circ$  (left to right).**

Furthermore, since UAS drop freely towards the ground in this scenario, it is assumed that the maximum impact velocity that can be achieved by the UAS is its terminal velocity. ASSURE (Arterburn and Investigator, n.d.) estimated the DJI Phantom III terminal velocity to be approximately 18 m/s by using a computational fluid dynamics model to determine aerodynamics force acting on the UAS. Because the DJI F450, Tarot LJI500 and Hypothetical UAS have similar size and weight, it is assumed that the terminal velocity of these UAS is equal to that of DJI Phantom III. For Parrot Bebop and TrueXS Racing UAS, because these UASs have much lighter weight than the DJI Phantom III, it is possible that the terminal velocity may be lower. Nevertheless, it is of interest to use the terminal drop velocity of the DJI Phantom III as it can represent a possible upper bound terminal drop velocity for Tarot LJI500 and TrueXS Racing UAS.

**Table 6.6. Simulation parameters for uncontrolled vertical drop impact.**

UAS Type	$\psi$	$\theta$	$\alpha$	$V$ [m/s]	$E$ [J]
DJI Phantom III	$0^\circ$	$90^\circ$	$0^\circ/45^\circ/90^\circ$	18	196
Hypothetical UAS	$0^\circ$	$90^\circ$	$0^\circ/45^\circ/90^\circ$	18	196
DJI F450	$0^\circ$	$90^\circ$	$0^\circ/45^\circ/90^\circ$	18	196
Tarot LJI500	$0^\circ$	$90^\circ$	$0^\circ/45^\circ/90^\circ$	18	196
Parrot Bebop	$0^\circ$	$90^\circ$	$0^\circ/45^\circ/90^\circ$	18	64
TrueXS Racing UAS	$0^\circ$	$90^\circ$	$0^\circ/45^\circ/90^\circ$	18	64

Based on the scenarios for uncontrolled vertical drop scenario, the impact attitude of each UAS is shown in Figure 6.15. The figure illustrates the different point of contact for each UAS on the human head at different pitch angle.



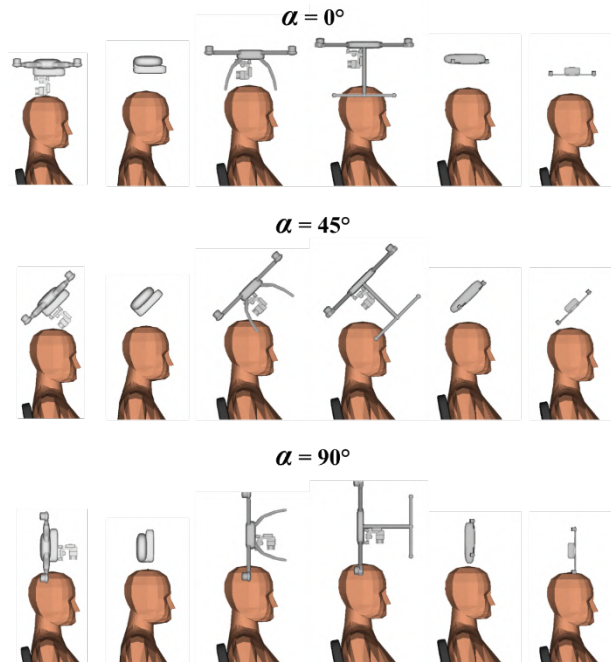


Figure 6.15. Visualization of vertical drop for each of the five UAS types under pitch angles of 0, 45 and 90 degrees.

## 6.4 MBS Results for Controlled Horizontal Flight Impact

### 6.4.1. Head Injury Criterion ( $HIC_{15}$ )

By simulating the integrated MBS models in MADYMO, head injury criterion ( $HIC_{15}$ ) results as a function of increasing impact energy have been obtained for each of the five UAS types; these results are presented in Figure 6.16. The figures show that  $HIC_{15}$  level increases non-linearly with impact energy. Serious and critical head injuries are confirmed by the  $HIC_{15}$  results above 700 for Hypothetical UAS, DJI Phantom III, Tarot LJI500, DJI F450, and TrueXS Racing UAS. Human head sustains a low injury from Parrot Bebop impact with highest  $HIC_{15}$  of 52 – much lower than the threshold of 700.

Hypothetical UAS produces the highest  $HIC$  results and has the steepest  $HIC_{15}$  curve. DJI Phantom III produces the same  $HIC_{15}$  results as presented in the previous work (Rattanagraikanakorn et al., 2020b). DJI Phantom III has the steepest  $HIC_{15}$  curve. Tarot LJI500 has the second steepest  $HIC_{15}$  curve. The third and fourth steepest  $HIC_{15}$  curves are DJI F450 and TrueXS Racing UAS, respectively. Lastly, Parrot Bebop has the lowest slope for  $HIC_{15}$  curve.

At maximum impact energy of 196 J, Hypothetical UAS inflicts  $HIC_{15}$  level 2750 higher than the DJI Phantom III which inflicts  $HIC_{15}$  level 2000. At the same energy, Tarot inflicts  $HIC_{15}$  level 1650, slightly lower than DJI Phantom III. DJI F450 inflicts  $HIC_{15}$  of 1460 at 196 J impact energy. At 196 J impact energy, TrueXS Racing UAS inflicts  $HIC_{15}$  of 1400 which is lower than the DJI Phantom III. However, at its maximum impact energy is 460 J, it inflicts  $HIC_{15}$  up to 4300. This is 2.1 times higher than the DJI Phantom III. Parrot Bebop inflicts the lowest  $HIC_{15}$  of 220 at a maximum impact energy of 52 J.

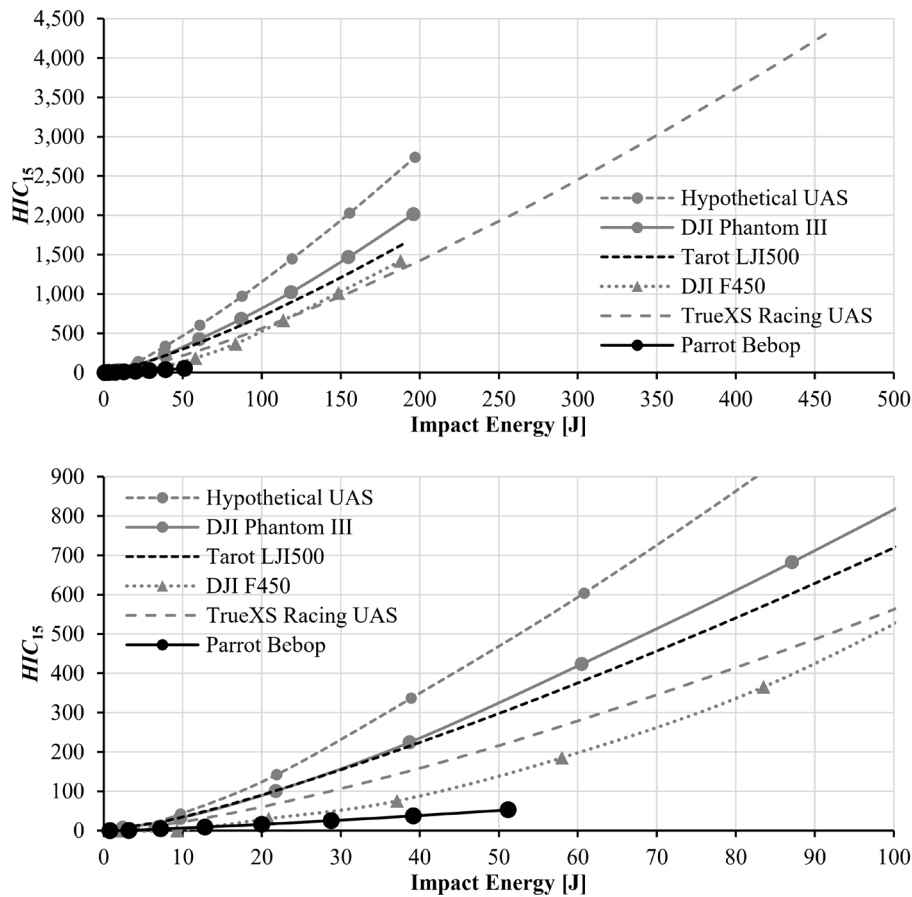


Figure 6.16.  $HIC_{15}$  results for controlled horizontal flight impact with the bottom figure zooming in on low  $HIC_{15}$  and impact energy range.

### 6.4.2. Probability of Fatality (PoF)

As has been analysed in appendix A, based on most recent live PHMS impact test results from Ohio State University (Stark et al., 2019) it is estimated that the MBS based assessment of  $HIC_{15}$  level is likely to be systematically underestimated by 11%. Taking into account the complexity of the MBS model as well as the live test scenarios, this 11% difference is such small that it contributes to the earlier MBS model validation (Rattanagraikanakorn et al., 2020a). However, having assessed such a systematic underestimation provides the opportunity to compensate the MBS assessed  $HIC_{15}$  curves in Figure 6.15. Hence prior to using the conversion curve of Figure 10, the  $HIC_{15}$  curves in Figure 6.16 are increased by a factor 1.11. This 11% compensation followed by PoF conversion yields the five PoF curves in Figure 6.17 as a function of impact energy, one for each UAS type.

For reference purpose, Figure 6.17 also shows the widely adopted Range Commanders Council (RCC) curve for head injury (RCC, 2001). In sequence of PoF severity ranks the RCC curve first. Second is the PoF curve for DJI Phantom III. Third the PoF curve for Tarot LJI500, Fourth the PoF curve for DJI F450. Fifth the curve for True XS Racing UAS. Sixth the PoF curve for Parrot Bebop.

The RCC curve shows an increase with impact energy and resembles an S-shape curve as impact energy increases with a plateau value of 1. The PoF curve for the DJI Phantom III clearly stays well below the RCC curve for the full range of possible impact velocities. For DJI Phantom III this PoF overestimation by the RCC curve has also been shown in (Rattanagraikanakorn et al., 2020b). Figure 6.17 shows that the overestimation by the RCC curve is even more severe for the other four UAS types.

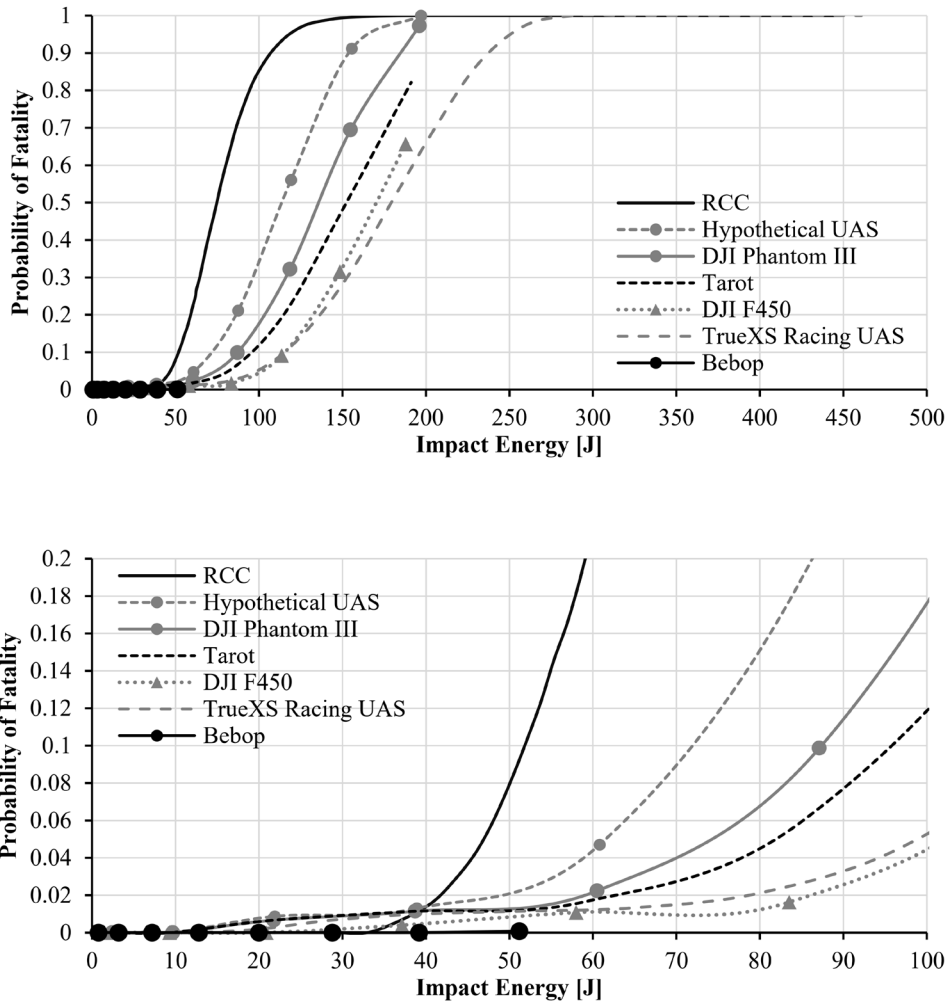


Figure 6.17. Probability of fatality (PoF) as a function of impact energy in case of horizontal impact by each of the five UAS types and the corresponding curve from RCC (RCC, 2001). The PoF curves are converted from the  $HIC_{15}$  curves that have been compensated for +11% systematic underestimation. The bottom figure zooming in on low  $HIC_{15}$  and impact energy range.

At impact energy of 50 J, each of the five UAS types has a PoF around 0, whereas the RCC curve predicts a non-zero PoF of 0.08.

At impact energy of 196 J, RCC curve predicts a PoF of 1, while Hypothetical UAS inflicts PoF of 0.97, DJI Phantom III inflicts PoF of 0.97, Tarot LJI500 inflicts PoF of 0.82, DJI F450 inflicts PoF 0.66, and TrueXS Racer UAS inflicts PoF of 0.51. Of these four UAS types, the TrueXS Racing UAS is the only one that can yield more than 196J impact energy. The PoF value of 1 is reached at about 70% of its maximum achievable impact energy of 460 J.

### 6.4.3. Head CG Acceleration-Time History

To understand the effect of different UAS types on head injury severity, head acceleration curves for each UAS at maximum impact energy were extracted and analyzed. This is because head acceleration is the measure for  $HIC_{15}$ . Figure 6.18 shows head CG acceleration-time history of the human head starting from the initial contact moment with the 5 UAS types at maximum impact energy.

The results show that the TrueXS Racing UAS has the highest peak acceleration of 614 g within 1 ms. Hypothetical UAS reaches the peak value of 500g at approximately 0.9 ms. DJI Phantom III reaches the peak value of 400 g at 1 ms. Tarot has a relatively high peak of

330 g which is reached at about 1.5 ms. It is observed that the Tarot has a small sharp rise in head acceleration at 0.5 ms, then followed by a flat region for a very short period before peak acceleration is reached.

DJI F450 induces lower head acceleration with a peak value of 283 g at 0.7 ms. DJI F450 has similar compression rate compared to the DJI Phantom III, but with slower rebound rate as the downslope is much less steep. Bebop yields significantly low peak head acceleration of only 74 g at 1.8 ms. This shows that the Parrot Bebop compressive phase is much slower than other UAS types.

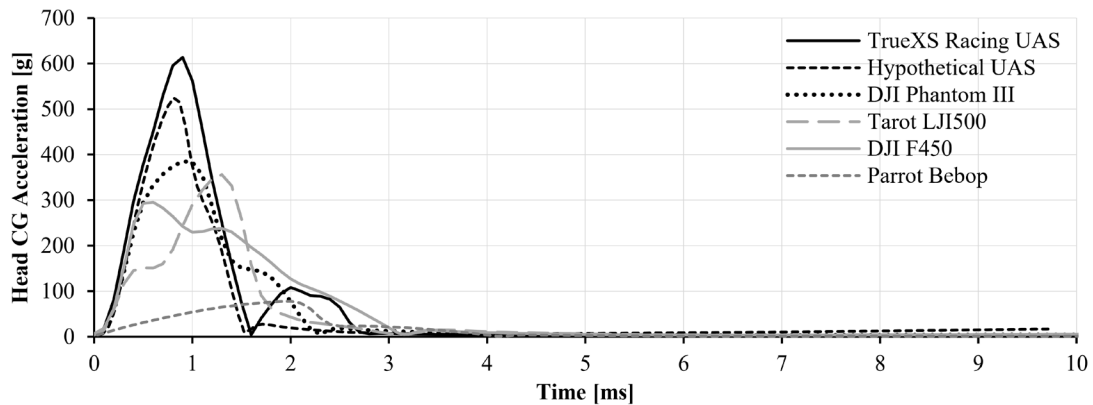


Figure 6.18. Head CG acceleration time-history curves at a maximum impact energy of each UAS type.

#### 6.4.4. Neck Injury ( $N_{ij}$ )

In addition to head injury, neck injury level on a human body due to UAS impact is assessed using the neck injury criterion ( $N_{ij}$ ). Figure 6.19 shows  $N_{ij}$  results at different impact energy for different UAS types. For all UAS types,  $N_{ij}$  values indicate non-critical neck injury. The highest  $N_{ij}$  observed is 0.401 which is inflicted by the TrueXS Racing UAS. This  $N_{ij}$  level is equivalent to 8.2% risk of moderate neck injury ( $AIS \geq 3$ ). Even the TrueXS Racing UAS, which inflicts life-threatening  $HIC_{15}$  level, does not inflict serious neck injury with a maximum  $N_{ij}$  level of less than 0.48 (9.3% of  $p(AIS \geq 3)$ )

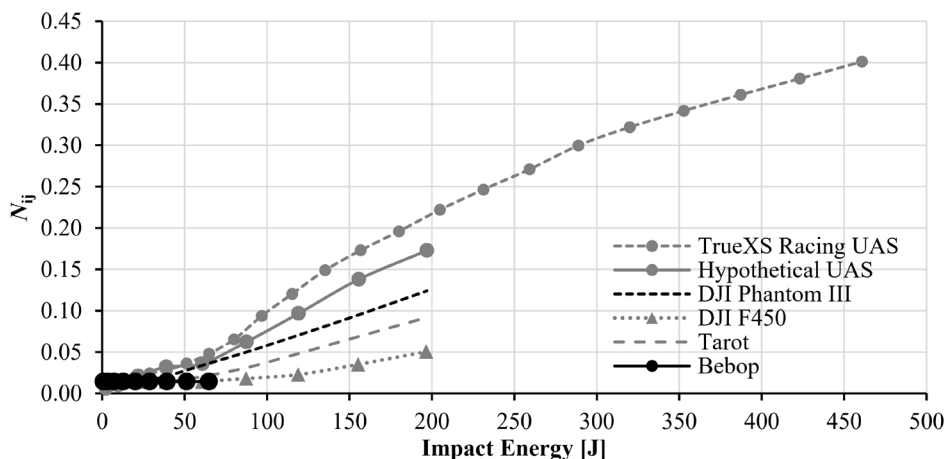


Figure 6.19. Neck Injury of horizontal-side impact.

#### 6.4.5. Discussion of Controlled Horizontal Flight Impact Results

In this section, controlled horizontal impact results for Hypothetical UAS, DJI Phantom III, Tarot LJI500, TrueXS Racing UAS, DJI F450 and Parrot Bebop are discussed. The PoF curves for all UAS types stay well below the RCC curve for the full range of possible impact velocities. Of all the six UAS types, the PoF curve of the Hypothetical UAS is closest

to the RCC curve and the second closest is the DJI Phantom III. Increasing differences have been found for Tarot LJI500, DJI F450, True XS Racer UAS and Parrot Bebop respectively. The aim of the discussion in this section is to identify an explanation for these differences in terms of differences in airframe design and materials used. To do so, the findings for each of the additional UAS types are compared to those of the DJI Phantom III.

First, the Hypothetical UAS which is a rigid-body representation of the DJI Phantom III shows 30% higher  $HIC_{15}$  and PoF level compared to the DJI Phantom III. The head acceleration curve is also in good agreement with the  $HIC_{15}$  and PoF results, which shows a sharp rise in head CG acceleration. The peak of 500 g is reached before 0.9 ms, which is higher and faster than the DJI Phantom III. This implies a quicker transfer of impact energy to the human head. This is reasonable since the Hypothetical UAS represents a rigid-body UAS type which does not contain any flexible components. All lumped masses of flexible components in the DJI Phantom III are concentrated into the center of the fuselage in Hypothetical UAS - this results in the stiffest airframe case. Out of all initial impact energy of the UAS, only minor energy loss in contact energy is dissipated but no impact energy is dissipated by structural compliance. Even though not realistic, this rigid-body impact case represents the worst impact case that UAS types within  $W0 \approx 1.2$  kg can inflict on human body.

Even the Hypothetical UAS inflicts higher PoF compared to the DJI Phantom III and highest among other UAS types, its PoF curve still is not close to the RCC curve. The Hypothetical UAS is still lower by approximately more than 80% in the range of 100 J to 150 J. This shows that the RCC curve overestimates the PoF level of human under UAS collisions. As found in the previous work (RattanaGraikanakorn et al., 2020b), the RCC curve is derived based on small debris explosive data. Hence, it is a representation of blast wave injury (Barnard and Johnston, 2013) or laceration and penetration injury, while UAS impact mostly caused blunt-force trauma injury. It is possible that the real UAS model can inflict penetration or laceration injuries on human body parts which may result in higher PoF curve comparable to the RCC curve. However, such injury mechanism is not possible to capture with MBS model used in this study, since the MBS only consider blunt-force impact of relatively large surface area contacts.

For Tarot LJI500 the  $HIC_{15}$  and PoF curves are about 25% lower than those for the DJI Phantom III. These 25% lower curves are also reflected by a small change in head acceleration curve in Figure 6.18 where the peak acceleration is reached at a later time compared to the DJI Phantom III. This implies that the slope of the head acceleration curve is slightly lower which means that impact energy transfer is not as abrupt as the DJI Phantom III. Because masses, impact velocity and contact stiffness are equal, the assessed difference may be due to differences in airframe materials and design (UAS shape and construction). An objective assessment of airframe materials and construction differences stem from the quasi-static compressive test on the airframes in Figure 6.7(a) and Figure 6.7(b). This shows that Tarot LJI500 is almost two times less stiff than DJI Phantom III. This results in a more compliance structure which absorbs and damp out impact energy during impact. However, these two times less stiff structure only results in 25% reduction in  $HIC_{15}$ . Even though structural stiffness has a direct influence on  $HIC_{15}$ , however, its effect is not one to one. This is because shape and mass distribution also play their roles. For instance, motor arm stiffness as shown in Figure 6.7(a) and Figure 6.7(b) connects to the main mass to lumped masses consist of motor and arm. Both for DJI Phantom III and Tarot LJI500 the masses of these four motors and arms are approximately 20% of the total mass. So, the amount of impact energy absorbed by these parts out of the total impact energy is less than what the main body absorbs. This explains why reduced motor arm stiffness has only a partial effect on  $HIC_{15}$  reduction. Complementary to

arm stiffness difference there are some differences in the shape of the two UAS types that will also have a non-linear effect on  $HIC_{15}$  difference.

For DJI F450, the  $HIC_{15}$  and PoF are about 40% lower than those for the DJI Phantom III. Although the acceleration curve in Figure 6.17 for DJI F450 shows a similar initial rise as the DJI Phantom III, the peak value is lower and the rebound takes longer. The longer rebound phase indicates a softer and damped structure where more energy is dissipated. Because masses, impact velocity, contact stiffness and airframe materials (ABS plastic) are equal, the assessed difference may be due to differences in airframe design (UAS shape and construction). An objective assessment of airframe materials and construction differences stem from the quasi-static compressive test on the airframes in Figure 6.7(a) and Figure 6.7(b). In these figures, the bending stiffness of DJI F450 motor arm is almost a factor 3 less steep than for DJI Phantom III. The likely explanation is that, as described in Table 6.1, DJI F450 has a sandwich plate structure, which is flexible, whereas DJI Phantom III has a shell structure, which is stiff. However, the significantly less stiff motor arms only result in 40% reduction in  $HIC_{15}$ . This again shows that the relation between structural stiffness and  $HIC_{15}$ , the level is not one to one; also shape and mass distribution play their roles. For instance, motor arm stiffness shown in Figure 6.7(a) and Figure 6.7(b) connects to the main mass to lumped masses consist of motor and arm. Both for DJI Phantom III and DJI F450 the masses of these four motors and arms are approximately 20% of the total mass. Therefore, out of the total impact energy, the amount of impact energy engaged by these parts is less than what the main body absorbs. Also, partial effect on  $HIC_{15}$  reduction can be explained by the reduction of motor arm stiffness. Apart from the difference in arm stiffness there are further differences in the shape of the two UAS types that will also have a non-linear effect on  $HIC_{15}$  change.

For the TrueXS Racing UAS the  $HIC_{15}$  and PoF values at 196 J impact energy are about 45% lower than those for DJI Phantom III. Because of its low mass, the 196 J impact energy is reached at a 2.5 higher impact velocity than DJI Phantom III. TrueXS Racing UAS inflicts 45% lower of  $HIC_{15}$  compared to DJI Phantom III because of its smaller geometrical characteristics. Due to its small size, the first point of contact is the two forwards motor arms. Upon impact, these two motor arms deflect outward, acting like a spring/damper system which increases impact time. Once the maximum deflection of the motor arms is reached, the energy from the main mass of the fuselage is then transferred to the head. This is not the case for DJI Phantom III where the main fuselage is the first point of contact. For the DJI Phantom III, the main mass of the fuselage hit directly on to the head, making a significant amount of impact energy being transferred at the first instance.

For the Parrot Bebop the  $HIC_{15}$  and PoF curves remain near-zero values. As shown in the lower-left corner of Figure 6.15, the Parrot Bebop has a very low maximum impact energy of only 51 J due to its low mass and limited maximum speed. The maximum  $HIC_{15}$  value that the Parrot Bebop can inflict on a human head in less than 60 J - well below the threshold of 700 J. In addition, by considering head CG acceleration induced by the Parrot Bebop in Figure 6.18, the curve shows a gradual rise in head acceleration which takes almost 2 ms to reach peak acceleration value. This gradual rise shows that the compressive phase for Bebop takes rather long in comparison to the other four UAS types. This aligns well with the low moment curves measured for Parrot Bebop in Figures 6.7(a) and 6.7(b). These low moment and force curves reflect that the frontal part of the Parrot Bebop frontal part is made out of soft polystyrene foam. This reduces moment and force curves, and as a result of this leads to increasing the compression phase, and thus, lowering the impact force on the human head.

## 6.5 MBS Results for Uncontrolled Vertical Drop Impact

This section addresses Head Injury Criterion ( $HIC_{15}$ ) and the probability of fatality (PoF) results for uncontrolled vertical drops of the five UAS types on human head. Because in these cases Neck injury is negligible to head injury (Rattanagraikanakorn, 2020a), the latter is evaluated only. In all cases the impact velocity of the UAS is 18 m/s, which means impact energy of 64 J for the two light UAS types, and 196 Joule for the other UAS types. This also means that the two light UAS types stay below the AIS level 3 based safety threshold of 95 Joule (Koh et al., 2018). Hence the other UAS types are about a factor two above this safety threshold.

The latter finding stems from earlier MBS simulation results of vertical drop of DJI Phantom III on human head (Rattanagraikanakorn et al., 2020a) and from similar findings for the other UAS types in the previous section on controlled horizontal flight impact.

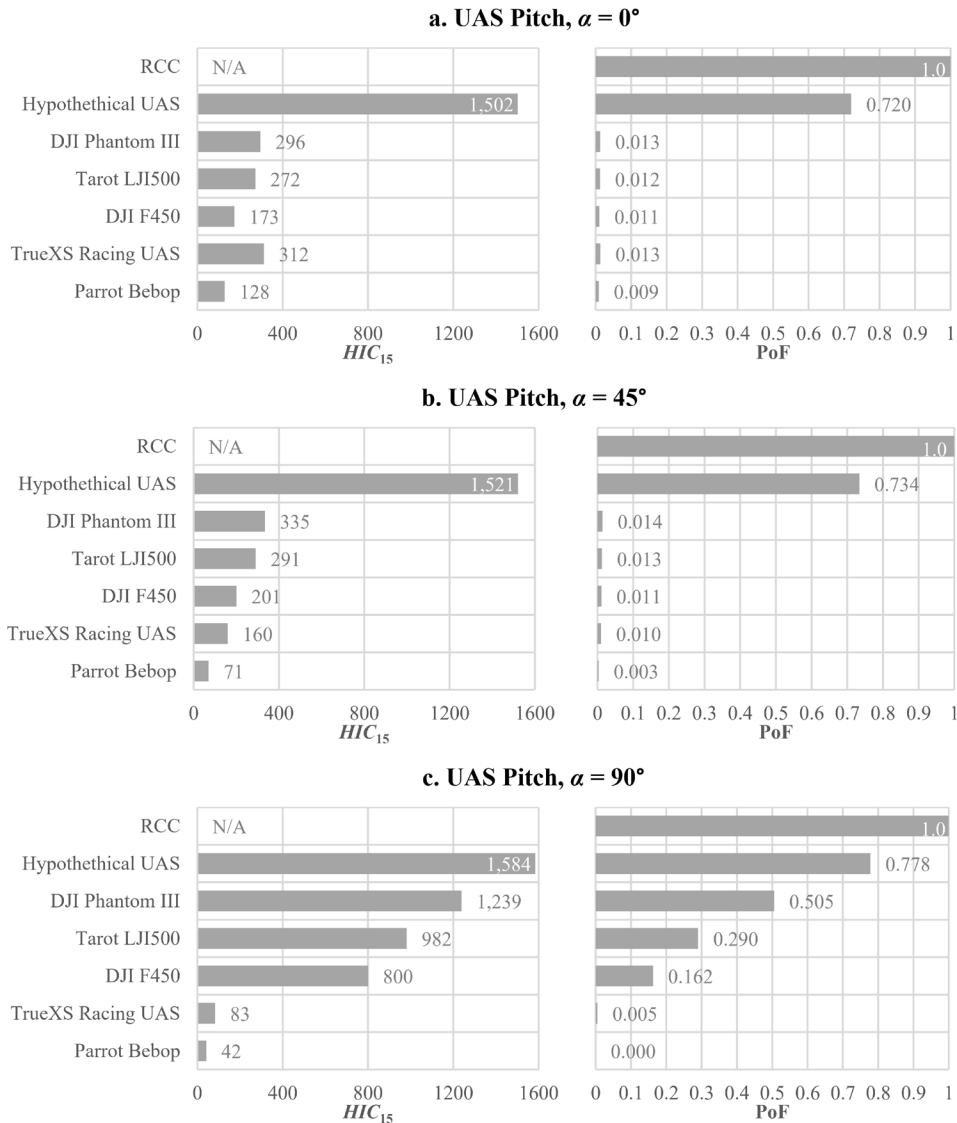
### 6.5.1. Head Injury Criterion ( $HIC_{15}$ ) & Probability of Fatality (PoF)

Figure 6.20.a-c shows  $HIC_{15}$  and PoF results for each UAS types at 18 m/s falling speed and at the pitch of  $0^\circ$ ,  $45^\circ$  and  $90^\circ$  respectively. Similar to the transformation of MBS-based  $HIC_{15}$  curves to PoF curves in Section 6.4.2,  $HIC_{15}$  values are multiplied by a factor 1.11 prior to conversion to PoF. This factor 1.11 is to compensate for the 11% systematic underestimation of  $HIC_{15}$  by the MBS model as has been analysed in Appendix 6A. Note that, in Figure 6.20.a-c, for RCC's PoF values no underlying  $HIC_{15}$  values are known.

For pitch angle of  $0^\circ$ , Hypothetical UAS inflicts the highest  $HIC_{15}$  of 1502. DJI Phantom III and Tarot LJI500 inflict similar head injury with  $HIC_{15}$  of 296 and 272, respectively. DJI F450 inflicts lower  $HIC_{15}$  of 173. TrueXS Racing UAS inflicts the highest head injury with  $HIC_{15}$  of 312. Bebop inflicts the least head injury with  $HIC_{15}$  of 128. In terms of PoF, the RCC curve predicts PoF of 1. The converted PoF from the  $HIC_{15}$  for the Hypothetical UAS is the second highest with PoF of 0.72, while the other UAS types PoF ranges between 0.009 and 0.013.

For pitch of  $45^\circ$ , the Hypothetical UAS also inflicts the highest  $HIC_{15}$  of 1502. DJI Phantom III and Tarot again inflict similar head injury with  $HIC_{15}$  value of 335 and 291, respectively. DJI F450 inflicts lower  $HIC_{15}$  of 201 compared to DJI Phantom III. TrueXS Racing UAS inflicts  $HIC_{15}$  of 160, and Bebop inflicts  $HIC_{15}$  of only 71. When compared  $45^\circ$  pitch cases to  $0^\circ$  pitch cases, Hypothetical UAS inflict similar  $HIC_{15}$  of 1500. DJI Phantom III, Tarot and DJI F450 inflict also similar head injury. However, TrueXS Racing UAS and Bebop see a noticeable difference in  $HIC_{15}$  level which reduce by almost 50% compared to  $45^\circ$  pitch cases. For PoF, the RCC still inflicts PoF of 1 and the Hypothetical UAS inflicts PoF of 0.734. PoF of TrueXS Racing UAS and Bebop reduce to 0.010 and 0.003, respectively.

For pitch of  $90^\circ$ , Hypothetical UAS still inflicts the highest  $HIC_{15}$  of 1584. Significant higher head injury levels are assessed for the DJI Phantom III, Tarot LJI500 and DJI F450, while head injury reduces for Bebop and TrueXS Racing UAS. DJI Phantom III now inflicts about a factor 4 higher  $HIC_{15}$  than for  $0^\circ$  and  $45^\circ$  pitch cases. Similarly, head injury sustained by Tarot LJI500 is now about a factor 3.3 times higher. DJI F450 also inflicts a factor 4 times higher  $HIC_{15}$ . The significant  $HIC_{15}$  differences at pitch of  $90^\circ$  lead for DJI Phantom III, Tarot LJI500 and DJI F450 to even larger differences in PoF values. In  $90^\circ$  pitch case, DJI Phantom III now inflicts a PoF of 0.5. Tarot LJI500 inflicts a PoF of 0.3. DJI F450 inflicts a PoF of 0.16.



**Figure 6.20. HIC<sub>15</sub> and PoF results for uncontrolled vertical drop impact. a) 0° pitch, b) 45° pitch; c) 90° pitch. The PoF values are converted from the HIC<sub>15</sub> values that have been compensated for a systematic underestimation of 11%.**

For pitch of 90°, Bebop and TrueXS Racing UAS inflict about a factor 2 lower (instead of higher) HIC<sub>15</sub> than under 0° and 45° pitch cases. This decrease in HIC<sub>15</sub> on TrueXS Racing UAS and Bebop leads to very low PoF values: TrueXS Racing UAS inflicts a PoF of 0.5%, and Bebop inflicts a PoF of less than 0.1%.

### 6.5.2. Head CG Acceleration-Time History

Figure 6.21 shows head CG acceleration-time history of the human head starting from the initial contact moment with the 5 UAS types at various pitch angles.

For 0° pitch, head CG acceleration curve shows that Hypothetical UAS inflicts the highest head acceleration with a rapid rise to peak acceleration at 400 g within 1 ms. The Racing UAS can induce the highest head acceleration with a peak value of 200 g at 1 ms. The Bebop has a slightly lower peak value of 127 g reached at 1.4 ms. Also, Bebop and Racing UAS only have one acceleration peak, while the other UASs have two distinct peaks. DJI Phantom III, Tarot and DJI F450 all have two head acceleration peaks. The first peaks reach approximately 110 g at 0.7 ms. The second peaks approximately 125 g at 2.4 ms for DJI Phantom III. The second peak for DJI F450 and Tarot a slight later reaching 169 g at 3.1 ms.



For 45° pitch, similar head acceleration responses are observed compared to 0° pitch case. Hypothetical UAS also inflicts the highest peak acceleration at 430 g at 1 ms. TrueXS Racing UAS and Bebop have slightly lower peak values of 160 at 1 ms and 98 at 2 ms, respectively. DJI Phantom III, DJI F450 and Tarot all induce similar head injury in terms of peak magnitude and timing compared to the 0° pitch case.

For 90° pitch case, peak acceleration of the Hypothetical UAS is similar to 0° and 45° pitch cases. Head acceleration induces by DJI Phantom III, Tarot, and DJI F450 now increase significantly from 0° and 45° pitch cases. DJI Phantom III has peak value of 340 g at 1.25 ms. Tarot is slightly lower with peak value of 295 g at 1.25 ms. DJI F450 peak value is reached earlier at 0.9 ms with value of 229 g. Head acceleration is also lower for True XS Racing UAS and Bebop. TrueXS Racing UAS peak value is reached at 103 g at 1.9 ms. Bebop reaches peak head acceleration at 3.5 ms with a value of 17 g.

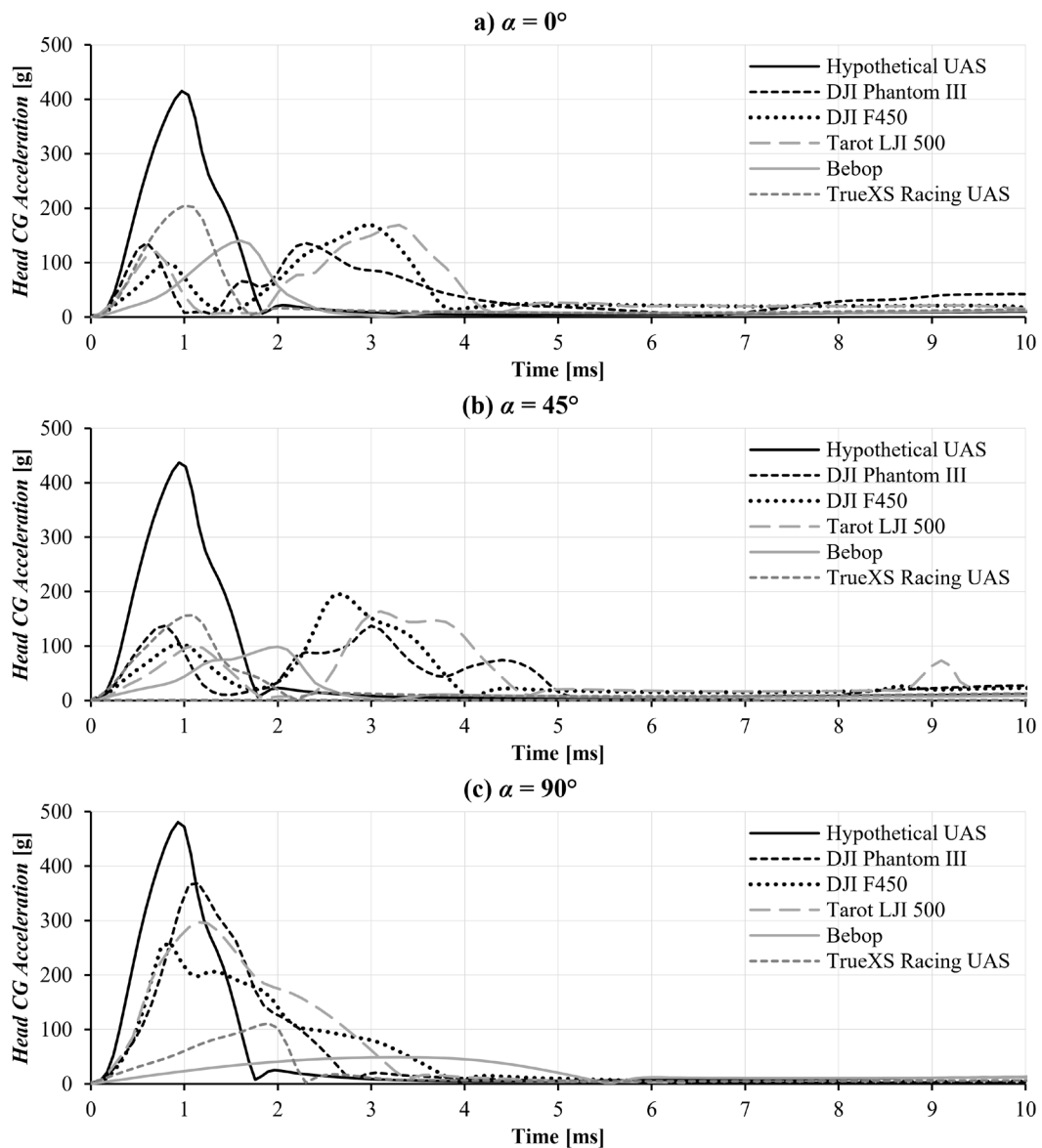


Figure 6.21. Head CG acceleration time-history of all UAS types for 0°, 45° and 90° pitch angle at maximum impact energy.

### 6.5.3. Discussion of Uncontrolled Vertical Drop Impact Results

In this section, impact injury results for Hypothetical UAS, DJI Phantom III, Tarot LJI500, TrueXS Racing UAS, DJI F450 and Parrot Bebop are discussed for uncontrolled vertical drop conditions at 0°, 45° and 90° pitch angles, at an impact velocity of 18 m/s.

Hypothetical UAS  $HIC_{15}$  and PoF is similar in all pitch cases. For DJI Phantom III, Tarot LJI500 and DJI F450, the largest  $HIC_{15}$  and PoF levels apply under pitch of 90°. However, for the two lighter UAS types, the largest  $HIC_{15}$  and PoF levels apply under pitch 0°.

When considering the worst pitch cases for each of the six UAS types, then the highest  $HIC_{15}$  and PoF values applies for Hypothetical UAS. The second follows DJI Phantom III, third is Tarot LJI500, fourth is DJI F450, fifth is TrueXS Racing UAS and sixth is Parrot Bebop. This sequence is the same as was found for controlled horizontal impact case in section 6.4. The Hypothetical UAS  $HIC_{15}$  and PoF does not differ between each pitch cases because its configuration is similar in all orientation due to its feature-less single rigid body fuselage. The value of the RCC PoF is constant for all UAS pitch cases because the model does not account for the effect of impact body orientation.

The aim of the discussion in this section is to identify an explanation for these differences in terms of differences in airframe design (shape and construction) and materials used. To do so, the findings for each of the four additional UAS types are compared to those of the DJI Phantom III.

Because the 90° pitch impact under uncontrolled vertical impact compares to a certain extent to the controlled horizontal impact of section 6.4, each of the five UAS types under 90° pitch uncontrolled vertical impact is considered first.

Under 90° pitch, the most severe impact risk applies to Hypothetical UAS. Nevertheless, the  $HIC_{15}$  level of uncontrolled vertical drop at 18 m/s is about 50% of the  $HIC_{15}$  level under 18 m/s controlled horizontal side impact; and the PoF is 30% of the PoF under 18 m/s controlled horizontal side impact. Similar difference applies to DJI Phantom III where the  $HIC_{15}$  level of uncontrolled vertical drop at 18 m/s is about 60% of the  $HIC_{15}$  level under 18 m/s controlled horizontal side impact; and the PoF is 45% of the PoF under 18 m/s controlled horizontal side impact. As has been explained in (Rattanagraikanakorn et al., 2020a) this is due to the biomechanics of human head and neck complex. Under vertical impact with 90° pitch, a significant amount of impact energy being transferred from head to neck complex. This is because UAS impact force is vertically aligned with the neck complex longitudinal axis. On contrary, under controlled horizontal case with 0° pitch, UAS collides horizontally onto the head. There is no body part to absorb impact force in this lateral direction, making head acceleration 40-60% higher than vertical impact case.

For DJI Phantom III, DJI F450 and Tarot LJI500, 0° and 45° pitch cases see head injury decreases substantially in comparison to 90° pitch case. The decrease in  $HIC_{15}$  is almost a factor 4 for the DJI Phantom III; which reduces PoF from 50% to 1.3%. For an explanation of this difference in head injury, head acceleration curves of DJI Phantom III, Tarot and DJI F450. For 0° and 45° pitch cases are investigated. These three UAS types induce head acceleration curves with two observable peaks, but these do not appear in Hypothetical UAS. This is because DJI Phantom III, Tarot and DJI F450 all have camera gimbal under the fuselage as the first point of contact, while Hypothetical UAS do not. Camera gimbal system acts as a spring and damper system that dissipates a large amount of impact energy. This gives rise to the first acceleration peak which represents this energy dissipation from camera gimbal. Once the camera gimbal is fully compressed, then the motor arms attached to main UAS fuselage

are compressed – giving rise to the second acceleration peak. Notice that the second peaks are larger because the main fuselage including motor arms contain more mass. These two peaks allow the amount of impact energy transfer to be spread out over time, reducing the maximum peak acceleration.

In the head acceleration curve of the 90° pitch case, only one head acceleration peak is observed for DJI Phantom III, DJI F450 and Tarot. This is because these four UASs now have the frontal fuselage as the first point of contact under 90° pitch. This contact area is stiff and does not deform as much as camera gimbal. Thus, impact energy is transferred through this contact force in a short period of time. As shown in head acceleration curve in Figure 20, UAS reaches its maximum crush only within 1 ms, the same time as peak head acceleration is reached.

For TrueXS Racing UAS head injury is higher under 0° and 45° pitch when compared to the 90° pitch. By examining the head acceleration curves, it has a slightly higher head acceleration peak under 0° and 45° pitch when compared to 90° pitch impact. This is because, under 0° pitch, flat bottom of the fuselage is the first point of contact, resulting in full impact energy transfer in a shorter period. As the pitch increases to 45°, the forward motor arms are in contact with the human head first which results in motor arm deflection. This deflection dissipates impact energy and reduces head injury.

For Parrot Bebop, 0° pitch case inflicts higher head injury when compared to 90° pitch cases. This is because the flat bottom of the fuselage is the first point of contact, and results in full impact energy transfer in a shorter period. At pitch angle of 45°, head injury is also lower than 90° pitch case because the soft frontal part of the fuselage that is made out of polystyrene foam partially hit the human head first. Since polystyrene foam is very compliance and able to dissipate a large amount of impact energy, head injury is therefore reduced. At 90° pitch, the soft frontal part of the Parrot Bebop fully collides onto the human head, resulting in the lowest head injury case.

## 6.6 Conclusions

In this paper, the effect of different UAS types on head injury severity is investigated using MBS modelling and simulation. The following five true UAS types have been selected: DJI Phantom III, DJI F450, Tarot LJI500, Parrot Bebop and TrueXS Racing UAS. In addition, a hypothetical UAS is defined in the form of a single-rigid body representation of the DJI Phantom III of same weight. Of the true UAS types, two have similar weight and maximum velocity as the DJI Phantom III and two have significantly lower weight as well as lower and higher maximum speeds. In addition, these UAS types have various differences in materials and design (shape and construction). MBS models of UAS collision with a human head are developed using the principles of MBS modelling. This MBS-based impact modelling approach has been validated and calibrated against experimental impact results for the DJ Phantom III (Huculak, 2016; Stark et al., 2019). In addition to the uncontrolled vertical drop scenario considered in (Rattanaikorn et al., 2020a, 2020b) in this paper also a controlled horizontal flight impact scenario has been studied. For each scenario both head injury (HIC15) level and neck injury (Nij) level have been evaluated using the MBS models. In all cases neck injury level appeared to be negligible relative to head injury level. For each scenario assessed injury level has been converted to probability of fatality (PoF), which is subsequently compared to the PoF value of the RCC (2001) model.

The MBS model findings obtained extend earlier results for DJI Phantom III (Rattanaikorn et al., 2020a, 2020b). One extension is that MBS modelling and simulation

shows that maximum speed of a UAS type has a major influence on injury level and PoF. The Parrot Bebop at its maximum speed of 16 m/s and weight of 0.4 kg has lowest injury level (PoF = 0). The micro racing UAS at its maximum speed of 48 m/s and same weight yields a far higher injury level (PoF = 1). The other UAS types at an intermediate maximum speed of 18 m/s and a higher weight of ~1.2 kg yield intermediate injury levels ( $0.5 < \text{PoF} < 1$ ).

Another extension is the confirmation that in all cases the assessed PoF values are lower than the PoF that is predicted by the RCC model. The RCC model predicts an S-shaped PoF curve as a function of impact energy. The MBS model for the hypothetical UAS type produces a curve that comes nearest to this RCC curve. The likely explanation for the differences is that the MBS model captures blunt force injuries only, whereas the RCC curve also includes debris-explosive impact laceration and penetration contributions to PoF (Feinstein et al., 1968).

The most important extension is the novel insight gained in the roles played by UAS configuration, airframe materials and airframe design. Central in this understanding is the applicable elasticity at the moment of impact of the true UAS versus the hypothetical UAS. Such elasticity may come in the form of flexibility of fuselage, of motor arm or of another component, such as camera gimbal, landing gears, or protective material. This means that the first point of contact plays a key role in the applicable elasticity and therefore in the PoF.

If the first point of contact is the fuselage of the UAS, then the elasticity largely depends on the kind of fuselage material and the fuselage design. Then a stiffer airframe design, such as the shell-structure used in the DJI Phantom III or the carbon reinforced plastic in the True XS Racer UAS yields less elasticity in spreading the full mass of the UAS, and therefore increased PoF.

If the first point of impact is with a motor arm, then the sandwich shell motor arm of the DJI Phantom III yields a small but relevant increase in elasticity relative to the hypothetical UAS without motor arm. For the molded plastic motor arm of the DJI F450 elasticity further increases as a result of which injury level and PoF further decrease.

If the first point of contact is another flexible component, then the elasticity at moment of impact may reduce injury level. One case is clearly demonstrated in uncontrolled vertical impact scenario where the difference in PoF is very large between hard frontal fuselage first contact by hypothetical UAS versus flexible camera gimbal contact at pitch zero by DJI Phantom III, DJI F450 and Tarot LJI500. Another case is clearly demonstrated in controlled horizontal impact scenario where soft polystyrene airframe material in the Parrot Bebop nose cone yields high elasticity at the moment of impact, and therefore a far lower PoF level than the same impact energy from the hypothetical UAS would inflict.

Thanks to the MBS modelling and simulation approach it has been possible to assess the variety in injury level and PoF as a function of differences in first point of impact for different UAS types and under different impact scenarios. For such powerful approach there also are directions for follow-on research. One direction is to extend the MBS based assessment of various UAS impact of human head to human thorax and abdomen, such as has been done for DJI Phantom III by Rattanagraikakorn et al. (2020b). Another direction is to study quadcopter UAS above 1.2 kg as well as fixed wing UAS. A third direction is to address the potential contributions of laceration/penetration to PoF; for example, by the development of a Finite Element Model (FEM) of UAS and an integration of this with human body FEM that have been developed for application in automotive domain, e.g. (Fahlstedt et al., 2016).

## Appendix 6A: MBS Model & Impact Test Comparison

In this appendix a systematic comparison is made between measured  $HIC_{15}$  levels by ASSURE (Huculak, 2016) and by Ohio State University (Stark et al., 2019) versus MBS model-based assessments of  $HIC_{15}$  levels. The UAS considered in these comparisons is the DJI Phantom III. There are three important differences between the test results used from (Huculak, 2016) and test results used from (Stark et al., 2019):

- The  $HIC_{15}$  results from ASSURE are for a 50<sup>th</sup> percentile male Hybrid III crash dummy; while the results from Ohio State University are for a male cadaver;
- The results used from ASSURE focus on uncontrolled vertical drop tests on the human head, while the results used from Ohio State University focus on controlled side impact on the head;
- The results from ASSURE did not measure the eccentricity of the UAS impact on the human head, while Ohio State University measured the eccentricity per test.

For DJI Phantom III, the cases from ASSURE and Ohio State University have been simulated using MBS model under corresponding conditions within MADYMO. More specifically, the differences between ASSURE and Ohio State University test conditions have been taken into account as follows within MADYMO:

- The MBS models used for the human within MADYMO are the 50<sup>th</sup> percentile male Hybrid III crash dummy and the 50<sup>th</sup> percentile male human body respectively;
- The scenarios simulated within MADYMO use the impact geometry and impact speed that applied for each test case from ASSURE and from Ohio State University.
- For the scenarios within MADYMO, the eccentricity of a test case from ASSURE is assumed to be zero, while for a test case from Ohio State University the eccentricity in the MBS simulation is at the same value as measured in each test.

Table 6.7 compares the  $HIC_{15}$  results obtained for the cases used from ASSURE. Table 6.8 compares the  $HIC_{15}$  results obtained for the cases used from Ohio State University.

**Table 6.7. Comparison of Hybrid III crash dummy  $HIC_{15}$  due to DJI Phantom III impact model against used impact tests from ASSURE (Huculak, 2016)**

Impact Case no.	Impact Direction, $\psi$ [°]	Impact Elevation, $\theta$ [°]	UAS Pitch, $\alpha$ [°]	Impact Speed, $V$ [m/s]	Resultant Eccentricity [mm]	$HIC_{15}$		Differ. %	Point of Contact
						Test	MBS		
1	0	0	0	5.3	N/A	24.36	24.8	+1.8	Fuselage
2	0	58	0	14	N/A	125	132.1	+5.5	Camera
3	0	65	0	11.3	N/A	28.6	26.5	-7.6	Camera
4	0	90	0	9.9	N/A	14.2	14	-1.4	Camera
5	0	90	0	15.1	N/A	49.9	63.3	+23.7	Camera

Impact case no. 1 in Table 6.7 is a horizontal impact at a low speed of 5.3 m/s only. Impact cases no. 2-5 in Table 6.7 are similar to the uncontrolled vertical drop impact scenario studied in this paper, with the exception that the impact speed is slightly lower, i.e., between 9.9 and 15.1 m/s versus 18 m/s in the Uncontrolled Vertical drop scenario studied in Section 6.5 of the current paper. For these four cases the MBS model estimated  $HIC_{15}$  level is for two cases lower (-7.6% and -1.4%) and for two cases higher (+5.5% and +23.7%). On average MBS overestimates the  $HIC_{15}$  level for these four cases by +5%. A possible explanation for an overestimation is that the MBS simulation assumes zero eccentricity of the UAS impact on

the head, whereas in realistic tests the eccentricity will be non-zero and is expected to lead to a lower  $HIC_{15}$  level.

**Table 6.8. Comparison of human  $HIC_{15}$  due to DJI Phantom III impact of MBS model against used impact tests from Ohio State University (Stark et al., 2019)**

Impact Case no.	Impact Direction, $\psi$ [°]	Impact Elevation, $\theta$ [°]	UAS Pitch, $\alpha$ [°]	Impact Speed, $V$ [m/s]	Resultant Eccentricity [mm]	$HIC_{15}$		Differ. %	Point of Contact
						Test	MBS		
6	90	0	0	17	28.2	866	689	-22.8	Motor Arm
7	90	0	0	18.5	17.7	1076	886	-19.4	Motor Arm
8	90	0	0	21.5	6	2892	2656	-8.5	Fuselage
9	90	0	0	18.5	43.4	500	527	+5.3	Motor Arm
10	90	58	58	21.5	42.1	929	828	-11.5	Motor Arm
11	90	58	58	18.5	43.4	412	381	-7.8	Motor Arm
12	90	58	58	21.5	20.7	2527	2251	-11.5	Fuselage

Cases no. 6-9 in Table 6.8 are similar to the controlled horizontal flight impact scenario investigated in section 4 of the current paper. The MBS estimated  $HIC_{15}$  values are three time lower (-22.8%, -19.4% and -8.5%) and one time higher (+5.3%). On average MBS underestimates the  $HIC_{15}$  level for these four cases by -11.5%. A similar level of  $HIC_{15}$  underestimation by MBS is found for cases 10-12 in Table 6.8 where the impact elevation is 58° instead of 0°.

Because the off-set is well measured during the Ohio State University tests, the most likely remaining explanation for the systematic difference between the  $HIC_{15}$  levels from the Ohio State University cases 6-11 is that MBS systematically underestimates  $HIC_{15}$  level by 11%. In view of this, it is best to compensate MBS based estimation of  $HIC_{15}$  levels by this 11% systematic underestimation. In the paper this 11% compensation of MBS estimated  $HIC_{15}$  levels is done in Sections 6.4.2 and 6.5.1 prior to the conversion of  $HIC_{15}$  values to PoF values.

## References

- Ambrósio, J., Dias, J., 2007. A road vehicle multibody model for crash simulation based on the plastic hinges approach to structural deformations. *Int. J. Crashworthiness* 12 1, 77–92. doi:10.1533/ijcr.2006.0171
- Arterburn, D., Ewing, M., Prabhu, R., Zhu, F., Francis, D., 2017. FAA UAS Center of Excellence Task A4: UAS Ground Collision Severity Evaluation. Huntsville.
- D. Arterburn, G. Olivares, J. Bolte, R. Prabhu, S. Duma, 2019, Task A14: UAS Ground Collision Severity Evaluation 2017-2019. FAA, Atlantic City, NJ.
- Belcastro, C.M., Newman, R.L., Evans, J., Klyde, D.H., Barr, L.C., Ancel, E., 2017. Hazards Identification and Analysis for Unmanned Aircraft System Operations. 17th AIAA Aviat. Technol. Integr. Oper. Conf. Jun. doi:10.2514/6.2017-3269
- Bernard, E., Johnston, A., 2013. Explosions and Blast Injuries – A Primer for Clinicians. *New England Journal of Medicines* 368 11, 1045-1045. doi:10.1056/nejmicm1203842
- Brake, M.R., 2012. An analytical elastic-perfectly plastic contact model. *Int. J. Solids Struct.* 49 22, 3129–3141. doi:10.1016/j.ijsolstr.2012.06.013
- Campolettano, E.T., Bland, M.L., Gellner, R.A., Sproule, D.W., Rowson, B., Tyson, A.M., Duma, S.M., Rowson, S., 2017. Ranges of Injury Risk Associated with Impact from Unmanned Aircraft Systems. *Ann. Biomed. Eng.* doi:10.1007/s10439-017-1921-6
- Eppinger, R., Sun, E., Bandak, F., Haffner, M., Khaewpong, N., Maltese, M., Kuppa, S., Nguyen, T., Takhounts, E., Tannous, R., Zhang, A., Saul, R., 1999. Development of Improved Injury Criteria for the Assessment of Advanced Automotive Restraint Systems – II, National Highway Traffic Safety Administration (NHTSA).
- Fahlstedt, M., Halldin, P., Kleiven, S., Comparison of multibody and finite element human body models in pedestrian accidents with the focus on head kinematics, *Traffic Injury Prevention*, Vol. 17 (2016), pp. 320-327. doi:10.1080/15389588.2015.1067803
- Feinstein, D.I., Haugel, W.F., Kardatzke, M.L., Weinstock, A., Personnel casualty study. Tech. Rep. Project No. J 6067, Illinois Institute of Technology Research, July 1968.
- Foster, J. V., Hartman, D.C., 2017. High-fidelity multirotor unmanned aircraft system simulation development for trajectory prediction under off-nominal flight dynamics. 17th AIAA Aviat. Technol. Integr. Oper. Conf. 2017 June, 1–19. doi:10.2514/6.2017-3271
- FPV Drone Reviews, 2018. Top 5 Fastest Racing Drones of 2018 - Buying Guide [WWW Document]. URL <https://fpvdronereviews.com/guides/fastest-racing-drones/> (accessed 10.10.19).
- Happee, R., Hoofman, M., Van Den Kroonenberg, A.J., Morsink, P., Wismans, J., 1998. A Mathematical Human Body Model for Frontal and Rearward Seated Automotive Impact Loading. SAE Tech. Pap. 724. doi:10.4271/983150
- Happee, R., Ridella, S., 2000. Mathematical human body models representing a mid size male and a small female for frontal, lateral and rearward impact loading. IRCOBI Conf. Proc. September, 1–18. doi:10.1378/chest.120.6\_suppl.464S
- Huculak, R., 2016. NIAR UAS Drop Testing Report. Wichita State University, Doc. CDL-TR-17-2163-UA01.

- Jenefeldt, F., Thomson, R., 2004. A methodology to assess frontal stiffness to improve crash compatibility. *Int. J. Crashworthiness* 95, 475–482. doi:10.1533/ijcr.2004.0303
- Klinich, K., Saul, R., Auguste, G., Backaitis, S., Kleinberger, M., 1996. Techniques for Developing Child Dummy Protection Reference Values, Measurement.
- Koh, C.H., Deng, C., Li, L., Zhao, Y., Tan, S.K., Chen, Y., Yeap, B.C., Li, X., Low, K.H., 2018a. Experimental and simulation weight threshold study for safe drone operations, in: *AIAA Information Systems-AIAA Infotech at Aerospace*, 2018. Kissimmee, Florida, pp. 1–11. doi:10.2514/6.2018-1725
- Koh, C. H., Low, K.H., Li, L., Zhao, Y., Deng, C., Tan, S.K., Chen, Y., Yeap, B.C., Li, X., 2018b. Weight threshold estimation of falling UAVs (Unmanned Aerial Vehicles) based on impact energy. *Transp. Res. Part C Emerg. Technol.* 93 June, 228–255. doi:10.1016/j.trc.2018.04.021
- Magister, T., 2010. The small unmanned aircraft blunt criterion based injury potential estimation. *Saf. Sci.* 48 10 , 1313–1320. doi:10.1016/j.ssci.2010.04.012
- Mukherjee, S., Chawla, A., Nayak, A., Mohan, D., 2006. Rollover crashworthiness of a rural transport vehicle using MADYMO. *Int. J. Crashworthiness* 11 5, 495–503. doi:10.1533/ijcr.2005.0121
- Parr, M.J.C., Miller, M.E., Bridges, N.R., Buhrman, J.R., Perry, C.E., Wright, N.L., 2012. Evaluation of the Nij neck injury criteria with human response data for use in future research on helmet mounted display mass properties. *Proc. Hum. Factors Ergon. Soc.* 2070–2074. doi:10.1177/1071181312561439
- Parrot Drones SAS, 2019. Parrot Bebop 2 FPV drone [WWW Document]. URL <https://www.parrot.com/global/drones/parrot-bebop-2-fpv> (accessed 10.10.19).
- Prasad, P., Mertz, H.J., 1985. The Position of the United States Delegation to the ISO Working Group 6 on the Use of HIC in the Automotive Environment. *SAE Tech. Pap.* January 1985. doi:10.4271/851246
- Rattanagraikanakorn, B., Schuurman, M.J., Gransden, D.I., Happee, R., Wagter, C. De, Sharpanskykh, A., Blom, H.A.P., 2019. Modelling Head Injury due to Unmanned Aircraft Systems Collision: Crash Dummy vs Human Body, in: *AIAA Aviation 2019 Forum*. Dallas, Texas. doi:10.2514/6.2019-2835
- Rattanagraikanakorn, B., Gransden, D.I., Schuurman, M., De Wagter, C., Happee, R., Sharpanskykh, A., Blom, H.A.P., 2020a. Multibody system modelling of unmanned aircraft system collisions with the human head. *Int. J. Crashworthiness*, Vol. 25 (2020), pp. 689-707.
- Rattanagraikanakorn, B., Blom, H.A.P., Sharpanskykh, A., de Wagter, C., Jiang, C., Schuurman, M.J., Gransden, D.I., Happee, R., 2020b. Modeling and Simulating Human Fatality due to Quadrotor UAS Impact, in: *AIAA Aviation 2020 Forum*. doi:10.2514/6.2020-2902
- Rattanagraikanakorn, B., Schuurman, M., Gransden, D.I., Happee, R., De Wagter, C., Sharpanskykh, A., Blom, H.A.P., 2020c. Modelling Head Injury due to Unmanned Aircraft Systems Collision: Crash Dummy vs Human Body. *Int. J. Crashworthiness* 1–14. doi:10.1080/13588265.2020.1807687
- RCC (Range Commanders Council), 2001. Range Safety criteria for Unmanned Air Vehicles, Rationale and methodology supplement; Supplement to Document 323-99



- Schmitt, K.-U., Niederer, P.F., Cronin, D.S., Morrison III, B., Muser, M.H., Walz, F., 2019. Trauma Biomechanics, Trauma Biomechanics. doi:10.1007/978-3-030-11659-0
- Stark, D.B., Willis, A.K., Eshelman, Z., Kang, Y.S., Ramachandra, R., Bolte, J.H., McCrink, M., 2019. Human Response and Injury Resulting from Head Impacts with Unmanned Aircraft Systems, Stapp car crash journal. doi:10.4271/2019-22-0002
- TASS International, 2017a. MADYMO Human Body Models Manual Release 7.7.
- TASS International, 2017b. MADYMO Theory Manual Version 7.7. MADYMO Utility Manual.
- Toyota, 2015, Documentation THUMS, AM50 occupant model academic version 5.0\_20150527, Toyota Motor Corporation.
- Tyrell, D.C., Severson, K.J., Marquis, B.P., 1995. Analysis of occupant protection strategies in train collisions. Am. Soc. Mech. Eng. Appl. Mech. Div. AMD 210 April 2015, 539–557.
- Vadlamudi, S., Blundell, M., Zhang, Y., 2011. A multi-body systems approach to simulate helicopter occupant protection systems. Int. J. Crashworthiness 16 2, 207–218. doi:10.1080/13588265.2011.554203



---

## Conclusion

*This chapter provides a discussion and conclusion of all research results obtained in this thesis as well as scientific contributions and recommendations for future research*

Since UAS operations are expected to be operated over people in rural and urban areas, human become more exposed and vulnerable to UAS collisions if accidents occur. An adequate approach to evaluate and mitigate ground third-party risks (TPR) of UAS operation is needed as one of the key enablers of the operation. This thesis addresses one of the key components of the TPR framework that is the quantification of UAS collision consequence on human on the ground. The main aim of this thesis is:

**To develop a quantitative, physical model-based collision consequence model for UAS impact on human body.**

Through a connected series of works performed in this thesis, the main aim has been achieved with various findings found in each chapter. These findings and result synthesis are discussed here in this concluding chapter. This chapter is structured as follow. First, the six sub-objectives posed in the introduction are addressed and answered. This includes summarization of key findings and discovered insights. Then, the contributions of the thesis, and future works are discussed.

## **7.1 Results obtained for Research Objectives**

Six research sub-objectives related to the main thesis aim are addressed. The main conclusion drawn for each sub-objective is presented below.

**Objective 1: To characterize collision consequence types due to UAS operations within very low-level airspace under the novel UTM concept**

Safe integration of UAS operations into manned airspace requires a good understanding of UAS collision risks on other airspace users or human on the ground. To assess collision risk of a complex UTM system where UASs are expected to be operated in, there is a need to develop a systematic approach to characterize both frequency and consequence of various UAS collisions.

In Chapter 2, a method for characterizing UAS collision consequences in future UTM system, focusing on only the VLL UAS operations which are below 500 ft. The proposed method consists of 5 systematic steps; (i) UTM dimension analysis, (ii) object identification and classification, (iii) zone of impact analysis, (iv) materials identification and classification and (v) collision consequence analysis. These steps would allow an establishment of a risk picture of the possible collisions with UAS and possible consequences that entail.

With this step-wise approach, the intermediate relations between the initiating events and the collision consequence outcomes are established through a systematic analysis and characterization process. This approach lays a basis for follow-up research which can benefit from this logical and well-structured decomposition. This helps organizing the detailed quantitative modeling and analysis of UAS collision consequences.

**Objective 2: To develop a parameterized impact model for blunt force injury assessment of UAS impact on human body.**

In Chapter 3, a parameterized MBS model of DJI Phantom III UAS was developed and integrated with a validated crash dummy and human body models. The DJI phantom III was selected to represent a typical small quadcopter UAS of the 1.2 kg weight class. The MBS modelling technique is an extension of lump mass modelling which consists of multiple rigid bodies, joints and restraints. Each joint is restrained using Kelvin spring and damper to replicate force-deflection characteristics of the real structural component that the joint represent. Force-deflection curve was obtained experimentally. To model impact interaction

between a crash dummy (or the human body) and a UAS, force penetration contact model based on Hertz model was derived analytically. This contact modelling also applies to interactions between UAS internal parts.

For validation, the DJI Phantom III MBS model is integrated with the Hybrid III crash dummy to simulate various impact conditions which were then compared against experimental drop tests on real crash dummies performed by ASSURE. The validation results show good convergence between the MBS model and impact data.

The model constructs of the MBS model significantly simplify the actual structure into a connected rigid body system. This gives the MBS a key strength in fast computational time over other impact modelling method. Hence, this means that a large impact scenario of UAS collision on human body can be simulated in a feasible amount of time and allowing a wide range of sensitivity analysis.

Using the validated UAS model, impact collision of the UAS collision on the head of 50th percentile male human was performed. Frontal side and rear impact on the human head were evaluated at different impact elevation angles. The evaluation of human head injury was based on the head injury criterion ( $HIC_{15}$ ). The neck injury was also evaluated using the predictor  $N_{ij}$  criterion. The injury evaluation result shows that human head can suffer from serious injury as a result of UAS impact but only non-serious neck injury was observed. This implies that the UAS with a mass of approximately 1.2 kg can inflict serious head injury on the human body.

The findings also revealed discrepancies in the measured head injury between the Hybrid III crash dummy and the human body models. Such discrepancies can be significant especially in a vertical load direction. This asks for further investigations to better understand the differences and underlying reasons. This investigation was performed in the Chapter 4.

**Objective 3: To investigate differences in head and neck injury levels on a Hybrid III dummy and on a human body due to UAS collisions.**

In Chapter 3, an investigation of UAS collision shows discrepancies of the measured head and neck injuries between the Hybrid III crash dummy and the human body models. This leads to Objective 3 where the investigation on the differences in head and neck injury between the 50<sup>th</sup> percentile Hybrid III crash dummy and a 50<sup>th</sup> percentile human body subjected to UAS collision were performed. The work for this sub-objective is presented in Chapter 4

The results reveal that a Hybrid III crash dummy is very well designed for horizontal-frontal and horizontal-rear impact directions. At these load directions, the measured head acceleration and neck force are very similar to a validated human model. The hybrid III crash dummy is not particularly well suited for horizontal-side impact or vertical load direction. Under these conditions, the crash dummy neck columns show to be substantially stiffer than the human body neck. This results in lower head acceleration in the Hybrid III crash dummy and hence, lower head injury but higher neck injury.

The main reason for the discrepancies of head and neck injury between the two models is the difference in neck complex. The Hybrid III has a straight neck column which limits head movement, especially in the vertical direction. Load applies in the vertical direction is transferred to the thorax region leading to lower head movement and larger neck force. This is different in human body model where human neck consists of complex small vertebrae which allow larger neck deformation. This makes human neck complex much more compliance and allowing the head mass to accelerate faster upon impact.

The key added value of this investigation is that the choice of the surrogate model has a high impact on the predicted injury and that the difference in results could have substantial effects on risk evaluations. If an inappropriate surrogate model is used under certain load conditions, this may lead to an unrealistic prediction of collision consequence.

Also, the results obtained revealed novel insights into how different impact condition can affect injury level, that is, a slight change in point of contact due to a shift in position or angle could potentially lead to completely different injury level. This motivates a subsequent work in Chapter 6 (under Objective 5) that is to investigate effect of impact parameters such as UAS impact positions, attitudes, off-set, or angle of attacks on head injury severity.

**Objective 4: To investigate the differences between the MBS model, the RCC curves, and the BC curves for DJI Phantom III impact of human head, thorax, and abdomen.**

In literature studies, two existing UAS collision consequence models identified are the RCC curve and the BC curve. These models predict PoF of UAS impact on human head, thorax and abdomen. However, these two models show large discrepancies in the predicted PoF which raise the question on how representative these models are for UAS collision on human scenario.

The work in Chapter 5 investigates the differences in PoF assessment by an MBS model versus those from an RCC curve and BC curve. An MBS model of the DJI Phantom III is presented and compared against the other two models. The comparison is done for impact on the head, thorax and abdomen of 50<sup>th</sup> percentile male human body.

For head impact, the RCC predicts highest PoF and BC predicts the lowest PoF when compared to the MBS model simulated under horizontal flight impact on human head. If UAS is simulated under vertical drop conditions, then the MBS model predicts lowest PoF when compared to the RCC and BC models. This shows that variation in UAS impact attitude affect human PoF. However, such variations in impact attitude are not captured by the RCC or BC models.

For thorax and abdomen impact, horizontal flight impact on human body is simulated using the MBS model. For this case, the RCC predicts higher PoF and the BC predicts lower PoF when compared to the MBS model. For impact on thorax and abdomen,

Taking all the results together, it is shown that the RCC models overestimates PoF of human subjected to UAS impact while the BC models under predict it. The reason for the RCC to over predict the PoF is because the RCC model was developed based on injury or fatality due to small debris explosion, which also involves penetration or laceration type injuries. In addition, the BC model under predicts human PoF due to UAS impact because it was developed based on impact tests on cadavers and animals where the diameter of the impactor is much larger than small debris explosion of the RCC or than the size of UAS.

**Objective 5: To investigate the effect of variations in UAS types on human injury and fatality.**

In Chapter 2, the characterization process of UAS collision consequence shows that there is a wide-range of UAS types participating in the novel UTM concept. This is due to the wide-spectrum of applications that UAS can perform, ranging from aerial racing using micro UAS to parcel delivery using large UAS. What entails is the variations in UAS size, mass and airframe design which can result in varying degree of human injury upon collision.

In Chapter 6, the investigation of the effect of UAS types variation on human injury levels is performed. The DJI Phantom III MBS model is used as a baseline for the model extension to other UAS types. Five others small UAS types were selected based on varying

mass, maximum speed, airframe materials and configuration design. The following five true UAS types have been selected: DJI Phantom III, DJI F450, Tarot LJI500, Parrot Bebop and TrueXS Racing UAS. In addition, a hypothetical UAS is defined in a form of a single rigid body representation of the DJI Phantom III with the same mass. These UAS models are developed and integrated with a validated MBS model of the 50<sup>th</sup> percentile human body. Impact simulations for horizontal flight and vertical drop impacts were performed for all UAS types. For each scenario, both head injury level and neck injury level were evaluated. For each scenario assessed head injury level was converted to a probability of fatality (PoF), which was subsequently compared to the RCC model.

The findings show that the maximum speed of UAS types has a major influence on impact injury severity and PoF. A micro racing UAS with a mass of 0.4 kg and a maximum speed of 48 m/s yields a higher head injury than a 1.2 kg DJI Phantom III with a maximum speed of 18 m/s. This shows that the size or mass of UAS alone is not adequate for the categorization of UAS risk level as was commonly done in the UAS rules and regulations. The maximum kinetic energy of UAS would be a better criterion for UAS class categorization.

Through the investigation of various UAS types with different design, it was found that UAS configuration, airframe materials and airframe design play an important role in the resulting impact injury. These factors contribute to the overall elasticity of UAS which helps to absorb and dampening impact energy. UAS airframe designs that are highly stiff, such as the shell design of the DJI Phantom III fuselage can inflict high impact injury, and the degree of injury reduces as airframe stiffness decreases.

Another aspect effecting injury levels is the applicable elasticity at the first point of contact which is influenced by UAS design configuration. Elastic components such as flexible landing gear, camera gimbal or soft protective materials can help to reduce inflicted impact injury if the first point of contact occurs at these elastic components. One case clearly demonstrated in an uncontrolled vertical impact scenario where the difference in PoF is very large between hard frontal fuselage first contact by hypothetical UAS versus flexible camera gimbal contact at pitch zero by DJI Phantom III, DJI F450 and Tarot LJI500. The injury level sustained by these two cases varies from fatal to non-serious injuries. These findings show how important elastic protective components can help reducing impact injury on human body. With the MBS modelling and simulation approach, it is now possible to assess the variation of injury level and PoF as a function of varying point of contact for different UAS types and of varying impact scenarios.

## **7.2 Contributions**

This thesis made contributions to three main domains: UAS impact modelling, collision consequence modelling of UAS impact on human body and ground third-party risk assessment of UAS operations.

### ***UAS Impact Modelling***

The studies in Chapter 3 to 6 on UAS impact modelling which applied the MBS modelling technique has not been performed before for the UAS impact on human body. The modelling work performed in this thesis provides a framework for UAS on human impact modelling based on MBS modelling approach, which includes system modelling, parameters calibration and validation.

Future researchers can employ this MBS modelling technique for impact analysis of UAS collision on human body, or similar types of blunt force impact analysis. The modelling

approach introduced in this thesis can also be used as a guideline for the model development process where impact validation data is scarce and that calibration data needs to come from different measured sources.

### ***Collision Consequence Modelling of UAS Impact on Human Body***

In literature, there are two main existing collision consequence models for UAS impact on human body; the RCC and the BC. These two models have been used in many UAS TPR assessment. However, a comparative study of MBS model results versus RCC and BC curves reveal large discrepancies in predicted PoF due to human impact of a UAS.

Upon investigation, it was realized that the two models were developed based on experimental impact data that were of different type. The RCC was derived from small-debris explosive test on human, while the BC was derived from large object impact on human. This quickly raise the question on whether these models are realistic representations of UAS impact on human body.

Thanks to the MBS impact model of UAS on human body, a more representative collision consequence model has been established. The MBS model developed in this work has three main advantages over the RCC and the BC; (i) MBS model directly represents UAS impact on human body, (ii) MBS model has capability to capture to account for variation in UAS impact parameters and (iii) MBS model results correspond better with experimental results.

For the first advantage, the MBS model was developed to directly represents UAS impact on human body. The modelling process considers realistic UAS models and their inertial characteristics. Thus, the predicted injury of human body in this work can be said to realistically represent the actual impact events between UAS and a real human. This is not the case for the RCC and BC model.

The second advantage is the flexibility to simulate a wide-range of impact scenario. As shown in Chapter 3 and 6, the MBS model is capable of simulating variations in UAS impact attitude and location on the human body parts, or the sensitivity of UAS point of contact on human injury. These variations have substantial effect on the predicted human impact injuries and have not been fully assessed before. Sensitivity studies of these parameters greatly contributes to a better understanding of the collision consequence of UAS on human and what parameters effect the degree of sustained injury.

Apart from serving as an alternative collision consequence model for UAS impact on human, the studied performed with MBS model in Chapter 5 also provides an answer to the discrepancies found between the RCC and BC models.

### ***Ground Third-Party Risk Assessment of UAS Operations***

The main motivation of this work has been to develop a collision consequence model to be used in third-party risk (TPR) analysis of UAS operations. The work performed in this thesis contributes to future research on UAS safety risk analysis by serving as one of the sub-components of TPR modelling approach that is used to predict the probability of fatality (PoF) of human subjected to UAS collision. The model developed in this thesis offers a possibility to evaluate UAS collision risk under various realistic impact scenarios. Future TPR research can either utilize the PoF findings from this work or integrate the MBS impact model into TPR simulator.

MBS approach allows to be applied to various other drone types than have been studied in this thesis. Also, other variables like human body size can be extended to the size other than



the 50<sup>th</sup> percentile male human. Such extensions would further extend TPR assessment to account for real-world variations of UAS types, or human body sizes and genders.

### 7.3 Future Work

Collision consequence model for UAS impact on human body based on MBS model proposed in this thesis is one of the important 5 sub-models for the UAS TPR analysis framework mentioned in the introduction. This model can be used to predict probability of fatality of human due to UAS blunt force impact.

A logical follow-on work extending from the MBS work in this thesis is to assess the effect of off-centred collision of UAS on human head, thorax and abdomen. Since the off-centred collision have effect on the resulting human PoF, accounting for such variations is important to TPR assessment.

Another aspect that can be easily extend to is to expand the variation of human body sizes under investigation. In this thesis, only 50<sup>th</sup> percentile human male body is evaluated for UAS impact injury. However, since the general population consists of various human body sizes and genders, it is needed to include modelling and simulation of other human sizes, such as, 5<sup>th</sup> percentile female or 95<sup>th</sup> percentile male human. This variation of human sizes should be evaluated and integrated in TPR analysis of UAS operations.

Furthermore, fatality due to blunt force impact injury is the first step needed to better understand and assess injury from UAS collision. However, in order to completely assess human injury arises from UAS collision, other injury types apart from blunt force impact injury need to be evaluated and integrated into a complete collision consequence model. Injury type such as penetration or laceration injuries due to UAS components are also important, but yet still understudied. Such injury may come from UAS blades rotating at high speed that can slice through skin tissue and damage critical internal organs or artery vein. ASSURE [1,2] have performed research on this using synthetic skin to study the skin depth of blade laceration. However, the data obtained is not yet sufficient to establish fatality threshold or applied directly in UAS impact scenario. To study penetration and laceration injuries, future work needs to employ different modelling approach than MBS modelling.

With the MBS modelling approach, its fast computational time only allows impact contact modelling between relatively large surfaces and, hence, permitting only a blunt impact force evaluation. However, local deformation and penetration of mesh is not possible with such an approach. This also means that human injury mechanism at skin tissue and organ level are not possible to be evaluated. To overcome this limitation, other modelling techniques need be resorted to.

In this thesis the MBS modelling approach has been applied to quadcopter UAS only. It would be a logical direction to also apply this MBS approach to other types, such as fixed wing UAS. Based on blunt-force injury, fixed-wing UAS can have higher kinetic energy which may lead to higher impact injury. The same MBS modelling approach may be applied to perform such study.

For the collision consequence model developed in this work, an area of improvement in future work is to extend validation of UAS impact on human body. The model in this work is already well validated for low and high speed on both crash dummy and human cadaver heads. This validation also includes various UAS impact angles and positions. Thus, the model can be used with confident on human head evaluation. However, validation of the MBS model for thorax and abdomen hit remains to be done. Therefore, future work may include

experimental work to obtain such data set for validation of the model, and an MBS model extension to UAS hitting human back and spine including validation of such case.

## References

- [1] Arterburn, D., Ewing, M., Prabhu, R., Zhu, F., and Francis, D., “FAA UAS Center of Excellence Task A4: UAS Ground Collision Severity Evaluation Revision 2.”
- [2] Huculak, R., “NIAR UAS Drop Testing Report,” Wichita: 2016, URL: [http://www.assureuas.org/projects/deliverables/a11/NIAR Test Report - FAA-UAH UAS Drop Testing.pdf](http://www.assureuas.org/projects/deliverables/a11/NIAR%20Test%20Report%20-%20FAA-UAH%20UAS%20Drop%20Testing.pdf).



---

# Curriculum Vitae

Borrdephong Rattanagraikanakorn was born on 26<sup>th</sup> April 1989 in Bangkok, Thailand. From 2008 to 2012, he attended Chulalongkorn University in Bangkok, Thailand where he received his BEng degree in Aerospace Engineering. During this time, Borrdephong established the first AIAA student branch in Southeast Asia, and started a UAS design team which then became the first team from Asia to participate in AIAA Aircraft Design/Build/Fly 2011 competition in Arizona, USA. In 2013, he moved to London, United Kingdom to pursue an MSc degree in Aerospace Engineering at Kingston University where the focus of his study was on drone design. In 2014, Borrdephong received his MSc degree from Kingston University with a final dissertation on the design of blended wing body tactical UAS.

After graduation in 2014, he returned to Chulalongkorn University as a lecturer and program coordinator for Aerospace Engineering programme. During his appointment at Chulalongkorn, he started UAS educational courses in Thailand and introduced UAS design to college students. He also worked with Thai government on UAS research and development for maritime survey and disaster relief operation. As the programme coordinator, he also worked on establishing international academic collaboration with universities abroad and also sat in the curriculum committee for international engineering programme.

In 2017, Borrdephong began his position as a PhD candidate at the faculty of Aerospace, Delft University of Technology (TU Delft) where he worked cross-disciplines with multiple departments, namely, Structural Integrity & Composite (SI&C), Air Transport & Operations (ATO) and MavLab. During his PhD, Borrdephong undertook research on collision consequence modelling of UAS impact on human using multibody system modelling technique. He also enrolled at doctoral training programme at TU Delft and undertook coaching tasks for three DSE projects.

In January 2021, Borrdephong commenced his role as a lecturer in Aerospace Engineering at the International School of Engineering (ISE), Faculty of Engineering, Chulalongkorn University in Bangkok, Thailand.



---

# List of Publications

- **Rattanagraikanakorn, B.**, Blom, H. A., Gransden, D. I., Schuurman, M. J., de Wagter, C., Sharpanskykh, A., and Happee, R., “Variation in Human Injury and Fatality from Impacts by Different UAS Types of Similar Weight”, Manuscript submitted for publication, September 2021.
- **Rattanagraikanakorn, B.**, Blom, H. A., Sharpanskykh, A., de Wagter, C., Jiang, C., Schuurman, M. J., Gransden, D. I., and Happee, R., “Modeling and Simulating Human Fatality due to Quadrotor UAS Impact,” AIAA Aviation 2020 Forum, 2020.
- **Rattanagraikanakorn, B.**, Gransden, D. I., Schuurman, M., De Wagter, C., Happee, R., Sharpanskykh, A., and Blom, H. A. P., “Multibody System Modelling of Unmanned Aircraft System Collisions With The Human Head,” International Journal of Crashworthiness, vol. 25, 2020, pp. 689-707.
- **Rattanagraikanakorn, B.**, Schuurman, M., Gransden, D. I., Happee, R., De Wagter, C., Sharpanskykh, A., and Blom, H. A. P., “Modelling Head Injury due to Unmanned Aircraft Systems Collision: Crash Dummy vs Human Body,” International Journal of Crashworthiness, 2020, pp. 1–14.
- **Rattanagraikanakorn, B.**, Schuurman, M. J., Gransden, D. I., Happee, R., Wagter, C. De, Sharpanskykh, A., and Blom, H. A., “Modelling Head Injury due to Unmanned Aircraft Systems Collision: Crash Dummy vs Human Body,” AIAA Aviation 2019 Forum, Dallas, Texas: 2019.
- Schuurman, M., **Rattanagraikanakorn, B.**, Kassapoglou, C., De Breuker, R., “Urban Air Mobility (UAM) Vehicle Design Considerations to Facilitate Future Accident Investigation,” AIAA Aviation 2019 Forum, Dallas, Texas: 2019.
- **Rattanagraikanakorn, B.**, Sharpanskykh, A., Schuurman, M., Gransden, D., Blom, H. A. P., and De Wagter, C., “Characterizing UAS Collision Consequences in Future UTM,” AIAA Aviation 2019 Forum, Atlanta, Georgia: 2018



PRAIYA  
THANYARAT  
THITHEVATHI  
PISISENEE  
PIMPHAPIT